National Research Council Canada
Conseil national de recherches Canada

THREE-DIMENSIONAL SWEPT SHOCK/TURBULENT BOUNDARY-LAYER SEPARATIONS WITH CONTROL BY AIR INJECTION

BY

D. J. PEAKE

NATIONAL AERONAUTICAL ESTABLISHMENT

OTTAWA

JULY 1976

NRC NO. 15579
ISSN 0077-5541

AERONAUTICAL
REPORT
LR-592

THREE-DIMENSIONAL SWEPT SHOCK/TURBULENT BOUNDARY-LAYER SEPARATIONS WITH CONTROL BY AIR INJECTION

DECOLLEMENT EN TROIS DIMENSIONS DE LA COUCHE LIMITE TURBULENTE A CAUSE D'UNE ONDE DE CHOC OBLIQUE, AVEC CONTROLE PAR INJECTION D'AIR

by/par

D.J. PEAKE

L.H. Ohman, Head/Chef
High Speed Aerodynamics Laboratory/
Laboratoire de l'aérodynamique à hautes vitesses

F.R. Thurston
Director/Directeur

SUMMARY

Experimentally determined wall pressure distributions, local surface shear stresses and their directions, and detailed turbulent boundary-layer traverses in near zero heat transfer conditions, are presented through skewed shock/boundary-layer interaction regions generated by a wedge standing normal to a test wall. The mainstream Mach numbers were 2 and 4, while the Reynolds number based on the undisturbed test boundary-layer thickness of 0.2-in., growing along the nozzle sidewall of the NAE 5 X 5-in. blowdown wind tunnel, was $\sim 2 \times 10^5$.

Tangential air injection at a jet exit Mach number of 3 was then introduced into the 3D shock separated Mach 2 boundary layer, to control the separation. The optimum direction of blowing was found to be along a line somewhere between the deflected surface of the wedge and the line of the oblique shock wave.

SOMMAIRE

Les pressions statiques sur la paroi d'essai, les frottements de surface avec les directions, et quelques profils de vitesse, sont présentés aux interactions en trois dimensions, dans lesquelles une onde de choc oblique (produite par un dièdre debout sur la paroi) a rencontré une couche limite turbulente. Les nombres de Mach à l'écoulement non-perturbé étaient 2 et 4, en même temps le nombre de Reynolds était 2×10^5, calculé avec l'épaisseur non-perturbé de la couche limite ($\simeq$ 0.2-inch). La couche limite existait sur la paroi du col convergent-divergent dans la soufflerie à jet d'air comprimé "NAE 5 X 5-inch".

L'injection d'air tangent à la paroi, au décollement en trois dimensions de la couche limite (produit par une onde de choc oblique dans un écoulement non-perturbé au nombre de Mach 2) afin de contrôler le décollement. La meilleure direction de la paroi-jet était trouvée le long d'une ligne entre la surface du dièdre et la projection sur la paroi de l'onde de choc oblique.

CONTENTS

CONTENTS (Cont'd)

CONTENTS (Cont'd)

TABLES

TABLES (Cont'd)

ILLUSTRATIONS

ILLUSTRATIONS (Cont'd)

ILLUSTRATIONS (Cont'd)

ILLUSTRATIONS (Cont'd)

ILLUSTRATIONS (Cont'd)

ILLUSTRATIONS (Cont'd)

ILLUSTRATIONS (Cont'd)

APPENDIX

SYMBOLS

Symbol	Definition
a	local speed of sound
a_{E1}	local speed of sound at outer edge of boundary layer at reference measuring Station 1 — see Figure 15
a_W	local speed of sound at wall
α_C	angle of incidence of 2D aerofoil section, corrected for tunnel boundary constraints — see Figure 3
α_W	angle of incidence of 2D aerofoil, measured in wind tunnel flow, uncorrected for tunnel boundary constraints — see Figure 3
blc	boundary-layer control
β	angle between local resultant velocity vector in the viscous flow and external stream resultant velocity vector at the outer edge of the boundary layer
β_{CL}	angle between resultant velocity vector in the viscous flow and tunnel centre-line
β_{CLE}	angle between resultant velocity vector at the outer edge of the boundary layer and tunnel centre-line

SYMBOLS (Cont'd)

Symbol	Definition
$\mathfrak{C}$	centre-line
C_D	total drag coefficient of 2D aerofoil section, sum of corrected profile drag measurement from wake survey and momentum coefficient of slot (plus jet flap) blowing air — see Figure 3
C_{DWC}	profile drag measurement from wake survey, corrected for slot (plus jet flap) blowing momentum added from source external to tunnel flow
C_F	local skin friction coefficient
C_μ	blowing momentum coefficient — see Section 1.3
C_L	lift coefficient of 2D aerofoil section — see Figure 3
c_p	specific heat of air at constant pressure
C_{pp}	surface pitot pressure coefficient = $(P_p - p)/q_E$
d_c	outer dimension of wall pitot in direction of traverse (whether circular tube or rectangular pitot)
d_s	diameter of static pressure orifice
Δ	displacement correction for circular or rectangular pitot probe
δ	boundary-layer thickness
δ_{995}	boundary-layer thickness where local resultant velocity is 0.995 of velocity at boundary-layer edge
$\delta_1{}^*$	streamwise displacement thickness = $\int_o^{h_E} \left(1 - \frac{\rho u}{\rho_E u_E}\right) dh$
$\delta_2{}^*$	crossflow displacement thickness = $-\int_o^{h_E} \frac{\rho v}{\rho_E u_E} dh$
δ_w	deflection angle of wedge shock generator measured with respect to tunnel centre-line
δ_{wi}	deflection angle of wedge at which incipient separation is encountered
h	height above test surface
h_E	height of outer edge of boundary layer above test surface
H	shape factor of streamwise boundary-layer profile, = $\delta_1{}^*/\theta_{11}$

SYMBOLS (Cont'd)

Symbol	Definition
HVG	height of vortex generator
$\dot{m}_j$	mass flux of blc jet
M	local mean Mach number
M_E	Mach number at outer edge of boundary layer
M_{E1}	Mach number at outer edge of boundary layer at reference measuring Station 1 — see Figure 15
M_∞	Mach number in the undisturbed freestream (considered to be the same as M_{E1})
M_j	local Mach number at exit of supersonic jet blowing nozzle for blc
M_N	component of Mach number in plane normal to swept shock wave
M_p	local Mach number at the surface pitot tube
$M_{\tau W}$	Mach number at the wall based on shear stress velocity and local speed of sound, $= u_{\tau w}/a_w$
M(P/PO)	Mach number calculated from ratio of static to stagnation pressure, see Equation (4.2.1)
M(P/PIT)	Mach number calculated from Rayleigh pitot relation, see Equation (4.2.9)
μ	absolute coefficient of viscosity
μ'	absolute coefficient of viscosity, corresponding with intermediate temperature, T′
μ_E	absolute coefficient of viscosity at outer edge of boundary layer, corresponding with T_E
μ_W	absolute coefficient of viscosity at wall, corresponding with T_W
υ	kinematic viscosity, $= \mu/\rho$
υ_E	kinematic viscosity at outer edge of boundary layer
υ_W	kinematic viscosity at wall
p	static pressure
p_B	pressure measured in static hole immediately upstream of obstacle block
p_E	static pressure at outer edge of boundary layer
p_1	static pressure at reference measuring Station 1 — see Figure 15
p_∞	static pressure in the undisturbed freestream (considered to be the same as p_1)

SYMBOLS (Cont'd)

Symbol	Definition
p_2	calculated static pressure, downstream of swept shock, according to 'Oblique Shock Tables'
P_o, PO	stagnation pressure of undisturbed mainstream flow
P_{o_j}, p_{o_j}	stagnation pressure of blc jet blowing air
P_p	pitot pressure
ϕ	angle defined on Johnston's triangular model for crossflow — see Figure 11(a)
q	dynamic pressure = $0.7\ pM^2$
q_E	dynamic pressure at outer edge of boundary layer
q_{E1}	dynamic pressure at outer edge of boundary layer at reference measuring Station 1
q_p	junction point velocity on Johnston's triangular model for crossflow — see Figure 11(a)
R	recovery factor for cobra probe thermocouple
R_D	Reynolds number based on pitot dimension, d_c, and local mainstream flow quantities
R_δ	Reynolds number based on boundary-layer thickness and local mainstream conditions
R_{ft}, R_{FT}	unit Reynolds number, based on undisturbed mainstream conditions
R_{FT1}	unit Reynolds number, based on undisturbed mainstream conditions at reference Station 1
$R_{h/2,\infty}$	Reynolds number based on half-height of cobra probe face and local mainstream flow conditions
R_T	ratio of measured total temperature to stagnation temperature (T_o) when calibrating probe thermocouple in a supersonic mainstream flow
$R_{\theta_{11}}$	Reynolds number based on streamwise momentum thickness of boundary layer and local mainstream conditions
ρ	mean density within boundary layer
ρ_E	mean density at outer edge of boundary layer
ρ_{E1}	mean density at outer edge of boundary layer at reference measuring Station 1 — see Figure 15
ρ_j	local density in blc jet flow at jet exit
ρ_{o_j}	density according to stagnation pressure and temperature in blc jet flow

SYMBOLS (Cont'd)

Symbol	Definition
ρ_W	mean density at wall corresponding with local wall temperature
s	span of blc jet blowing slot, = 3.60-in.
T	static temperature
T_{AW}, TAW	adiabatic wall temperature
T_{AW1}	adiabatic wall temperature at reference measuring Station 1 - see Figure 15
T'	intermediate temperature, defined by Equation (4.2.28)
T_E	static temperature at outer edge of boundary layer
T_{E1}	static temperature at outer edge of boundary layer at reference measuring Station 1 — see Figure 15
T_o	stagnation temperature measured in settling chamber of wind tunnel
T_{PM}	uncorrected total temperature measured by cobra probe thermocouple
T_{PC}	corrected total temperature at cobra probe thermocouple
T_{PCE}	corrected total temperature at outer edge of boundary layer
T_{TOT}	total temperature
T_{TOTE}	total temperature at outer edge of boundary layer
T_W	wall temperature
τ_W	shear stress at wall
2D	two-dimensional
3D	three-dimensional
Θ_j, θ_j	rotation of blc jet blowing nozzle unit with respect to perpendicular to tunnel centre-line in (x, y) — plane
θ_{11}	$\int_o^{h_E} \frac{\rho u}{\rho_E u_E} \left(1 - \frac{u}{u_E}\right) dh$
θ_{12}	$\int_o^{h_E} \frac{\rho v}{\rho_E u_E} \left(1 - \frac{u}{u_E}\right) dh$

} Various momentum thicknesses in streamline co-ordinates

SYMBOLS (Cont'd)

Symbol	Definition
θ_{21}	$-\int_0^{h_E} \frac{v}{u_E} \frac{\rho u}{\rho_E u_E}\, dh$ — Various momentum thicknesses in streamline co-ordinates
θ_{22}	$-\int_0^{h_E} \frac{\rho v^2}{\rho_E u_E^2}\, dh$ — Various momentum thicknesses in streamline co-ordinates
u	component of mean velocity within boundary layer parallel to direction of external streamline at outer edge of boundary layer — called streamwise flow
u_B	resultant mean velocity within boundary layer, (in 2D flow, $u_B \equiv u$)
u_E	mean velocity at outer edge of boundary layer
u_{E1}	mean velocity at outer edge of boundary layer at reference measuring Station 1
u_∞	mean velocity in the undisturbed freestream (considered to be the same as u_{E1})
u_j	mean velocity of blc jet blowing air at jet nozzle exit
u1	component of mean velocity within boundary layer parallel to direction of tunnel centre-line
v	component of mean velocity within boundary layer normal to direction of external streamline at outer edge of boundary layer — called crossflow
v1	component of mean velocity within boundary layer normal to direction of tunnel centre-line
x, X	axial distance from centre of rotation of turntable jet blowing nozzle on tunnel centre-line — see Figures 15 and 24
XT	location of traverse station of cobra probe or circular pitot tube orifices along x-axis
XVGLE	axial location of upstream point on vortex generators used to control endwall boundary layer at Mach 2 and floor boundary layer at Mach 4
XWLE	axial location of leading-edge of movable wedge shock generator
XSWINV	axial location of calculated shock wave from deflected wedge, assuming inviscid flow on either side of shock
y	lateral distance in plane of tunnel floor from centre of rotation of turntable jet blowing nozzle — see Figures 15 and 24. Positive is in direction away from deflection test surface of wedge shock generator
Subscript	
∞	Undisturbed freestream condition of tunnel flow

THREE-DIMENSIONAL SWEPT SHOCK/TURBULENT BOUNDARY-LAYER SEPARATIONS WITH CONTROL BY AIR INJECTION

1.0 INTRODUCTION

1.1 Objective

The goal of the present study is the control by tangential air injection of a three-dimensional turbulent boundary-layer separation in a Mach 2 mainstream flow, that is caused by a swept shock wave standing normal to a flat test wall. The injectant air issues at a nominal Mach number of 3, with an excess of momentum in the jet somewhat more than the momentum deficit of the undisturbed boundary layer, θ_{11}. The Reynolds number based upon θ_{11} at the slot location and the mainstream flow conditions is nominally 14,000. The stagnation temperatures of the jet and mainstream are the same while the direction of the jet may be altered relative to the three-dimensional separation line.

A secondary objective is the detailed measurement of the three-dimensional interaction between the swept shock wave and the turbulent boundary layer at Mach numbers of 2 and 4, at shock pressure ratios near and greater than the pressure ratio for incipient three-dimensional separation.

The course of presentation of the results will proceed from a discussion of the swept interaction phenomena to the mechanism of the boundary-layer control by jet blowing.

1.2 Overview

The potential usefulness of artificially controlling the behaviour of the boundary layer has been recognized from the earliest days of research in viscous flow. It was in 1904 that Ludwig Prandtl, to support his discovery of the boundary layer, described several experiments to show the great influence that suction boundary-layer control could exert upon the flow about a circular cylinder.

We may conveniently classify the subject of boundary-layer control under three sub-headings concerned respectively with: the prevention of separation and the increase of lift in subsonic flow; control for low drag; and the problem of shock-induced separation (and heat transfer) at supersonic speeds and its prevention by boundary-layer control with cool gas injection. Most practical schemes so far have been concerned with suppressing separation over leading-edge and trailing-edge flaps on wing top surfaces in subsonic flow — the 'Buccaneer' aircraft is one prominent example — although a well-known application in supersonic flow has been the suction control of boundary layers in supersonic air inlets, upstream and at the location of the intake throat normal shock wave.

Boundary-layer control (blc) may be accomplished with either 'active' or 'passive' systems. 'Active' or powered systems may be moving surfaces, discrete or distributed suction, or blowing at some angle to the surface. 'Passive' systems include slats, slots, fences and small plate-type vortex generators, where some part of the higher energy local mainstream is redirected by the passive device to mix with the sluggish viscous flow, and fill out, on average, the mean velocity profile.

On aerofoils, boundary-layer control by blowing may be employed to give high lift, but usually only for short periods of time to improve take-off and landing performance. The injected air, in re-energizing the turbulent boundary layers, delays the stall, and enables high angles of attack and large flap deflexions to be used. In contradistinction, to provide low drag at cruise, distributed suction over the entire aerofoil surface may be installed as in the speculative laminar flow wing. Such low drag aerofoils are usually provided with suction slits for artificially maintaining a laminar flow across the aerofoil chord. The suction ensures a thin stable boundary layer while laminarization removes the relatively high skin friction drag associated with transition to a turbulent boundary layer. These two categories of boundary-layer control, specifically for either high lift or for low drag, are quite distinct; and a system for one will not in general be applicable to the other. The research and full scale flight work on suction and blowing blc on subsonic aircraft up to 1961 is fully and lucidly described in Lachmann's two volumes[1] on the subject.

It is worthy of note that the present and future high cost of aviation fuel, combined with the interest in flying large commercial and cargo transport aircraft at speeds approaching Mach 1, are causing a reappraisal of employing 'active' boundary-layer control during cruise. One recent study[2] suggests that the concept of the laminar flow wing should be resurrected to be coupled with the new supercritical wing technology; and that tangential blowing should be used for boundary-layer control at several stations along the fuselage particularly near the wing fuselage junction, where separations usually exist. The penalty for the blc installation might well be offset, if considerable drag savings were to result. An earlier investigation by Whitcomb[3] at NASA Langley, yielded results that a 'passive' device incorporated into a supercritical wing could be beneficial for controlling shock/boundary-layer interactions. A wing section with a pronounced flattened upper surface was equipped with a fixed slot near the trailing-edge, at about the 80 percent chord station. Supersonic flow was maintained across the top surface of the aerofoil as far as the slot, where the flow then diffused through a normal shock wave, to recover to a level of positive (subsonic) pressure coefficient at the trailing-edge. The slot directed high pressure air from the lower surface to mix with the low-energy air of the top surface boundary layer. The advantages claimed for the supercritical wing with boundary-layer control included a significant delay in the drag rise corresponding with a notable increase in cruise Mach number. A noteworthy example given in Reference 4 was that the incorporation of such a wing into the Boeing 707 aircraft would potentially improve the cruise efficiency by 15 percent and permit cruise Mach numbers in excess of 0.9 to be used without requiring any increase in engine thrust.

The advent of the supersonic commercial jet transport aircraft, with a continuing emphasis on reducing direct operating costs, is encouraging the further development of efficient boundary-layer control schemes in the diffusion, from supersonic to subsonic speeds, of the air to the propulsion engines. Control by bleed or suction is currently favoured, but there is a good potential for control by blowing[5]. The advantages of re-energizing the momentum deficient fluid on the intake wetted areas compared with removing it by bleed are several. Only a small volume is required for the ducting of high pressure air, relatively large pressure ratios are available by tapping a compressor stage, duct losses are low and there is no loss of the intake capture flow upstream of the compressor face as there is in the case of bleed.

Boundary-layer control has been recognized as an acceptable and practical means of achieving performance gains on aerodynamic configurations especially in subsonic flow. However, there is a dearth of information on the control of boundary-layer separation in supersonic flow, especially in a typical three-dimensional flow configuration, and it is hoped that the present study will at least rectify a small part of this deficiency.

1.3 Previous Work on Supersonic Blowing

To provide a background to the present study, we shall present a brief appraisal of work-to-date on wall jets mixing with boundary layers in adverse pressure gradients. Such work has almost exclusively dealt with quasi/two-dimensional flows and two-dimensional separations, whereas on aircraft we are usually dealing with complex three-dimensional flow-fields. The work herein attempts to rectify previous omissions by dealing with blowing boundary-layer control of shock-induced three-dimensional separation, and is one topic in the continuing investigation of three-dimensional boundary layers by the senior authors of Reference 6.

The performance of a supersonic speed blowing jet is based on the premise that for a given configuration, a prescribed value of jet excess momentum flux compared with the momentum deficiency of the boundary layer to be re-energized, will result in virtually the same result, regardless of the mass flow and jet velocity chosen for the excess momentum. The excess momentum flux at the jet exit, is defined as $[\dot{m}_j (u_j - u_E)]_{exit}$, in order to correspond with the momentum deficiency of a boundary layer. The definitions are virtually the same except for sign for $\rho_E u_E{}^2 \theta_{11} = \int \rho u(u_E - u)dy = \int (u_E - u)d\dot{m}$. Clearly, unless the jet velocity exceeds the local velocity outside the boundary layer, there will be a decrease in the boundary-layer momentum, the reverse of the desired goal of blc. The consequence will be an increase in form drag, although the skin friction may be reduced. We should note that the majority of recent publications on tangential injection[7-14] with supersonic mainstreams,

both analytical and experimental, have been to determine the magnitudes of reduction in skin friction that might be possible with low energy air injection from discrete slots. Such reduction is achieved by altering, distorting and thickening the boundary-layer profile such that the gradient of mean velocity at the surface, which is a direct measure of local skin friction, is reduced. A thorough review of concepts for reducing surface friction and reducing wall temperature at high supersonic speeds is presented in Reference 15. It is claimed that for effectiveness of cooling the surface, a slow mixing rate between the original boundary layer and the injected fluid is desirable; and the effects of compressibility are such that when compared with equivalent incompressible flow injectant velocity to freestream ratios, the mixing in compressible flow takes a much longer downstream distance.

We will emphasize that we shall be dealing with an injectant fluid velocity greater than the external stream, where the injected gas behaves as a wall jet and an increase in local skin friction occurs. Such an increase in skin friction is obviously desirable if control of boundary-layer separation is to be achieved in strong adverse pressure gradient conditions.

Let us now define the terms 'jet peak' and 'wake trough', for a high energy wall jet mixing with a boundary layer, where the velocity of the injected air is larger than the external stream. Let us refer to Figure 1. At the exit plane of the blowing nozzle, the jet velocity is zero at the nozzle lip and at the lower wall because of the internal boundary layers on the nozzle wetted areas. Immediately downstream of the lip, a mixing region forms between the jet and the original boundary layer. The mean velocity profile downstream of the jet exit has consequently a maximum and a minimum: the maximum is called the 'jet peak' and the minimum, the 'wake trough'. These maxima and minima vary with distance downstream of the jet exit to eventually merge.

Stratford[16] in 1953 suggested that the concept of high energy air injection for boundary-layer control in adverse pressure gradients, showed considerable promise although more basic experimental evidence was desirable. It was proposed that, ideally, instantaneous mixing between the jet and the boundary layer would permit an adverse pressure gradient to be applied immediately without fear of separating the boundary layer. For this ideal conception it was reckoned the excess momentum of the injection fluid should equal the momentum deficiency of the original boundary-layer fluid.

It was pointed out, however, that for a practical flow the mixing of the two streams required a finite distance; also, that a new wall boundary layer grew under the jet. Neither the extent of the mixing region nor the history of the jet peak downstream of the injection point appeared calculable at that time, and for a quantitative estimate, experimental results were required. It was thought that about 2.5 times the ideal quantity of jet excess momentum would be necessary for total removal of the boundary-layer momentum defect and to give a reserve of total pressure in the jet for any subsequent control needs.

It was mentioned that the idealized treatment might no longer be appropriate for flow with lower energy injection, that is, when the jet velocity was only slightly more than the local mainstream velocity. If an adverse pressure gradient were applied too quickly before adequate mixing had occurred, then the low energy air in the mixing region would be slowed considerably or reversed in flow direction.

Some experiments were performed by staff of the National Physical Laboratory at about the same time[17,18]; these were to estimate the use of blowing to reduce the fall in control effectiveness associated with separation of the boundary layer that was caused by an upper surface normal shock wave. These tests were made at transonic speeds. It was stated that air injection reduced the effects of shock-induced separation of the boundary layer.

A blowing slot was located at about 2/3 chord in the convex top surface of a half section aerofoil (chord of 6-in.). The boundary layer on the aerofoil was turbulent and local jet conditions were sonic at the blowing slot. Two sizes of blowing slot were used: these were 0.009-in. and 0.005-in. in height. The former height was about 0.1 of the thickness of the original boundary layer at the

blowing slot. Blowing stagnation pressures up to 10 times the mainstream stagnation pressure were used, with blowing momentum coefficients, C_μ, up to 0.05*.

The authors[17] suggested that the injected air altered the flow development by preventing the original boundary layer from growing normally. They proposed that the effects of blowing with the narrower slot were the same as those obtained with the wider one, but smaller quantities of air were required for the narrower slot to produce similar effects on the flow development.

It was also reported that with the slot immersed in the dead air or separation bubble region of the normal shock/boundary-layer interaction, the injection of small quantities of air produced a large effect on the separation. In fact, for a blowing total pressure of about 2.3 times the mainstream total pressure, the boundary layer was able to withstand the full pressure rise through a normal shock without separating. From the figures in Reference 17, we infer that the static pressure ratio across the shock was of the order of two. With the slot upstream of the separation and the mixing region length about 15 original boundary-layer thicknesses (estimates from the data given) larger quantities of air were required to produce an appreciable effect on flow development.

Although in Reference 17 it was proposed that the overall effect of injecting into the separated region of the boundary layer was beneficial, no pitot traverses were taken to indicate any flow irregularities (with consequent losses) in the mixing region — the flow characteristics described in Reference 17 were obtained by considering the static pressure distribution on the aerofoil surface and Schlieren flow visualization.

The potential advantages of slot blowing on aerofoils claimed by the NPL some twenty years ago, have been proved correct by Peake and Yoshihara[19] in some recent tests at NAE, to determine the transonic lift augmentation of two-dimensional supercritical aerofoils by means of aft camber, slot blowing and jet flaps, in high Reynolds number flow. Figure 2(a) illustrates the type of supercritical aerofoil examined, having a 'peaky' nose, an aft camber of about 20-degrees at the trailing-edge and a chord of 15-in. The aerofoil was provided with a sonic blowing slot on the upper surface at the 80 percent chord station, as we see on Figure 2(b). The 0.045-in. slot gap was approximately 25 percent of the local boundary-layer thickness.

The usefulness of slot blowing is seen in the chord-wise pressure distributions on Figure 3, in some tests at a mainstream Mach number of 0.85, at a Reynolds number of 30 million based on the 15-in. chord. With no boundary-layer control, the aerofoil is close to a condition of maximum lift, and at or on the verge of buffet onset. The upper surface shock wave is positioned near mid-chord, with shock-induced separated flow extending from the shock to the trailing-edge. The flow has attained a local Mach number of about 1.5 upstream of the shock, and the static pressure ratio across the shock wave is greater than two.

On applying slot blowing, with a momentum coefficient, C_μ, equal to 0.01 (that is a jet excess momentum about equal to the momentum deficiency of the boundary layer) the upper surface pressure distribution changes dramatically. The overall effect of the slot blowing is particularly beneficial for it increases the effective aft camber, as evidenced by the increased plateau loading and the large rearward displacement of the upper surface shock wave, by almost 30 percent of the wing chord. In spite of a local separation bubble downstream of the jet slot position, the flow almost recovers to a positive pressure coefficient at the trailing-edge. Even allowing a penalty on drag equal to C_μ for supplying the blowing air, we note a better than 30 count reduction in profile drag, and an increase in lift coefficient of 0.27.

Bradshaw and Gee[20] explain some interesting flow features in their work on turbulent wall jets with and without an external stream. Although their mainstream and jet velocities were subsonic,

---

* C_μ is defined as $\dot{m}_j u_j / q_\infty S_w$, where $\dot{m}_j$ and u_j are the mass flow rate and jet velocity (assuming isentropic expansion to mainstream static pressure), and q_∞ and S_w are the mainstream dynamic pressure and wing area respectively.

their results bear quoting because of their observations of jet excess momentum required. The mainstream speed was varied up to 120-ft/s and the jet velocities were 650-ft/s and 350-ft/s for slot sizes of height 0.018-in. and 0.040-in. respectively. A calculation suggests that the slot heights were approximately 0.01 and 0.10 of the original boundary-layer thicknesses at the blowing slot. Pressure traverses were made from which the mean velocity distributions were obtained. Distances downstream from the injection point of up to 15 original boundary-layer thicknesses were investigated for flow with and without adverse pressure gradient. No comment was offered on any effect of slot size.

It was suggested from the experimental measurements, that for a tangential wall jet to 'absorb' the initial boundary layer in zero pressure gradient, the jet excess momentum must be about five times the original boundary-layer momentum deficiency. The main part of the original boundary-layer velocity defect was absorbed quickly and the jet peak was still pronounced at about 15 original boundary-layer thicknesses from the blowing slot. A non-zero value of the turbulent component of the shear stress at the jet peak was also found.

With positive pressure gradient, a value of jet excess momentum of about twice that of the original boundary-layer momentum deficiency appeared adequate to prevent separation, but not enough to entrain completely the original boundary layer. The value of jet excess momentum was suggested as being lower for the flow with adverse pressure gradient since the high speed jet suffered relatively less retardation than the mainstream — also with adverse pressure gradient, the skin friction coefficient was less. Stratford's[16] proposal that the jet excess momentum should be about 2.5 times that of the original boundary-layer momentum deficiency was thus reasonable when compared with the results of Bradshaw and Gee.

Neale and Stratford[21] related an attempt to re-energize an intake sidewall boundary layer whose flow direction had been subject to three-dimensional shock wave/boundary-layer interactions*.

A convergent-divergent blowing nozzle of slot height 0.5-in. (about 0.4 of a boundary-layer thickness) on each sidewall, injected air tangential to the wall into the three-dimensional separated flow region. The jet flow expanded in the nozzle to match the local condition of static pressure in the rig. Pressure traverses were made further downstream at the throat where the mainstream Mach number was 1.75. Two locations of jet nozzle exit were tried: the first was at about 3.5 and the second at roughly two original boundary-layer thicknesses upstream of the throat traverse position.

For the first jet nozzle exit position, the wake trough total pressure at the throat traverse location was slightly more than the local value of static pressure and equalled 0.15 of rig inlet total pressure. The Mach number in the wake trough was 0.27, so that the flow in the mixing region was still considerably retarded. The jet peak Mach number was not known, but was greater than 2.5.

Blowing nearer to the throat traverse position produced a wake trough total pressure of 0.06 tunnel entry pressure, which was equal to the local static pressure. The minimum Mach number in the wake was measured as zero and it was therefore likely that the wake flow was reversed. As before, the jet peak Mach number was greater than 2.5.

For both blowing positions, therefore, the throat traverses revealed little or no mixing between the jet and the original boundary layer. With the application of further static pressure rise downstream of the injection point, the intake flow system broke down entirely.

The extent of mixing of about two to 3.5 boundary-layer thicknesses was evidently insufficient to destroy the three-dimensional separated flow of the original boundary layer. The inference

---

* The intake was an all-internal compression type designed to operate at Mach 3. The upper and lower surfaces consisted of a series of ramps, the oblique shock waves from which focussed at the intake throat. These shock waves interacted with the boundary layers on the flat sidewalls to cause significant three-dimensionality and eventual separation of the sidewall flows near the intake throat.

to be obtained from the work of Neale and Stratford[21] was that blowing into a three-dimensional separated boundary layer did not produce the favourable effects as reported in References 17 and 18 for two-dimensional interactions. Reference 21 concluded that a fundamental comprehension of the injection phenomena in two and three dimensions was necessary before re-energization techniques could be justified in intake applications.

The foundation stones were hence laid for a new experiment to elucidate the qualitative and quantitative aspects of a supersonic wall jet mixing with a retarded and supersonic, turbulent boundary layer. Peake, in Reference 5, attempted such an investigation in a quasi/two-dimensional flow, with a mainstream Mach number of 1.8 at the jet exit. The Reynolds number at the slot based upon the momentum deficit thickness of the undisturbed boundary layer was about 7000. High energy air, of variable total pressure and momentum was injected into the boundary layer, tangential to the wall, to minimize mixing losses. The injection nozzle was a convergent/divergent design, with straight walls downstream of the injection throat, yielding a Mach number of roughly 2.4 at design pressure ratio. The slot height of 0.1-in. was less than one half the original boundary-layer thickness. The combined boundary layer and the jet with and without the imposition of adverse pressure gradient was studied optically via Schlieren records and by pressure measurements. An incident oblique shock wave and its reflection created the region of adverse pressure gradient, whose strength could be varied by altering the flow deflection angle of a wedge in the tunnel ceiling. Provision was made for changing the injection position relative to the position of the applied adverse pressure gradient. Pitot traverses, static pressure traverses, wall static pressure measurements and Schlieren photographs enabled the properties of the new wall boundary layer under the jet and the mixing between the jet and the original boundary layer to be measured. A check was made on the quasi/two-dimensionality of the flow by establishing that the tunnel centre-line flow quantities with and without injection, more or less satisfied the momentum integral equation.

For a physical evaluation of the flow, it was found possible to subdivide the flow of the jet/boundary-layer combination into (a) the new wall boundary layer under the jet and a consideration of jet peak characteristics; and (b), the wake or mixing region between the jet and the original boundary layer. To prevent flow reversal in an adverse pressure gradient, in either of (a) or (b) above, it was necessary to choose a length downstream for mixing so that (i) the wake trough total pressure was greater than the local static pressure from the applied pressure gradient — otherwise reversal of the wake flow resulted; and (ii), the falloff in jet peak total pressure was not severe. The indication from Reference 5 was that at best, the wake trough total pressure approached a constant value of about 0.6 of the mainstream total pressure. The initial rate of mixing between the jet and the original boundary layer within the range tested was much the same for all injection stagnation pressures and jet excess momentum rates.

Tests showed that with a jet excess momentum slightly more than the momentum deficiency of the original boundary layer and a mixing region extent of six to ten reference boundary-layer thicknesses, or approximately 100 undisturbed momentum deficit thicknesses, control (of shock-induced separation) could be maintained at least up to static pressure ratios of three. (The Mach number of the mainstream approaching the jet slot was 1.8.) The injection of air actually at the location of the shock-induced separation produced an overall beneficial effect in that the flow satisfactorily negotiated the shock system: although it was probable that the wake flow or the wall boundary layer was reversed. The wall boundary layer separation, if present, was always short in extent and was followed by a rapid reattachment. The use of injection decreased the upstream distance over which the pressure rise occurred and increased the pressure rise obtained compared with the no-injection case. This latter feature would appear plausible because the jet Mach number is greater than the freestream value; while the former observation results from the increased supersonic velocity region close to the wall.

An empirically derived equation was presented that correlated the minimum velocity of the wake with distance downstream of the injection point. The velocity defect in the wake was shown to be roughly proportional to the inverse square root of the distance downstream of the injection point. With reasonable satisfaction of the momentum integral equation as was demonstrated in Reference 5, the equation might thus be utilized as a first step in predicting the characteristics of a jet mixing with either a boundary layer or a wake.

A subsequent quasi/two-dimensional investigation on blowing in supersonic flow to alleviate shock-induced separation was reported by Howell and Tatro[22]. They developed an analysis based on previously observed experimental separation pressure ratios and the boundary-layer momentum deficiency, to predict criteria for control. In this author's view, the analysis contained several anomalies, a discussion of which is presented in Reference 129. A written critique from this author to Howell and Tatro elucidated no response. They obtained results at mainstream Mach numbers of 3.2 and 4.2 and at a flow deflection angle of 10-degrees. No momentum quantities were quoted in terms of the undisturbed boundary-layer deficiency, and this author would disagree with Howell and Tatro's observations from wall static pressure distributions of 'separation' and 'no separation'.

Alzner and Zakkay[10] investigated the shock/boundary-layer interaction in axisymmetric flow at Mach 6, where a 10-degree axisymmetric wedge-shaped ramp was fitted around an axisymmetric centre-body, which was used for the test boundary layer. Pitot and static pressure profiles, stagnation temperature profiles, wall static pressure and heat transfer measurements, and optical data were obtained in this comprehensive investigation. Both air and hydrogen were used as injectant fluids with choked jet exit Mach numbers. The slot height varied between one and three percent of the undisturbed boundary-layer thickness, δ = 0.85-in.

An inspection of the results reveals that separation was not destroyed, although the prime objective of these tests was to realise the potential benefit of wall cooling from the jet.

In summary, the work of Reference 5 appeared to offer a sound base for determining whether the control characteristics would be carried over to a three-dimensional swept shock/turbulent boundary-layer interaction at Mach 2. Such a flow situation is pertinent to swept wing flows, to flows in wing/body junctions, and to sidewall boundary-layer interactions in quasi/two-dimensional supersonic inlets currently installed on present-day aircraft. In addition, no work had been reported on the effectiveness or otherwise of changing the wall jet direction relative to the three-dimensional separation and/or the mainstream direction. An investigation of the three-dimensional turbulent flow downstream of swept slot injection in hypersonic Mach 6 flow, in zero pressure gradient, was reported recently, however, by Hefner et al[23], in which the film-cooling effectiveness of the injectant fluid was the essential target of the study, as well as the reduction in skin friction because of the low (sonic) Mach number of injection. Due to the latter, the jet flow injected tangential to the wall, at 22.5 or 45 degrees to the mainstream direction, also appeared to not penetrate more than typically 20 slot heights downstream before returning to the mainstream direction.

The present investigation was begun in 1966 and the 5-in. X 5-in. blowdown wind tunnel modifications completed in 1968. The tests were completed during 1974 and the review of previous work compiled at that time.

1.4 Two-Dimensional Interactions Between Shock Waves and Supersonic Turbulent Boundary Layers

Most of the investigations of shock wave/turbulent boundary-layer interactions during the last twenty years have focussed on the largely qualitative, and sometimes quantitative mean flow aspects of nominal two-dimensional flows. There is no firm indication that there is quantitative similarity between two and three-dimensional interactions[30] and we should preferably refer to the nominal-2D interaction as the limiting case of the more general, and certainly more often found, 3D swept interaction.

To illustrate the conceptual difference between the nominal-2D shock wave/boundary-layer interaction and the 3D swept shock interaction, let us turn to Figure 4. We see that both types of interactions may be produced by a wedge in a rectangular duct. Such a geometry is representative of the initial compression surface of a supersonic inlet currently employed on military and commercial supersonic aircraft, where the 3D interaction is formed on the flat sidewall of the inlet. The boundary layer on the sidewall skews in the interaction region and tends to flow in a downstream direction close to the line of intersection of the shock with the sidewall.

In deference to the historical development of the subject of interactions between shock waves and turbulent boundary layers, however, we comment briefly on some of the important findings by investigators of the nominal-2D flows.

It is well-known that the presence of a boundary layer developing along a solid surface causes an oblique shock wave to reflect as a complex pattern of waves, rather than as a single reflected wave in inviscid flow. The boundary layer is essentially composed of two strata, an outer supersonic region that merges with the mainstream, and a subsonic inner layer adjacent to the wall. The subsonic nature of the latter implies that the pressure is continuous there, and that disturbances may be transmitted in both upstream and downstream directions. In the shock interaction region, large shear stress gradients perpendicular to the wall are generated in the inner layer, which assist in dragging low energy air downstream into areas of high pressure. The outer supersonic layer, on the other hand, may be thought of as more nearly inviscid, and may be qualitatively described by a pattern of waves. The incoming shock wave is refracted as it passes through the rotational supersonic part of the boundary layer, becoming negligible in strength as the sonic line is approached. The refraction mechanism, however, involves both a change in strength of the incoming wave and the generation of outgoing secondary waves, the latter merging to produce the 'reflected' shock. In addition, other compression waves are generated by the outwardly concave shaping of the sonic line, due to thickening of the subsonic layer in the adverse pressure gradient.

If the inner layer does not separate from the wall, the streamwise extent of the interaction is typically two or three undisturbed thicknesses for turbulent boundary layers. Once separation commences, the growth of the separated flow region causes the outer flow pattern to depart increasingly from that which would be seen in inviscid flow. With large regions of separation, there is strong coupling between the viscous and inviscid flow régimes and it is debatable whether the boundary layer and mainstream may still be considered as separate entities, with a suitably defined 'edge' to the viscous flow.

The qualitative aspects and quantitative mean-flow measurements in nominal two-dimensional shock wave/turbulent boundary-layer interactions have been assessed by many investigators in the last two decades; notable authors in the subject being Gadd, Holder, Pearcey and Green in the United Kingdom, and Bogdonoff and his co-workers at Princeton University in the United States. References 24 to 29, for instance, provide the essential constituents to our understanding of the complexities of shock/boundary-layer interactions. Green[30] has compiled a well-organized review of the work in two-dimensional shock/boundary-layer interactions investigated prior to 1969, which almost exclusively have involved mean-flow measurements. To advance the state of knowledge, measurements of the turbulence structure in the interaction region are required, and some recent experimental investigations[31,32] have attempted this.

The experiment of Grande and Oates[31] was performed using constant temperature hot wire anemometry and miniature pressure transducers in nominal two-dimensional shock/boundary-layer interactions in a Mach 2.4 mainstream, with combined incident and reflected shock strengths high enough to cause separation. The Reynolds number based on the undisturbed boundary-layer thickness of 0.2-in. was equal to R_δ of 3.4×10^4. Grande and Oates found that the turbulence levels in the boundary layer increased as a result of the interaction and increased with increasing shock wave strength. Rose[32] made a similar experiment to Grande and Oates, measuring the rms intensities of fluctuating mass flux and total temperature, and their correlation coefficients, through a Mach 4, axisymmetric shock wave/turbulent boundary-layer interaction. The Reynolds number based on the test boundary-layer thickness of 0.2-in. was $R_\delta = 8.7 \times 10^4$, again, a relatively low dynamic pressure flow to prevent destruction of the hot wires. In agreement with Reference 31, Rose also found that the intensity of the boundary-layer turbulence increased as a result of the interaction, while the fluctuations of mass flux and total temperature remained highly correlated over most of the boundary layer throughout the interaction. Rose also noticed that the intensity of the turbulence increased at certain frequencies more than others at the same h/δ above the wall. On the basis of the above findings, we might expect that a shear layer passing through a Prandtl-Meyer expansion fan would provide large decreases in turbulence intensity; and the experiments of Lewis and Behrens[33] appear to support this contention.

In closing this brief discussion on nominal two-dimensional shock/boundary-layer interactions, we should note that the mean value of surface shear stress generated by a strong adverse pressure gradient

in supersonic flow has not been readily amenable to calculation. For example, Peake et al[34] demonstrated that the surface shear stress beneath an axisymmetric decelerating flow from Mach 4 to Mach 2 could not be duplicated by present day calculation methods. Bradshaw[35] used the results of References 34 and 36 to demonstrate that the consistent discrepancies between calculation and experiment were due to unexpectedly large effects of mean dilatation (or compression) on the Reynolds stresses. Bradshaw found that agreement between calculation and experiment was substantially improved by representing the effects of mean dilatation in the same way as that used satisfactorily to represent the effects of extra rates of strain in low-speed flows. (We recollect that according to Morkovin's hypothesis[37] the effects of density fluctuations produced by the turbulence itself are relatively small at speeds less than hypersonic.)

Finally, the separation point and the length of separation in supersonic flow have been shown dependent[38] on the manner of diagnosis, whether by a mean flow or fluctuating flow technique. Pitot pressure surveys and surface skin friction data indicated the furthest downstream separation and the shortest separation bubble in an axisymmetric flow with adverse pressure gradient at Mach 7.2, $\delta \doteq 1$-in. and $R_\delta = 0.2 \times 10^6$. Both surface pressure data (between inflection points) and oil flow results indicated a slightly earlier separation, while power spectra and correlation measurements (using thin platinum films flush mounted with the wall on pyrex glass) indicated a still earlier separation. These results imply, therefore, that the onset and reattachment locations of separation in quasi-2D flow are intermittent.

1.5 Three-Dimensional Separations in Swept Interactions

Although the fundamentals of skewed boundary layers and three-dimensional separations were reported almost twenty years ago, it is perhaps opportune to reflect upon the physical aspects of three-dimensional separations. We must desist from thinking only in terms of two-dimensional criteria for separation and endeavour to promote a suitable and general concept of flow separation. Ideas based on two-dimensional flow where separation lines must be perpendicular to the external flow direction are of limited value in synthesizing flow separations in three dimensions. For the sake of simplicity, the calculation of boundary layers still tends to exclude the third space dimension, leading to overt emphasis by experimenters on flows with similar (it is hoped) two-dimensional restrictions in order to allow comparison with theory.

Considering the subject of three-dimensional viscous flows* in its historical context, Sears in 1948, utilized the very important concept of 'limiting streamlines' in a paper[39] discussing the laminar boundary layer on an infinite yawed cylinder. Each streamline near the surface, in the inner collinear part of the boundary layer, is one of a continuous pattern of streamlines that approaches the surface at an attachment point or line and leaves the surface at some point or line of separation. (We remember that an aerofoil with attached flow over its surface still suffers separation at a cusped trailing-edge.) Clearly, if the distance of a streamline above the surface is infinitesimal, its direction is everywhere tangential to the vanishing fluid velocity as the surface is approached. It is then identifiable as a limiting streamline, or, in other words, it possesses the same direction as a skin friction line or surface shear stress trajectory. These limiting streamlines at the base of the boundary layer must not be confused with the streamlines of the external inviscid flow over the surface, and they will in general follow paths that are different in direction to those of the external (inviscid) streamlines. The terms: limiting streamline and surface shear stress trajectory are hence synonymous for all practical purposes.

Sears, moreover, included a sketch[39] which showed the convergence of limiting streamlines towards a three-dimensional separation line (and from either side of it) although he did not call it by name; and later, Wild[40] substantiated Sears' physical interpretation of separation, in his investigation of the laminar boundary layer on yawed 'infinite' wings. In subscribing to the Cornell University work, Eichelbrenner and Oudart[41,42] proposed that a line of three-dimensional separation was the envelope of the limiting streamlines (conversely, a line of attachment is the origin of divergent limiting streamlines) and this was also supported by Susan Brown[43] in a mathematical treatise of the Royal Society.

---

* The term viscous region or viscous flow is used instead of boundary layer because both separated and unseparated flows may be discussed together, without ambiguity.

Lighthill[44], on the other hand, disputed the term 'envelope', in spite of flow visualization experiments apparently supporting the previous authors. Coalescence of the limiting streamlines is perhaps an acceptable description to avoid argument.

It remained for Maskell[45], however, to lay the ground rules for the precise interpretation of the physical composition of three-dimensional viscous flows (including the effects after the flow leaves the surface) by demonstrating that the limiting streamlines provide a 'three-dimensional skeleton structure of the viscous flow'. Provided a flow visualization indicator is very thin on a wind tunnel model, it has been shown[46] that the direction indicated by the streaks on the surface is very close to the direction of surface shear and the limiting direction of the velocity when the indicator is absent. Thus the many surface flow visualization techniques yield a powerful means of diagnosing the qualitative features of three-dimensional viscous flows.

Two types of separation were conceived by Maskell[45]: a bubble type and a free shear layer type, both of which may exist together. The latter would appear to be the more common flow found in practice. Fluid accumulating at a three-dimensional separation line, which in general is set obliquely to the direction of the external and essentially inviscid flow field, leaves the separation line as a free shear layer and rolls up in the process of passing downstream. The shear stress is usually finite *along* such a three-dimensional separation line, although it may be zero at a singular point. High local suction pressures are frequently induced on the surface beneath the resulting viscous vortices, close to which are noted inflection points in the limiting streamline patterns. Some examples are the delta wing flow (the ONERA and RAE work being the most extensive — see the subject list in Reference 47) and cones[47,48,49], the flows on long pointed slender bodies at incidence, those about upswept fuselages[50], and those about bluff protuberances[47]. In the bluff or slender protuberance case, for example, which applies to many junction problems, the rolled-up shear layer departing from the three-dimensional separation line occurs within the depth of the oncoming boundary layer, but the changes to the pressure distribution are still significant.

In the swept shock wave/turbulent boundary-layer interaction, the flow in the plane normal to both the shock wave and the wall is frequently quoted as resembling a two-dimensional flow through a normal shock. In Figure 5(a), we show schematically, the result of a weak shock/boundary-layer interaction, where although the limiting streamlines are deflected substantially more than the inviscid streamlines, there is no coalescence of them, and no three-dimensional separation. The small sketch on the right-hand side is a view along the shock wave, showing a pattern and interaction analogous to that for a weak normal shock wave in nominal two-dimensional flow.

With increasing shock strength, from small to larger static pressure ratios, there reaches a stage in the flow development where three-dimensional separation just begins, and important qualitative flow changes start to occur. When the pressure rise is sufficiently strong to cause coalescence of the limiting streamlines, the picture might be that shown on Figure 5(b). The view along the shock wave might provide us with an 'open' or 'closed' separation bubble, with a consequent lambda foot to the shock and a vortical slip line passing downstream from the triple point of shock intersection. In the left-hand sketch, the 'open' or 'closed' bubble commences at the 3D separation line upstream of the inviscid shock wave position. Limiting streamlines emanating from a reattachment line downstream of the shock pass through the line of the inviscid shock to run with the separation line. The upstream limiting streamlines run with the separation line from ahead of the shock*. A more detailed cross-section of the flow when viewed along the shock might follow the picture produced by Seddon[52] in 2D flow, as we see on Figure 6.

The shear stress is finite along the separation line, and the flow is generally in the direction of the shock wave. In the immediate neighbourhood of the junction of a shock generator with the wall, where the interaction is spreading quickly the scale of the separation increases with distance outwards

---

* If the bubble is 'open' the flow leaves the surface along the separation line as a free shear layer and rolls up to form a viscous vortex.

along the shock, tending it is felt, from a conical type flow to one of cylindrical similitude further away from the shock generator. The reattachment stream surface passes over the stream surface springing from the separation line.

When an incident oblique shock wave collided with a turbulent boundary layer in nominal two-dimensional flow, Kuehn[51] observed that incipient separation coincided with the appearance of three inflection points in the surface static pressure distribution (Fig. 8) although Seddon[52] did not notice the same feature in a 2D normal shock/turbulent boundary-layer interaction. On the other hand, Stanbrook[53] did observe the phenomenon in his 3D swept shock investigation. Clearly, if the boundary layer is relatively thin, and the pressure rise is very steep, then the physical extent of the interaction region will be short, and inflection points will not be discerned[5].

Green[30] in other incident oblique shock wave experiments in 2D flow, detected abrupt changes in the reflected wave pattern, that he linked with the appearance of separation. He noted that there was a sudden doubling of strength of the outgoing shock and as a consequence an almost eight fold increase in stagnation pressure loss through it.

We have seen that the characteristic feature of a 3D separation line is that the limiting streamlines or surface shear stress trajectories approach the line asymptotically from both sides, or as appear in experiment, they coalesce to form an envelope (Fig. 7(a)). McCabe[54], utilizes the envelope concept in his study of a three-dimensional sidewall interaction by means of a shock wave generator standing normal to the test wall. He obtained the shear stress trajectories in and about the 3D interaction region by overall coating of the surface with an oil base emulsion. Coagulation of large amounts of the emulsion occurred in the vicinity of separation due to local boundary-layer thickening and the consequent reduced shear stresses at the wall. In principle, it would appear difficult to define incipient separation from such a technique, unless the mixture can be constituted to provide feather-fine streaks[55].

Lowrie[56] used a criterion devised by Rogers and Hall[57] for separations on swept wings (Fig. 7(b)) that defined incipient separation as occurring when the upstream surface shear stress trajectories converge into one line that is parallel to the surface shear stress trajectories immediately just downstream of it, and that still further downstream, they turn progressively away from it. Again, this criterion is probably adequate, provided the flow visualization pattern is sufficiently detailed. It is for this reason that the oil dot technique[58] is to be generally preferred for limiting streamline definition, for no messy coagulation of surface oil occurs.

Stanbrook[53] used the observation to define incipient separation, that at their maximum deflection, the limiting streamlines run parallel to the shock wave.

So far, it has not been proven which criterion is best, but it is probable that the pressure ratios obtained at incipient separation from any of the techniques, would differ little. We should note, however, that for a general three-dimensional flow case, say on a body, the commencement of a three-dimensional separation is difficult to pin-point. Figure 9, for example, shows a typical result of the surface shear stress trajectories obtained with the oil dot technique, where there are three-dimensional separations and attachments on the upswept afterbody of a cargo transport aircraft model. The test was conducted at a Mach number of 0.72, and at a Reynolds number of 15 million based on the afterbody length of 1.5-ft. with turbulent boundary layers present. The convergence of the limiting streamlines implying local thickening of the boundary layers followed by the formation of an 'envelope' is well illustrated — but it should be emphasized that we can only guess the absolute point of envelope commencement. These remarks, perhaps, provoke some thoughts about how three-dimensional separation should be defined in a general case. The features of boundary-layer convergence and hence thickening into lobes of flow, resulting finally in shedding of fluid from the region of the separation line might better be perceived together as a *region* of 'three-dimensional separation'. We will reiterate that along the envelope, the resultant surface shear stress is non-zero in general, whereas for a nominal two-dimensional separation, the converse is true. We should also note[47] that the effects of three-dimensional separation may be beneficial and not necessarily catastrophic as is usual in the two-dimensional case. It appears that the shedding of the vortices in the three-dimensional situation is quasi-steady, and unlike the random, pulsating separated flow in nominal two-dimensional cases such as stall of high aspect ratio wings.

Indeed, the very interaction problem under investigation herein has been used to direct the boundary layers on intake sidewalls into the ramp throat bleed on the compression surface perpendicular to the sidewall.

The length of the swept interaction in the streamwise sense depends upon the pressure ratio across the shock wave, the nature of the disturbance causing it, and the upstream Mach number, Reynolds number and oncoming boundary-layer thickness, δ_o. The latter has been commonly used as a scaling parameter for streamwise distance through the interaction, utilizing the inviscid shock wave position as origin. Equally well, the streamwise displacement thickness δ_1*, would also be suitable. The streamwise momentum thickness, θ_{11}, is also a characteristic parameter for scaling purposes, for it changes rapidly with distance through the interaction, but varies only slowly in regions of constant pressure upstream and downstream of the interaction.

Korkegi[64] has found that a simple correlation exists for incipient turbulent boundary-layer separation due to a skewed shock wave. He took the incipient separation data of McCabe[54] and Lowrie[56], along with the corresponding shock wave angles, Mach numbers and pressure rises, and concluded that the flow deflection angle at incipient separation δ_{wi}, was inversely proportional to the upstream mainstream Mach number, where

$$\delta_{wi} = \frac{0.30}{M_1}$$

Korkegi also associated incipient separation occurring at an approximate constant pressure rise, $p_i/p_1 = 1.5$, independent of Mach number, at least over the range of $3.44 \geqslant M_1 \geqslant 1.96$. (We note that such behaviour is contrary to that for two-dimensional turbulent boundary-layer separation, where δ_i and p_i/p_1 both increase with increase of M_1.)

By comparison, Goldberg[65] has reported that the angle for 3D incipient separation at $M_1 = 5.9$ is virtually insensitive to Reynolds number based on boundary-layer thickness in the range $10^5 < R_\delta < 10^6$, and is about 9°. This is not consistent with an extrapolation of Korkegi's correlation.

1.6 Some Previous Experiments in Swept Shock/Boundary-Layer Interactions

As we noted previously, there is little quantitative understanding of interactions between swept shock waves and turbulent boundary layers. Stalker[59] and Stanbrook[53] introduced and discussed some qualitative features of the swept interaction region, while McCabe[54] at Manchester University and Lowrie[56] at Cambridge provided some quantitative insight into the cross flows developing in the interaction. Much of the existing analysis has been developed for so-called 'infinite' swept flows, and so is of a quasi two-dimensional nature; while most experiments have been conducted using the nozzle boundary layers in relatively small supersonic wind tunnels.

In 1960, Stalker[59] published the results of some experiments using the sidewall turbulent boundary layer of a 6 × 3-in. intermittent type blowdown wind tunnel. He investigated the separation regions produced by swept forward and swept rearward-facing steps, and in a flow generated by an oblique shock wave standing normal to the test surface Stalker demonstrated his results to be broadly consistent with simple extensions of two-dimensional flow analyses. In his forward-facing step experiment, the plateau pressure rise ahead of the step decreased as the angle of sweep of the step increased. The 2D free-interaction* analysis of Crocco and Probstein[60] was used for the flow normal to the step face and appeared to correlate Stalker's results. The Mach number, normal to the step face, was the flow parameter that most affected the plateau pressure rise, as it did the extent of upstream influence. Miller and Redeker[66] also reported that a simple modification of Chapman's[67] order of magnitude

---

* 'free-interaction' implies that the region of disturbed flow up to the separation point (in two-dimensional flow) is free from the influence of flow downstream.

analysis provided an effective means to account for sweep effects on plateau and separation pressures. One evident difficulty in likening the swept interaction to the two-dimensional interaction is that the boundary-layer integrals of flow quantities resolved in a direction perpendicular to the swept shock are not typical of their edge Mach number. This is because density (like temperature) is a scalar, and its distribution across the boundary layer characterizes the flow in the streamwise direction. We see, therefore, that even though the behaviour of the flow perpendicular to the swept shock may appear quasi/two-dimensional, the various integral thicknesses calculated in a direction normal to the shock, will be distorted by an uncharacteristic density distribution.

Stanbrook[53] made some exploratory investigations of a swept shock/turbulent boundary-layer interaction on the sidewall of a 4 X 4-in. wind tunnel at Mach numbers 1.6, 1.8 and 2.0, at Reynolds numbers based on the 0.14-in. boundary-layer thickness of 0.25×10^5. The shock was generated by a wedge standing perpendicular to the test wall. It was found that incipient separation occurred at a pressure ratio across the shock wave roughly equal to 1.5, which corresponded to a flow deflection of between 7.5 and 8-degrees. This ratio was substantially lower than that found in 2D flow, where the value was between 1.6 and 1.8 in the same Mach number range. At distances of more than ten boundary-layer thicknesses from the shock generator, Stanbrook expected the flow to approach asymptotically a cylindrical (that is, infinite swept back) form.

McCabe[54] used a wind tunnel configuration not unlike Stanbrook's, to conduct experiments at Mach numbers of 1.96 and 2.94 at Reynolds numbers close to 0.4×10^5 based on the boundary-layer thickness of 0.14-in. To determine the onset of 3D separation, Maskell's criterion of the formation of an envelope of the limiting streamlines was used, and above a pressure ratio of 1.5, McCabe also found 3D separation to exist at both test Mach numbers. Like Stanbrook, McCabe indicated that at a distance of about 20 boundary-layer thicknesses from the wedge apex, measured along the shock, the flow pattern tended towards a cylindrically symmetric form. He also presented an approximate theory to relate the deflection of the flow close to the surface to the changes in the mainstream. Upstream of the interaction, an element of vortex tube was defined whose height was equal to the boundary-layer thickness. The circulation around the element was determined and assumed to be conserved as it was transported downstream through the interaction at the mainstream velocity. The flow was assumed inviscid and slip allowed at the wall. McCabe sliced the element downstream of the shock in a place perpendicular to the local mainstream direction, to determine a 'cross flow' slip velocity. He added this vectorially to the streamwise velocity in the 'boundary layer', that was taken equal to the local mainstream velocity, to obtain the flow direction at the surface. This latter assumption of uniform streamwise velocity in the downstream boundary layer is a gross simplification of the real flow, although McCabe's measured directions of the wall limiting streamlines agreed satisfactorily with his theory for flow deflections up to those when separation was approached (see Fig. 10).

Lowrie[56] performed some experiments in a 3 X 8-in. working section of a blowdown wind tunnel, the 8-in. width being used for his test surface. A shock generator perpendicular to the test wall provided the swept interaction. Tests were conducted at Mach numbers of 2.50 and 3.44 at nominal Reynolds numbers of 0.3×10^6 based on an undisturbed boundary-layer thickness of 0.3-in. Lowrie's measurements included wall static pressures, surface oil flow patterns and pitot and (chamfered two tube) yaw probe traverses through the test boundary layer. Incipient separation was quoted as occurring at flow deflection angles of about 7½ and 5-degrees at Mach numbers of 2.50 and 3.44. These conditions corresponded with overall static pressure ratios across the shock wave of about 1.60 and 1.50 respectively. Lowrie provided some analysis of the development of cross flows within the interaction, by extending the compressible flow, Johnston's[61-63] suggestion that over most of the boundary layer, the cross flow velocity is proportional to the streamwise velocity defect.

Johnston's polar plot of velocity is shown on Figure 11(a). The velocity u is parallel to the mainstream at the boundary-layer edge, and the cross flow velocity, v, is in a transverse direction within the boundary layer and normal to the local mainstream. The line, PE, of the outer region represents the virtually 'inviscid' response to transverse pressure gradients of the flow between the viscous wall region and the mainstream. The inner line, OP, is more-or-less straight signifying co-planar velocity profiles in the wall region that is dominated by viscous effects. The junction point where the inner and outer regions join is not found to be discontinuous in experiments (see Ref. 56 for example).

Provided the pressure gradient was the dominant feature of the flow, and hence, the cross flow angle was increasing, Lowrie derived a criterion for the junction by considering the equilibrium of the inner layer on the basis of a balance between shear and pressure forces (assuming inertial effects were negligible). If in the outer region the shear stress is in the direction of the shear strain (along PE), an elemental balance between pressure and shear forces perpendicular to this line permits the height of the inner region to be found as that over which the pressure force is just equal to the normal component of only the wall shear stress. If the law of the wall is applicable to the inner region, the wall shear stress direction may be determined in relation to the slope of PE, the local pressure gradient perpendicular to PE, and the wall friction velocity, $u_{\tau w}$. Figure 11(b) demonstrates satisfactory agreement between Lowrie's predicted magnitude of the velocity, q_p, at the junction point, when tested against some low speed data.

Green[30] quotes that the direction of the surface friction can be adequately estimated by letting the vector, q_p, be proportional to $u_{\tau w}$ (based on local wall conditions) and the ratio of the local to upstream, undisturbed mainstream velocity, u_{E1}, in the form:

$$\frac{q_p}{u_E} = 19.5 \frac{u_{\tau w}}{u_{E1}}$$

Using the sine rule on Figure 11(a), the angle, β, between the surface shear stress direction and the local flow direction at the boundary-layer edge is

$$\beta = \arcsin \left[\frac{1}{(q_p/u_E)} \sin \phi \right] - \phi$$

where Green[30] suggests that $\tan \phi$ is the ratio of the transverse volume flow integral or cross flow displacement thickness to the streamwise displacement thickness integral ($= \delta_2^*/\delta_1^*$).

The polar plot profiles of cross flow velocity versus streamwise velocity that Lowrie illustrates in his thesis[56], provide some evidence of triangularity. Nevertheless, Lowrie omitted altogether any boundary-layer pitot profiles where there were indications of wave patterns in the outer region, and so perhaps lost some of the interaction details near the position of the calculated shock wave location*. In any event it would seem doubtful that any profile form based on equilibrium boundary-layer results would apply in the non-equilibrium interaction region.

Finally, in this review of three-dimensional interaction phenomena we will mention the supersonic interference flow along the corner of intersecting wedges discussed at length in References 68-74, and the side-mounted supersonic intake problem, discussed, for example, in References 75 and 76.

The work on the symmetrical streamwise corner problem[68-74], where two wedges of equal deflection to the oncoming stream are jointed, has identified the complex shock structure, and the inviscid flow features. There are strong cross-stream pressure and entropy gradients both at the corner and away from it, which presumably should not be disregarded in analyses of the boundary layers. The importance of corner interactions in high supersonic and hypersonic flows is that they can give rise to high local heating rates at reattachment zones. The wedge bow shock waves do not intersect, but are joined by a third corner shock. The internal flow includes two embedded shocks which terminate at the wedge surfaces, and a triangular region bounded by two slip surfaces and the corner shock. The embedded shocks interact with the boundary layers on the wedge surfaces and, depending

---

* The calculated location of the oblique shock wave in an inviscid supersonic mainstream (upstream and downstream of the shock wave) is sometimes referred to as 'inviscid shock wave location'. The nomenclature is admittedly odd, but it does provide a shorthand notation.

on the wedge angles, may be strong enough to cause separation. Kutler[73] has modelled the conical flow generated by two intersecting wedges immersed in a supersonic stream, and obtained a numerical solution for the inviscid corner flow surface pressure distributions, which compare quite favourably with the experiments of West and Korkegi[71].

In flow field measurements in an asymmetric corner at Mach 12.5, where laminar boundary layers were present, and where the wedge angle of incidence was 15-degrees, Cooper and Hankey revealed two large vortices within the floor boundary layer that were responsible for high local heating. These appeared to emanate from three-dimensional separation lines. A complex shock pattern dominated by a triple point structure was determined, essentially conical in nature. Cooper and Hankey's asymmetric corner corresponds with the wedge mounted normal to the flat test wall that we have previously discussed, except now the test boundary layer commences at the leading-edge of the wall, which is the same station as the leading-edge of the shock generator.

A side-mounted supersonic half-cone intake centre body, causes junction problems[76] not unlike those already discussed. It was demonstrated in Reference 75 that the quasi-conical half-cone pressure field impressed on the adjacent surrounding wall of a fuselage, could be modelled experimentally by choosing a suitable deflection angle of a wedge mounted normal to a flat plate. Pressure distributions between the half-cone and its shock wave (calculation) and the wedge and its shock wave (experiment) were compared as shown in Figure 9 of Reference 75, with relatively good agreement. Downstream of the wedge apex, the interacting viscous and non-viscous flows produced a quasi-conical flow.

1.7 Prospectus

We have noted then, some agreement and some contradictory findings in the three-dimensional swept shock/turbulent boundary-layer work already reported. We shall endeavour in our experiments to present a fuller picture of the interaction region, by measuring at close-spaced intervals, boundary-layer pitot, total temperature and yaw angle profiles, wall temperatures and pressures, and surface shear stress directions. Such measurements will be conducted with a swept shock wave standing normal to the test surface of strength near to that producing incipient separation at Mach 2, to provide a background for interpreting the later results of blowing boundary-layer control; and at shock pressure ratios slightly more and well above those required for incipient separation at Mach 4. Where appropriate, the present results will be tested against those obtained by previous experimenters.

2.0 APPARATUS

2.1 The 5 × 5-IN. BLOWDOWN WIND TUNNEL

The 5 × 5-in. blowdown wind tunnel was constructed as a 1-in. to 1-ft. scale aerodynamic model to evolve the aerodynamic design of the NAE 5 × 5-ft. trisonic blowdown wind tunnel. The 5-in. tunnel has interchangeable transonic and supersonic test sections, but only the supersonic nozzle block assembly was used for the tests described herein.

The 5-in. tunnel may be supplied with compressed air at 300 psia from the 50,000 ft.^{3} storage tanks connected to the 5-ft. facility; or alternatively, it can use air from smaller reservoirs fed by 15-hp and 24-hp compressor sets in series. Using the small reservoirs, the run time is restricted to about 20 seconds, but the main tunnel storage tanks provide the means for continuous running. The absolute humidity of the air in the large reservoirs is kept below 0.0002 lb. water per lb. mass of air. The settling chamber air is stabilized via thermal matrices and is typically about 70°F, with no provision for heat addition, so that the limiting Mach number to which the flow may be expanded is about 4.2 → 4.5 without condensation and liquefaction problems occurring. Upon initiation of a tunnel run, the air passes from either of the reservoir facilities along pipes that connect to the automatic pressure control valve. This sleeve valve maintains the settling chamber pressure at a constant, pre-selected value. From

the settling chamber, the air exhausts to atmosphere via the nozzle, working section and variable geometry supersonic/subsonic diffuser. Figure 12 indicates the scheme of the 5-in. tunnel installation.

The supersonic nozzle section of the tunnel is compoased of flat top and bottom plates (the 'sidewalls') that are separated by two contoured nozzle blocks, see Figure 13. The supersonic expansion of the flow ends about 6.49-in. upstream of the exit of the nozzle blocks; the length of working section is this latter dimension, along which the nozzle blocks possess a straight, divergent taper to correct for the boundary-layer displacement thickness and maintain a constant Mach number in the test section. One of the nozzle blocks has two slots to accept the support legs of the wedge shock generator (Fig. 13). In the opposite nozzle block, there is a circular window to provide artificial illumination of the tunnel interior. There are nozzle blocks available for mainstream Mach numbers of 1.5, 2.0, 3.0 and 4.0.

The test boundary-layer flow is along the sidewall that is also the 'floor' of the tunnel. In the region of the working-section, there is a rectangular cut-out in the test floor that is filled with an instrumented, removable insert that provides the necessary instrumentation and equipment (the blowing nozzle for boundary-layer control, for example) for any particular test requirement. Three such inserts are illustrated on Figures 15, 22 and 24, and are the subjects of Paragraphs 2.3, 2.5 and 2.6.

Tunnel total pressures may be taken up to at least 12 atmospheres, giving a Reynolds number of approximately 7×10^6 based on the tunnel cross-section dimension of 5-in.

An additional supply pipe for compressed air to the blowing nozzle for boundary-layer control is affixed to the floor beneath the wind tunnel working-section. Stagnation pressures up to 300 psia are also available for this blc supply.

There is a large glass window in the tunnel top plate, Figure 13, that may be quickly unclamped to apply flow visualization material to the test floor, or to view and photograph the flow visualization patterns. A Schlieren system may be set up if transparent floor panels are used. The settling chamber stagnation pressure and temperature were measured respectively on 50 psia or 250 psia pressure transducers, and with a glass bulb thermometer and calibrated diode.

2.2 The Movable Shock Generator

The shock (or expansion) generator is a very thin triangular profile supersonic aerofoil mounted vertically between the tunnel sidewalls, whose leading-edge and trailing-edge included angle are 4.8-degrees. The foot of the generator makes firm contact with the test floor of the working section and a brass edge ensures non-abrasion of the steel floor. The installation of the generator, hereinafter called 'wedge', and its dimensions are shown on Figures 13 and 16 respectively. Slots in the tunnel wall allow passage for the two support struts of the wedge, which are attached to mechanisms outside of the wind tunnel that provide wedge movement in translation and rotation.

The wedge may be rotated about its leading-edge between the angular limits of 20-degrees compression and 15-degrees expansion, when referenced to the tunnel axis. It may also translate parallel to the tunnel centre-line and 0.985-in. from it for a total excursion of 6-in. where the most downstream position of the leading-edge that may be selected is 5.25-in. ahead of the exit of the nozzle blocks. The useful movement of the wedge is indicated on Figures 15, 22, and 24.

The cross-sectional thickness of the wedge support legs and their spacing were chosen to avoid choking in the small channel between the tunnel wall and the wedge for the range of expansion angle mentioned above. The maximum stagnation blowing pressures that were used in the tests were chosen so that with a normal shock spanning the test flow between the sidewall and the flat face of the wedge, the design stress levels in the wedge supports and attachments were not exceeded (that is, the wedge was stressed to handle the so-called starting loads). These maximum pressures, for the four available tunnel mainstream Mach numbers are listed on Table 1. The region within the hatching on the tunnel performance chart (Fig. 17) shows the range of flow conditions available for safe operation of the wedge.

Hydraulic jacks provide the means to move the wedge in its axial and rotation modes, as we see on Figure 14. Usually, the axial location of the wedge was set prior to the tunnel run, and for wedge deflection angles up to 8-degrees, the wedge angle was also preset. For angles much larger than 8-degrees, however, the internal contraction ratio was too large to establish supersonic flow throughout the working section and additional movement in rotoation was only attempted once the tunnel run was in progress. Both of the piston strokes were calibrated to provide direct readings of the wedge angular and translational positions, and were checked frequently during the course of the tests. The respective movements could be guaranteed to better than ±0.1-degree in rotation and ±0.010-in. in distance setting. The deflection angle of the wedge was also checked by measuring static pressures at several mid-chord stations on the wedge face adjacent to the tunnel axis, and comparing these in terms of the local pressure ratio and mainstream Mach number, with values of flow deflections listed in oblique shock tables. (This latter check was unreliable when a significant region of 3D separation existed.) The agreement between the wedge angle and that assessed from the wedge pressures was usually within the movement tolerance, up to a wedge deflection angle of 8-degrees.

2.3 Plain Floor

Figure 15 shows a plan view of the dummy floor provided to measure the wall static pressures beneath the boundary layer in the working-section without the shock generator; and through the swept shock/boundary-layer interaction with the wedge in situ. There are more than 200 static pressure orifices contained in the insert, and in the fixed part of the tunnel wall further downstream, along lines parallel and perpendicular to the tunnel centre-line. The spanwise and longitudinal wall static distributions may hence be obtained virtually anywhere in the working section, while provision was made at two transverse stations for three pitot traverses at each to investigate the profiles in the nominal two-dimensional boundary layers. All of the static pressure orifices are 0.015-in. in diameter excepting those through which the pitot tube stems passed, which were enlarged to 0.032-in. diameter (see Rows 4 and 18 on Fig. 15). The locations of the static pressure orifices were referenced to a station 8.625-in. upstream of the geometric exit of the tunnel nozzle. This was labelled as x = 0.0 and was the centre-line of the turntable blowing assembly to be described in Section 2.6.

The wall static pressure points are connected to automatic scan wafer valve assemblies and sampled at one point per second. The pressures are measured with differential or absolute 'Statham' unbonded strain gauge type transducers and thence to a digital voltmeter or an analogue chart recorder. All static pressures were referenced to that measured at Station 1, that was situated upstream in the test section just within the test diamond at Mach 2, as we see on Figure 15.

2.4 Traverse Gear to Investigate the Nominal Two-Dimensional Boundary Layer in the Empty Wind Tunnel

The equipment shown on Figure 18 permits the remote positioning by an electric servo of one to three circular pitot probes to traverse the nominal two-dimensional boundary layer along the tunnel floor. A traverse height of 0.5-in. is available in any given run. The probe is inserted into one of the enlarged static pressure orifices from inside the working section and clamped to the probe holder outside of the wind tunnel. The external diameter of the pitot tube is 0.0164-in. The pitot pressure is fed to either a differential or an absolute pressure transducer, depending on the blowdown pressure and Mach number of the run. At the wall, the hook shape of the probe enables it to be used as a Preston tube to measure local skin friction. Figure 18(c) shows the dimensions of a Preston tube device whose stem may be inserted into one of the enlarged static pressure orifices along Lines 4 and 18. The hook geometry of each traversing circular pitot probe was identical with that depicted on Figure 18(c).

The servo has two sections, the probe unit mounted to the wall that we see on Figure 18; and the control chassis to which the probe unit is connected with shielded cables.

The probe unit consists essentially of a two rpm reversible dc motor with an integral reduction gearbox, an error correcting element in the form of a ten-turn potentiometer; and a worm gear driving a slider, to which the probes are attached. The probe unit may be located at various lengthwise stations along the tunnel working-section by slackening the wing nuts shown on Figure 18(b) and sliding the probe unit along its mounting rails.

The control servo determines the direction of motor shaft rotation and the position of the probe relative to the wall. The control chassis has three parts: a position control and two power channels, each channel consisting of a low frequency amplifier and an electronic switch. A voltmeter indicates a decreasing signal amplitude as the probe approaches its dialled position set on the control panel. Limit switches are incorporated to protect the error-correcting potentiometer from damage that would result from motor overshoot. Point-by-point measurements are taken with this system, rather than a continuous traverse.

2.5 'Cobra' Probe Traverse Gear to Investigate the Three-Dimensional Shock Wave/Boundary-Layer Interaction Region

The pneumatic sensor part of this tiny boundary-layer probe comprises a flattened three-tube measuring head, where the two outer tubes are each chamfered back at 45-degrees to form a yawmeter, while the centre tube (0.028-in. wide × 0.012-in. high) is a rectangular pitot. Figure 19 illustrates the neat and tidy design appearance of the probe head, the shape of which bears some resemblance to the reared head of a cobra snake — hence the name, 'cobra' probe. Figure 20, on the other hand, shows the less tidy frontal view of the manufactured probe head when viwed through a microscope at approximately 50 times true size.

Each time a cleaning tool is passed across the brass faces of the pneumatic tubes, it is advisable to re-check the probe dimensions, for small changes occur.

As the probe is traversed through the viscous flow, from an initial position 0.0005-in. from the wall to a maximum extension of about 0.8-in., a yaw servo-system turns the probe head to align it with the oncoming flow direction. Local flow angles in a plane parallel to the test floor, and pitot pressures, can thus be measured in a skewed boundary layer. Probe height above the surface and yaw angle are measured by geared multi-turn potentiometers. The pitot pressure was recorded by a close-coupled 50 psia pressure transducer. The probe extension rate can be preselected: the fastest rate was chosen that was consistent with obtaining the same pitot profile at the slowest available traverse rate, and a traverse height of 0.5-in. was usually sampled in about 10-15 seconds.

A 0.5-in. diameter flattened steel cylinder into which the triangular-section probe stem is effectively keyed provides the means of yawing the probe. Figure 21 shows the assembly of the probe and its appearance above a test wall.

To measure the variation of stagnation temperature through the viscous flow, an unshielded iron-constantan thermocouple, of bead diameter 0.002-in., was mounted above the pitot orifice (Figs 19 and 20). The distinct advantage of this installation was its small size and its relative robustness in a sometimes contaminated wind tunnel stream.

As the probe was required for use in relatively thin boundary layers neither the shielded probes (Winkler[77], Meier[78], East[79]) nor the hot-wire type of Vas[80] were considered appropriate. Instead, the design of stagnation line probe introduced by Bradfield et al[81] and Harris[82], was adapted to the cobra probe head thereby enabling pneumatic and temperature measurements to be taken simultaneously. The thermocouple wires were 'sandwiched' between two pieces of cigarette paper and the assembly soaked, secured and insulated from the probe head by epoxy resin. The thickness of the sandwich added 0.004-in. to the probe height. The hair-thin wires were then affixed in slots at the back of the probe support stem and connected in series with a reference temperature source at 103-degrees F.

The cobra probe assembly was mounted to a special floor insert, at one of four available stations, see Figure 22. The Stations T3 and T4 were located along a line at 8-degrees to the tunnel centre-line, which would be in the direction of the calculated inviscid flow streamline for the same wedge compression angle with the wedge leading-edge situated at XWLE = 0.0-in.

The same floor insert was also used to accommodate embedded thermocuples to measure the local near adiabatic wall temperature. Clearly, the principal requirement is that the thermocouple device

should not change the conditions of heat transfer that would exist if it were absent. Hence, the wall temperature measurement was made by setting a thin (0.010-in.) steel plate into a 0.5-in. outside diameter insulated cylinder, which was in turn inserted into Stations T1 through T4, so that the plate surface was flush with the surrounding wall. To the backside of the thin plate element the same size of 0.002-in. diameter thermocouple bead was secured as used on the cobra head. The wall temperature measuring device is illustrated in section on Figure 23. Such thin wall plates attain equilibrium conditions quickly[83], and data were taken throughout a tunnel run to verify that a plateau in temperature was indeed achieved. The wall temperature inserts were coupled to the same electronic circuitry as the stagnation probe, a switching device permitting the selection of any one of six temperature channels.

All of the cobra probe outputs were amplified and registered on X-Y charts, while the cobra and wall temperature voltages (again amplified) were also displayed on a Hewlett-Packard digital voltmeter.

2.6 Floor Insert Containing the Supersonic Blowing Nozzle for Boundary-Layer Control

The arrangement of the blowing slot for tangential air injection at a chosen supersonic Mach number is shown on Figures 13, 24 and 25. The two-dimensional blowing nozzle profile is illustrated on Figure 26. The straight nozzle surfaces in the supersonic expansion region are at 4-degrees to the line of the test floor, these being prescribed to overcome the problem of machining an accurately profiled upper wall with an associated very thin lip (0.005-in. radius), yielding the possibility of lip deflections. The straight chamfer to the thin lip provides rigidity to the lip, as well as permitting the use of a small tip radius to minimize wake disturbances downstream.

Provision is included in the design of the nozzle to rotate the injection slot exit at different angular settings relative to the shock wave angle. The blowing nozzle is part of a turntable, the centre of which is located on the tunnel centre-line, 8.625-in. ahead of the end of the tunnel nozzle blocks, see Figure 24. All of the locations of the static pressure orifices in the plain floor and in the floor containing the blowing nozzle are referenced to the turntable centre of rotation. The range of angular movement of the turntable is ±60-degrees about the transverse normal to the mainstream flow direction, a protractor scale on the underside of the tunnel indicating the angle.

The exit height of the blowing nozzle is 0.1-in. but may be doubled using a spacer beneath the upstream nozzle block. Because of this finite slot height above the nominal level of the test wall, a 3-degree ramp leads the undisturbed boundary layer over the top of the injection nozzle, as we see on Figure 25. The span of the slot is 3.6-in.

To change the Mach number of the injectant air, a series of blocks has been made to alter the throat dimension, see Figure 26. The nominal injection Mach numbers range from 1.5 to 4.5, the 'A' and 'B' dimensions indicated on Figure 23 and the design pressures of the injected flow being annotated on Table 2. The contraction ratio from the entrance of the blowing nozzle to the throat varies from 10:1 at M_j = 1.5 to 145:1 for M_j = 4.5. The throat radius of curvature changes from 1.76 to 24.8 times the throat height for the same two Mach numbers, both values exceeding those necessary for satisfactory operation[84] of an effuser. A transition duct, of virtually constant area, takes the blowing air from the circular supply pipe to the rectangular entrance of the blowing nozzle settling chamber.

The layout of the 0.015-in. diameter static pressure orifices about and downstream of the blowing slot are shown on Figure 24. There are 155 static pressure points in the floor and at the throat of the blowing nozzle. In addition, the state of the blowing air supply is measured via a pitot and static pressure orifices, and a glass bulb thermometer in the transition duct. As before, the static pressures were collected via wafer valves to pressure transducers, and read subsequently from analogue charts.

3.0 TEST CONDITIONS

3.1 Stagnation Pressures in the 5 × 5-in. Tunnel

The maximum value of tunnel stagnation pressure is governed by the strength of the wedge shock generator supports. Maximum safe values of blowing pressure versus mainstream Mach number

are shown on Table 1, with the corresponding nominal starting pressures and Reynolds numbers based on the tunnel span of 5-in. for the four available supersonic nozzle blocks. Only the Mach 2 and Mach 4 nozzles were used in the current investigation. The available run conditions are illustrated graphically on Figure 17 within the hatched border, the usable stagnation pressures increasing from two to twelve atmospheres for the two chosen test Mach numbers (q is dynamic pressure).

3.2 Blowing Quantities for Boundary-Layer Control

The jet stagnation pressures listed on Table 3 indicate those required to give the static pressure at the jet nozzle exit equal to the local ambient pressure of the supersonic mainstream for $1.5 \leqslant M_j \leqslant 4.5$. The jet excess momentum values for each blowing condition taking the span of the blowing slot equal to 3.6-in. (Table 3) are plotted on Figure 27, with reference to the calculated momentum deficit of the undisturbed tunnel wall boundary layer at the jet slot position (Table 4) for the listed tunnel stagnation pressures. We note that at a mainstream Mach number of 2, a jet nozzle Mach number of 3 provides a jet excess momentum somewhat more than the 'old' boundary-layer momentum deficit. This injection Mach number of 3 was used throughout the $M_1 = 2$ boundary-layer control experiment pursued herein.

4.0 RESULTS

The essential results of the two experiments are shown respectively on Figures 43 to 87 for the swept interaction phenomena at Mach numbers of 2 and 4; and on Figures 88 to 103, demonstrating the results of air injection at Mach 2. To provide a datum against which to view these results, the Mach 2 and 4 empty tunnel flows are presented on Figures 30 to 42. Amongst the results, we find static pressure and Mach number distributions in the test section; streamwise flow and crossflow velocity profiles in three-dimensional boundary layers along with their integral parameters, surface flow visualization, and the distributions of local skin friction coefficient calculated according to various available correlations for Preston tube devices.

Relevant information regarding the tunnel settings for each test will be found on Table 5, while integral parameters and local skin friction coefficients from the circular pitot and cobra probe traverses are listed on Tables 6 and 7. No tabulations of point-by-point data through the viscous flows will be found herein, but are available from the NAE upon request.

4.1 Accuracy and Calibrations

4.1.1 Surface Finish

The rms surface finish on the test wall was close to ten micro inches with surface waviness better than 0.0002-in. per in. of surface.

4.1.2 Cobra Probe Pressures and Displacement Effects

The pitot pressures collected with the cobra probe were accurate to within ±0.04 psia for a typical pitot pressure range of 3 to 25 psia. The positioning and backlash errors in the probe unit potentiometers and gearbox were assessed by means of a laboratory workshop comparator, resulting in translation and yaw accuracies within ±0.0005-in. and ±0.2-degree respectively.

On the two-dimensional pitot traverse gear, the height was measurable to better than ±0.001-in.

The flattened three-tube geometry of the cobra head probe results in a displacement correction that is somewhat larger than that normally taken for circular pitot tubes[85] in incompressible flow. Young and Maas[86], in some experiments with flattened tubes, made a tentative suggestion of an outward displacement correction of 0.24 d_c towards the region of higher velocity, where d_c is the width of the probe face in the direction of traverse. This value was used in experiments utilizing the cobra probe, that were reported in Reference 34 (for $h > 2\,d_c$) as Marson and Lilley[87] provide some evidence that displacement errors are not affected significantly by compressibility. Since the publication of Reference 34,

however, Ozarapoglu[88] has shown that the displacement effect in incompressible flow for a flattened tube of similar height to width ratio as the cobra probe is closer to 0.32 d_c for $h > 4\,d_c$. For distances closer to the wall, the displacement error decreases continuously as the wall is approached, and Macmillan expressed this reduction for circular pitots in terms of d_c/h and $u_{\tau w}\, d_c/\upsilon_w$. This latter quantity in the present experiments is in the range 100 to 500. Ozarapoglu's result may be written as

$$\frac{\Delta}{d_c} = 0.32 - 0.4\left[\frac{d_c}{h} - 0.25\right]$$

where the second term is included only when $h < 4\,d_c$. (For the circular pitot tube, $\frac{\Delta}{d_c} = 0.15$ for $h > 2\,d_c$.) For distances closer to the wall than 0.7 d_c, Δ/d_c was negative and taken to be -0.15, a nominal mean value of the scattered data of Reference 88.

We should comment that Allen in Reference 89, reported a circular pitot tube displacement correction found in a Mach 2 air stream that was very much larger than the values determined in incompressible flow. His assessment yielded $\Delta/d_c > 0.4$ when the probe was away from the wall. On this basis, we might expect the rectangular or flattened probe to yield an even larger correction. However, since the substantial body of data so far is towards somewhat lower corrections than Allen's*, and since Hall and Dickens[90], when using a similar probe form to that of the cobra found a displacement correction to be no larger than 0.15 d_c in a Mach 1.6 to 2.0 airflow, we have chosen to use the above equation as a reasonable compromise. In fact, the displacement correction of $\sim$0.005-in. away from the wall is virtually indiscernible on the velocity plots.

No corrections for the effect of turbulence on the pitot readings have been employed.

4.1.3 Static Hole Errors

Errors due to large static pressure holes (i.e. relative to the boundary-layer displacement thickness δ_1*) can be important in the reduction of boundary-layer profile measurements and when using surface Preston tubes to determine surface shear stress. Rainbird[91] found that in subsonic and supersonic zero pressure gradient flow at high Reynolds numbers, large static orifices (where $d_s/\delta_1 * \cong 10$) gave pressure errors, ΔP, typically twenty times the value of the undisturbed surface shear stress. In the present experiments, the parameter d_s/δ_1* was $\leqslant 1$, so that the influence of d_s/δ_1* was not significant. In fact, we may compute the correction to static pressure, using the convenient correlation of Franklin and Wallace[92] for deep static holes, but extended to compressible flow by inserting the local wall conditions of density and temperature. The following curve fit was chosen to represent the correlation[92], namely

$$\frac{\Delta P}{\tau_w} = 3.71\left[1 - \exp\left\{-0.0021\left[\frac{u_{\tau w}\, d_s}{\upsilon_w} - 95\right]\right\}\right]$$

except when $u_{\tau w}\, d_s/\upsilon_w < 200$, when

$$\frac{\Delta P}{\tau_w} = \frac{1}{800}\left[\frac{u_{\tau w}\, d_s}{\upsilon_w}\right] + 0.5\left[\frac{u_{\tau w}\, d_s}{\upsilon_w} \cdot \frac{1}{200}\right]^2$$

---

* Wilson[99], in fact, pointed out that the displacement effects quoted by Allen were unnecessarily large and that they were applicable only to his particular pitot tube and support configuration.

The functional relationship in the above expression follows from the law of the wall and the assumption that the static pressure hole error will be a function of the mean velocity u at a distance h from the wall, which is dependent on d_s[91]. Provided a law of the wall region exists in adverse pressure gradient flow, we may argue that the hole error correction should be applicable there, as in the zero pressure gradient flow case, noting that local conditions at the wall should be used in the hole error formula.

In the present experiment, the 0.015-in. diameter static orifice yields a static hole error of amount typically twice the local shear stress. This value is the approximate uncertainty in measuring static pressure, and hence has not been subtracted from the experimental measurement.

4.1.4 Tunnel Mainstream Flow

The inaccuracies in measurement of tunnel flow quantities and repeatability indicate that the maximum likely errors in local Mach number and skin friction are $\Delta M = \pm 0.02$ and $\Delta C_F = \pm 0.0001$.

The tunnel stagnation pressure is controlled typically to within ±0.1 percent of the mean stagnation pressure level during any given run, which is to within ±0.03 psi at Mach 2 and ±0.2 psi at Mach 4.

4.1.5 Tunnel Noise

Intense pressure fluctuations have been found[93] in the settling chamber of the 5 X 5-in. blowdown wind tunnel. These fluctuations are a function of the flow conditions at the control valve, implying that they are aerodynamic noise originating from the jet of the control valve. Below a working section Mach number of 3, the fluctuations in the working section were found[93] to be predominantly those which had been transmitted from the settling chamber. The attenuation of the transmission increased as the nozzle throat area closed, and at Mach numbers greater than 3, the working section fluctuations were almost independent of the settling chamber fluctuation level.

At Mach 4, the overall sound pressure level in the working section $20 \log_{10} (\Delta p/0.0002$ dynes/cm^2), was 146* dB[93] at the stagnation pressure level used in the present experiment. At Mach 2, on the other hand, where the pressure drop across the control valve was greater than four (a feature of our present tests), the overall sound pressure level increased to 158 dB*. This is a substantial fluctuation level, and Green[94] argues that such noise might artificially increase the effective Reynolds number of the flow by significant amounts.

If we assume acoustic waves propagating parallel with a uniform flow, then the ratio of pressure and velocity fluctuations in the flow is

$$\Delta p = \rho a \Delta u$$

The local speed of sound is denoted by a, ρ is the mean density and the Δp, Δu are the fluctuating pressure and velocity terms. Now the ratio of Δp to $\rho(\Delta u)^2$ is typically very large in a sound field. In contrast, the same ratio becomes small for fluctuations of spatially homogeneous and isotropic turbulence[95], with the result that $\Delta p \simeq \rho(\Delta u)^2$. If we accept the former definition as more representative of the blowdown wind tunnel flow, especially at Mach 2, the overall sound pressure level of 158 dB in the working section corresponds with a fluctuation velocity of about 1.4 percent of the local mainstream velocity, which although being an upper bound estimate, indicates a substantial fluctuation level.

As Mabey discusses in Reference 96, the spectrum of surface pressure fluctuations for a nominal 2D turbulent boundary layer approaching separation may be divided into high-frequency and low-frequency components. The high-frequency fluctuations are much the same as those measured

---

* The two dB levels quoted correspond with rms fluctuating pressure levels at Mach 4 and Mach 2 of 0.03 and 0.7, expressed as percentages of the tunnel flow stagnation pressure.

under a boundary layer in zero pressure gradient, and are generated in the small-scale inner region of the boundary layer associated with the law of the wall. On the other hand, the low-frequency pressure fluctuations are generated in the large-scale outer region. It has been shown by McDonald[109], and is further discussed by Zwarts[97], that increase of the mainstream turbulence level does produce higher shear stresses in the outer region and does change the mean velocity profile. In addition, the measurements of Fiedler and Head[98] demonstrate that pressure gradient has a large effect on the distribution of intermittency in the outer region of a turbulent boundary layer. As the turbulent boundary layer approaches separation and the shape parameter†, $\delta_1 */\theta_{11}$, decreases, the intermittent zone *decreases in width* and moves farther from the surface. The structure of a turbulent boundary layer approaching separation, then, does not approximate to that of a free wake flow, the latter, which in contrast, is characterized by a *very wide spread* of intermittency.

The measurements of Fiedler and Head would seem to indicate that an inner region does exist as the boundary layer approaches separation, even though the log law region appears to shrink with increase of adverse pressure gradient. The congruent laws of the wall found for both a turbulent boundary layer and a fully developed pipe flow demonstrate that the degree of intermittency in the outer region does not significantly affect the mean flow of the small scale inner region. If this follows for the 2D turbulent boundary layer approaching separation, we might expect the same for the 3D case, where the flow properties of the inner region should still be scaled by local conditions at the wall. Hence we would expect the onset of separation or incipient separation to be dominated by the same wall properties.

4.1.6 Cobra Probe Thermocouple Measurements

The cobra probe assembly was placed in still air in a controlled oven enclosure, to first of all check the integrity of the iron/constantan thermocouple bead circuit and its junction constant, measured in degrees F per millivolt output.

The probe was fitted in the 5 × 5-in. blowdown wind tunnel at its maximum extension of 0.8-in. (and hence in the mainstream). The oncoming Mach number to the probe was then changed by adjusting the deflection of the shock generator wedge that was installed upstream of the probe station. The probe was allowed to align itself with the local mainstream velocity vector.

The true stagnation temperature was read on the glass bulb thermometer in the settling chamber, along with the temperature diode in the same location. In this manner, the recovery factor was determined at Mach numbers between 1.6 and 2.0, and from 2.7 to 4.0, at Reynolds numbers based on the half-height of the probe and the local stream conditions, in the range 6 to 12×10^4.

The recovery factor, R, of the probe thermocouple, is defined as the ratio of the indicated temperature rise, $T_{PM} - T$, to the adiabatic temperature rise, $T_o - T$; that is

$$R = \frac{T_{PM} - T}{T_o - T} = \frac{R_T - \dfrac{T}{T_o}}{1 - \dfrac{T}{T_o}}$$

R_T is the ratio of the measured total temperature at the thermocouple, T_{PM}, to the local true stagnation temperature, T_o, and T is the local static temperature. Clearly, R and R_T are related through the local stream Mach number, and Figure 28 illustrates this relationship.

Within our limits of measurement, we found that $R_T = 0.981 \pm 0.00\frac{2}{4}$ for Mach 1.6 to 2.0, and $0.971 \pm 0.0\frac{1}{2}$ from Mach 2.7 to 4.0. The corresponding recovery factors were 0.957 and 0.962

---

† Compressible

respectively, being slightly less than the factors found by Bradfield et al[81], Figure 29, and due, presumably, to enhanced conduction losses from the present design. There was no conclusive effect of Reynolds number in the range investigated.

Once the probe is calibrated, the local static temperature in an unknown flow may be written as

$$T = \frac{T_{PM}}{1 + R\left(\frac{\gamma - 1}{2}\right) M^2}$$

provided R does not vary significantly through the range of Mach number and Reynolds number to be encountered in the new flow field.

(In a given traverse of the cobra probe at Mach 2, for example, the excursion in total temperature, T_{PM}, measured through the boundary layer was usually 8-10 degrees F, while superimposed on the mean temperature profile we observed† a maximum peak-to-peak fluctuation of about ±0.3 degree F.)

The resultant velocity in our skewed boundary-layer flow is

$$\frac{u_B}{u_E} = \frac{M}{M_E} \cdot \frac{a}{a_E} = \frac{M}{M_E}\sqrt{\frac{T}{T_E}}$$

which in terms of recovery factor is

$$\frac{u_B}{u_E} = \frac{M}{M_E}\sqrt{\frac{T_{PM}}{T_o}\left(\frac{1 + 0.2\,RM_E^2}{1 + 0.2\,RM^2}\right)}$$

noting $\gamma = 1.4$ and the boundary-layer edge is at the temperature of the mainstream.

Alternatively, in terms of the temperature ratio, where T_{PC} is the corrected probe temperature,

$$\frac{u_B}{u_E} = \frac{M}{M_E}\sqrt{\frac{T}{T_{PC}} \cdot \frac{T_o}{T_E} \cdot \frac{T_{PC}}{T_o}} = \frac{M}{M_E}\sqrt{\left(\frac{1 + 0.2\,M_E^2}{1 + 0.2\,M^2}\right) \cdot \frac{1}{R_T} \cdot \frac{T_{PM}}{T_o}}$$

4.1.7 Wall Thermocouple Measurements

At the same time as checking out the cobra probe thermocouple, the wall temperature thermocouple plugs (Fig. 23) were also placed in the controlled environment of a warm oven to check their circuit continuity. The thermocouple junction constant, measured in degrees F per millivolt output, was then used in determining subsequent wall temperature measurements with the flow on. As the circuitry of the temperature measuring system for the cobra probe was used also for the wall thermocouples, the accuracy of measurement as mentioned in the last subsection should apply here.

Since the thermal inertia of the thin flat plate surface element should not be significant on the time scale of the present measurements (≅ 1 min.), it should take up the wall temperature relatively soon

† On the chart recorder

after establishment of the tunnel flow. We might also expect that temperature gradients across the 0.010-in. thick steel surface element would be small after seconds, or minutes of tunnel blowdown, so that the measurement of temperature on the inner surface of the steel element should yield a value close to that adjacent to the stream. No corrections to account for the finite thickness of the surface element such as those discussed by Naysmith[110] and Harris[82] have been included.

4.2 Data Reduction

4.2.1 Quantities in the External Flow at the Tunnel Reference Station 1

If we assume that the expansion of the flow from the settling chamber to the working section is isentropic, then the local Mach number at the boundary-layer edge, M_{E1}, is given by the local static to stagnation pressure ratio. If, as we assume in boundary-layer theory, that the static pressure is constant normal to the wall, and $\gamma = 1.4$, then

$$M_{E1} = 5^{0.5} \left[\left(\frac{P_o}{p_1} \right)^{0.2857} - 1 \right]^{0.5} \tag{4.2.1}$$

where P_o is the stagnation and p_1 the static pressures.

The isentropic flow relationships for the local static temperature, T_{E1}, density, ρ_{E1}, and velocity, u_{E1}, are:

$$T_{E1} = \frac{T_o}{1 + 0.2\, M_{E1}^2} \qquad (^\circ R) \tag{4.2.2}$$

$$\rho_{E1} = \frac{p_1}{R T_{E1}} \qquad (\text{slugs/ft}^3) \tag{4.2.3}$$

where R is the gas constant for air, 1716 ft lbf/slug °R and T_o is the stagnation temperature in the settling chamber.

$$u_{E1} = a_{E1} M_{E1} = \left(1.4\, R T_{E1} \right)^{0.5} M_{E1} \qquad (\text{ft/sec.}) \tag{4.2.4}$$

and a_{E1} is the local speed of sound.

The absolute coefficient of viscosity, based on Sutherlands's temperature law and using °R may be written as

$$\mu_{E1} = 2.27 \times 10^{-8} \left[\frac{T_{E1}^{1.5}}{T_{E1} + 198.6} \right] \quad \text{slugs/ft sec.} \tag{4.2.5}$$

so that the local unit Reynolds number per ft may be computed, where

$$R_{E1} = \frac{\rho_{E1} u_{E1}}{\mu_{E1}} \tag{4.2.6}$$

Allowing a recovery factor of 0.89 at the wall, the adiabatic wall temperature is

$$T_{AW1} = \frac{0.89\, u_{E1}^2}{2\, c_p} + T_{E1} \qquad (^\circ R) \qquad (4.2.7)$$

where c_p is the specific heat at constant pressure = 6006 ft^2/sec.^{2} °R.

4.2.2 Measurements Through the Boundary Layer

The local wall static pressure, p, measured in the absence of the probe measuring device, was assumed to be constant along a normal to the wall at all measurement stations through the swept interaction region. Static pressure through a boundary layer, where shock waves are present, is a difficult quantity to measure with a conventional static pressure probe[5], for the interaction between the shocks and the local boundary layer on the probe itself will lead to spurious pressures at the static measuring orifices. For example, in the very complex mixing between a wall jet and a separated shock/turbulent boundary-layer interaction region at Mach 1.8, a static pressure variation at the most of about ten percent of the wall static pressure was indicated by a cone/cylinder type static pressure probe[5]. In our swept interaction, except when large-scale 3D separation is present, we might expect variation from the wall to the mainstream, to be substantially less than four percent of the local dynamic pressure at the outer edge of the boundary layer.

The wall static pressure was then combined with the measured values of circular or cobra probe pitot pressure, P_p, to form the ratio of P_p/p from which the local Mach number in the flow was computed. The subsonic Mach numbers ($P_p/p < 1.893$) were calculated from the isentropic flow equation

$$\frac{P_p}{p} = \left(1 + \frac{\gamma - 1}{2} M^2\right)^{\frac{\gamma}{\gamma - 1}} = \left(1 + 0.2\, M^2\right)^{3.5} \qquad (4.2.8)$$

whence Mach number is obtained explicitly.

The supersonic Mach numbers, where $P_p/p > 1.893$, were calculated via an iteration routine from the Rayleigh pitot formula

$$\frac{P_p}{p} = \left(\frac{\gamma + 1}{2} M^2\right)^{\frac{\gamma}{\gamma - 1}} \left(\frac{\gamma + 1}{2\gamma M^2 - \gamma + 1}\right)^{\frac{1}{\gamma - 1}} = \frac{166.9\, M^2}{\left(7 - \frac{1}{M^2}\right)^{2.5}} \qquad (4.2.9)$$

The resultant velocity with respect to that at the boundary-layer edge is

$$\frac{u_B}{u_E} = \frac{M}{M_E}\left[\left(\frac{T}{T_{TOT}}\right)\left(\frac{T_{TOTE}}{T_E}\right)\left(\frac{T_{TOT}}{T_{TOTE}}\right)\right]^{0.5} \qquad (4.2.10)$$

where T_{TOT} is the local total temperature in the boundary layer, where

$$\frac{T_{TOT}}{T} = 1 + \frac{\gamma - 1}{2} M^2 = 1 + 0.2\, M^2 \qquad (4.2.11)$$

and

$$\frac{T_{TOTE}}{T_E} = 1 + \frac{\gamma - 1}{2} M_E^2 = 1 + 0.2\, M_E^2 \qquad (4.2.12)$$

When using the circular pitot tube in the empty tunnel boundary layers, the distribution of total temperature across the boundary layer was assumed constant and equal to the settling chamber value, then

$$\frac{u_B}{u_E} = \frac{u}{u_E} = \frac{M}{M_E}\left[\frac{1 + \frac{\gamma - 1}{2} M_E^2}{1 + \frac{\gamma - 1}{2} M^2}\right]^{0.5} = \frac{M}{M_E}\left[\frac{1 + 0.2\, M_E^2}{1 + 0.2\, M^2}\right]^{0.5} \qquad (4.2.13)$$

On the other hand, the cobra probe thermocouple provided the facility to measure the total temperature distribution through the boundary layer in the swept interaction region. The corrected probe temperature, T_{PC}, (see Section 4.1) is now equivalent to T_{TOT} in the equation for local velocity, so that

$$\frac{u_B}{u_E} = \frac{M}{M_E}\left[\left(\frac{1 + 0.2\, M_E^2}{1 + 0.2\, M^2}\right)\frac{T_{PC}}{T_{PCE}}\right]^{0.5} \qquad (4.2.14)$$

the total temperature at the boundary-layer edge being typically no greater than the stagnation temperature in the tunnel settling chamber, T_o*, by more than 0.2 percent.

The mean velocity components within the boundary layer in streamwise co-ordinates, that is, with respect to the local flow direction at the boundary layer edge are

$$\frac{u}{u_E} = \frac{u_B}{u_E} \cos\left(\beta_{CL} - \beta_{CLE}\right) \qquad (4.2.15)$$

for the streamwise flow; and for the crossflow,

$$\frac{v}{u_E} = \frac{u_B}{u_E} \sin\left(\beta_{CL} - \beta_{CLE}\right) \qquad (4.2.16)$$

where β_{CL} is the measured angle of yaw between the resultant velocity vector at the cobra probe pitot orifice and the (datum) tunnel centre-line direction.

Alternatively, the corresponding local velocity components through the boundary layer, parallel and perpendicular to the tunnel centre-line (the nominal undisturbed mainstream direction) are

$$\frac{u1}{u_E} = \frac{u_B}{u_E} \cos\beta_{CL} \qquad (4.2.17)$$

---

* A single point measurement

and

$$\frac{v1}{u_E} = \frac{u_B}{u_E} \sin \beta_{CL} \tag{4.2.18}$$

With constancy of static pressure assumed through the viscous flow, we have for the ratio of local density in the boundary layer to that at the boundary-layer edge

$$\frac{\rho}{\rho_E} = \frac{T_E}{T} = \left(\frac{T_E}{T_{PCE}}\right)\left(\frac{T_{PCE}}{T_{PC}}\right)\left(\frac{T_{PC}}{T}\right) \tag{4.2.19}$$

that is,

$$\frac{\rho}{\rho_E} = \left(\frac{1 + 0.2\,M^2}{1 + 0.2\,M^2}\right) \frac{T_{PCE}}{T_{PC}} \tag{4.2.20}$$

4.2.3 Integral Parameters

The experimental values of streamwise and crossflow displacement and momentum thickness parameters were calculated according to the expressions in the list of symbols, by performing numerical integrations of the traverse data using the trapezoidal rule. No special curve fitting was employed between the wall and the first data point. As we see in the list of symbols, the integrands of the various integral parameters are composed of combinations of the terms ρ/ρ_E, u/u_E and v/u_E, so that by recourse to Equations (4.2.14), (4.2.15), (4.2.16) and (4.2.20), we may calculate all of the chosen integral parameters.

We note that in a 3D boundary-layer flow the thickness of the true displacement surface cannot be related directly to an integral of the mean velocity profile at one position on the test wall[117,118]. Instead, it can be determined from the normal component of velocity of the boundary-layer edge by means of a partial differential equation: see the calculation method of Nash in Appendix 1 (Eqn. A.1.16).

4.2.4 Determination of Local Skin Friction Coefficients Using Preston-Tube Correlations

The flow in the inner-layer (or wall law region) of an incompressible turbulent boundary layer is determined entirely by the local wall shear stress and fluid properties; and is not influenced by the conditions further from the surface except insofar as these determine the skin friction. Dimensional analysis then shows that the only velocity scale is

$$u_{\tau W} = \left(\frac{\tau_W}{\rho}\right)^{0.5} \tag{4.2.21}$$

and that the only length scale is $\upsilon/u_{\tau W}$. Hence, as argued first by Preston, the difference between surface pitot pressure and the local static pressure (in the absence of the pitot) may be expressed in such forms as

$$\frac{\Delta p}{\tau_W} = f\left(\frac{u_{\tau W} d_c}{\upsilon}\right) \tag{4.2.22(a)}$$

or more conveniently

$$\frac{\tau_W d_c^2}{\rho \upsilon^2} = F\left(\frac{\Delta p d_c^2}{\rho \upsilon^2}\right) \tag{4.2.22(b)}$$

where d_c is the outer diameter of the (circular) surface pitot tube, and Δp is the difference in pressure between the surface pitot and a local static pressure, measured in the absence of the pitot.

In compressible flow over adiabatic walls, the local speed of sound at the wall is a suitable parameter as a measure of the compressibility effects. The corresponding dimensionless parameter is called the 'friction Mach number', $M_{\tau W}$, where

$$M_{\tau W} = \frac{u_{\tau W}}{a_W} \tag{4.2.23}$$

and if we define the fluid properties at the wall,

$$\frac{\Delta p}{\tau_W} = f\left(\frac{u_{\tau W} d_c}{\upsilon_W}, \frac{u_{\tau W}}{a_W}\right) \tag{4.2.24}$$

The best form of calibration law for Preston tubes in compressible flow, according to Bradshaw[101], is

$$\frac{\Delta p}{\tau_W} = f_i\left(\frac{u_{\tau W} d_c}{\upsilon_W}\right) + f_c\left(\frac{u_{\tau W} d_c}{\upsilon_W}, \frac{u_{\tau W}}{a_W}\right) \tag{4.2.25}$$

where $f_i\,(u_{\tau W} d_c/\upsilon_W)$ is the well-proven formulation of, say, Patel[107] in low Mach number flow, and f_c is a compressibility correction function. To determine the form of f_c, Bradshaw re-plotted Allen's data of Reference 119 as $\Delta p/\tau_W$ versus $u_{\tau W} d_c/\upsilon_W$ for various values of $M_{\tau W}$, and demonstrated that an adequate correlation was

$$f_c = 10^4\, M_{\tau W}^2 \left[\left(\frac{u_{\tau W} d_c}{\upsilon_W}\right)^{0.26} - 2.0\right] \tag{4.2.26}$$

in the range $50 < u_{\tau W} d_c/\upsilon_W < 1000$, $0 < M_{\tau W} < 0.1$. Bradshaw thought it reasonable to claim an accuracy of ±10 percent for f_c in the range stated. The error in Patel's data for f_i, on the other hand, was about ±2 percent or less, so that using Equation (4.2.25) with (4.2.26), we should expect maximum errors in skin-friction of ±10 percent for the above ranges of $u_{\tau W} d_c/\upsilon_W$ and $M_{\tau W}$.

Combining Patel's and Allen's results, Bradshaw wrote an implicit equation to determine the wall shear stress as

$$\begin{aligned}\frac{\Delta p}{\tau_W} = 96 + 60 \log_{10} \frac{u_{\tau W} d_c}{50\,\upsilon_W} + 23.7 \left(\log_{10} \frac{u_{\tau W} d_c}{50\,\upsilon_W}\right)^2 \\ + 10^4\, M_{\tau W}^2 \left[\left(\frac{u_{\tau W} d_c}{\upsilon_W}\right)^{0.26} - 2.0\right]\end{aligned} \tag{4.2.27}$$

in the ranges $50 < u_{\tau W} d_c/\upsilon_W < 1000$, $0 < M_{\tau W} < 0.1$. The equation was left deliberately in this complicated form to facilitate modifications to the compressibility factor, or extension to Patel's low-speed calibration at higher Reynolds numbers, (see Ref. 88). Moreover, the calibration law expressed in Equation (4.2.27), will clearly only apply to air flow over adiabatic walls, for heat transfer will introduce the additional parameter $H_W/\rho_W c_p T_W u_{\tau W}$, where H_W is the heat flux per unit area of wall. At this point in time, we have no reliable theory for the effect of heat transfer on Preston tube calibrations.

Some other less recent Preston tube correlations have also been used, to compare with the results obtained from Equation (4.2.27). These are the correlations of Hopkins and Keener[100], where in one, an 'intermediate temperature', T', and in the second, the local wall temperature, T_W, is used. It will be remembered that the intermediate temperature hypothesis proposes that one relation for surface shear stress may be found for both incompressible and compressible flows if the density and kinematic viscosity are calculated at T', a value between the wall and external stream static temperature. The form of T' given in Reference 120 has been used herein

$$T' = T_E \left[1 + 0.035\, M_E^2 + 0.45 \left(\frac{T_W}{T_E} - 1 \right) \right] \tag{4.2.28}$$

where the wall temperature, $T_W = T_{AW}$, the adiabatic wall temperature, with recovery factor of 0.89. As an alternative representation of Equation (4.2.7), we may write

$$T_{AW} = T_E \left(1 + 0.178\, M_E^2 \right) \tag{4.2.29}$$

Hopkins and Keener arrived at their correlations by collapsing the compressible flow Preston tube data onto a relevant incompressible correlation

$$R_{D_i}^2\, C_{pp_i} = f\left[R_{D_i}^2\, C_{F_i} \right] \tag{4.2.30}$$

by writing

$$R_{D_c}^2\, C_{pp_c} = f\left[R_{D_c}^2\, C_{F_c} \right] \tag{4.2.31}$$

the subscripts i and c referring to incompressible and compressible flow, respectively. R_D is the Reynolds number based on the Preston tube dimension d_c (the outer diameter of the forward facing circular wall pitot, for example), C_{pp} is the Preston tube pressure coefficient, and C_F is the local skin friction coefficient.

The resulting functional equations for compressible flow in the form of Equation (4.2.31) are[100]

Method	Calibration Factors		Equation Number
	$\log_{10}[R_{D_c}^2\, C_{pp_c}]$	$m \log_{10}[R_{D_c}^2\, C_{F_c}]$+Constant	
Hopkins/Keener, T', (Ref. 100, Eq. 4)	$\log_{10}[f_2(T')R_D^2(M_p/M_E)^2]$	$1.132 \log_{10}[f_2(T')R_D^2 C_F]$+1.517	(4.2.32)
Hopkins/Keener, T_W, (Ref. 100, Eq. 9)	$\log_{10}[f_2(T_W)R_D^2\, C_{pp}]$	$1.162 \log_{10}[f_2(T_W)R_D^2 C_F]$+1.552	(4.2.33)

where, with T in °R,

$$f_2(T') = \left[\frac{\mu_E}{\mu'}\right]^2 \frac{\rho'}{\rho_E} = \left[\frac{T' + 198.6}{T_E + 198.6}\right]^2 \left[\frac{T_E}{T'}\right]^4 \tag{4.2.34}$$

$$R_D = \frac{u_E d_c}{\upsilon_E} \tag{4.2.35}$$

and M_p is the Mach number calculated from the local static pressure and the Preston tube pitot pressure, via the Rayleigh pitot equation.

To provide a comparison with the methods using the wall pitot pressure, the Sommer/Short correlation[120] was also tried, in which we used the momentum thickness Reynolds number of the boundary-layer profiles, based on the *streamwise* momentum thickness, θ_{11}. The Sommer/Short correlation also utilizes the intermediate temperature and is written

$$\left(\frac{T'}{T_E}\right) C_F = \frac{1}{17.076\left[\log_{10}\left(R_{\theta_{11}} \frac{\mu_E}{\mu'}\right)\right]^2 + 25.112 \log_{10}\left(R_{\theta_{11}} \frac{\mu_E}{\mu'}\right) + 6.012} \tag{4.2.36}$$

In the three-dimensional boundary layer, we have assumed that the above 2D correlations (using wall pitot pressure) hold for the cobra probe geometry, provided the wall pitot is aligned with the local shear stress trajectory at the wall. Further comments regarding the measurements from the circular and cobra surface pitots are left until Section 4.3, when the empty tunnel flow is under discussion. Moreover, all of the above correlations were developed in nominally zero pressure gradient, 2D flat plate turbulent boundary-layer flows. The effect of pressure gradients on Preston tube calibrations in incompressible flow was discussed by Patel[107], where the general conclusion was that provided a logarithmic law of the wall region existed, the calibrations could be used as long as the Preston tube was suitably restricted in size. In addition, the more recent calculations of surface shear stress by Bradshaw, to compare with experimental flows with significant adverse pressure gradients at Mach 4, and in which the effects of bulk compression and dilatation are included, show very favourable agreement with Preston tube results[35]. Since also, the outside vertical dimensions of the circular Preston tube and rectangular pitot tube of the cobra probe are well within the maximum and minimum tolerances on size specified by Hopkins and Keener[100] for good operation, we believe that the two pitot geometries used to measure surface skin friction in our empty tunnel and swept interaction flows provided satisfactory results.

4.3 Flow in the Empty Tunnel at Mach 2 and 4

4.3.1 Surface Pressures and Flow Visualization at Mach 2

Some initial tests in the empty wind tunnel were conducted to determine the two-dimensionality of the undisturbed test boundary layer on the tunnel floor at nominal mainstream Mach numbers 2 and 4. The uniformity of the flow was assessed by reviewing wall static pressures, surface oil flow visualization, mean velocity profiles at several lateral positions and at two axial stations in the working section, and local surface skin friction.

Figure 30 shows surface pressure and oil dot flow visualization results at Mach 2, with a stagnation pressure of the mainstream flow equal to 34 psia. This value of blowing pressure was used for all of the Mach 2 traverse measurements through the swept interaction to be discussed in subsequent sections. The surface pressures were made non-dimensional by reference to the static pressure at Station 1 in the upstream part of the working section as shown on Figure 15. On the top half of Figure 30, the surface pressures and oil flow visualization indicate reasonable uniformity across the

width of the test section. Reference to Figure 15 will assist in placing the 0.5-in. apart lines of static pressure holes (labelled Y, Z, ℄, A, B, D and E) on the test floor, and the two axial stations numbered 4 and 18 where pitot traverses were taken. We should note that the origin of the X-abscissa is arbitrarily set at the position of the turntable centre-line of the blowing blc experiment that we see on Figure 24 — this is for convenience in referencing the later data with blowing. Such origin is situated 8.625-in. upstream of the exit of the tunnel working section.

Small 'wiggles' in the floor pressure distributions across the tunnel flow at $X \cong 4$-in. would appear to be caused by a compression-expansion wave disturbance from the upstream edge of a non-flush fitting of the ceiling window. The corresponding maximum peak-to-peak Mach number deviations are within the spread $\Delta M = \pm 0.022$. The oil flow visualization indicates some small convergence towards the tunnel centre-line — a residue from the lateral pressure gradient in the nozzle, but the overall parallelism may be deemed quite satisfactory.

The effect of the boundary layers on the tunnel walls* perpendicular to the test surface is not usually significant if a weak adverse pressure gradient is superimposed on the floor test boundary layer. With increase of adverse pressure gradient, such as will occur when we deflect the wedge (Fig. 13) more than, say 6-degrees, the degree of influence of these 'boundary constraints' will increase, to eventually affect the test flow in a gross manner when strong separations are present. One way of alleviating the endwall constraint is to partially remove the boundary layer, but this is not usually practical in a supersonic facility where local static pressures within the flow are low. An alternative means of removal is by a sweptback boundary-layer fence, or vortex generator (v.g.), submerged within the boundary layer, whose height is roughly 0.3δ. We experimented with a vortex generator whose leading-edge was set close to the intersection of the floor and the wall of the tunnel (facing the deflected surface of the wedge) at XVGLE = -6.25-in. and 0.0-in., where the angle of the v.g. to the floor was 20-degrees i.e., a sweepback angle of 70-degrees. The lower illustrations on Figure 30 show the results for the more upstream v.g. position.

The pressure distributions along lines Y to B show no effect of the installation of the v.g. Only along lines D and E, closes to the corner, is there seen evidence of the v.g., which, however, is not evident on the floor oil dot flow visualization between Stations 4 and 18. The mechanism of the v.g. is to cause a three-dimensional separation of the oncoming boundary layer which rolls up along and from the sharp free edge of the vertical fence, and passes downstream in the corner between the wall and the tunnel ceiling. In so doing, a new boundary layer commences from the attachment line downstream of the v.g. to produce a substantially reduced local boundary-layer thickness on the endwall in the region of the test, and a consequent reduction in induced upstream/downstream lengths of reflected shock/boundary-layer interaction. The lower right-hand photograph of Figure 30 illustrates a large divergence in the limiting streamline pattern on the tunnel endwall just downstream of the v.g., and we interpret this as the attachment region where the growth of the 'new' endwall boundary layer commences.

At Mach 4, the empty tunnel flow on the test floor is disappointingly non-uniform — a result that, in retrospect, might have been anticipated! Figure 31, on the top left-hand side, shows large perturbations along all lines of static pressure orifices away from the tunnel centre-line. This is clearly the result of using the *tunnel nozzle sidewall* as the test floor, where the transverse pressure gradients in the acceleration from the tunnel throat to the Mach 4 working-section, cause the test boundary layer to converge towards the tunnel centre-line, as we see on the flow visualization on the top right-hand side of Figure 31.

---

* Because of the orientation of the wind tunnel nozzle assembly, see Figure 13, there may be some confusion with respect to terminology used. The surface or wind tunnel '*floor*' on which we have the test boundary layer is, in fact, the *sidewall of the nozzle*. The profiled nozzle blocks provide the vertical boundaries to the test section flow. In the ensuing discussion, these *vertical walls* will be denoted the *endwalls or sidewalls to the test floor*.

In an attempt to alleviate the non-uniformity, we investigated the installation of a V-type vortex generator, of height typically equal to 0.3δ, but this time situated symmetrically on the *test floor*, upstream of the test section. A sketch of the position of the v.g. is shown on the lower left-hand side of Figure 31, where the semi-apex angle was 30-degrees (i.e. each v.g. was swept back at 60-degrees). The v.g. apex was situated on the tunnel centre-line, and each swept 'arm' of the v.g. was sufficiently long to span the floor between the centre-line and the endwall.

With the vortex generator in, we note from the illustrations on the lower half of Figure 31, a gross improvement in the smoothness of the surface pressure distributions, and a change from overall convergence of the limiting streamlines towards the centre-line, to one of slight divergence in the centre-region of the flow. A hump in the pressure distribution appears on the centre-line near X = 0.0-in., the reason for which is unclear. The corresponding perturbation in Mach number is $\Delta M = 0.091$. Towards the endwalls, the oil flow visualization allows the induced effects of the rolled-up vortical fluid from the V-type vortex generator to be detected as local ripples in surface shear stress direction.

The mode of operation of the vortex generator is to again cause a three-dimensional separation, but on this occasion, of the test boundary layer upon the floor. The thicker centre-line region is caused to flow outwards towards the endwalls by means of the induced separated flow, to provide some improvement in uniformity of the lateral distribution of boundary-layer thickness.

On the lower right-hand side of Figure 31, we see small horse-shoe type three-dimensional separations generated by the Preston tubes at Stations 4 and 18; and the local effects of the v.g. flow upon the limiting streamlines on the starboard endwall.

The stagnation pressure level was about 170 psia for these empty tunnel Mach 4 tests, and this value was used in the cobra probe traverses to be discussed later.

4.3.2 Velocity Profiles at Mach 2 Measured with Circular Pitot Tube

Figure 32 displays velocity profiles at Mach 2 as deduced from the traverse measurements of the circular pitot tube at the axial Stations of 4 and 18 (see Figs 15 and 30 for station identification). The velocity profiles were computed assuming, through the boundary layer, constant static pressure equal to the local wall condition in the absence of the pitot tube; and constant stagnation temperature equal to the tunnel settling chamber temperature. The boundary-layer thickness, δ_{995}, is that where the local velocity is 99.5 percent of the local boundary-layer 'edge' velocity, and a displacement correction for the circular tube corresponding with that of Section 4.1 has been incorporated.

We see on Figure 32, that the uniformity is acceptable at both Stations 4 and 18. The locations C and X are 1.25-in. or six undisturbed boundary-layer thicknesses from the tunnel centre-line. At Station 18, the nominal two-dimensional profiles are described better by a $1/7^{th}$ than a $1/9^{th}$ power law, although towards the edge of the boundary layer, the profiles indicate more fullness than either power law would predict. The high mainstream turbulence level might be a contributing factor here, producing, in conjunction with the rapid acceleration of the boundary layer from tunnel throat to Mach 2 conditions and associated non-equilibrium situation, an increase in width of the zone of intermittency[98].

We note from the table above the profiles on Figure 32, that the nominal undisturbed boundary-layer thickness, δ_{995}, is 0.2-in. near X = 0.0, and the shape factor is about 3.3. The latter value is ten percent higher than the predicted profile shape parameter for flat plate turbulent boundary layers, by the 2D momentum integral method of Stratford and Beavers[103]. The Reynolds number based on δ_{995} = 0.2-in. and the local mainstream conditions is $R_\delta \cong 1.5 \times 10^5$.

Some confirmation of the repeatability of measurements of the mean velocity profiles is shown on Figure 33 at Stations 4 and 18, before and after a rebuild of the tunnel settling chamber which involved the replacement of baffles in the wide angle diffuser at the settling chamber entry. The differences between profile measurements at Station 4, in particular, are perhaps associated with the recontouring of the settling chamber wall that has produced small changes in the tunnel nozzle

boundary layers; rather than to measurement errors. We note satisfactory agreement on profile shape factor, H, from run to run.

The pitot velocity profiles on Figures 32 and 33 are replotted in semi-logarithmic (law of the wall) form, as $u/u_{\tau W}$* versus $hu_{\tau W}/\upsilon_W$ on Figure 34. Linear wall law regions are displayed for all profiles, and their slopes are compared with three published laws of the wall in the literature. We see that the slope of the present data falls between Spalding's 2D incompressible law[104], and the compressible formulations of Winter/Gaudet (2D)[105] and Hall/Dickens (3D)[90]. The latter law was obtained from profile measurements in a specially constructed supersonic nozzle at Mach 1.6 to 2.0, where there were three-dimensional test boundary layers; Hall's formulation appears somewhat closer to our measurements than the other two.

4.3.3 Velocity Profiles at Mach 4 Measured with Circular Pitot Tube

Figure 35 shows pitot velocity profiles corresponding with the Mach 4 empty tunnel flow conditions displayed on Figure 31, with the floor vortex generator not installed (the left-hand side results); and then with the v.g. location as shown on the bottom of Figure 31. Again constancy of static pressure and stagnation temperature through the boundary layer has been assumed in reducing the data.

At Station 18, the convergence of the floor boundary layer towards the centre-line, without the v.g., is well illustrated on the left-hand plots of Figure 35. The transverse pressure gradient is favourable towards the tunnel centre-line and that results in a centre-line boundary-layer thickness about twice that at Stations C and X, 1.25-in. from the centre-line.

With the floor v.g. installed, we actually 'over-correct' the transverse thickness distribution of the test boundary layer, for now, the thickness conditions at C and X are greater than on the centre-line, but the non-dimensional velocity profiles show somewhat better agreement in shape across the flow than without the v.g. The stagnation pressure level of about 171 psia has also been used in gathering cobra probe traverse data at Mach 4, and this pressure level corresponds with the pitot data shown on the right-hand graph of Figure 35. The centre-line nominal boundary-layer thickness of δ = 0.2-in. (0.18-in. with cobra) is similar to that at Mach 2, but now the Reynolds number, R_δ has increased to 2.5×10^5.

There would appear to be an effect of Reynolds number on the pitot profiles measured with the floor v.g. installed. The profiles at Station 18 on the extreme right of Figure 35 were taken with the stagnation pressure reduced to 151 psia and somewhat closer agreement appears between the normalized profiles across the wind tunnel flow.

The Mach 4 pitot profiles with the floor v.g. installed are shown in semi-logarithmic form on Figure 36, with the slopes of the log law regions compared against Spalding's incompressible law[104], and the compressible formulation of Winter/Gaudet[105]. Again, the slope of our experimental results falls somewhere between these two wall laws, although now, the measurements provide 'bumpier' distributions.

4.3.4 Effect of Reynolds Number on Pitot Velocity Profiles at Mach 2 and 4

The effect on the pitot measurements at a given station, of changing Reynolds number, is illustrated on Figure 37. An increase of Reynolds number per foot at Mach 2, from roughly 9 to 14 million produces a slight increase in profile fullness and small reductions in boundary-layer thickness, as we see on the left-hand plot. At Mach 4, we see on the right-hand graph of Figure 37, that the effects of a small increase in Reynolds number from 12 to 14 million appears more impressive in the lower regions of the normalized profiles, but only yields a small reduction on profile shape factor from 8.0 to 7.7.

---

*$u_{\tau W}$ Was computed using Bradshaw's Preston tube correlation (Ref. 101).

4.3.5 Cobra Probe and Pitot Measurements in Empty Tunnel at Mach 2

Figure 38 provides us with a comparison between empty tunnel Mach 2 profile measurements taken with the cobra probe and with the circular pitot tube, at axial stations two undisturbed boundary-layer thicknesses apart, near X = 0.0-in. On the left of Figure 38, vertical traverse height in inches of movement is plotted versus local Mach number through the boundary layer, while on the right-hand side the profiles are normalized and plotted as $h/\delta_1{}^*$, h/θ_{11} and h/δ_{995} versus u/u_E.

Although the cobra and pitot profiles were not measured at exactly the same locations, the discrepancy in Mach number profiles is perhaps larger than one would have thought based on the 0.5-in. distance apart of the stations. The relevant displacement corrections in Section 4.1 have been included. The upstream (circular pitot) Mach number profile demonstrates less retardation in the inner region of the boundary layer than does the more downstream cobra result, and this is further emphasized on the normalized profiles. Changing the displacement correction of the rectangular-mouth cobra probe within reason near the wall, does not collapse the cobra data on to the circular tube data, and we feel that in all likelihood, the proximity of the support stem of the cobra head to the measuring pitot orifice is perhaps the cause for the discrepancy. Figure 19 shows the design dimensions of the cobra head, where the leading-edge of the support stem is better than five probe head heights aft of the pitot orifice. This should be satisfactory for most measurements away from the wall, and the comparison between cobra and circular tube results is satisfactory for $h > 0.050$-in. It is conceivable that the flow passage formed between the probe head, the probe stem and the test surface, as the latter is approached, provides too much internal contraction, and the shock wave about the wedge-shaped support stem detaches and pops forward to disturb and attenuate the local Mach number at the cobra pitot orifice. We note all measurements near the wall yield supersonic flow. Clearly, the local three-dimensional separation about the circular tube and the cobra head very close to the wall will show differences, which will also affect the results.

If we accept the circular tube measurements as the more definitive, because of the previous vast experience with that frontal geometry, then we should keep in mind the observed discrepancies between the circular and rectangular tubes when we review the skewed boundary-layer profiles in Sections 4.5, 4.6 and 4.7. On the other hand, the circular pitot tube results demonstrate some unusual 'kinks' in the normalized distributions for $h/\delta_{995} < 0.2$, and we might then prefer the smoother cobra probe results. However we argue the merits of either probe geometry, the profile results from the cobra probe will be systematic amongst themselves, and better than satisfactory results appear to have been obtained with this cobra probe in previous experiments[34,49], when compared with calculations.

4.3.6 Integral Parameters for Flow in the Empty Tunnel at Mach 2 and 4

The boundary-layer integral parameters and local surface skin friction results as deduced from the circular pitot and cobra probes, are plotted on Figures 39 to 42, for the two empty tunnel cases at Mach 2 and 4. The Mach 2 flow illustrates a very small increase in boundary-layer thickness, displacement thickness and momentum thickness, along more than 3-in. of the test region (equivalent to 150 momentum thicknesses). The discrepancy between the circular tube and cobra probe profiles is again demonstrated, with slightly smaller thicknesses given by the circular pitot.

The locally measured wall temperature, T_W, is plotted on the lower graph of Figure 39, with respect to the stagnation temperature in the tunnel settling chamber. The wall appears to be warmer than the adiabatic temperature, T_{AW}, at the corresponding test Mach number, although with increasing run time, the wall tended to cool. Such a change in temperature with run times from 20 seconds up to 20 minutes, is indicated by the change in wall temperature ratio from close to 0.97 to less than 0.96. Most run times, when continuous motion cobra probe traverses were taken, were of the order of 20 to 30 seconds, and under these conditions, we would expect the most heat flux from the wall to the flow.

Pitot pressures at the wall, expressed as pressure coefficients, C_{pp}, and some corresponding local skin friction coefficients from Bradshaw's correlation[101*], are shown next on Figure 40. The

---

* See Equation 4.2.27.

surface pitot measurements from the cobra probe provide us with a local skin friction coefficient consistently less than that given by the circular tube by $\Delta C_F \cong 0.00035$. Although the measurements of skin friction by Quarmby and Das[106] with rectangular pitot tubes in incompressible flow demonstrated insignificant difference from the circular tube calibration of Patel (where the height of the probe was used in correspondence with the outer diameter of the circular tube), we interpret the cobra probe geometry with its chamfered flattened side tubes, to require a calibration in a high Reynolds number pipe flow. It is worthy of note that a chamfered three-tube surface yaw probe, but with three circular tubes affixed together, was used in conjunction with Patel's calibration in Reference 108, when the surface direction of the flow was initially unknown.

We further note in Figure 40, that the circular tube result from Bradshaw's correlation[101] is less by $\Delta C_F \cong 0.0004$ than the adiabatic wall, Spalding/Chi[102] result. The discrepancy is in all likelihood bound up with the recovery of the test boundary layer from its large degree of three-dimensionality in the expanding nozzle flow to one with a very small residual convergence (toward the centre-line) in the working section. This would cause a lesser C_F value in our case than the Spalding flat plate answer at corresponding values of $R_{\theta_{11}}$. The small increase in wall temperature above that of the adiabatic wall condition should not be a reason for the discrepancy. No wall temperature measurements were taken at Mach 4. The Mach 4 centre-line values of integral parameters that we see in Figure 41 again show only small variation with distance along the working section. The enhanced values of thickness to the sides of the centre-line, at Stations C and X, illustrate the effect of the upstream vortex generator (Fig. 31) on the floor boundary layer, in overcorrecting the massive convergence of the empty tunnel flow. A reduced height, plus a reduction in sweep of the v.g. would tend to flatten the transverse distribution of boundary-layer thickness.

The local skin friction results in the empty tunnel Mach 4 flow are shown in Figure 42. There is a small increase in C_F as we move downstream, no doubt from the mild 'attachment type' flow along the tunnel centre-line that is caused by the floor vortex generator. Again the cobra probe provides a local skin friction coefficient less than the circular tube result (both using Bradshaw's correlation) of $\Delta C_F \cong 0.0002$. In this Mach 4 flow, the adiabatic wall, Spalding/Chi result is greater than Bradshaw's circular pitot result by $\Delta C_F \cong 0.0005$. Any discrepancy here between our nozzle boundary layer experiment and flat plate results is hardly surprising because of the substantial disturbances introduced to change the transverse distribution of boundary-layer thickness.

We see, then, that with the uniform discrepancy between the C_F results from the pitot and cobra probes, we can tentatively propose that the cobra probe pitot measurements at the surface may be used in a circular Preston tube correlation, provided the probe height is input instead of the diameter, and the offset in C_F is noted, that was measured in near zero pressure gradient flow conditions between the cobra probe and circular pitot.

4.4 Surface Pressure Distributions and Flow Visualization at Mach 2 and 4

The static pressure distributions along the boundary-layer test surface and a selection of photographs of oil streak patterns obtained with the wedge in the wind tunnel test section, are shown on Figures 43 to 50 for the flow at Mach 2; and on Figures 51 to 54 for the flow at Mach 4. The limits on axial position of the wedge are shown on Figure 15.

The test surface pressure distributions were taken at closely spaced intervals in wedge angle particularly near flow deflections where incipient separation was predicted to occur from various experiments[54,64]. On each pressure distribution, we shall observe that the theoretical shock pressure rise in inviscid flow corresponding with the mainstream Mach number has been plotted, while the origin of the X-abscissa of each pressure plot will be the calculated shock wave position where it intersects the given line of pressures. We should note that since the nominal undisturbed boundary-layer thickness is 0.2-in., each inch along the test surface corresponds with five undisturbed boundary-layer thicknesses. Because of the ease of this transformation, all distances in the X-direction remain as absolute units on the figures. The static pressure was measured relative to the static pressure at position one, upstream of the interaction region; see Figure 15. Each pressure distribution was in the direction of the undisturbed

stream parallel to the tunnel centre-line at different y values or lateral distances from the wedge apex. For clarity, only lines Z, ℄ and A pressures were usually plotted. The photographs of the tunnel floor were taken with the optical axis of the camera either parallel to the wedge deflection surface or just to one side of it. The flow along the floor is from left-to-right, thus we frequently view a reflection of the flow visualization on the test floor in the smooth-machined wedge surface. The triangular section of the wedge furthest from the floor was usually out of focus, and has consequently been outlined in ink to assist the reader. The wedge deflections, δ_w, are quoted with respect to the tunnel centre-line direction, or in other words, to a nominal stream direction. In Sections 4.5 to 4.7 we shall see small angles of skew of typically 1-degree detected by the cobra probe in the nominal two-dimensional flow upstream of the swept interaction region.

4.4.1 At Mach 2

Figure 43 displays surface pressure results when the incident shock wave is weak. Here we see results for wedge angles of 0, 2 and 4-degrees. The surface pressures with the undeflected wedge compare reasonably well with those already discussed on Figure 30 in the empty tunnel flow. The one difference is that just downstream of the wedge trailing-edge at X = 3.0-in. we observe local perturbations in the pressure distributions, which are largest near the wedge, and which perhaps are due to effects of the deflection of the flow about the wedge surfaces opposite to the test deflection surface, feeding around the trailing-edge.

Where the shock wave meets the boundary layer, and we have attached flow, we see on Figures 43 and 44 (δ_w up to 7.5-degrees) a steep rise in pressure, not dissimilar to the measurements of McCabe[54]. The pressure rises smoothly over typically five boundary-layer thicknesses upstream of the inviscid shock wave position and this length increases with increasing lateral distance from the wedge apex. In comparison with the nominal 2D interaction measured by Seddon[52], we see from Figure 6 that the extent of the upstream influence is not unlike the 3D case, but that the region of interaction downstream of the inviscid shock position appears to be many times larger in 2D than in the 3D flow.

Above δ_w = 4-degrees, the maximum pressure downstream of the shock decreases with increasing distance from the wedge, and this may be due to the upstream influence of the expansion fan from the wedge trailing-edge, as it approaches the shock with increasing lateral distance from the wedge. It is interesting to note that McCabe[54] used both short and long wedges, but still found the attenuation of the maximum pressure with increasing distance from the wedge. He suggested that the reduction in maximum pressure level was just a result of the increasing extent of the downstream influence of the shock, with the asymptote in pressure level not reached before the trailing-edge expansion causes a massive fall in the pressure field.

As the wedge angle becomes larger (see Fig. 44 for δ_w up to 7.5-degrees) the continuing rise in shock pressure ratio turns the limiting streamlines more and more away from the deflection angle of the mainstream flow. We note the significant upstream influence, with turning of the surface oil flow well upstream of the calculated shock wave location. The upstream effect increases with distance from the wedge over the limited region investigated (about 10δ from the wedge*), and Stanbrook[53] conjectures that this might be explained by a form of spanwise influence. He proposed that the effects of the shock presence would be propagated along rearward-facing local Mach cones, which in a large part of the boundary-layer thickness possess angles greater than the shock wave angle. Figure 45 continues the story up to a wedge deflection angle of 9-degrees. The spacing of the wall static orifices is such that the beginning of inflections in the pressure distributions is difficult to observe to provide evidence of incipient separation. From the previous experiments[53,54] with swept shock interactions, we expect incipient separation at δ_w = 7.5 to 8-degrees (Stanbrook[53]) when $p_2/p_1 \cong 1.5$; or δ_w = 8.5-degrees (McCabe[54]).

From the oil flow photographs on Figure 45, in particular, we see no evidence of major coalescence of the limiting streamlines, nor of the streamlines becoming parallel with the calculated shock

---

* Along the direction of the shock wave.

wave position. Indeed, only as we approach a wedge angle of 10-degrees on Figure 49 do the limiting streamlines, from the wedge apex outwards, align themselves with the calculated shock wave direction in the inviscid flow; and by 11-degrees, the occurrence of a prominent 3D separation line is obvious. The limiting streamlines coalesce into an envelope (originating at the wedge apex) that lies just upstream of the calculated shock wave position. The boundary layer separates and rolls up as a free shear layer, while the indication is of an attachment on the wedge face or on the floor somewhere near the intersection of the wedge with the floor. We can suggest this, for virtually all of the limiting streamlines downstream of the 3D separation line emanate from a location near the intersection of the orthogonal surfaces.

From the pressure distributions at δ_w = 11.5-degrees on Figure 49, we see that the pressure rises sharply up to the position of the 3D separation line. Thereafter the pressure gradient falls, since the rapidly thickening 3D separated flow does not withstand a large adverse pressure gradient. The gradient increases once more downstream of reattachment.

Our incipient separation result at Mach 2 of about 10-degrees wedge angle is greater than the values found previously and correlated by Korkegi[64]. It is noteworthy that although McCabe observed separation to commence at δ_w = 8.5-degrees, his vorticity theory[54] predicted separation at $\delta_w \cong 11$-degrees at a nominal Mach number of 2. Moreover a comparison of our maximum limiting streamline deflections downstream of the shock at Mach 2, for wedge angles up to almost 12-degrees demonstrate reasonable agreement with McCabe's vorticity model, as we see on Figure 10.

In these comparisons with previous results, one distinctive feature is evident. Previous investigations used wedges with deflection angles such that shocks were produced on either side of the wedge body. Our thin triangular section shock generator allows expansions to be produced from the leading-edge in the channel opposite to the test flow for $\delta_w \geqslant 5$-degrees. Hence the influence of the flow about the back-side of the wedge should be negligible when we are searching for incipient separation details. The bluffness of the wedge leading-edge coupled with relatively large included angles at the apex, in previously reported work has also often provided a protuberance type separation about the wedge, in the junction with the floor (see Ref. 54). The 0.006-in. leading-edge radius on our triangular-section generator plus the small included angle, caused only a very small horse-shoe type separation about the wedge foot, as we can observe on many of the flow visualization pictures.

For wedge angles much greate than 12-degrees, the internal contraction to the mainstream is such that it is difficult to isolate the test flow on the floor from that on the endwall, and no further useful results can be obtained.

4.4.1.1 Effect of Sidewall Vortex Generator at Large Wedge Angles

No sidewall vortex generator was present in the flow fields discussed on Figures 43, 44, 45 and 49. In contrast, Figure 48 displays the surface oil flow visualization results at δ_w = 9-degrees obtained without and with the sidewall v.g. situated at XVGLE = 0.0-in. We should first of all explain, however, that much of the disturbance to the endwall boundary layer that we can view on the aforementioned figures was due to upstream propagation and re-circulatory flow in a small slot existing at the intersection of the floor with the endwall. When this slot was filled, the improvement in the corner flow was dramatic. For example, if we compare the upper photograph in Figure 48, with the corresponding δ_w = 9-degree case on Figure 45, we note that the separation bubble in the corner flow on the latter figure has been eliminated. The addition of the sidewall vortex generator does not appear to alter the test surface flow to any noticeable extent. We remark again, however, that the limiting streamlines pass through the calculated shock wave position at δ_w = 9-degrees and no separation is perceived.

The effect of the sidewall vortex generator on the surface pressures closes to the wall, along line D and E, is to restrict the upstream influence of the shock wave because of the thinner sidewall boundary-layer flow — see Figure 46 for δ_w = 8-degrees. At δ_w = 11.5-degrees, the sidewall v.g. now permits useful pressure distributions to be obtained as far as line E as we note on Figure 50.

4.4.1.2 Effect of Reynolds Number at δ_w = 8-Degrees

Figure 47 shows surface oil flow visualization at δ_w = 8-degrees in a Mach 2 flow, for a small change in Reynolds number, R_δ, from 1.5 to 2.3 X 10^5. In an overlay of the surface shear stress directions, we are not able to detect any significant effect of this limited Reynolds number increase.

4.4.2 At Mach 4

There is significant correlation between the qualitative flow features at Mach 4 and those at Mach 2. The experimental arrangement was altered in the Mach 4 tests, however, to include a crude Schlieren system plus a transparent floor, to provide the location of the mainstream shock wave superimposed upon the oil dot flow visualization. All of the pressure and flow visualization results were taken with the floor vortex generator situated as shown on Figure 31.

Figure 51 illustrates surface and Schlieren flow visualization at small wedge angles. The calculated shock wave and leading expansion wave from the wedge leading and trailing edges, are now inclined very much closer to the wedge deflection surface than for the corresponding Mach 2 wedge deflections. The flow is again from left-to-right. The shock and expansion waves on the Schlieren photographs bear close resemblance with their calculated counterparts. Moreover, the boundary layer on the wedge surface and its wake downstream are clearly visible, and we observe the significant turning of the limiting streamlines on the floor, far ahead of the actual leading wave of the expansion fan. Such effect causes a drastic fall in the pressure rise through the shock as we see on Figure 52. The upstream influence at δ_w = 6-degrees stretches as far as five to ten undisturbed boundary-layer thicknesses ahead of the calculated shock wave position. In proceeding from static pressure orifice lines Z to A, there is rapid attenuation of the peak pressure rise as distance increases from the wedge apex, while the calculated shock pressure rise is never reached.

From the flow visualization records at δ_w = 6 and 8-degrees on Figure 52, we note parallelism of the limiting streamlines with the calculated shock wave directions at both angles, but more particularly at the larger wedge deflection. In addition, there is evidence of inflections on the Z and $\mathbb{Q}$ pressure distributions at both 6 and 8-degrees, so that incipient separation is deemed to occur close to 6-degrees.

With an increase of flow deflection angle to 10 and 14-degrees, that we see on Figure 53, strong three-dimensional separations are caused by the shock wave. The upper photograph on Figure 53 demonstrates limiting streamline motion beneath the calculated shock wave location, towards a separation envelope far upstream of the shock. With the wedge angle increased to 14-degrees, the leading expansion from the wedge trailing-edge becomes close to the calculated shock location and, on the tunnel centre-line, attenuates the pressure rise sharply at six undisturbed boundary-layer thicknesses aft of the calculated shock. There is a divergent region of limiting streamlines just ahead of the leading expansion wave, where we anticipate flow reattachment. The view of the wedge surface at the bottom of Figure 53 shows a downflow of limiting streamlines on the wedge face close to the corner, preceded by an attachment region. The corresponding pattern on the tunnel sidewall of the so-called nominal 2D interaction is very three-dimensional in character!

Finally, an extreme case of three-dimensional flow separation is illustrated on Figure 54, for δ_w = 16-degrees. The attachment on the wedge face is particularly noticeable now, near its intersection with the tunnel ceiling (the identical flow occurs near the test floor). The lower attachment zone would appear to extend off the wedge face on to the test floor along the line of the trailing-edge expansion. The sidewall flow demonstrates a cellular structure not unlike that found on 2D aerofoils in buffet in transonic flow[19].

4.5 Cobra Probe Traverses at Mach 2 and δ_w = 8-Degrees

4.5.1 Moving the Swept Interaction Region Relative to the Cobra Probe

A secondary objective to that of controlling a shock-induced 3D separation was to obtain a better physical knowedge than currently exists, of the mean flow details through a swept interaction, near or at incipient separation, and in the presence of a shock wave sufficiently strong to cause a large-scale 3D separation.

We saw in Section 4.4, that at Mach 2, there was no clear evidence of separation from the oil flow and surface pressure distributions up to wedge deflection angles of about 10-degrees. The δ_w = 8-degree case was chosen, therefore, as indicative of flow approaching the condition of incipient separation. (The corresponding wedge angle at Mach 4 was also chosen, as representative of a flow just past incipient separation, while the δ_w = 16-degree case at Mach 4 was selected to illustrate the details of the rolled-up free shear layer.)

With the availability of only four traverse stations for the cobra probe (see Fig. 22) we elected to move the interaction region relative to the probe, by utilizing the 6-in. range of available axial movement of the wedge shock generator. In so doing, we would have the option of traversing at any axial station through the pressure rise that was of interest.

We have already seen in the empty tunnel flow discussed in Section 4.3, that especially at Mach 2, there is only a very small change of mean flow boundary-layer properties with distance downstream in the working section of the wind tunnel. But if we cause the wedge to be situated anywhere in the test section, will the static pressure distributions along any given line be congruent, when plotted with respect to the calculated shock wave location?

We resolved this question by first of all looking at the surface oil flow visualization with the wedge leading-edge situated at various stations between XWLE = −2.5-in. and +3.0-in.: a range of 280 undisturbed momentum thicknesses in length along the test section.

Figure 55 illustrates these oil flow visualization results, where by superposition, we can detect no significant changes in the surface patterns along the test section. With this encouragement, we measured the wall static pressure distributions for δ_w = 8-degrees, with the wedge leading-edge at XWLE equal to −2.0, 0.0, 1.0 and 2.0-in. Figures 56, 57 and 58 show these wall pressures along the tunnel centre-line, and on either side of it along lines Z and A, that border the cobra probe traverse locations. We note that the measurements along each line at each wedge position overplot satisfactorily, when referenced to the calculated shock wave location and we detect the aforementioned spanwise attenuation of maximum pressure level with increase of distance from the wedge apex.

With these results in hand, we felt it a logical procedure to investigate the swept interaction by moving the wedge relative to the probe station.

4.5.2 Cobra Profile Measurements as Pitot Pressure, Total Temperature and Yaw Angle

Figure 59 provides a map of the cobra probe traverse stations with respect to the shock wave position in a δ_w = 8-degrees inviscid flow at Mach 2. We remember from Figure 22 that the traverse stations labelled T1 and T2 are situated on the tunnel centre-line while T3 and T4 are at lateral distances: y = 0.028 and 0.15-in. respectively away from the centre-line. Two traverses, downstream of the shock, numbered 24806 and 24702, were positioned to be on the projection of one inviscid flow streamline, that is, along a line sloped at 8-degrees to the centre-line. Constant reference to Figure 59 will assist the reader with the ensuing chapter. Additional traverse information and integral parameters are listed on Tables 7.1 to 7.3.

The measurements from the cobra probe (before their manipulation into velocity profiles) are shown on Figure 60, as corresponding pitot pressures, total temperatures and yaw angles (with respect to the tunnel centre-line direction) plotted against vertical distance from the test surface, h. The profiles exhibited are those taken along the tunnel centre-line only, where, as on the static pressure plots, the calculated shock wave location is the origin for the X-axis. The flow is from left-to-right. Although we follow the tunnel centre-line in presenting this profile information, we can infer from the integral parameters that the qualitative features to be discussed may equally well represent the flow along the path of an inviscid streamline, because of the relatively small wedge deflection angle.

The pitot pressure profiles as related to the settling chamber stagnation pressure are at the top of Figure 60. The local wall static pressure at each profile station is written beneath the X-axis adjacent to the start of the profile. Any local value of pitot pressure may hence be determined using the given horizontal scale and the pressure at the wall.

The upstream profiles exhibit the characteristics of the nominal two-dimensional flow existing there. At two undisturbed boundary-layer thicknesses upstream of the calculated shock wave location, we observe a movement away from the wall of the sonic line and a rapid decrease in pitot pressure signal as the mainstream is approached. This pitot pressure deficit would be consistent with passage through a densely packed fan of compression waves, that commences ahead of the location of the calculated shock front. This outer gradient of pitot pressure disappears suddenly at the calculated shock position, denoting a sudden increase in local Mach number as $h \rightarrow 0.5$-in. With further distance downstream, the sonic line slopes back towards the wall at two undisturbed boundary-layer thicknesses downstream of the calculated shock position. We note that especially through the interaction, the pitot pressure adjusts very slowly to a constant level in the region adjacent to the boundary-layer edge.

With these non-uniformities in view in the non-equilibrium interaction region as the mainstream is approached, how do we determine the 'edge' of the boundary-layer flow? A local edge condition is desirable to provide normalizing parameters for the traverses, in order to remove any small inconsistencies that may appear from moving the interaction region with respect to the probe.

We selected the 'edge' as that location away from the wall where the pitot pressure first attains its maximum value, and this is shown by a small horizontal line on each pitot profile on Figure 60. The corresponding reference boundary-layer thickness where the resultant velocity is 99.5 percent of the edge condition is also shown as a solid dot.

Some previous experiments in 2D flow (see Zwarts[97], for example) have estimated the boundary-layer thickness by writing a power law velocity profile relation

$$\frac{u}{u_E} = \left(\frac{h}{\delta}\right)^{\frac{1}{n}}$$

in the form

$$\log_e \left(\frac{u}{u_E}\right) = \frac{1}{n} \log_e h - \frac{1}{n} \log_e \delta$$

The outer 60 percent of the boundary-layer traverse points were fitted via a least squares routine to this logarithmic equation, to yield values of the exponent n and boundary-layer thickness δ. We felt that such a technique for the flow herein was questionable because of the non-equilibrium appearance of the profiles. Our visual approach of inspecting the pitot profiles appears to provide valid and consistent results, as we see on Figures 66, 67 and 68, where integral parameters and local streamwise skin friction coefficients are plotted for centre-line as well as off-centre traverses.

The total temperature, referenced to the stagnation temperature in the tunnel settling chamber, is viewed next on the centre display of Figure 60. The total temperature rises rapidly in the laminar sublayer immediately adjacent to the wall, before assuming some constancy in the wall law region. Thereafter it continues to increase and to overshoot the mainstream flow level by typically one half of one percent of T_o. The distance from the wall of the peak stagnation temperature value increases with progression downstream through the interaction. The asymptotic approach to the tunnel mainstream flow value for total temperature is again slow. We note that the boundary-layer edge as obtained from the pitot profiles is usually close to the position on the total temperature profile where unit temperature ratio is reached subsequent to the overshoot (see Fig. 61).

The corresponding yaw angles are illustrated on the lowest of the three graphs. The skew at the wall, in a direction that turns away from the wedge deflection surface, begins to increase from its nominal 2D value, at least three boundary-layer thicknesses upstream of the calculated shock wave location. As we move downstream (but still upstream of the shock) the extent of the yawed flow region normal to the wall, and the maximum yaw angle, grow progressively; while at our prescribed boundary-layer

edge, the yaw angle has not returned to the nominal mainstream flow direction parallel to the tunnel centre-line. The yaw angle continues to reduce up to two undisturbed boundary-layer thicknesses away from the surface (profile 25004, for instance). Immediately upstream of the shock, at profile 25101, we note the opposite behaviour, see Figure 61: above the boundary-layer edge, the yaw angle increases slowly, this trend carrying over into the recovering flow downstream of the calculated shock position.

We recollect that our diagnosis of the oil flow visualization records on Figure 45 contended that no separation existed at δ_w = 8-degrees. The raw profile information that we have just examined would seem to support this view, for we shall see in Section 4.7 that the stagnation temperature profiles appear to be sensitive indicators of three-dimensional separated flow regions. In contrast, the Mach 2, δ_w = 8-degree temperature profiles on Figure 60 display no sudden variation in characteristics.

4.5.3 Crossflow and Streamwise Flow

Let us now examine the cobra profile information from the four traverse stations. Where profiles at nominally the same distances upstream or downstream of the calculated shock position along the lateral traverse lines y = constant have been gathered, they will be overplotted.

To begin, Figure 62 illustrates the yaw angle distributions with respect to the boundary-layer edge yaw direction, and the corresponding total temperature plots at selected intervals through the swept interaction at δ_w = 8-degrees at Mach 2. The pressure ratio* increases in the direction of proceeding 'downstairs', to the left for the yaw cases and to the right for the temperature measurements. The symbol code at the top left-hand corner distinguishes the traverse locations, and Figure 59 should be sought as an aid in identifying these traverse positions relative to the caclulated shock wave. The solid lines are usually drawn on the graphs through the mean value positions of the data from one or more traverses.

In the centre of the page, we observe some small residual skew of about 1-degree in the upstream boundary layer at four undisturbed boundary-layer thicknesses ahead of the calculated shock wave location, that swings from a direction towards the wedge at the test surface, to one of away from the wedge at $h/\delta_{995} \cong 0.1$. In contrast, a significant skewing of the flow very close to the surface is established at one to two boundary-layer thicknesses ahead of the calculated shock wave location (XT - XSW1NV $\cong -0.3$). With continuing distance dowstream, the yaw angle continues to increase very close to the wall, indicating some collinear flow at stations close to the swept shock wave. Yaw data from traverses at different (lateral) y locations at corresponding distances on either side of the shock overplot to a satisfactory degree of comparison.

On the right-hand side of Figure 62, the overshoot character of the total temperature distributions in the outer region of the boundary layer is very evident when referenced against the vertical bar at $T_{PC}/T_o = 1$. As we saw in the empty tunnel flow that was discussed in Section 4.3, and as we see on Figure 67 for the swept interaction flow, the wall temperatures are slightly higher than those expected on an adiabatic surface, implying some heat transfer from the wall to the boundary layer. The presence of the significant overshoot in the temperature distributions means that the total enthalpy defect in the layer

$$\int_o^{\delta} \frac{\rho u_B}{\rho_E u_E} \left(1 - \frac{T_{PC}}{T_{PCE}} \right) \, dh$$

should be a small value, tending to zero for a boundary layer on a thermally insulated surface.

---

* Wall static pressure.

We might also offer the comment that if the total temperature distributions are expressed in terms of the quotient

$$F = \frac{T_{PC} - T_W}{T_{PCE} - T_W}$$

they can be compared against the Crocco relationship[111] put into a 3D formulation,

$$F = \frac{u_B}{u_E}$$

where u_B is the resultant velocity in the viscous flow. We noted that when plotting the ratio of temperature differences as ordinate versus u_B/u_E as abscissa, the results were situated well above the line of 100 percent correlation on the graph. The parabolic relation of Walz[112],

$$F = \left(\frac{u_B}{u_E}\right)^2$$

provided even worse comparison. Neither of these frequently assumed 2D type temperature distributions appear to exist, therefore, in the swept interaction flowfield presently under discussion.

Taking the measured total temperature through the viscous flow, the distribution of mean velocity can also be found. (We might interject at this stage, that since at any given Mach number in the flow, the resultant velocity, u_B, depends only upon the half power of the local absolute stagnation temperature, whether we use a constant stagnation temperature through the boundary layer equal to T_o, or whether we use that measured locally in the flow, causes little change in the calculated result for u_B.) Knowing the flow conditions at our prescribed boundary-layer edge, the local mean velocity can be resolved into streamwise and crossflow components, u and v, with $u = u_E$ and $v = 0$ at the boundary-layer edge.

Representative boundary-layer profiles showing the streamwise and crossflow components of mean velocity are exhibited on Figure 63, for some of the traverses at δ_w = 8-degrees and $M_1 = 2$. The traverse height perpendicular to the wall and the velocities have been normalized by δ_{995} and u_E respectively.

The difficulties of finding adequate representation for the crossflow profiles is illustrated on the left-hand side of Figure 63, where the experimental measurements at the calculated shock location are compared with the parabolic form suggested by Mager[90], which is

$$\frac{v}{u_E} = \frac{u}{u_E}\left(1 - \frac{h}{\delta}\right)^2 \tan\beta$$

The angle, β, on the test surface is between the local limiting streamline direction and the projection on to the surface of the inviscid streamline at the boundary-layer edge. This profile representation clearly forces agreement immediately adjacent to the surface*, but is substantially more full throughout the

---

* There is a discrepancy, however, between the flow near the surface from the cobra probe traverse and that on the parabolic distribution. This is due to the fact that the local wall shear stress direction from the oil flow visualization has been inserted for β, rather than the cobra probe determined yaw angle closest to the wall.

boundary layer than its experimental counterpart. The maximum value of crossflow velocity ratio and flow angle tends almost to a constant value downstream of the calculated shock position.

In contrast with the crossflow profiles on Figure 63, the corresponding streamwise flow demonstrates an almost self-preserving character through the region of strong interaction, reminiscent of a typical 2D-type power law profile.

As we have discussed in the introduction, the thesis of Lowrie[56] dealt almost exclusively with representing *chosen* velocity profiles in a swept interaction region by Johnston's[61,62,63] triangular model for crossflow, that is sketched on Figure 11(a). Figure 64 shows our Mach 2 swept interaction results at δ_w = 8-degrees re-plotted in polar or hodograph form. Although some evidence of triangularity exists in the flow downstream of the calculated shock position, the outer regions in the flow at stations upstream of the shock may clearly not be approximated by a straight line. Moreover, the frequently assumed collinear inner region would also appear to be a doubtful proposition here, for the limiting streamline angle at the surface, as measured from the oil flow, always appears larger than the yaw angle at the smeared-over junction point. The equation established by Green, based on Lowrie's results for the junction point velocity, in terms of the undisturbed upstream velocity in the mainstream and the local shear stress velocity at the wall (see Section 1.6), does not provide a suitable relationship to explain the junction point data of the profiles illustrated on Figure 64. A test of our experimental results against the Lowrie/Green junction point criterion on Figure 11(b) indicates poor comparison with their line of 100 percent correlation.

It remains to be seen whether the family of hodograph crossflow models suggested by Shanebrook and Hatch[113] and discussed in terms of the compressible, 3D turbulent boundary layer in Reference 114, would yield any satisfactory degree of comparison in a non-equilibrium boundary layer, such as in the swept interaction. Comparisons between selected members of the hodograph family of Shanebrook and Hatch[113] and the nozzle wall crossflow profile data of Hall and Dickens[90] were good. But to find the analytical profiles, the method of least squares must be used to fit the experimental hodographs with the crossflow models from the subfamilies[114]. Such technique is not too helpful when attempting to calculate a flowfield before experimental results are taken. For reasons such as these, the use of a three-dimensional boundary-layer calculation method utilizing the turbulent kinetic energy equation[115] would appear a more worthwhile pursuit, in which no assumptions about crossflow profile shapes have to be made.

4.5.4 Comparison of Experimental Velocity Profiles with the 3D Compressible Turbulent Boundary-Layer Calculation Method of Nash[115]

Since we have so far failed to find a model of the crossflow that compares with the experimental results, we discussed with John Nash[116], whether the existing formulation of his 3D compressible turbulent boundary-layer calculation method (see Appendix 1) could cope with the swept interaction problem. The method had been set up in a form[115] suitable for calculating the skewed boundary layer on a swept wing in transonic flow, where the mainstream at infinity is parallel to the root chord of the wing and no flow is allowed across the streamwise wing tip. Nash considers his formulation as adequate for mainstream Mach numbers up to at least 2.

Using the swept wing programme as supplied, but with zero sweep, we entered the Mach numbers, calculated from the experimental static pressure distributions as measured on the tunnel floor at δ_w = 8-degrees and M_1 = 2, as well as the upstream 2D experimental momentum deficit thicknesses across the width of the test flow. In the method, conditions in the external flow are considered to be isentropic and irrotational. The programme was then run as though the line through the wedge leading-edge parallel to the tunnel centre-line was the root chord line, and the presence of the deflected wedge boundary was thus ignored. This clearly will lead to under-turning of the calculated flow, in the direction away from the wedge surface.

As an example, Figure 65 shows the measured experimental profiles in directions *parallel and normal to the tunnel centre-line* at traverse 25104 downstream of the calculated swept shock wave location, compared with calculated profiles at lateral stations 0.5-in. on either side of the traverse point.

Calculated shear stress profiles are also presented. We observe qualitative agreement between calculation and experiment, but the calculated 'crossflow' is substantially less than that measured, while the calculated 'streamwise' flow evidences a fuller profile. We would postulate, however, that a satisfactory modelling of the experimental flow might well result if the bounding constraint of the deflected surface of the wedge could properly be input to the programme.

4.5.5 Integral Parameters, Local Skin Friction and Wall Conditions

Figure 66 illustrates the growth of the boundary layer through the δ_w = 8-degree, Mach 2 swept interaction region. All of the data from the profiles are plotted, taken along both the tunnel centre and off/centre-line stations, at y = 0.028 and 0.150-in.; and where the three lines of results are identified with different symbols. The shaded symbols are at those two traverse stations along the projection on the floor of one inviscid streamline, downstream of the calculated shock wave position. We note that the qualitative interpretation of the results is the same whether we stay on one line of traverse measurements, or whether we follow the inviscid streamline direction.

All of the plots on Figure 66, whether they be boundary-layer thickness, δ_{995}; streamwise and crossflow displacement thickness; or streamwise and crossflow momentum thickness, indicate a thickening of the viscous flow with increase of lateral distance from the wedge apex along the calculated shock wave location — even with the small lateral change of five to six undisturbed boundary-layer thicknesses* that exists between the borders of the traverse points (see Fig. 59). As such, the flow appears more quasi-conical than quasi-cylindrical, as we discussed in Reference 75.

In the axial direction, there is a lag in the growth of the streamwise and crossflow thickness parameters, until about one undisturbed boundary-layer thickness downstream from the commencement of the pressure rise (Fig. 67), where the local static pressure gradient is at its maximum. During the next two undisturbed boundary-layer thicknesses downstream, the streamwise flow displacement and momentum thickness parameters show rapid growth until the calculated shock position is reached, and the pressure gradient begins to reduce significantly.

The shape factor, H, the ratio of the displacement to the momentum thickness parameters of the streamwise flow, (see Fig. 67), is non-responsive to the imposition of the pressure rise, but does begin to reduce where the pressure rise tends asymptotically towards the calculated value, and where the expansion fan from the wedge trailing-edge is approached. This behaviour of H is consistent with the almost self-preserving character of the streamwise flow profiles that was evident on Figure 63, but would, on the other hand, appear an insensitive indicator of what surely is a non-equilibrium flow. The distribution of streamwise shape factor H, however, does indicate a small dip close to where the maximum pressure gradient occurs. This dip amplifies with increasing shock strengths as we see on Figure 75 at Mach 4.

Supplementing the performance of the streamwise flow parameters, we see that the corresponding crossflow thicknesses increase throughout the interaction region, reducing only as the wedge trailing-edge expansion field is approached.

On Figure 66, we show the thickness parameters along the tunnel centre-line, calculated by the Nash 3D turbulent boundary layer method[115], for this Mach 2, δ_w = 8-degree flow case. The calculated results offer a near invariancy of boundary-layer thickness, and only a small increase in the growth of the true displacement surface (see Appendix 1) with distance downstream through the swept interaction, in contra-distinction with the rapid growth of the measured individual streamwise and crossflow components. The plot of displacement thickness, illustrates clearly, that the viewing of the components in only the streamwise and crossflow directions, does not necessarily provide the correct physical impression of the true displacement effect. In a qualitative sense, the true displacement thickness differs from the streamwise flow value because the boundary layer causes some flow at right angles to the direction of the external streamlines[118].

---

* Measured from wedge apex.

On Figure 67, we also show the measured wall temperatures plotted with regard to the corresponding adiabatic wall condition. At the slightly elevated temperature of the test wall, the measured temperature rise through the maximum pressure gradient region, is not as noticeable as on the corresponding calculated adiabatic wall temperature distribution.

Most 2D compressible calculation methods of turbulent boundary-layer flows, when compared with experiment, will determine the momentum thickness adequately, the displacement thickness satisfactorily, and the skin friction (very often) to only fair or poor accuracy[34]. Clearly, the crucial test for the success or failure of a computation method in compressible flow will still be the accurate prediction of the most sensitive and important parameter: the local skin friction coefficient, C_F. The measured distribution of surface pressure shown on Figure 67 is not unlike that measured in an unseparated, two-dimensional flow — see Figure 8. The distribution of local skin friction coefficient, C_F, that is shown on Figure 68, also appears to possess the same qualitative form as in 2D flow — a rapid fall in C_F as the shock induced pressure ratio increases to its maximum pressure gradient condition, followed by a more gentle reduction where the pressure gradient is virtually constant, to a near exponential return to equilibrium further downstream.

Let us examine the plot of local skin friction coefficient more closely. We first note, as reference datums, the empty tunnel C_F values for the circular pitot tube and the cobra probe calculated according to Bradshaw's correlation[101], and the offset between them of $\Delta C_F \simeq 0.00035$ that we discussed in Section 4.3. The various wall pitot correlations for the cobra probe that were introduced in Section 4.2 are plotted as the large bulk of data points that are referenced against the 'ZPG, CFBRAD, COBRA PROBE' line. Towards the upper part of the C_F plots, we see the C_F results calculated according to the correlation of Sommer and Short[120] that is based on the streamwise momentum thickness Reynolds number and the intermediate temperature hypothesis. This latter correlation produces data points from the cobra probe profiles in the upstream undisturbed boundary layer that are in good agreement with the undisturbed values calculated according to Bradshaw's correlation with the circular pitot tube.

In the region where the gradient of wall static pressure remains more-or-less constant, the crossflow component of wall shear stress increases steadily as we may infer from the lower graph on Figure 68, where the divergence in limiting streamline direction is plotted with reference to the direction of the undisturbed boundary-layer flow upstream of the interaction. On this basis, we would expect that the magnitude of the resultant surface shear stress would fall less rapidly (as determined by the cobra surface pitot measurements) than the streamwise component alone (computed from the cobra probe velocity profiles) and displayed on the top of the C_F plot. That the opposite observation is made from the C_F measurements on Figure 68, is difficult to rationalize. We note moreover, that the Nash calculation method provides quite satisfactory agreement with the correlation of the velocity profile data according to the Sommer and Short[120] C_F method.

Some further points regarding the Bradshaw and Hopkins/Keener Preston tube correlations are in order, because of differences obtained depending on the manner in which the Mach number is calculated at the boundary-layer outer edge.

The graph at the top of Figure 68 shows three distributions of Mach number, calculated according to (i) the Rayleigh pitot equation, using pitot measurements at the outer edge of the boundary layer; (ii) the same equation with pitot measurements at roughly two undisturbed boundary-layer thicknesses away from the wall; and (iii) according to the ratio of local static pressure to tunnel stagnation pressure in the settling chamber. In all three computations, the local static pressure measured at the wall was assumed to be constant and to exist along a normal to the wall into the local mainstream. The three computed Mach number distributions are plotted against the nominal Mach number in inviscid flow.

The Mach numbers calculated according to the local static to stagnation pressure ratio, are shown by square symbols and fall progressively through the interaction region, consistent with the static pressure rise illustrated on Figure 67. But the pitot derived Mach numbers only follow the same trend up to 2.5 undisturbed boundary-layer thicknesses ahead of the calculated shock position. Thereafter

those pitot measurements at the boundary-layer edge (the circle symbols) result in a higher level of Mach number throughout the interaction region; while the pitot measurements taken further out in the flow (circle symbols with tails) yield a rapid fall in local Mach number up to one undisturbed boundary-layer thickness ahead of the calculated shock location, followed by an almost instantaneous jump back to the Mach numbers calculated at the outer edge of the boundary layer. In shock-separated 2D flows, the work of Bogdonoff[28] and Green[29], for instance, has indicated that in the vicinity of the separation, the outgoing wave field may be seen as a 'compression field generated by a strong interaction, but interrupted by an expansion fan which is the constant pressure reflection of the incident shock wave' (see Ref. 29). But even before 2D separation commenced, Bogdonoff and Kepler[28] observed an expansion generated at the foot of the incident shock wave. That we observe the same expansion phenomenon in the 3D swept interaction, where there is no 3D separation, is of interest; and we must presumably ascribe the differences in Mach number distribution from the two sets of pitot measurements as those arising from a non-uniform static pressure normal to the wall, as a result of the axial stretching of the shock foot into a compression fan.

If we now return to the distributions of local skin friction coefficient in the centre of Figure 68, we note the Hopkins/Keener correlation based on wall temperature (adiabatic), yields lower C_F results with the Mach number from the pitot measurement at the outer edge of the boundary layer than from the Mach number calculated according to the ratio of static pressure to undisturbed mainstream stagnation conditions. However, the differences in the C_F results are probably not significant. Based on M(P/PO), the Bradshaw correlation provides a slightly increased value of C_F near the calculated shock position than either of the Hopkins/Keener results.

To conclude, the lower graph on Figure 68 shows a rapid initial growth in the divergence of the local limiting streamline direction with respect to the upstream flow direction, followed by a more-or-less constant value of β_{CL} and a subsequent region of slow decay. We note that the limiting streamline direction through the interaction region as measured from the oil flow visualization, always leads the nearest value of yaw angle to the wall that is obtainable from the cobra probe (the vertical bars on the measurements from the oil flow indicate the maximum variations in β_{CL} determined from seven separate tunnel runs); but that in the relaxing region downstream of the calculated shock position, the measurements recover to one of good comparison. We infer from this discrepancy in β_{CL} through the interaction region, that yaw conditions near the wall, between the wall and the first data point measurable with the cobra probe are still changing rapidly and that regions of collinear flow are very small. Such an observation has already been implied by the polar velocity plots on Figure 64 and suggests that a significant law of the wall region does not exist in this interaction region.

As we would expect, the omission of the deflected wedge surface as a boundary constraint in the 3D boundary-layer calculation, causes the computed skew angle at the wall to be less than that measured, by a value roughly equal to the deflection angle of the wedge.

In general, the yaw angle at the outer edge of the boundary layer downstream of the calculated shock position, is somewhat less than that measured well away from the surface (at two undisturbed boundary-layer thicknesses), and which in turn is less than the deflection angle to the flow provided by the 8-degree wedge setting.

4.6 Cobra Probe Traverses at Mach 4 and δ_w = 8-Degrees

4.6.1 Cobra Profile Measurements as Pitot Pressure, Total Temperature and Yaw Angle

In discussing the oil flow visualization and wall static pressure distributions at Mach 4, we discovered that incipient separation occurred at a wedge deflection angle close to 6-degrees (see Fig. 52). Hence, we might expect to observe some significant qualitative differences between the unseparated δ_w = 8-degree flow profiles at Mach 2 (Fig. 60) and those at the same wedge angle at Mach 4 (Fig. 70) where large scale 3D separation is imminent. The centre-line pitot, stagnation temperature and yaw profiles on Figure 70 follow the presentation arrangement established on Figure 60 in Section 4.5, and the qualitative aspects of the Mach 4 flow are analogous to those interpreted at Mach 2. The Mach 4 traverse locations are shown on Figure 69, and it will be noted that no off/centre-line measurements were taken.

Two distinctive features between the Mach 4 and Mach 2 flows at δ_w = 8-degrees are clear, however. Close to the calculated shock wave location at Mach 4 in Figure 70, the rate of change of pitot pressure with distance normal to the surface is small, in sharp contrast with the measurements at Mach 2 (on Fig. 60). Such behaviour is reminiscent of the pitot profiles through a 2D shock separated boundary layer[29]. Secondly, the rate of change of total temperature with distance from the wall increases as the calculated shock position is approached, implying more vigorous exchange of stagnation enthalpy in the flow.

The yaw angle at the prescribed boundary-layer edge is close to zero degrees up to the calculated shock position, and a tendency toward the wedge deflection angle is shown only farther out in the flow.

4.6.2 Crossflow and Streamwise Flow

In comparison with the δ_w = 8-degree flow at Mach 2 illustrated on Figure 62, Figure 71 shows the Mach 4 profile distributions of yaw (with respect to the resultant velocity vector at the outer edge of the boundary layer) and total temperature, at the same wedge deflection angle. The most obvious qualitative feature of difference between the two flows is that the characteristic smoothness of the distributions at Mach 2 appears to be changed to one of 'hills and valleys' at Mach 4, particularly on the total temperature distributions. Whether the 'wiggles' on the temperature plots are introduced from disturbances propagating from the floor vortex generator upstream of the test section, is debatable. The yaw distributions at Mach 4 have also changed in character in comparison with their Mach 2 counterparts, the middle region of the Mach 4 boundary layer holding a more constant yaw angle up to the calculated shock wave position.

The streamwise flow and crossflow velocity ratio profiles are drawn on Figure 72. The features of the yaw distributions seen on Figure 71 are carried over to the crossflow plots, while the absolute magnitude of the non-dimensional crossflow velocity is about the same as at Mach 2. The normalized streamwise flow velocity profiles at Mach 4 have also changed character in the region close to the wall, tending toward a 2D type separated flow profile. The Mach 4 polar plots of velocity on Figure 73, as at Mach 2, do not resemble a triangular form except at the traverse station just upstream of the calculated shock wave location.

4.6.3 Integral Parameters, Local Skin Friction and Wall Conditions

The boundary-layer thickness parameters are shown on Figure 74 for the Mach 4, δ_w = 8-degree flow case. Again the locus of the point of 99.5 percent of local mainstream velocity, δ_{995}, indicates little change with distance downstream. But at roughly seven undisturbed boundary-layer thicknesses ahead of the calculated shock wave position, there is a noticeable decrease in the growth of the streamwise displacement thickness, δ_1*, much like that measured in the 2D Mach 4 decelerating flow of Peake et al in Reference 34. For this decrease in δ_1* to occur in a decelerating flow, the normalized density, ρ/ρ_E, must be increasing at a more than compensating rate than the normalized velocity, u/u_E, is decreasing, in the inner region of the boundary layer.

While δ_1* shows a small dip, the effect is amplified when we transfer across to the streamwise shape factor, H, displayed on Figure 75. The reduction in H occurs in the region of maximum adverse pressure gradient, but H recovers again towards the calculated shock wave location. No wall temperature measurements were made at Mach 4, but the adiabatic wall temperature is shown for reference as the lower graph on Figure 75.

The local skin friction coefficients derived from the cobra wall pitot measurements and the cobra velocity profiles are illustrated on the centre graph of Figure 76. The arrangement of the plotting of the various C_F correlations is analogous to those measurements for δ_w = 8-degrees at Mach 2 that we saw on Figure 68. There is a continuing fall in C_F towards the calculated shock wave location, but as no wall pitot measurements were made further downstream, we see no subsequent plateau or recovery towards the flat plate value. The C_F correlation of Sommer and Short[120], utilizing the Reynolds number based on the streamwise momentum thickness at each profile station follows the result obtained in the empty

tunnel in nominally zero pressure gradient flow. As at Mach 2, the relative differences between the Sommer/Short and surface pitot correlations are in the opposite direction to instinct: that the resultant wall shear stress reduces at a faster rate through the interaction than the corresponding component of streamwise wall shear stress.

The sudden increase in local Mach number that was determined at h ≅ 0.5-in. above the wall, as the calculated shock location was approached in the Mach 2, δ_w = 8-degree flow case, is now more evident at Mach 4 (Fig. 76). The trends in limiting streamline angle at the wall on Figure 76 follow closely those explained on Figure 68.

4.7 Cobra Probe Traverses at Mach 4 and δ_w = 16-Degrees

4.7.1 Cobra Profile Measurements at Pitot Pressure, Total Temperature and Yaw Angle

Figure 78 illustrates the cobra probe pitot, total temperature and yaw profiles along the tunnel centre-line through the Mach 4, δ_w = 16-degree flow, where as we have already seen on the oil flow visualization of Figure 54, there is extensive upstream influence and a significant three-dimensional separated flow region.

A map of the seven stations relative to the calculated shock wave location at which the cobra traverses were taken, is given on Figure 77. The stations were chosen to provide profile measurements from upstream of the three-dimensional separation line to a position downstream of the calculated shock wave location. The stations are situated along the centre-line only.

The pitot pressure profiles on the top graph of Figure 78 are sufficiently close in spacing through the interaction to allow a construction of the forward oblique leg of the shock bifurcation at the foot of the wedge shock. The position of the oblique shock leg is given by the noticeable and sudden deficit in pitot pressure observable on the plotted distributions, and as we would expect, the three-dimensional separation line is positioned very close to the intersection of this oblique shock wave and the test surface. Downstream of the 3D separation line, the presence of shear layers with heat transfer is indicated by developing troughs in the pitot distributions that are closely matched in position by similar troughs on the total temperature plots. Figure 79 shows the three measured profiles at the calculated shock wave location re-drawn in close proximity. The arbitrariness in choosing δ_{995} is particulary important here and should be noted on Figures 78 and 79. Along with the correspondence of peaks and troughs on the pitot and total temperature distributions, we observe a sudden slowdown in the change of yaw angle between these maxima and minima.

From these distributions, we may postulate that the deficit troughs correspond with the core flow of a flattened vortex structure of the rolled-up free shear layer from the 3D separation line, much like the flow measured by Cooper and Hankey and reported in Reference 74. The axis of the vortex would appear close to the line of the calculated shock wave, the origin of which is the wedge apex. A stream surface in the upstream boundary layer will pass over the rolled-up flow and attach to the floor and wedge surface at the divergence locations of the limiting streamlines already pointed out in Section 4.4. Clearly, the cobra probe can only resolve the local angle of the mean flow in planes parallel to the tunnel wall. If there is significant pitch of the oncoming streamlines to the cobra pitot, where the resultant velocity vector resolves into a larger component in the pitch plane than in the yaw plane, the streamwise and crossflow profiles, as resolved herein, will be in error. The largest pitch angles relative to the cobra probe will occur in a plane parallel to the floor that cuts the vortex core position. In other words, the cobra probe might be providing low values of pitot pressure at the troughs of the profiles illustrated on Figures 78 and 79.

The rapid development in skew at the wall as the 3D separation line is approached is illustrated on Figure 80, where the yaw at the wall is more than 40-degrees with respect to the direction of the resultant velocity at the assumed outer edge of the boundary layer. Of particular relevance is the overshoot in yaw along the outer part of each profile approaching the calculated shock wave location. That this region of the flow yields the maximum overshoot, at the calculated shock wave location, provides tentative support to claim that concentrated roll-up of the free shear layer is somewhere close-by. On

Figure 81, we have again plotted some of the total temperature distributions measured in the Mach 4, δ_w = 16-degree flow, to show the relatively small movement away from the surface of the troughs with distance downstream. Further out in the viscous flow, other sudden reductions or troughs in total temperature are seen (see Fig. 78) that become more pronounced with increasing distance downstream.

4.7.2 Crossflow and Streamwise Flow

The features of the crossflow and streamwise flow velocity profiles, Figures 82 and 83, follow closely on the remarks made about the yaw and the pitot pressure distributions. Analogous troughs are viewed on the streamwise flow profiles consistent with the troughs in pitot pressure on Figure 78, and S-shaped crossflow velocity profiles emerge because of the overshoot in yaw angle discussed previously.

At the 3D separation line, the streamwise flow profile resembles in shape the corresponding profile in 2D flow.

The polar velocity plots on Figure 84 for the Mach 4, δ_w = 16-degree flow case, exhibit substantial differences in the separated flow to those measured at the lower 8-degree wedge angle, near to incipient separation, as shown on Figure 73. As we progress downstream in the former flow, from the 3D separation line towards the calculated shock wave location, the shape of the hodograph in the outer region resembles the cresting of a wave on the sea-shore!

4.7.3 Integral Parameters, Local Skin Friction and Wall Conditions

Since following the 3D separation, a new boundary layer must commence to grow from an attachment line on the wedge surface close to the intersection of the wedge foot with the floor (see the oil flow visualization on Fig. 54) this new boundary layer can withstand a relatively large pressure gradient imposed upon it (but modulated presumably by the roll-up of the free shear layer above it). We thus note a rapid increase in all of the boundary-layer thickness parameters downstream of the 3D separation line as shown on Figure 85. The streamwise shape parameter, on Figure 86, shows a large decrease at the 3D separation line position compared with that in the upstream undisturbed mainstream, and this follows the trend established in the weaker shock pressure rises discussed on Figures 67 and 75. However, the distribution of H shows large up-and-down variations as we approach the calculated shock wave position.

The arrangement of the local skin friction information on Figure 87 is consistent with that already discussed on Figures 68 and 76. Of significant interest, however, is the fact that the wall pitot (cobra probe) does not measure the lowest pitot pressure at the 3D separation line, but at one undisturbed boundary-layer thickness further downstream. The local resultant skin friction as calculated from the Preston tube correlations, exhibits a rapid increase as we move away from the minimum towards the calculated shock-position, in a region where the limiting streamline angle at the wall has virtually constant deflection, see Figure 87. In contrast, the streamwise flow component (Sommer/Short) is decreasing as the resultant C_F is increasing.

Outside of the boundary layer and downstream of the 3D separation line, we again see the trough in the Mach number distribution; but this feature now seems to be carried over to the three Mach number distributions that we see at the top of Figure 87.

Downstream of the 3D separation line, the crossflow angle at the wall, β_{CL}, tends to a plateau value of about 45-degrees.

4.8 Air Injection Into a Swept Shock/Turbulent Boundary-Layer Interaction in a Mach 2 Mainstream Flow

4.8.1 Wall Jet Flow in the Empty Tunnel

In our initial statement of objectives, we stipulated that the goal of the present investigation was the control by tangential air injection of a three-dimensional separated flow region induced by a

swept shock wave. As a follow-on to the successful two-dimensional blc experiment reported in Reference 5, we planned to use a Mach 3 wall jet beneath a Mach 2 mainstream, to provide a jet velocity greater than that of the mainstream, coupled with an excess of jet momentum flux slightly more than the momentum deficit of the tunnel boundary layer upstream of the jet slot.

Section 2.6 described the jet blowing apparatus consisting of a 2D convergent/divergent supersonic nozzle installed in the wind tunnel floor as part of a turntable. The wedge leading-edge could be situated at a distance up to 14 original boundary-layer thicknesses downstream of the jet exit (with θ_j = 0-degree)*.

Before commenting on the degree of control exercised by blowing into a swept interaction region, we first of all review the downstream penetration qualities of the Mach 3 jet in the empty tunnel flow. Figure 88 illustrates the surface pressure distributions and oil flow visualization from one such configuration, where the jet flow (displayed by superposing small black arrows) exits at -12-degrees relative to the normal to the nominal mainstream flow direction (large clear arrow). The negative sign given to the jet exit setting implies anti-clockwise rotation of the turntable from the nominal zero line with the jet exit plane perpendicular to the mainstream flow, when we look at the floor from above and the mainstream flow is from left-to-right. The turntable periphery is made visible by the dark material inserts used in its construction. The rearward facing steps situated between the extremities of the jet nozzle and the tunnel endwalls introduce regions of disturbed flow bordering the jet**.

The surface oil flow visualization on Figure 88 indicates negligible change in direction of the jet flow about its redirected centre-line along the test floor, whose limiting streamline *directions* (not magnitudes of shear stress) are plotted on Figure 89 to compare with a flow case at θ_j = 0-degrees. The jet stagnation pressure of 167 psia yields a calculated static pressure in the Mach 3 jet flow about equal to the Mach 2 mainstream static pressure.

The abrupt change in slope of 4-degrees between the jet nozzle wall and the tunnel floor in the plane of the jet exit (see Fig. 26) generates a shock wave and consequent increase in local static pressure, which is almost immediately cancelled by the reflection of the shock wave within the jet, as an expansion from the free jet boundary. (Figure 103, showing some Schlieren results in a 2D flow[5], may assist the reader to visualize the disturbances near the jet exit. We should note, however, that the nomenclature of β and P_I/P_{IN} refer to the deflected wedge angle and the ratio of stagnation pressure in the jet to that in the mainstream.) At one inch or ten jet slot heights downstream of the jet exit, the wall static pressure has returned to the nominal mainstream value within the limits of ±10 percent of the reference undisturbed static pressure of the mainstream at station α1Z*** (see Fig. 24).

What of the uniformity of the jet flow across the width of the jet nozzle exit? Because of the large number of static pressure orifices in the wind tunnel floor, and the physical obstruction of the supply pipe to the blowing nozzle beneath the jet nozzle insert (Fig. 13), it was not possible to install either the cobra probe or the circular pitot probe traversing gear. Instead, as well as relying on local static pressure distributions and accompanying oil flow visualization, we chose to use the obstacle block indirect skin friction measuring devices that Nituch[125] had investigated (following the suggestion of Rainbird) in a low speed tunnel flow.

The optimum dimensions that Nituch found for the obstacle block are sketched on Figure 90, where the height, width and length of the block are typically 3, 4.5 and 9 times the diameter of the static hole against which the block is to be abutted. A semi-circular cut-out, positioned at the centre

---

* The so-called 'mixing length' along which distance the blc jet and original boundary-layer flows merge together, may conveniently be defined as the distance between the jet exit and the calculated shock wave position from the wedge (in the Mach 2 flow) along the line of the jet. Hence, for any given rotation of the jet efflux, and shock wave angle from the wedge, the local mixing length will vary along the length of the shock front.

** Table 8 lists the run parameters for the blowing blc tests.

*** α1Z is sometimes written as A1Z.

of the forward facing side of the block, along with a drill bit in the static hole, facilitates the accurate location of the block with respect to the inside of the static hole. As with the geometrically similar Preston tube devices, the disturbance to the local flow produced by a congruent family of obstacle blocks, provided they are immersed within the law of the wall region of a turbulent boundary layer, will be governed only by wall variables and a characteristic size of the obstacle (the height). The blocks can be calibrated in a pipe flow and Vinh[126] has demonstrated that under high Reynolds number conditions, the calibration for the geometry of block described is similar to that of Patel's calibration for the Preston tube.

For a qualitative determination of the variation of local wall shear stress in a flow, we can clearly observe the disturbance pressure due to the obstacle block and compare it with the undisturbed static pressure, p_1, at our reference Station 1.

Figure 90 shows the static and obstacle block pressures (with reference to p_1) across the wind tunnel at Line A2* upstream of the jet slot — see Figure 24, with the Mach 3 wall jet on and off. Neither the changing or yawing of the blocks, by 10-degrees, nor the status of blowing affected the nominal uniformity of both the block and static pressure distributions across the tunnel upstream of the jet slot.

The static and obstacle block pressures are next shown across Line 10 (see Fig. 24), at six slot heights or about three undisturbed boundary-layer thicknesses downstream of the jet exit. Figure 91 shows that the distribution of static pressure across the Mach 3 jet flow is nominally uniform, but the block pressures display a triangular distribution reminiscent of a preferential cellular type flow, and thus a very uneven shear stress. (Note the relevant scales for pressure ratio!) That the tunnel flow was not itself responsible for the unevenness is shown by the jet-off pressure distribution measured with the same blocks, which again indicates relatively good spanwise uniformity.

We tried the same measurements across Line 17 with the Mach 3 jet on, where the location was 17.5 slot heights or almost nine undisturbed boundary-layer thicknesses downstream of the jet exit — see Figure 92. The same qualitative results were obtained but the relative dispositions of the peaks and troughs in the block pressure distributions had moved by 0.5-in. (or five slot heights) in the lateral direction! Again the flow with the jet off showed only a small variation in the lateral distribution of block pressures.

We postulated that perhaps the thermometer or the screen in the blowing pipe upstream of the jet nozzle contraction was responsible for the anomalies in the spanwise distribution of shear stress, and these were consequently removed. Figure 93 shows the block pressures again across Line 10 (Fig. 24) which demonstrate once more the aforementioned triangular shape to the block pressure distributions, irrespective of whether or not the screen and thermometer were in the settling chamber**.

We thus concluded that the jet flow provided a high mean level of local shear stress at the wall, but was modulated substantially by a triangular waveform across the span of the jet. As the local skin friction coefficient is very roughly proportional to $(p_B/p - 1)$, all other parameters being equal, we can see that the jet flow has introduced a wall shear stress about five times that existing in the empty wind tunnel (compare Figs 90 and 91). However, the amplitude of modulation generated by the triangular waveform across the jet is typically 0.7 times the level of the wall shear stress in the undisturbed flow.

4.8.2 Effect of θ_j with δ_w = 8-Degrees, with XWLE = 1.5-in.

Section 4.4 and 4.5 have included a comprehensive discussion of the flow in the swept interaction region at Mach 2, generated by an 8-degree wedge deflection, where it was considered that in spite of substantial skewing of the boundary layer, three-dimensional separation had not yet begun. Hence, this flow régime provides an initial datum against which to check the effects of adding the Mach 3 jet flow.

---

* A2 means $\alpha 2$ on Figure 24.

** There were no 'nicks' or scratches across the width of the jet nozzle, to cause the flow imperfections.

Figure 94 is comprised of a series of illustrations depicting the jet efflux issuing beneath and at various angles to the direction of the undisturbed boundary-layer flow, of between -20 and +30-degrees, where the mixing distance between the jet exit and the shock front varies from about 2 to 20 upstream boundary-layer thicknesses, depending on θ_j.

In the early days of planning the blc experiment, it was thought that directing the blowing at say θ_j = 30-degrees would perhaps offer most benefit for controlling the 3D separated flows, for in so doing, the direction of the jet surface shear must be turned through more than 60-degrees for it to follow the line of a typical 3D separation at Mach 2, generated by a wedge standing normal to the floor. It was suggested that the penetration ability of the jet flow should be sufficient to erase the separation line.

In this simple-minded approach, the effect of the solid wedge obstruction was neglected when, of course, it acts as a bluff protuberance to produce a near normal shock to the oncoming jet flow, and a consequent massive 3D separation that we view on the lowest photograph on Figure 94. We have now obtained a flow with substantial separation with the jet on as compared with the swept interaction at δ_w = 8-degrees with no jet, where no separation existed! If we now rotate the jet efflux such that it is parallel with the undisturbed boundary layer at the jet slot, we still see that there is a 3D separation. Incipient separation of the new boundary layer growing beneath the jet peak will occur at a wedge angle corresponding with the local jet peak Mach number, provided the latter is greater than the Mach number of the mainstream. We remember from Sections 4.5 and 4.6 that the wedge angle for incipient separation decreases as the local oncoming Mach number to the wedge increases. Evidently, with the jet peak Mach number close to three, the wedge angle for incipient separation is less than 8-degrees. But the enhanced surface shear stress provided by the jet is inadequate to destroy the 3D separation at the given mixing distance of about four undisturbed boundary-layer thicknesses, between the jet exit and the wedge leading-edge.

If we follow the photographs in the centre of Figure 94 to the top of the page, we see that by aligning the jet efflux somewhere between the wedge deflection angle of 8-degrees and the shock wave deflection angle of 37-degrees (at Mach 2), the three-dimensional separation line is caused to disappear. The flow in the junction of the wedge foot with the floor when θ_j = -12-degrees is well displayed on the photograph at the top left-hand corner, where no coalescence of the limiting streamlines is observed. In contrast, similar photographs on the right-hand side of the page show, very clearly, the 3D separation lines at θ_j = 20 and 0-degrees. The mainstream and jet flow directions are again indicated with the superposed transparent and solid arrows.

On the left-hand side of Figure 94, we observe the surface static pressure distributions along the centre-line and Line A for the range of wedge angles used on the flow visualization. We see that one aspect of the controlling mechanism of the jet at θ_j = -12 and -20-degrees (the half-shaded circular symbols) is to cause a local expansion fan around the wedge leading-edge. This reduces the maximum value of shock pressure rise generated by the wedge deflection angle to a value less than the calculated shock pressure rise. In addition, the jet is now blowing in a direction along which, from the wedge apex, there exists a *favourable* pressure gradient (in the absence of the jet) due to the attenuation of maximum pressure rise with distance from the shock generator. For these reasons, coupled with the substantial wall shear stress introduced by the jet flow, the 3D separation would appear to be erased. The corresponding pressure distributions along each line of static holes at the respective θ_j angles shown on Figure 94 are displayed on Figures 95(a) to 95(e).

4.8.3 Effect of θ_j with δ_w = 11.5-Degrees, with XWLE = 1.5-in.

As we have seen on Figure 94, the jet flow may be orientated with respect to the wedge deflection angle to alleviate the shock pressure field. In a swept interaction with δ_w = 11.5-degrees where a large scale separation was generated (see Section 4.4), we see on the oil flow visualization on Figure 96 that a jet angle of θ_j = -20 or -25-degrees would again appear to remove the three-dimensional separation. The mechanism of jet control is once more indicated by the reduction in shock pressure ratios displayed in the pressure distributions along Line A and ℄ on the left-hand side of Figure 96. It is noteworthy that the rolled-up shear layers from the 3D separation lines at θ_j = 0 and -12-degrees induce substantial troughs in the pressure distributions that are consistent with the presence of vortex flows. A full set of pressure information for each turntable angle shown on Figure 96 is given on Figures 97(a) to 97(d).

4.8.4 Effect of Jet Stagnation Pressure in Empty Tunnel; and with δ_w = 11.5-Degrees

On the left-hand side of Figure 98, we illustrate the effect on the empty tunnel wall limiting streamline patterns of increasing the jet blowing pressure progressively from 0 to 214 psia. As the blowing pressure escalates, the local static pressure in the jet at the exit plane increases from a value below (with P_{o_j} = 114 psia) to a value above that in the tunnel mainstream (where P_{o_j} = 214 psia. The manifestation of this increase in blowing pressure is a progressive outward lateral movement of the mixing region between the side extremities of the jet and the base flows of the rearward facing steps bordering the jet exit.

At a wedge angle of 11.5-degrees, a doubling of the blowing pressure (and hence the jet excess momentum) from an overexpanded to an underexpanded jet flow condition with θ_j = 0-degrees and XWLE = 3.0-in. has no appreciable effect on destroying the 3D separation, as we see on the right-hand side of Figure 98. Pressures along the test wall corresponding with the flow visualization photograph at the design blowing pressure conditions of P_{o_j} = 171 psia, are shown on Figure 99, where evidence of a pressure trough along the centre-line downstream of the calculated shock position indicates the presence of a rolled-up vortical flow and no meaningful control of the 3D separation. Clearly, to understand the character of the new wall boundary layer beneath the jet peak, and the mixing region above the jet peak in these highly skewed flows, we require boundary-layer profile measurements to supplement the static pressure distributions and oil flow visualization results.

4.8.5 The 2D Shock Wave/Turbulent Boundary-Layer Interaction and Its Control by Blowing

As a postscript to blowing into the 3D swept interaction, we thought it meaningful to repeat as near as possible, one of the 2D flow cases reported in Reference 5. To the glass window in the ceiling of the empty wind tunnel (see Fig. 13), we affixed an 8-degree wedge as depicted in the top left-hand drawing on Figure 100, and which causes a gross 2D separation in the absence of blowing[5,29]. The wedge was positioned in such a way that its oblique shock wave would strike the test flow on the tunnel floor somewhere between six to ten original boundary-layer thicknesses downstream of the jet exit, when set at θ_j = 0-degrees, and in line with the recommendations for jet/boundary-layer mixing length reported in Reference 5. Two injection Mach numbers were tried: $M_j \cong 2.5$, a value close to the 2.4 value used in Reference 5; and $M_j \cong 3$.

The oil flow visualization patterns for the 8-degree wedge angle in the Mach 2 mainstream, at each jet Mach number, are shown on the right of Figure 100. The mainstream and jet flows are parallel to the tunnel centre-line in a direction from left-to-right.

At each jet Mach number, we observe a nominal 2D separation line at the 'collision' location of the incident shock with the turbulent boundary layer, with almost immediate reattachment of the flow thereafter. We note on the left-hand pressure distributions of Figure 100 the static pressure ratio through the combined incident and reflected shocks is approximately 2.4 and decreases quickly to a level nearer to the calculated pressure rise of 2.2, just downstream of the separation. The jet would appear to be of benefit in providing a substantial wall shear stress downstream of the interaction, in accordance with the findings of Reference 5.

The experiment was then repeated with a wedge angle of 11.5-degrees, a jet Mach number of three, and a mixing region between the jet and original boundary layer of about six original boundary-layer thicknesses. A 2D separation was again obtained, as we see on Figure 101, with a more extensive separation bubble length than at the 8-degree wedge angle. The experimental shock pressure ratio is now 3.6.

Downstream of the separation bubble, we again view a substantial length to the oil streaks, implying a satisfactory level of wall shear stress. Clearly, the expansion fan from the wedge trailing-edge will in part be responsible for the re-establishment of the flow downstream of the separation bubble, as will the jet flow.

A series of profiles through the jet/boundary-layer combination is shown on Figure 102 and taken from Reference 5 for a shock pressure rise just slightly less than three, but in most other respects analogous to the flow on Figure 101. The velocity profile that was taken nearest to the peak of the pressure rise demonstrates retardation to the wall boundary layer beneath the jet peak and to the mixing region between the jet peak and the tunnel mainstream, when compared with the velocity profile at the commencement of the pressure rise. Nevertheless, the corresponding Schlieren flow visualization photograph from Reference 5, that is shown as Test N on the right-hand side of Figure 103, would appear to illustrate that control of the test flow had been maintained through the pressure rise. The shock/expansion train in proximity to the jet exit will introduce a considerable increase in turbulence into the flow field, and we can detect no large-scale regions of separated flow beneath the Mach reflection type of shock formation. The jet has apparently provided sufficient momentum flux to 'carry' the original boundary layer through the shock pressure rise of almost three, although further downstream, the expansion from the trailing-edge of the wedge shock generator in the ceiling of the wind tunnel will also support the flow re-establishment.

5.0 CLOSING DISCUSSION

5.1 About the Swept Interaction

What then have we found from this investigation into swept interaction phenomena in the absence and in the presence of the boundary-layer control, that is a new contribution to the understanding of such flows?

In the swept interactions investigated at Mach 2 and Mach 4, we have measured for the first time, to the author's knowledge, the mean flow and total temperature distributions in a compressible three-dimensional turbulent boundary layer prior to, and just past incipient separation, as well as profiles where a large-scale 3D separation existed. The temperature profiles appeared to be particularly sensitive at indicating the presence of rolled-up free shear layers from 3D separation lines.

We have also managed to document the near incipient separation flow (δ_w = 8-degrees at Mach 2) with closely spaced traverses through the interaction region, using a servocontrolled self-nulling three-tube yawmeter that provided pitot pressure, yaw angle and total temperature in a continuous motion traverse from the test wall to the local mainstream. The large number of traverse stations was facilitated by the design of the wedge shock generator employed, standing normal to the test wall, that possessed an axial movement in the test flow of 30 undisturbed boundary-layer thicknesses ($\delta \cong 0.2$-in.). To a lesser degree of completeness, we also sampled the post-incipient separation flow and a strong interaction case, both at Mach 4 (δ_w = 8 and 16-degrees) where in the latter, the existence of a flattened rolled-up free shear layer within the confines of the boundary-layer depth was postulated from the profile measurements, and the corresponding surface oil flow visualization. We did not observe any closed separation bubbles that have been suggested for infinite swept wing flows[30]. The rolled-up vortical flow from the 3D separation line, as discussed by Cooper and Hankey[74] would appear applicable to our separated flow. The interaction between the viscous and the external flow field is noticeable in all the traverse measurements through the swept interaction region by the very slow return towards the calculated external flow field outside of our prescribed boundary-layer edge.

By comparison with the extensive number of flow profiles obtained through the interaction region, neither the Johnston triangular model for crossflow[61,62], that Lowrie adopted[56], nor the Mager parabolic representation[49,90], appeared to fit our measurements. On the other hand, our limiting streamline deflections at the wall compared very closely with the simple vorticity model suggested by McCabe[54]. Rather than pursue the fruitless task of trying to find a suitable model for the velocity profiles in the swept interaction region, we felt that a relevant analytical tool resided in the use of a turbulent kinetic energy boundary-layer calculation method, where the history of the boundary layer is properly taken account of, and the appropriate boundary conditions can be inserted. In fact, the only 3D compressible turbulent boundary layer method readily available (to the author) that is based on turbulent kinetic energy principles is that due to Nash[115,121], wherein no assumptions regarding families of velocity profile shapes, nor the magnitude of the crossflows, require to be inserted. The results from Nash's method[115]

when compared with the Mach 2, δ_w = 8-degree experimental measurements, appeared promising. The programme was formulated to treat swept wing flows and consequently requires a suitable modification to the side domain boundary condition to allow for the presence of the deflected surface of the wedge. A two-stage calculation, where the initial boundary layer is first-of-all computed up to the line of the rearward facing Mach cone from the wedge leading-edge utilizing a rectangular co-ordinate system, followed by a second calculation based on a conical co-ordinate system whose origin is the wedge apex, should, in principle, improve the prediction of the flow. The solution of the first-stage calculation would be used to start the second stage.

The empty wind tunnel provided a uniform test boundary layer at Mach 2 on the nozzle sidewall. A single sweptback fence-type vortex generator was used to control the thickness of the end-wall boundary layer opposite to the deflected surface of the wedge, and to reduce the upstream influence of the interaction of the test shock wave with that boundary layer. At Mach 4, on the other hand, the wind tunnel nozzle sidewall boundary layer was highly non-uniform and a V-type fence vortex generator was situated upstream in the nozzle on the test floor to redistribute the converged boundary layer. The redistribution provided only a qualitatively acceptable flow in terms of uniformity of boundary-layer thickness across the tunnel width.

As McCabe and other workers have shown[54], the calculated shock wave position provides a satisfactory origin against which to compare the test wall static pressure distributions, in our case, effectively plotted on a base of x/δ. In the lateral extent of flow region available to us, of typically 12 undisturbed boundary-layer thicknesses from the wedge apex, the flow appeared to develop on a quasi-conical basis. Incipient separation at Mach 2, in particular, was not diagnosed until $\delta_w \cong 10$-degrees, a wedge deflection angle much higher than previous experiments had found[54].

In the Mach 4 tests, we installed a transparent floor in the wind tunnel and we were able to obtain Schlieren records of the wedge generated shock wave superimposed on the oil dot flow visualization record. The experimental shock angle was in good agreement with that calculated from oblique shock tables.

Vas[127] has queried whether the effects of bluntness of the wedge leading-edge could propagate laterally and downstream, to modulate the flow field generated from a sharp wedge leading-edge.

The blunt leading-edge, of course, acts as a bluff protuberance to the oncoming boundary layer, producing a horse-shoe shaped local 3D separation about the foot of the wedge. Westkaemper[128] has concluded that, in supersonic flow about circular section protuberances and for cylinder length to diameter ratios >1, the distance of the singular separation point ahead of the cylinder leading-edge (on the axis of symmetry) is approximately 2.7 times the diameter of the cylinder. That is, this separation distance is virtually independent of cylinder length to diameter ratio, the ratio of the cylinder diameter to the undisturbed momentum deficit thickness of the oncoming boundary layer, and of mainstream Mach number and Reynolds number (based on cylinder diameter). This independence would appear due to the 'swamping' influence of the very strong pressure field. In our experiment, however, the radius of the wedge leading-edge is 0.006-in., and the (undisturbed) boundary-layer thickness is 0.2-in. The ratio of 'effective' cylinder diameter, D, to boundary-layer thickness is only 0.06 in our case, and we would expect that the 3D separation would be relatively much closer to the leading-edge than Westkaemper's result due to the very small D/δ. (Clearly, in the limit of vanishingly small D/δ, the separation should disappear altogether.) As far as we can determine from our oil dot flow visualization, the effect of this localized 3D separation is, in fact, confined to the immediate neighbourhood of the wedge meeting the wall, and is masked by the larger scale interaction produced by the wedge shock wave. Nevertheless, one does sight convergence of the limiting flow very close to the wedge apex adjacent to the test deflection surface before the angle for incipient separation of the test boundary layer is reached; and this could be caused by a lateral movement of the protuberance 3D separation line towards the wedge shock wave.

Of greater significance to the stand-off distance of this protuberance type separation line, we feel, is the deflection angle of the wedge shock generator on the side opposite to the test deflection

surface. Spurious effects from strong 3D interactions here may well feed around the wedge leading-edge, to cause some change in the flow development, and to perhaps incite earlier incipient separation of the test flow than would be obtained otherwise.

5.2 About Blowing

Before attempting the blowing experiment, it was thought that the most beneficial direction of the blc air was at a sweep angle set such that the jet efflux must turn through more than 90-degrees to become parallel with the direction of the 3D separation (in the absence of blowing). However, as we have seen, the jet is directed against the deflected surface of the wedge, which acts as a bluff protuberance, and causes a substantial 3D separation.

The present results illustrate that in a junction-type problem, such as we have investigated, tangential air injection introduced with a jet excess momentum slightly more than the momentum deficit of the undisturbed boundary layer, and with a mixing length of about two to fifteen undisturbed boundary-layer thicknesses between the jet and the shock wave†, should be orientated to blow in a direction somewhere between the deflected wedge surface and the angle of the shock wave (i.e. blowing in a direction roughly along the shock). In this manner, the mode of operation of the jet is to substantially reduce the pressure rise of the wedge shock that is experienced on the surface, by the amount of turning of the jet allowed around the wedge leading-edge, coupled with the significantly enhanced wall shear stress.

We have measured no flow profiles in the 3D jet/boundary-layer combination, and consequently we can only rely on our 2D results[5] as a qualitative guide. In the few limited experiments with blowing that we have managed, it is not clear, for example, whether the advised direction of blowing herein would carry over to controlling a 3D shock-induced separation on a swept wing.

More work clearly needs to be done on a flow model producing a 3D separation without the constraint of a solid vertical wall in proximity to the jet.

6.0 CONCLUSIONS

Based on measurements of the near-zero heat transfer turbulent boundary layer on a flat wall in a swept interaction at Mach 2 and 4, generated by a wedge standing normal to the test wall, and at a Reynolds number of $\sim 2 \times 10^5$ based on the undisturbed boundary-layer thickness of 0.2-in., we conclude that:

(1) The development of the viscous flow in the swept interaction region leading eventually to 3D separation with increasing deflection angle of the wedge, is a gradual, progressive, relatively steady, and essentially quasi-conical process near the wedge, in which the flow leaves the 3D separation line as a free shear layer to roll-up into a flattened vortex roughly within the depth of the original undisturbed boundary layer. There appears to be no sudden eruption of vortical fluid from the test surface. In fact, the precise wedge angle at which incipient separation occurs is particularly elusive, unless the observation of parallelism of the limiting streamlines with the calculated (or visualized) shock wave is adopted as the incipient separation criterion.

(2) The optimum direction of a Mach 3 supersonic wall jet to control or destroy the shock-induced separation (produced by the aforementioned wedge in a flow at Mach 2) is along a line between the wedge deflection angle and its shock wave angle.

---

† From the wedge leading-edge, in a direction along the shock wave.

7.0 ACKNOWLEDGMENTS

The work reported herein is part of an internal project sponsored by the NAE, Ottawa, as one investigation into the mechanics of three-dimensional viscous flows. This report is essentially the same as a Ph.D thesis presented to Carleton University in April 1975.

The author is indebted to Frank Kisko's technical assistance in managing the 5 × 5-in. wind tunnel and helping with the measurements; to Fred Ellis, Gerry Lanouette and Ron Charette for their expert help with instrumentation; and to Prof. Bill Rainbird of Carleton University, who provided challenging and motivating discussion throughout the research. Rob Galway's input to the design of the experiment is gratefully acknowledged.

8.0 REFERENCES

1. Lachmann, G., Ed. — *Boundary Layer and Flow Control.* Pergamon Press, 1961.

2. Lloyd-Jones, J. Covault, C., Ed. — *Transport Concept Would Halve Fuel Use.* Aviation Week and Space Technology, July 29, 1974, pp. 27-29.

3. Whitcomb, R.T. Clark, L.R. — *An Airfoil Shape for Efficient Flight at Supercritical Mach Numbers.* NASA TM X-1109, 1965.

4. Thomas, B.K., Jr. — *New Wing Promises Design Breakthrough.* Aviation Week and Space Technology, July 24, 1967, p. 25.

5. Peake, D.J. — *The Use of Air Injection to Prevent Separation of the Turbulent Boundary Layer in Supersonic Flow.* NGTE R256, November 1973; ARC CP 890, 1966; M. Sc. Thesis, University of Bristol, 1962.

6. Peake, D.J. Rainbird, W.J. Atraghji, E. — *Three-Dimensional Flow Separations on Aircraft and Missiles.* AIAA J., Vol. 10, No. 5, May 1972, pp. 567-580.

7. Czarnecki, K.R. — *Analytical Investigation of Reduction in Turbulent Skin Friction on a Flat Plate by Means of Air Injection Through Discrete Slots.* NASA TN D-2102, November 1964.

8. Schetz, J.A. Gilreath, H.E. — *Tangential Slot Injection in Supersonic Flow.* AIAA Paper 67-198, January 1967.

9. Parthasarathy, K. Zakkay, V. — *An Experimental Investigation of Turbulent Slot Injection at Mach 6.* AIAA J., Vol. 8, No. 7, July 1970.

10. Alzner, E. Zakkay, V. — *Turbulent Boundary-Layer/Shock Interaction with and without Injection.* ARL 70-0092, June 1970.

11. Bushnell, D.M. — *Calculation of Relaxing Turbulent Boundary Layers Downstream of Tangential Slot Injection.* J. Spacecraft and Rockets, Vol. 8, No. 5, May 1971.

12. Gilreath, H.E.
Schetz, J.A.
Transition and Mixing in the Shear Layer Produced by Tangential Injection in Supersonic Flow.
ASME Paper 71-FE-24, May 1971.

13. Kenworthy, M.
Schetz, J.A.
An Experimental Study of Slot Injection into a Supersonic Stream.
NASA CR-2128, January 1973.

14. Miner, E.W.
Lewis, C.H.
Supersonic Turbulent Boundary-Layer Flows with Tangential Slot Injection.
AIAA Paper 73-696, July 1973.

15. Fischer, M.C.
Ash, R.L.
A General Review of Concepts for Reducing Skin Friction, Including Recommendations for Future Studies.
NASA TM X-2894, March 1974.

16. Stratford, B.S.
Boundary Layer Control by Injection from Aircraft Gas Turbine Engines.
NGTE NT 87; ARC FM 1949, July 1953.

17. Chinneck, A.
Jones, G.C.A.
Tracey, C.M.
Interim Report on the Use of Blowing to Reduce the Fall in Control Effectiveness Associated with Shock-Induced Separation at Transonic Speeds.
ARC 17564, FM 2231, April 1955.

18. Pearcey, H.H.
Stuart, C.M.
Methods of Boundary-Layer Control for Postponing and Alleviating Buffetting and Other Effects of Shock-Induced Separation.
IAS FF 22, June 1959.

19. Peake, D.J.
Yoshihara, H. et al.
Transonic Life Augmentation of Two-Dimensional Supercritical Aerofoils by Means of Aft Camber, Slot Blowing and Jet Flaps, in High Reynolds Number Flow.
ICAS Paper 74-11, August 1974.

20. Bradshaw, P.
Gee, M.T.
Turbulent Wall Jets with and without an External Stream.
ARC R and M 3252, 1962.

21. Neale, M.C.
Stratford, B.S.
Some Experiments with Compression Shock Focussing and Jet/Boundary-Layer Mixing.
ARC 22995, FM 3108, 1961.

22. Howell, G.A.
Tatro, R.E.
Tangential Fluid Injection for Control of Shock/Boundary-Layer Interaction.
AIAA Paper 66-656, June 1966.

23. Hefner, J.N.
Cary, A.M.
Bushnell, D.M.
Investigation of the Three-Dimensional Turbulent Flow Downstream of Swept Slot Injection in Hypersonic Flow.
AIAA Paper 74-679, July 1974.

24. Gadd, G.E.
Interactions Between Shock Waves and Boundary-Layer.
Paper presented at IUTAM Symposium on Boundary-Layers Research, Freiburg, August 1957. Published by Springer Berlin 1958, ed. by H. Görtler.

25. Gadd, G.E.
Interactions Between Normal Shock Waves and Turbulent Boundary Layers.
ARC R and M 3262, 1962.

26. Holder, D.W.
Pearcey, H.H.
Gadd, G.E.
The Interaction Between Shock Waves and Boundary Layers.
ARC CP 180, 1955.

27. Bogdonoff, S.M.
Remarks on Interactions Between Wholly Laminar or Wholly Turbulent Boundary Layers and Shock Waves Strong Enough to Cause Separation.
J. Aero. Sci., Vol. 21, February 1954, pp. 138-139.

28. Bogdonoff, S.M.
Kepler, C.E.
Separation of a Supersonic Turbulent Boundary Layer.
J. Aero. Sci., Vol. 22, 1955, pp. 414-424.

29. Green, J.E.
Reflection of an Oblique Shock Wave by a Turbulent Boundary Layer.
RAE TR 68256, 1968.

30. Green, J.E.
Interactions Between Shock Waves and Turbulent Boundary Layers.
RAE TR 69098, May 1969; Progress in Aerospace Sciences, Vol. 11, Pergamon Press at Oxford, 1970, pp. 235-340.

31. Grande, E.
Oates, G.C.
Unsteady Flow Generated by Shock-Turbulent Boundary Layer Interactions.
AIAA Paper 73-168, January 1973.

32. Rose, W.C.
Turbulence Measurements in a Compressible Boundary Layer.
AIAA J., Vol. 12, No. 8, August 1974, pp. 1060-1064.

33. Lewis, J.E.
Behrens, W.
Fluctuation Measurements in the Near Wake of a Wedge with and without Base Injection.
AIAA J., Vol. 7, No. 4, April 1969, pp. 664-670.

34. Peake, D.J.
Romeskie, J.
Brakmann, G.
Comparisons Between Some High Reynolds Number Turbulent Boundary-Layer Experiments at Mach 4, and Various Recent Calculation Procedures.
AGARD CP - 93, September 1971.

35. Bradshaw, P.
The Effect of Mean Compression or Dilatation on the Turbulence Structure of Supersonic Boundary Layers.
J. Fluid Mech., Vol. 63, Part 3, 1974, pp. 449-464.

36. Lewis, J.E.
Gran, R.L.
Kubota, T.
An Experiment on the Adiabatic Compressible Turbulent Boundary Layer in Adverse and Favourable Pressure Gradients.
Jour. Fluid Mech., Vol. 51, Part 4, 1972, pp. 657-672.

37. Favre, A., Ed.
The Mechanics of Turbulence.
Gordon and Breach, New York, 1964.

38. Horstman, C.C.
Owen, F.K.
New Diagnostic Technique for the Study of Turbulent Boundary-Layer Separation.
AIAA J., Vol. 12, No. 10, October 1974.

39. Sears, W.R.
The Boundary Layer of Yawed Cylinders.
Jour. Aero. Sci., Vol. 15, No. 1, January 1948, pp. 49-52.

40. Wild, J.M.
The Boundary Layer of Yawed Infinite Wings.
Jour. Aero. Sci., Vol. 16, No. 1, January 1949, pp. 41-45.

41. Eichelbrenner, E.A.
Oudart, A.
Observations on a Criterion of Three-Dimensional Laminar Boundary-Layer Separation.
Original in La Recherche Aéronautique, No. 40, July/August 1954, pp. 3-5; also NRC (Canada) TT-962, 1961.

42. Eichelbrenner, E.A.
Oudart, A.
Three-Dimensional Laminar Boundary-Layer Separation.
Original in La Recherche Aéronautique, No. 47, 1955, pp. 11-14; also NRC (Canada) TT-963, 1961.

43. Brown, S.
Singularities Associated with Separating Boundary Layers.
Roy. Soc. Phil. Trans., Series A, Vol. 257, 1965, pp. 409-444.

44. Lighthill, M.J.
Attachment and Separation in Three-Dimensional Flow.
Section 2.6 of Laminar Boundary Layers, Ed. by L. Rosenhead, Oxford University Press, 1963, pp. 72-82.

45. Maskell, E.C.
Flow Separation in Three-Dimensions.
RAE Aero Rept. 2565, November 1955.

46. Stalker, R.J.
A Note on the China-Film Technique for Boundary Layer Indication.
Roy. Aero. Soc., Vol. 60, August 1956, pp. 543-544.

47. Rainbird, W.J.
Crabbe, R.S.
Peake, D.J.
Meyer, R.F.
Some Examples of Separation in Three-Dimensional Flow.
CASI Jour., Vol. 12, No. 6, December 1966, pp. 409-423.

48. Rainbird, W.J.
The External Flow Field About Yawed Circular Cones.
AGARD CP-30, May 1968.

49. Rainbird, W.J.
Turbulent Boundary-Layer Growth and Separation on a Yawed Cone.
AIAA J., Vol. 16, No. 12, December 1968, pp. 2410-2416.

50. Peake, D.J.
Three-Dimensional Flow Separations on Upswept Rear Fuselages.
CASI Jour., Vol. 15, No. 10, December 1969, pp. 399-408.

51. Kuehn, D.M.
Experimental Investigation of the Pressure Rise Required for the Incipient Separation of Turbulent Boundary Layers in Two-Dimensional Supersonic Flow.
NASA Memo 1-21-59A, February 1959.

52. Seddon, J.
The Flow Produced by Interaction of a Turbulent Boundary Layer with a Normal Shock Wave of Strength Sufficient to Cause Separation.
ARC R and M 3502, 1960.

53. Stanbrook, A.
An Experimental Study of the Glancing Interaction Between a Shock Wave and a Turbulent Boundary Layer.
ARC CP 555, 1961.

54. McCabe, A.
The Three-Dimensional Interaction of a Shock Wave with a Turbulent Boundary Layer.
Ph.D. Thesis, University of Manchester, October 1963; Aero. Quart., Vol. XVII, August 1966, pp. 231-252.

55. Oskam, B. — Private Communication at Princeton University, November 1973.

56. Lowrie, B.W. — *Cross-Flows Produced by the Interaction of a Swept Shock Wave with a Turbulent Boundary Layer.* Ph.D. Thesis, University of Cambridge, December 1965.

57. Rogers, E.W.E. Hall, I.M. — *An Introduction to the Flow About Plane Swept Back Wings at Transonic Speeds.* Jour. Roy. Aero. Soc., Vol. 64, 1960, p. 449.

58. Meyer, R.F. — *A Note on a Technique of Surface Flow Visualization.* NRC Aero. Rept. LR-457, July 1966.

59. Stalker, R.J. — *Sweepback Effects in Turbulent Boundary-Layer/Shock Wave Interaction.* Jour. Aero. Sci., Vol. 27, No. 5, May 1960, pp. 348-356.

60. Crocco, L. Probstein, R.F. — *The Peak Pressure Rise Across an Oblique Shock Emerging from a Turbulent Boundary Layer Over a Plane Surface.* Princeton Aero. Lab. Rept. 254, March 1954.

61. Johnston, J.P. — *On the Three-Dimensional Turbulent Boundary Layer Generated by Secondary Flow.* J. Basic Eng., Series D, Trans. ASME, Vol. 82, 1960, p. 223.

62. Johnston, J.P. — *Three-Dimensional Turbulent Boundary Layers.* MIT Gas Turbine Lab., Rept. 39, May 1957.

63. Wheeler, A.J. Johnston, J.P. — *Three-Dimensional Turbulent Boundary Layers — An Assessment of Prediction Methods.* Stanford University Rept. MD-30, July 1971.

64. Korkegi, R.H. — *A Simple Correlation for Incipient Turbulent Boundary-Layer Separation Due to a Skewed Shock Wave.* AIAA J., Vol. 11, No. 11, November 1973, pp. 1578-1579.

65. Goldberg, T.J. — *Three-Dimensional Separation for Interaction of Shock Waves with Turbulent Boundary Layers.* AIAA J., Vol. 11, No. 11, November 1973, pp. 1573-1575.

66. Miller, D.S. Redeker, E. — *Three-Dimensional Flow Separation.* Bumblebee Aerodynamics Panel, Minutes of 48th Meeting, September 1963, at Defence Research Lab., University of Texas, November 1963.

67. Chapman, D.R. Kuehn, D. Larson, M.K. — *Investigation of Separated Flows in Supersonic and Transonic Streams with Emphasis on the Effect of Transition.* NACA TR 1356, 1958.

68. Charwat, A.F. Redekopp, L.G. — *Supersonic Interference Flow Along the Corner of Intersecting Wedges.* AIAA J., Vol. 5, No. 3, March 1967, pp. 480-488.

69. Korkegi, R.H. — *A Limiting Condition for Supersonic Inviscid Interaction in the Corner of Intersecting Wedges.* ARL-68-0099, May 1968.

70. Comfort, E.
Todisco, A.
Experimental Investigation of Two Shock Wave Boundary-Layer Interaction Configurations.
AIAA Paper 69-8, January 1969.

71. West, J.E.
Korkegi, R.H.
Interaction in the Corner of Intersecting Wedges at a Mach Number of 3 and High Reynolds Numbers.
ARL-71-0241, October 1971.

72. West, J.E.
Korkegi, R.H.
Supersonic Interaction in the Corner of Intersecting Wedges at High Reynolds Numbers.
AIAA Paper 72-6, January 1972.

73. Kutler, P.
Supersonic Flow in the Corner Formed by Two Intersecting Wedges.
AIAA J., Vol. 12, No. 5, May 1974, pp. 577-578.

74. Cooper, J.R.
Hankey, W.L.
Flowfield Measurements in an Asymmetric Axial Corner at M = 12.5.
AIAA J., Vol. 12, No. 10, October 1974, pp. 1353-1357.

75. Peake, D.J.
Jones, D.J.
Rainbird, W.J.
The Half-Cone Pressure Field and its Significance to Side-Mounted Intakes.
AGARD CP-71, 1971.

76. Culley, M.
A Side-Mounted Supersonic Intake and the Problem of Three-Dimensional Boundary-Layer Separation.
ARL (Australia) ME 137, June 1972.

77. Winkler, E.M.
Design and Calibration of Stagnation Temperature Probes for Use at High Supersonic Speeds and Elevated Temperatures.
Jour. App. Phys., Vol. 25, 1954, pp. 231-232.

78. Meier, H.U.
A Combined Temperature and Pressure Probe for Compressible Flow.
AIAA J., Vol. 7, No. 3, March 1969, pp. 529-530.

79. East, R.A.
Perry, J.H.
A Short Time Response Stagnation Temperature Probe.
ARC CP 909, 1967.

80. Vas, I.E.
Flow Field Measurements Using a Total Temperature Probe at Hypersonic Speeds.
AIAA Paper 71-273, March 1971.

81. Bradfield, W.S.
Hanson, A.R.
Sheppard, J.J.
Design, Calibration and Application of a Miniature Total Temperature Probe.
Jour. Heat Transfer (ASME), August 1964, pp. 462-464.

82. Harris, H.
An Investigation of Turbulent Boundary-Layer Characteristics with Particular Reference to the Effects of Heat Transfer and Pressure Gradient.
Ph.D. Thesis, London University, 1970.

83. Ferri, A.
Bogdonoff, S.M.
Design and Operation of Intermittent Supersonic Wind Tunnels.
AGARDograph 1, May 1954.

84. McGarry, J.B.
The Development of a Variable Mach Number Effuser.
ARC R and M 3097, 1958.

85. MacMillan, F.A.
Experiment on Pitot Tubes in Shear Flow.
ARC R and M 3128, 1957.

86. Young, A.D.
Maas, J.N.
The Behaviour of a Pitot Tube in a Transverse Total-Pressure Gradient.
ARC R and M 1770, 1936.

87. Marson, G.B.
Lilley, G.M.
The Displacement Effect of Pitot Tubes in Narrow Wakes.
College of Aeronautics, Cranfield: COA Report No. 107, 1956.

88. Ozaropoglu, V.
Measurements in Incompressible Turbulent Flow.
Ph.D. Thesis, Laval University, June 1973.

89. Allen, J.M.
Pitot-Probe Displacement in a Supersonic Turbulent Boundary Layer.
NASA TN D-6759, April 1972.

90. Hall, M.G.
Dickens, H.B.
Measurements in a Three-Dimensional Turbulent Boundary Layer in Supersonic Flow.
ARC R and M 3537, 1968.

91. Rainbird, W.J.
Errors in Measurement of Mean Static Pressure of a Moving Fluid Due to Pressure Holes.
DME/NAE Quarterly Bulletin, No. 1967(3), National Research Council Canada, October 1967.

92. Franklin, R.E.
Wallace, J.M.
Absolute Measurements of a Static-Hole Error Using Flush Transducers.
Jour. Fluid Mech., Vol. 42, Part 1, 1970, pp. 33-48.

93. Westley, R.
Aerodynamic Sound and Pressure Fluctuations in a Supersonic Blowdown Wind Tunnel.
National Research Council Canada Aero. Report LR-274, January 1960.

94. Green, J.E.
On the Influence of Free Stream Turbulence on a Turbulent Boundary Layer, as it Relates to Wind Tunnel Testing at Subsonic Speeds.
Paper on 'Fluid Motion Problems in Wind Tunnel Design', AGARD-R-602 (1973).

95. Fuchs, H.V.
Survey of Pressure Fluctuations Associated with Turbulence.
University of Southampton ISAV Memo 282, June 1969.

96. Mabey, D.
Analysis and Correlation of Data on Pressure Fluctuations in Separated Flow.
J. Aircraft, Vol. 9, No. 9, September 1972, pp. 642-645.

97. Zwarts, F.J.
The Compressible Turbulent Boundary Layer in a Pressure Gradient.
Ph.D. Thesis, McGill University, July 1970.

98. Fiedler, H.
Head, M.R.
Intermittency Measurements in the Turbulent Boundary Layer.
J. Fluid Mech., Vol. 25, Part 4, 1966, pp. 719-735.

99. Wilson, R.
Aerodynamic Inteference of Pitot Tubes in a Turbulent Boundary Layer at Supersonic Speed.
AIAA J., Vol. 11, No. 10, October 1973, pp. 1420-1421.

100. Hopkins, E.J.
Keener, E.R.
Study of Surface Pitots for Measuring Turbulent Skin Friction at Supersonic Mach Number — Adiabatic Wall.
NASA TN D-3478, 1966.

101. Bradshaw, P.
Unsworth, K.
A Note on Preston Tube Calibrations in Compressible Flow.
Imperial College Aero Report 73-07, September 1973.

102. Spalding, D.B.
Chi, S.W.
The Drag of a Compressible Turbulent Boundary Layer on a Smooth Flat Plate with and without Heat Transfer.
Jour. Fluid Mech., Vol. 18, Part 1, 1964, pp. 117-143.

103. Stratford, B.S.
Beavers, G.S.
The Calculation of the Compressible Turbulent Boundary Layer in an Arbitrary Pressure Gradient — a Correlation of Certain, Previous Methods.
ARC R and M 3207, 1961.

104. Spalding, D.B.
A Single Formula for the Law of the Wall.
Jour. App. Mech., September 1961, pp. 455-458.

105. Winter, K.G.
Smith, K.G.
Gaudet, L.
Measurements of Turbulent Skin Friction at High Reynolds Numbers at Mach Numbers of 0.2 and 2.2.
Recent Developments in Boundary-Layer Research, AGARDograph 97, May 1965, pp. 103-123.

106. Quarmby, A.
Das, H.K.
Measurement of Skin Friction Using a Rectangular-Mouthed Preston Tube.
Aero. Jour., Vo. 73, No. 699, March 1969, pp. 228-230.

107. Patel, V.C.
Calibration of the Preston Tube and Limitations on its Use in Pressure Gradients.
J. Fluid Mech., Vol. 23, 1965, p. 185.

108. Rajaratnam, N.
Muralidhar, D.
Yaw Probe Used as Preston Tube.
Aero. Jour., Vol. 72, No. 696, December 1968, pp. 1059-1060.

109. McDonald, H.
Kreskovsky, J.P.
Effect of Freestream Turbulence on the Turbulent Boundary Layer.
United Aircraft Rept. M-110887-1, United Aircraft Research Laboratories, East Hartford, Conn., USA, 1973.

110. Naysmith, A.
Measurement of Aerodynamic Heat Transfer in Intermittent Wind Tunnels.
ARC CP 780, 1964.

111. Crocco, L.
Transformation of the Compressible Turbulent Boundary Layer with Heat Exchange.
AIAA J., Vol. 1, No. 12, December 1963, pp. 2723-2731.

112. Walz, A.
Compressible Turbulent Boundary Layers.
Mechanics of Turbulence, Gordon and Breach Science Publishers, New York, 1964.

113. Shanebrook, J.R.
Hatch, D.E.
A Family of Hodograph Models for the Crossflow Velocity Component of Three-Dimensional Turbulent Boundary Layers.
ASME Paper 71-FE-1, 1971.

114. Shanebrook, J.R.
Summer, W.J.
Crossflow Profiles for Compressible Turbulent Boundary Layers.
J. Aircraft, Vol. 8, No. 3, 1971, pp. 188-189.

115. Nash, J.F.
Scruggs, R.M.
Three-Dimensional Boundary-Layer Computations for a Finite Swept Wing.
NASA CR-112158, 1973.

116. Nash, J.F.
Private Communications, 1974.

117. Moore, F.K.
Displacement Effect of a Three-Dimensional Boundary Layer.
NACA Rept. 1124, March 1952.

118. Lighthill, M.J.
On Displacement Thickness.
J. Fluid Mech., Vol. 4, 1958, pp. 383-392.

119. Allen, J.M.
Evaluation of Compressible-Flow Preston Tube Calibrations.
NASA TN D-7190, 1973.

120. Sommer, S.C.
Short, B.J.
Free-Flight Measurements of Turbulent Boundary-Layer Skin Friction in the Presence of Severe Aerodynamic Heating at Mach Numbers from 2.8 to 7.0.
NACA TN 3391, 1955. (Also J. Aero. Sci., Vo. 23, No. 6, June 1956.)

121. Nash, J.F.
Patel, V.C.
Three-Dimensional Turbulent Boundary Layers.
SBC Technical Books, Atlanta, Georgia, 1972.

122. Bradshaw, P.
Ferriss, D.H.
Atwell, N.P.
Calculation of Boundary-Layer Development Using the Turbulent Energy Equation.
J. Fluid Mech., Vol. 28, Part 3, p. 593.

123. Bradshaw, P.
Calculation of Three-Dimensional Turbulent Boundary Layers.
J. Fluid Mech., Vol. 46, Part 3, 1971, pp. 417-445.

124. Nash J.F.
An Explicit Scheme for Calculation of Three-Dimensional Turbulent Boundary Layers.
J. Basic Eng. 94D, No. 1, 1972, p. 131.

125. Nituch, M.J.
The Use of Congruent Obstacle Blocks for the Indirect Measurement of Turbulent Skin Friction on Smooth Surfaces.
M. Eng. Thesis, Carleton University, Ottawa, August 1972.

126. Vinh, N.
Private Communication, 1974.

127. Vas, I.E.
Private Communication, 1973.

128. Westkaemper, J.C.
Turbulent Boundary-Layer Separation Ahead of Cylinders.
AIAA J., Vol. 6, No. 7, July 1968, pp. 1352-1355.

129. Peake, D.J.
Some Comments on Jet Momentum Requirements for the Tangential Injection Method of Boundary-Layer Control in Supersonic Flow.
NAE NRC Lab. Memo. HSA-28, April 1967.

TABLE 1

TYPICAL RUN CONDITIONS

M_∞	P_o atm.	P_o psia	$R_{5"}$	Nominal (min.) Starting Pressure (atmos.)
1.5	2.05	30.15	4×10^6	1.16
2.0	2.44	36.8	4×10^6	1.58
3.0	5.13	75.3	5×10^6	3.9
4.0	11.8	174.0	7×10^6	10.0

Limited by strength of wedge

TABLE 2

INJECTION NOZZLE PROFILE DIMENSIONS (SEE FIG. 26)

Jet Mach No. M_j	Throat Ht. h_t in.	Dimension 'A' in.	Dimension 'B' in.
1.5	0.0850	.3454	.0073
1.8	0.0695	.4567	.0151
2.0	0.0593	.5300	.0202
2.5	0.0379	.6829	.0309
3.0	0.0236	.7855	.0380
4.0	0.0093	.8879	.0452
4.5	0.0060	.9105	.0469

TABLE 3
BLOWING QUANTITIES

M_∞	$\left\{\frac{p}{P_o}\right\}_\infty$	P_{o_∞} ATM. psf	p_∞ psf	$\left\{\frac{u}{\sqrt{T_o}}\right\}_\infty$	u_∞ ft/sec
1.5	0.2724	2.05;4335	1182	81.947	1409

M_j	$\left\{\frac{p}{P_o}\right\}_j$	P_{o_j} psf psi	ρ_{o_j} slugs/ft^3	$\left\{\frac{\rho}{\rho_o}\right\}_j$; ρ_j slugs/ft^3	$\left\{\frac{u}{\sqrt{T_o}}\right\}_j$; u_j ft/sec	$\dot{m}_j$ slugs/sec per ft.	(u_j-u_∞)	$\dot{m}_j(u_j-u_\infty)$ lb.wt./ ft. span	$\dot{m}_j(u_j-u_\infty)$ for nozzle
1.5	.2724	4335; 30.1	.00477	0.395 ; .001887	81.947; 1409	.02215	0.0	0.0	0
1.8	.1740	6805; 47.2	.00750	0.2868 ; .00215	92.241; 1584	.0284	175	4.97	1.491
2.0	.1278	9260; 64.3	.01020	0.2301 ; .00235	98.067; 1684	.0330	275	9.08	2.724
2.5	.0585	20,220; 140.6	.02225	0.1317 ; .002935	109.64 ; 1882	.0461	473	21.8	6.54
3.0	.02722	43,500; 302.2	.0478	0.07623; .003645	117.94 ; 2023	.0615	614	37.8	11.34

M_∞	$\left\{\frac{p}{P_o}\right\}_\infty$	P_{o_∞} ATM. psf	p_∞ psf	$\left\{\frac{u}{\sqrt{T_o}}\right\}_\infty$	u_∞ ft/sec
2.0	0.12780	2.44;5160	660	98.067	1683

M_j	$\left\{\frac{p}{P_o}\right\}_j$	P_{o_j} psf psi	ρ_{o_j} slugs/ft^3	$\left\{\frac{\rho}{\rho_o}\right\}_j$; ρ_j slugs/ft^3	$\left\{\frac{u}{\sqrt{T_o}}\right\}_j$; u_j ft/sec	$\dot{m}_j$ slugs/sec per ft.	(u_j-u_∞)	$\dot{m}_j(u_j-u_\infty)$ lb.wt./ ft. span	$\dot{m}_j(u_j-u_\infty)$ for nozzle
1.5	.2724	2421; 16.83	.002665	0.395 ; .001053	81.947; 1409	.01237	-275	- 3.40	- 1.02
1.8	.1740	3795; 26.4	.00418	0.2868 ; .00120	92.241; 1584	.01584	-100	- 1.584	- .4752
2.0	.1278	5160; 35.85	.00568	0.2301 ; .001308	98.067; 1684	.01838	0.0	0.0	0
2.5	.0585	11,280; 78.4	.01242	0.1317 ; .001637	109.64 ; 1882	.02565	198	5.08	1.524
3.0	.02722	24,220; 168.5	.0267	.07623; .002038	117.94 ; 2023	.0344	339	11.67	3.501

T_o in °K., in ratio $\left\{\frac{u}{\sqrt{T_o}}\right\}$

TABLE 3 (Cont'd)

M_∞	$\left\{\frac{p}{P_o}\right\}_\infty$	P_{o_∞} ATM. psf	p_∞ psf	$\left\{\frac{u}{\sqrt{T_o}}\right\}_\infty$	u_∞ ft/sec
3.0	0.02722	5.13;10,830	295.5	117.942	2025

M_j	$\left\{\frac{p}{P_o}\right\}_j$	P_{o_j} psf psi	ρ_{o_j} slugs/ft^3	$\left\{\frac{\rho}{\rho_o}\right\}_j$; ρ_j slugs/ft^3	$\left\{\frac{u}{\sqrt{T_o}}\right\}_j$; u_j ft/sec	$\dot{m}_j$ slugs/sec per ft.	(u_j-u_∞)	$\dot{m}_j(u_j-u_\infty)$ lb.wt./ ft. span	$\dot{m}_j(u_j-u_\infty)$ for nozzle
1.5	.2724	1083; 7.53	.001192	0.395 ; .000472	81.947; 1409	.00554	-616	-3.415	-1.0245
1.8	.1740	1698; 11.80	.001868	0.2868 ; .000536	92.241; 1584	.00708	-441	-3.12	- .936
2.0	.1278	2315; 16.09	.00255	0.2301 ; .000587	98.067; 1684	.00824	-341	-2.81	- .843
2.5	.0585	5050; 35.1	.00556	0.1317 ; .000732	109.64 ; 1882	.01148	-143	-1.642	- .4926
3.0	.02722	10,830; 75.3	.01192	0.07623; .000910	117.94 ; 2025	.01536	0.0	0.0	0
4.0	.00659	44,800; 311.5	.0493	0.02766; .001363	128.3 ; 2205	.02505	180	4.51	1.353

M_∞	$\left\{\frac{p}{P_o}\right\}_\infty$	P_{o_∞} ATM. psf	p_∞ psf	$\left\{\frac{u}{\sqrt{T_o}}\right\}_\infty$	u_∞ ft/sec
4.0	0.00659	11.8;24,960	164.7	128.3	2205

M_j	$\left\{\frac{p}{P_o}\right\}_j$	P_{o_j} psf psi	ρ_{o_j} slugs/ft^3	$\left\{\frac{\rho}{\rho_o}\right\}_j$; ρ_j slugs/ft^3	$\left\{\frac{u}{\sqrt{T_o}}\right\}_j$; u_j ft/sec	$\dot{m}_j$ slugs/sec per ft.	(u_j-u_∞)	$\dot{m}_j(u_j-u_\infty)$ lb.wt./ ft. span	$\dot{m}_j(u_j-u_\infty)$ for nozzle
1.5	.2724	604; 4.2	.000666	0.395 ; .000263	81.947; 1409	.003085	-796	-2.46	- .738
1.8	.1740	946; 6.57	.001042	0.2868 ; .0002995	92.241; 1584	.003958	-621	-2.46	- .738
2.0	.1278	1289; 8.95	.001420	0.2301 ; .000327	98.067; 1684	.00459	-521	-2.395	- .7185
2.5	.0585	2818; 19.57	.003102	0.1317 ; .0004085	109.64 ; 1882	.00641	-323	-2.07	- .621
3.0	.02722	6050; 42.1	.00666	0.07623; .000508	117.94 ; 2023	.00858	-182	-1.56	- .468
4.0	.00659	24,960; 173.3	.02747	0.02766; .000762	128.3 ; 2205	.01402	0.0	0.0	0
4.5	.00346	47,600; 331.0	.0524	0.01745; .000915	131.5 ; 2260	.01722	55	0.948	.2844

TABLE 4

BOUNDARY LAYER MOMENTUM DEFICIT AT BLOWING SLOT

s = 3.6 ins., span of jet slot

M_∞	$\left\{\frac{\frac{1}{2}\rho u^2}{P_o}\right\}_\infty$	atmos P_o psf	lbwt/ft^2 $\{\frac{1}{2}\rho u^2\}_\infty$	lbwt/ft^2 $\{\rho u^2\}_\infty$	in. θ_{11} ft.	lbwt/ft span $\{\rho u^2\}_\infty \theta_{11}$	lb.wt. $\{\rho u^2\}_\infty \theta_{11} s$
1.5	0.4290	2.05 4335	1862	3724	.01519 .001267	4.72	1.416
2.0	0.3579	2.87 6065	2173	4346	.01690 .001408	6.12	1.836
		2.44 5160	1848	3696	.01730 .001442	5.33	1.599
3.0	0.1715	5.94 12,580	2157	4314	.01750 .001458	6.28	1.884
		5.13 10,830	1860	3720	.01796 .001497	5.57	1.671
4.0	0.07376	9.72 20,550	1517	3034	.01727 .001440	4.37	1.311
		11.8 24,960	1842	3684	.01675 .001396	5.15	1.545

TABLE 5

RUN LOG FOR MEASUREMENT OF FLOOR STATIC PRESSURES AND OIL FLOW VISUALIZATION

Run No.	δ_W	XWLE	XVGLE*	P_o	T_o	p_1	M_{E1}	q_{E1}	$R_{FT1} \times 10^{-6}$	COMMENTS
100		OUT	-6.25							
101	9	0.0	0.0							
102	9	0.0	0.0	Oil Flow Visualization; Mainstream Flow Conditions						slot between endwall and floor sealed
103	11.5	0.0	0.0	same as for Run No. 106						
104	11.5	0.0	OUT							
105	9	0.0	OUT							
106		OUT	OUT	33.97	535.0	4.27	2.011	12.08	8.79	
107		OUT	0.0	34.03	535.0	4.27	2.012	12.10	8.81	
108	0	0.0	0.0	34.03	535.0	4.28	2.010	12.11	8.81	
109	0	0.0	OUT	34.17	535.0	4.31	2.008	12.18	8.85	
110	8	0.0	OUT	34.17	535.0	4.31	2.009	12.17	8.85	
111	8	0.0	OUT	53.42	535.0	6.77	2.005	19.06	13.86	
112	8	0.0	0.0	53.45	435.0	6.77	2.006	19.06	13.86	
113	8	0.0	0.0	34.08	535.0	4.27	2.012	12.11	8.81	
114	2	0.0	OUT	33.92	535.0	4.27	2.009	12.08	8.78	
115	4	0.0	OUT	33.90	535.0	4.28	2.008	12.08	8.79	
117	7	0.0	OUT	33.93	535.0	4.26	2.011	12.06	8.78	
118	7.5	0.0	OUT	33.95	535.0	4.26	2.012	12.07	8.78	
119	8.5	0.0	OUT	33.93	535.0	4.27	2.009	12.08	8.79	
120	9	0.0	OUT	34.23	535.0	4.32	2.008	12.20	8.87	
121	10	0.0	OUT	34.24	535.0	4.34	2.006	12.21	8.88	
122	11.5	0.0	OUT	34.24	535.0	4.31	2.009	12.19	8.87	
123	8	1.0	OUT	33.93	535.0	4.28	2.009	12.08	8.79	
124	8	2.0	OUT	33.97	535.0	4.27	2.011	12.08	8.79	
125	8	2.5	OUT	33.96	535.0	4.27	2.010	12.09	8.79	
126	8	-1.0	OUT	33.99	535.0	4.28	2.009	12.10	8.80	
127	8	-2.0	OUT	33.95	535.0	4.28	2.009	12.09	8.79	
128	8	-2.5	OUT	33.96	535.0	4.29	2.008	12.10	8.80	
---	degrees	in.	in.	psia	°R.	psia	--	psi	--	

(i) $^*\delta_{VG}$ = 20-degrees to floor; HVG = 0.1-in.; on endwall; see Figure 30, for example.

TABLE 5 (Cont'd)

Run No.	δ_W	XWLE	XVGLE$^*_\dagger$	P_o	T_o	p_1	M_{E1}	q_{E1}	$R_{FT1} \times 10^{-6}$	COMMENTS
129	8	3.0	OUT	33.93	535.0	4.25	2.012	12.06	8.77	
130	8.5	0.0	0.0*	34.04	535.0	4.29	2.008	12.12	8.82	
131	9	0.0	0.0*	33.97	535.0	4.29	2.008	12.11	8.80	
132	10	0.0	0.0*	34.04	535.0	4.29	2.009	12.12	8.82	
133	11.5	0.0	0.0*	34.04	535.0	4.27	2.013	12.10	8.80	
134	11.5	0.0	OUT	53.55	535.0	6.79	2.005	19.11	13.89	
139		OUT	OUT	154.32	535.0	0.99	4.017	11.22	14.68	
140	0	0.0	OUT	151.00	535.0	0.82	4.144	9.88	13.54	
141	8	0.0	OUT	151.06	535.0	1.10	3.927	11.84	14.99	
147		OUT	-9.3†	} Oil Flow Visualization; Mainstream Flow Conditions same as for Run No. 141						
150	6	0.0	-9.3†	151.41	536.7	1.09	3.931	11.83	14.92	
151	8	0.0	-9.3†	151.40	537.8	1.11	3.920	11.94	14.95	
152	4	0.0	-9.3†	151.34	537.5	1.08	3.939	11.75	14.83	
153	17	0.0	-9.3†	171.24	537.8	1.21	3.946	13.22	16.71	
158		OUT	-9.3†	171.24	540.8	1.21	3.950	13.17	16.53	
159		OUT	-9.3†	151.46	541.7	1.11	3.918	11.97	14.80	
160	0	0.0	-9.3†	171.32	545.3	1.24	3.930	13.40	16.47	
161	17	0.0	-9.3†	171.37	541.2	1.25	3.925	13.46	16.72	
162	16	0.0	-9.3†	171.33	541.8	1.26	3.920	13.51	16.72	
163	15	0.0	-9.3†	171.31	543.4	1.22	3.943	13.26	16.46	
164	14	0.0	-9.3†	171.30	544.9	1.22	3.940	13.28	16.41	
165	13	0.0	-9.3†	171.37	542.8	1.23	3.934	13.36	16.57	
166	12	0.0	-9.3†	171.33	540.7	1.22	3.939	13.29	16.62	
167	11	0.0	-9.3†	171.36	542.0	1.21	3.946	13.22	16.51	
168	10	0.0	-9.3†	171.35	540.5	1.21	3.946	13.23	16.59	
---	degrees	in.	in.	psia	°R.	psia	--	psi	--	

(i) $^*\delta_{VG}$ = 20-degrees to floor; HVG = 0.1-in.; on endwall; see Figure 30, for example.

(ii) $^\dagger\delta_{VG}$ = 30-degrees (half-angle of 'V'); HVG = 0.1-in.; on floor; see Figure 31.

TABLE 5 (Cont'd)

Run No.	δ_W	XWLE	XVGLE†	P_o	T_o	p_1	M_{E1}	q_{E1}	$R_{FT1} \times 10^{-6}$	COMMENTS
169	9	0.0	-9.3	171.35	543.3	1.21	3.945	13.23	16.45	
170	8	0.0	-9.3	171.34	541.3	1.22	3.943	13.26	16.57	
171	7	0.0	-9.3	171.36	541.1	1.21	3.946	13.23	16.56	
172	6	0.0	-9.3	171.38	540.4	1.22	3.943	13.25	16.61	
173	5	0.0	-9.3	171.40	544.8	1.21	3.951	13.17	16.34	
174	4	0.0	-9.3	171.42	538.2	1.20	3.952	13.17	16.66	
175	2	0.0	-9.3	171.45	539.8	1.19	3.962	13.05	16.50	
176	16	-1.0	-9.3	171.43	538.8	1.22	3.942	13.28	16.71	
177	14	-1.0	-9.3	171.44	536.8	1.22	3.945	13.24	16.79	
178	12	-1.0	-9.3	171.44	n.a.	1.20	3.953	13.15	n.a.	
179	10	-1.0	-9.3	171.32	546.5	1.22	3.944	13.24	16.31	
180	8	-1.0	-9.3	171.31	542.3	1.23	3.933	13.37	16.59	
181	6	-1.0	-9.3	171.33	542.2	1.22	3.943	13.25	16.52	
182	4	-1.0	-9.3	171.35	543.4	1.22	3.944	13.25	16.46	
183	2	-1.0	-9.3	171.38	541.7	1.22	3.944	13.25	16.54	
184	0	-1.0	-9.3	171.44	540.6	1.22	3.941	13.29	16.63	
185	0	-1.0	-9.3							
186	17	-1.0	-9.3							
187	10	-1.0	-9.3							
188	14	-1.0	-9.3							
189	18	-1.0	-9.3							Oil Flow Visualization; Mainstream Flow Conditions same as Run No. 184
190	12	-1.0	-9.3							
191	16	-1.0	-9.3							
192	8	-1.0	-9.3							
193	6	-1.0	-9.3							
200		OUT	OUT							
201	- 8	-1.0	-9.3							Oil Flow Visualization; Mainstream Flow Conditions same as Run No. 184
202	4	-1.0	-9.3							
---	degrees	in.	in.	psia	°R.	psia	--	psi	--	

(i) †δ_{VG} = 30-degrees (half-angle of 'V'); HVG = 0.1-in.; on floor; see Figure 31.

TABLE 5 (Cont'd)

Run No.	δ_W	XWLE	XVGLE[†]	P_o	T_o	P_1	M_{E1}	q_{E1}	$R_{FT1} \times 10^{-6}$	COMMENTS
203	2	-1.0	-9.3							
204	16	0.0	-9.3							
205	18	0.0	-9.3							
206	14	0.0	-9.3							
207	12	0.0	-9.3							
208	10	0.0	-9.3							
209	8	0.0	-9.3							Oil Flow Visualization; Mainstream Flow Conditions same as for Run No. 184
210	6	0.0	-9.3							
211	4	0.0	-9.3							
212	0	0.0	-9.3							
213	5	0.0	-9.3							
214	2	0.0	-9.3							
215	0→18 0→-6	-1.0	-9.3							Schlieren Flow Visualization; Mainstream Flow same as for Run No. 184
216	10	-1.0	-9.3							
217	8	-1.0	-9.3							
218	6	-1.0	-9.3							
219	4	-1.0	-9.3							
220	16	-1.0	-9.3							
221	18	-1.0	-9.3							Schlieren plus Oil Flow Visualization; Mainstream Flow same as for Run No. 184
222	14	-1.0	-9.3							
223	12	-1.0	-9.3							
224	0	-1.0	-9.3							
225	7	-1.0	-9.3							
---	degrees	in.	in.	psia	°R.	psia	--	psi	--	

(i) $^{\dagger}\delta_{VG}$ = 30-degrees (half-angle of 'V'); HVG = 0.1-in; on floor; see Figure 31.

TABLE 6.1

REFERENCE MAINSTREAM CONDITIONS AT STATION 1 FOR CIRCULAR PITOT PROFILES MEASURED AT MACH 2

Run No.	Traverse STN ; XT		P_o	T_o	p_1	M_{E1}	$\rho_{E1} \times 10^3$	u_{E1}	q_{E1}	T_{E1}	$\mu_{E1} \times 10^6$	$R_{FT1} \times 10^{-6}$	T_{AW1}
66	4	-0.72	33.99	535.0	4.32	2.003	1.222	1691.1	12.14	296.8	0.2343	8.82	508.7
67	4	-0.72	39.13	535.0	4.91	2.011	1.395	1694.8	13.91	295.7	0.2335	10.12	508.6
68	4	-0.72	54.03	535.0	6.75	2.014	1.920	1696.1	19.18	295.4	0.2333	13.96	508.5
70	4C	-0.72	54.18	535.0	6.78	2.013	1.928	1695.6	19.25	295.5	0.2334	14.01	508.5
71	4C	-0.72	39.88	535.0	4.97	2.017	1.413	1697.4	14.14	295.0	0.2330	10.29	508.5
72	4C	-0.72	34.68	535.0	4.28	2.022	1.222	1699.9	12.26	294.3	0.2325	8.93	508.4
73	4X	-0.72	34.83	535.0	4.43	2.003	1.253	1691.0	12.44	296.8	0.2343	9.04	508.7
74	4X	-0.72	39.70	535.0	4.90	2.022	1.399	1699.7	14.04	294.3	0.2326	10.23	508.4
75	4X	-0.72	54.79	535.0	6.76	2.023	1.928	1700.2	19.36	294.2	0.2324	14.10	508.4
76	18	2.85	54.51	535.0	6.77	2.018	1.928	1698.1	19.31	294.8	0.2329	14.06	508.5
77	18	2.85	39.47	535.0	4.86	2.024	1.388	1700.5	13.94	294.1	0.2324	10.16	508.4
78	18	2.85	34.75	535.0	4.27	2.026	1.219	1701.5	12.26	293.8	0.2322	8.93	508.3
79	18X	2.85	34.60	535.0	4.28	2.021	1.220	1699.4	12.24	294.4	0.2326	8.91	508.4
80	18X	2.85	34.66	535.0	4.24	2.027	1.214	1702.3	12.21	293.6	0.2320	8.90	508.3
81	18X	2.85	39.45	535.0	4.92	2.016	1.399	1697.1	13.99	295.1	0.2331	10.18	508.5
82	18X	2.85	54.54	535.0	6.73	2.022	1.921	1699.9	19.27	294.3	0.2325	14.04	508.4
83	18C	2.85	34.54	535.0	4.31	2.015	1.227	1696.5	12.26	295.3	0.2332	8.92	508.5
84	18C	2.85	39.53	535.0	4.84	2.027	1.384	1702.3	13.93	293.6	0.2320	10.16	508.3
85	18C	2.85	54.52	535.0	6.72	2.024	1.917	1700.5	19.25	294.1	0.2324	14.03	508.4
88	4	-0.72	34.21	535.0	4.28	2.013	1.217	1695.6	12.15	295.5	0.2334	8.84	508.5
89	4X	-0.72	34.22	535.0	4.28	2.014	1.216	1696.2	12.15	295.4	0.2333	8.84	508.5
90	4C	-0.72	34.18	535.0	4.30	2.011	1.219	1694.6	12.16	295.8	0.2336	8.85	508.6
---	---	in.	psia	°R.	psia	from p_1/P_o	slugs/ft^3	ft/sec	psi	°R.	slugs/ft.sec	---	°R.

(i) No sidewall V.G.
(ii) No flow visualization.

TABLE 6.2

INTEGRAL PARAMETERS FROM CIRCULAR PITOT PROFILES IN EMPTY TUNNEL AT MACH 2

Run No.	Traverse STN	; XT	p/p_1	M_E	δ_{995}	δ_1^*	θ_{11}	δ_1^*/θ_{11}	$R_{\theta_{11}} \times 10^{-4}$
66	4	-0.72	1.002	2.014	0.2170	0.0507	0.0149	3.40	1.11
67	4	-0.72	1.002	2.012	0.2105	0.0492	0.0145	3.40	1.23
68	4	-0.72	1.003	2.017	0.2049	0.0466	0.0137	3.41	1.60
70	4C	-0.72	1.034	1.950	0.1926	0.0447	0.0136	3.29	1.53
71	4C	-0.72	1.030	1.954	0.1955	0.0460	0.0136	3.37	1.12
72	4C	-0.72	1.030	1.966	0.1928	0.0463	0.0137	3.38	0.99
73	4X	-0.72	0.994	1.999	0.2231	0.0530	0.0156	3.40	1.16
74	4X	-0.72	0.994	2.024	0.2072	0.0514	0.0145	3.55	1.23
75	4X	-0.72	0.996	2.020	0.2040	0.0497	0.0143	3.47	1.67
76	18	2.85	1.012	1.990	0.2249	0.0546	0.0164	3.32	1.89
77	18	2.85	1.011	2.009	0.2302	0.0583	0.0170	3.42	1.43
78	18	2.85	1.011	2.007	0.2315	0.0594	0.0175	3.39	1.29
79	18X	2.85	1.033	1.975	0.2416	0.0626	0.0189	3.32	1.38
80	18X	2.85	1.033	1.994	0.2380	0.0599	0.0178	3.37	1.31
81	18X	2.85	1.033	1.971	0.2326	0.0577	0.0171	3.37	1.43
82	18X	2.85	1.037	1.973	0.2236	0.0552	0.0168	3.11	1.93
83	18C	2.85	1.010	1.993	0.2405	0.0606	0.0180	3.36	1.32
84	18C	2.85	1.010	2.011	0.2297	0.0564	0.0167	3.39	1.40
85	18C	2.85	1.008	2.001	0.2188	0.0521	0.0155	3.36	1.78
88	4	-0.72	1.002	2.017	0.2027	0.0514	0.0150	3.42	1.12
89	4X	-0.72	0.994	2.036	0.2069	0.0510	0.0148	3.45	1.11
90	4C	-0.72	1.030	1.997	0.1994	0.0499	0.0151	3.31	1.13
---	---	in.	---	from p/P_p	in.	in.	in.	---	---

TABLE 6.3

LOCAL SKIN FRICTION COEFFICIENTS FROM CIRCULAR PITOT MEASUREMENTS IN EMPTY TUNNEL AT MACH 2

Run No.	Traverse Station	M_E	C_{FSS}	M_E	C_{pp}	C_{FHKTAW}	C_{FBRAD}
66	4	2.014	0.00187	2.002	0.370	0.00175	0.00180
67	4	2.012	0.00184	2.010	0.389	0.00176	0.00179
68	4	2.017	0.00175	2.012	0.395	0.00163	0.00169
70	4C	1.950	0.00179	1.992	0.389	0.00160	0.00167
71	4C	1.954	0.00190	1.998	0.382	0.00172	0.00177
72	4C	1.966	0.00194	2.003	0.378	0.00177	0.00181
73	4X	1.999	0.00186	2.007	0.310	0.00149	0.00159
74	4X	2.024	0.00183	2.026	0.323	0.00150	0.00158
75	4X	2.020	0.00173	2.026	0.342	0.00144	0.00153
76	18	1.990	0.00171	2.011	0.373	0.00155	0.00162
77	18	2.009	0.00179	2.017	0.369	0.00168	0.00173
78	18	2.007	0.00182	2.019	0.367	0.00173	0.00178
79	18X	1.975	0.00182	2.000	0.262	0.00129	0.00142
80	18X	1.994	0.00182	2.007	0.265	0.00130	0.00143
81	18X	1.971	0.00181	1.995	0.262	0.00124	0.00137
82	18X	1.973	0.00171	1.999	0.289	0.00124	0.00136
83	18C	1.993	0.00182	2.009	0.360	0.00170	0.00176
84	18C	2.011	0.00179	2.021	0.375	0.00170	0.00175
85	18C	2.001	0.00172	2.018	0.391	0.00161	0.00167
88	4	2.017	0.00187	2.012	0.361	0.00171	0.00177
89	4X	2.036	0.00186	2.018	0.389	0.00183	0.00185
90	4C	1.997	0.00188	1.992	0.352	0.00167	0.00174
			Sommer & Short: $R_{\theta_{11}}$			Hopkins & Keener: TAW	Bradshaw TAW
			M_E from p/P_p d_c = 0.0164-in.			M_E from p/P_o d_c = 0.0164-in.	

TABLE 6.4

REFERENCE MAINSTREAM CONDITIONS AT STATION 1 FOR CIRCULAR PITOT PROFILES MEASURED AT MACH 4

Run No.	Traverse STN ; XT		P_o	T_o	p_1	M_{E1}	$\rho_{E1} \times 10^3$	u_{E1}	q_{E1}	T_{E1}	$\mu_{E1} \times 10^6$	$R_{FT1} \times 10^{-6}$	T_{AW1}
142	18	2.85	151.00	538.5	1.06	3.953	0.681	2213.1	11.58	130.5	0.1029	14.65	493.4
144	18X	2.85	151.35	538.5	1.04	3.967	0.674	2214.9	11.48	129.8	0.1023	14.59	493.3
145	18C	2.85	150.75	538.5	1.07	3.946	0.684	2212.1	11.63	130.9	0.1032	14.67	493.4
146*	18C	2.85	151.29	538.5	1.08	3.943	0.689	2211.7	11.70	131.0	0.1033	14.75	493.5
148*	18	2.85	151.34	537.0	1.09	3.936	0.696	2207.7	11.78	131.0	0.1033	14.87	492.1
194*	18X	2.85	171.48	553.8	1.24	3.932	0.767	2241.3	13.39	135.3	0.1070	16.07	507.5
195*	18	2.85	171.45	551.7	1.27	3.913	0.784	2234.5	13.60	135.8	0.1074	16.31	505.7
196*	18C	2.85	171.37	548.9	1.30	3.895	0.802	2226.3	13.80	136.1	0.1076	16.58	503.3
197*	4	-0.72	171.46	549.0	1.32	3.885	0.810	2225.0	13.93	136.6	0.1081	16.67	503.4
198*	4C	-0.72	171.38	549.0	1.29	3.899	0.799	2227.0	13.76	135.9	0.1075	16.54	503.3
199*	4X	-0.72	171.44	548.7	1.29	3.902	0.797	2226.8	13.73	135.7	0.1073	16.54	503.0
---	---	in.	psia	°R.	psia from p_1/P_o		slugs/ft^3	ft/sec	psi	°R.	slugs/ft.sec	---	°R.

(i) *With floor vortex generator, with XVGLE = -9.3-in., See Figure 31.

(ii) No flow visualization

TABLE 6.5

INTEGRAL PARAMETERS FROM CIRCULAR PITOT PROFILES IN EMPTY TUNNEL AT MACH 4

Run No.	Traverse STN ; XT		p/p_1	M_E	δ_{995}	δ_1^*	θ_{11}	δ_1^*/θ_{11}	$R_{\theta_{11}} \times 10^{-4}$
142	18	2.85	1.047	3.797	0.4405	0.2160	0.0263	8.20	2.89
144	18X	2.85	1.057	3.723	0.2405	0.0866	0.0109	7.93	1.13
145	18C	2.85	1.028	3.726	0.2353	0.0852	0.0108	7.90	1.12
146*	18C	2.85	0.992	3.859	0.3650	0.1417	0.0174	8.14	1.97
148*	18	2.85	1.106	3.606	0.2290	0.0716	0.0095	7.55	0.97
194*	18X	2.85	1.013	3.777	0.3528	0.1381	0.0179	7.71	2.12
195*	18	2.85	1.039	3.704	0.2405	0.0693	0.0091	7.62	1.07
196*	18C	2.85	0.987	3.730	0.3653	0.1375	0.0182	7.56	2.14
197*	4	-0.72	1.023	3.715	0.2084	0.0700	0.0089	7.89	1.09
198*	4C	-0.72	0.963	3.768	0.3253	0.1257	0.0164	7.67	1.94
199*	4X	-0.72	0.985	3.696	0.3322	0.1281	0.0170	7.53	1.93
---	---	in.	---	from p/P_p	in.	in.	in.	---	---

*With floor vortex generator, with XVGLE = -9.3-in., See Figure 31.

TABLE 6.6

LOCAL SKIN FRICTION COEFFICIENTS FROM CIRCULAR PITOT MEASUREMENTS IN EMPTY TUNNEL AT MACH 4

Run No.	Traverse Station	M_E	C_{FSS}	M_E	C_{pp}	C_{FHKTAW}	C_{FBRAD}
142	18	3.797	0.00097	n.a.	n.a.	n.a.	n.a.
144	18X	3.723	0.00118	3.926	0.238	0.00144	0.00116
145	18C	3.726	0.00118	3.926	0.197	0.00122	0.00104
146*	18C	3.859	0.00102	3.949	0.192	0.00120	n.a.
148*	18	3.606	0.00126	3.862	0.230	0.00136	n.a.
194*	18X	3.777	0.00103	3.922	0.199	0.00120	0.00102
195*	18	3.704	0.00120	3.885	0.269	0.00154	0.00120
196*	18C	3.730	0.00104	3.905	0.196	0.00117	0.00100
197*	4	3.715	0.00119	3.868	0.238	0.00137	0.00111
198*	4C	3.768	0.00105	3.927	0.215	0.00128	0.00106
199*	4X	3.696	0.00107	3.913	0.198	0.00118	0.00101
			Sommer & Short: $R_{\theta_{11}}$			Hopkins & Keener: TAW	Bradshaw TAW
			M_E from p/P_p			M_E from p/P_o	
			d_c = 0.0164-in.			d_c = 0.0164-in.	

*δ_{VG} = 30-degrees (half-angle of 'V'); HVG = 0.1-in; on floor; see Figure 31.

TABLE 7.1

REFERENCE MAINSTREAM CONDITIONS AT STATION 1 FOR COBRA PROFILES MEASURED AT MACH 2

Run No.	Traverse STN	Traverse XT	δ_W	ε	XWLE	XT-XSWINV	P_o	T_o	p_1	M_{E1}	u_{E1}	q_{E1}	$\mu_{E1} \times 10^6$	$R_{FT1} \times 10^{-6}$	T_{AW1}
24501	T4	2.21	0	29.7	0.0		34.18	533.5	4.25	2.018	1695.4	12.11	0.2323	8.85	507.0
24601	T4	2.21	8	36.7	0.0	0.71	33.98	535.6	4.17	2.026	1702.4	11.98	0.2324	8.72	508.8
2	T4	2.21	8	36.7	0.5	0.21	33.98	535.7	4.17	2.026	1707.3	11.98	0.2336	8.65	511.9
3	T4	2.21	8	36.7	1.0	-0.30	34.03	536.7	4.18	2.025	1703.9	12.01	0.2329	8.71	510.0
4	T4	2.21	8	36.7	1.5	-0.80	34.03	537.2	4.18	2.025	1704.7	12.01	0.2331	8.70	510.4
5	T4	2.21	8	36.8	2.0	-1.30	33.98	537.5	4.18	2.024	1704.7	12.00	0.2333	8.68	510.7
24701	T4	2.21	8	36.8	-0.5	1.21	34.00	535.5	4.20	2.021	1700.3	12.02	0.2328	8.75	508.9
2	T4	2.21	8	36.8	-0.2	0.91	34.06	534.0	4.21	2.021	1697.7	12.05	0.2322	8.80	507.5
3	T4	2.21	8	36.9	0.2	0.51	33.95	533.0	4.22	2.017	1694.5	12.03	0.2322	8.81	506.6
4	T4	2.21	8	36.8	0.7	0.01	34.00	533.2	4.20	2.021	1696.7	12.02	0.2319	8.80	506.7
24801	T3	1.34	8	36.8	0.7	-0.70	33.92	530.5	4.19	2.022	1692.8	11.99	0.2307	8.84	504.1
2	T3	1.34	8	36.8	1.0	-1.00	33.92	528.8	4.18	2.024	1690.8	11.97	0.2299	8.87	502.5
3	T3	1.34	8	36.8	0.4	-0.40	33.89	528.0	4.17	2.024	1689.7	11.96	0.2296	8.88	501.7
4	T3	1.34	8	36.7	0.3	-0.30	33.94	527.3	4.17	2.025	1689.0	11.98	0.2292	8.91	501.0
5	T3	1.34	8	36.8	0.0	0.0	33.89	527.5	4.18	2.023	1688.5	11.97	0.2294	8.90	501.3
6	T3	1.34	8	36.8	-0.2	0.20	33.92	527.5	4.18	2.024	1688.7	11.97	0.2294	8.90	501.2
24901	T3	1.34	8	36.8	0.0	0.0	34.11	544.8	4.20	2.025	1716.5	12.04	0.2361	8.55	517.7
2	T3	1.34	8	36.8	0.5	-0.50	34.11	545.8	4.20	2.025	1718.1	12.04	0.2365	8.53	518.6
25001	T2	0.72	0	29.6	0.0	-0.99	34.14	550.0	4.19	2.026	1725.3	12.04	0.2380	8.44	522.6
2	T2	0.72	8	36.7	0.0	-0.59	34.16	543.8	4.19	2.026	1715.8	12.05	0.2356	8.58	516.7
3	T2	0.72	8	36.7	-0.2	-0.39	34.11	548.4	4.19	2.026	1722.9	12.03	0.2374	8.47	521.1
4	T2	0.72	8	36.8	-0.3	-0.29	34.00	541.9	4.19	2.023	1711.4	12.01	0.2351	8.60	514.9
5	T2	0.72	8	36.8	-0.4	-0.19	34.06	537.3	4.19	2.024	1704.5	12.02	0.2332	8.71	510.6
---	---	in.	deg.	deg.	in.	in.	psia	°R.	psia	from p_1/P_o	ft/sec	psi	slugs/ ft.sec.	---	°R.

TABLE 7.1 (Cont'd)

Run No.	Traverse STN ; XT		δ_W	ε	XWLE	XT-XSWINV	P_o	T_o	p_1	M_{E1}	u_{E1}	q_{E1}	$\mu_{E1} \times 10^6$	$R_{FT1} \times 10^{-6}$	T_{AW1}
25101	T2	0.72	8	36.8	-0.5	-0.09	34.01	544.8	4.19	2.024	1716.3	12.00	0.2362	8.53	517.7
2	T2	0.72	8	36.8	-0.7	0.12	34.01	544.5	4.19	2.024	1715.8	12.00	0.2360	8.54	517.4
3	T2	0.72	8	36.8	-0.9	0.32	33.98	545.1	4.18	2.024	1716.9	11.99	0.2363	8.51	518.0
4	T2	0.72	8	36.8	-1.0	0.42	34.06	544.8	4.20	2.024	1716.1	12.03	0.2362	8.54	517.7
5	T2	0.72	8	36.7	0.2	-0.79	33.95	546.8	4.17	2.026	1720.1	11.98	0.2368	8.47	519.6
25201	T1	-0.16	8	36.7	-1.2	-0.26	34.07	548.5	4.19	2.025	1722.5	12.02	0.2375	8.46	521.2
2	T1	-0.16	8	36.8	-1.4	-0.06	34.07	550.0	4.21	2.022	1723.5	12.04	0.2384	8.44	522.7
3	T1	-0.16	8	36.8	-1.6	0.14	33.99	549.5	4.18	2.024	1723.8	12.00	0.2380	8.42	522.1
4	T1	-0.16	8	36.8	-1.8	0.34	33.96	548.8	4.18	2.025	1722.8	11.99	0.2377	8.43	521.5
25301	T1	-0.16	8	36.7	-2.0	0.54	34.07	541.9	4.19	2.025	1712.0	12.02	0.2350	8.61	514.9
2	T1	-0.16	8	36.8	-2.2	0.74	33.96	538.8	4.19	2.023	1706.1	12.00	0.2340	8.66	512.0
3	T1	-0.16	8	36.7	-1.0	-0.46	34.09	537.3	4.18	2.026	1705.3	12.02	0.2331	8.71	510.5
4	T1	-0.16	8	36.8	-0.8	-0.66	33.93	535.3	4.18	2.023	1700.7	11.99	0.2326	8.73	508.7
5	T1	-0.16	8	36.8	0.0	-1.46	33.85	534.0	4.18	2.021	1697.9	11.97	0.2322	8.74	507.5
6	T1	-0.16	8	36.8	-0.5	-0.96	33.88	534.0	4.18	2.022	1698.2	11.98	0.2321	8.75	507.5
25401	T1	-0.16	0	29.6	3.0		34.14	541.4	4.20	2.025	1711.3	12.05	0.2348	8.64	514.4
2	T1	-0.16	0	29.6	-1.75		34.17	543.8	4.20	2.025	1715.3	12.05	0.2357	8.59	516.7
3	T1	-0.16	8	36.8	-2.0	0.54	34.03	537.3	4.20	2.023	1703.8	12.02	0.2334	8.71	510.6
---	---	in.	deg.	deg.	in.	in.	psia	°R.	psia	from p_1/P_o	ft/sec	psi	slugs/ ft.sec.	---	°R.

TABLE 7.2

INTEGRAL PARAMETERS FROM COBRA PROBE PROFILES MEASURED AT MACH 2

Run	Traverse Station	XT-XSWINV	p/p_1	M_E	δ_{995}	δ_1^*	δ_2^*	θ_{11}	θ_{21}	θ_{12}	θ_{22}	δ_1^*/θ_{11}	$R\theta_{11} \times 10^{-4}$
24501	T4(0°)		1.013	1.998	0.2366	0.0615	-0.0012	0.0195	-0.0010	0.0002	-0.0000	3.15	1.43
24601	T4	0.71	1.445	1.824	0.2729	0.0939	-0.0188	0.0307	-0.0132	0.0057	-0.0024	3.06	2.56
2	T4	0.21	1.395	1.882	0.2828	0.1023	-0.0155	0.0314	-0.0103	0.0052	-0.0017	3.26	2.69
3	T4	-0.30	1.272	1.942	0.2567	0.0877	-0.0096	0.0265	-0.0069	0.0027	-0.0007	3.31	2.23
4	T4	-0.80	1.018	2.021	0.2396	0.0648	-0.0031	0.0201	-0.0025	0.0006	-0.0001	3.22	1.48
5	T4	-1.30	1.005	2.035	0.2415	0.0641	-0.0008	0.0197	-0.0007	0.0001	-0.0000	3.25	1.45
24701	T4	1.21	1.472	1.785	0.2689	0.0811	-0.0180	0.0281	-0.0131	0.0049	-0.0023	2.89	2.30
2	T4	0.91	1.458	1.808	0.2715	0.0895	-0.0200	0.0299	-0.0143	0.0057	-0.0026	2.99	2.51
3	T4	0.51	1.430	1.840	0.2826	0.0994	-0.0179	0.0317	-0.0122	0.0056	-0.0021	3.13	2.72
4	T4	0.01	1.352	1.918	0.2937	0.1048	-0.0116	0.0313	-0.0075	0.0041	-0.0011	3.35	2.76
24801	T3	-0.70	1.055	1.983	0.2325	0.0633	-0.0032	0.0195	-0.0027	0.0005	-0.0001	3.25	1.45
2	T3	-1.00	1.005	2.042	0.2378	0.0635	-0.0020	0.0192	-0.0018	0.0002	-0.0000	3.31	1.46
3	T3	-0.40	1.230	1.933	0.2190	0.0728	-0.0061	0.0224	-0.0045	0.0016	-0.0003	3.25	1.84
4	T3	-0.30	1.270	1.937	0.2382	0.0804	-0.0079	0.0243	-0.0057	0.0022	-0.0005	3.31	2.08
5	T3	0.0	1.352	1.918	0.2697	0.0932	-0.0133	0.0285	-0.0091	0.0042	-0.0014	3.28	2.53
6	T3	0.20	1.392	1.887	0.2763	0.0971	-0.0140	0.0297	-0.0093	0.0047	-0.0015	3.27	2.63
24901	T3	0.0	1.352	1.926	0.2764	0.0978	-0.0109	0.0293	-0.0071	0.0038	-0.0010	3.34	2.53
2	T3	-0.50	1.175	1.904	0.2088	0.0646	-0.0034	0.0211	-0.0025	0.0009	-0.0001	3.06	1.53
25001	T2	-0.99	1.005	2.026	0.2288	0.0624	-0.0015	0.0192	-0.0013	0.0002	-0.0000	3.25	1.36
2	T2	-0.59	1.118	1.910	0.2092	0.0599	-0.0071	0.0189	-0.0059	0.0012	-0.0003	3.17	1.32
3	T2	-0.39	1.232	1.941	0.2188	0.0752	-0.0057	0.0227	-0.0041	0.0016	-0.0003	3.31	1.80
4	T2	-0.29	1.272	1.956	0.2466	0.0838	-0.0072	0.0249	-0.0051	0.0022	-0.0004	3.36	2.11
5	T2	-0.19	1.302	1.931	0.2403	0.0847	-0.0055	0.0253	-0.0033	0.0022	-0.0004	3.35	2.15
---	---	in.	---	from p/P_p	in.	in.	in.	in.	in.	in.	in.	---	---

TABLE 7.2 (Cont'd)

Run	Traverse Station	XT-XSWINV	p/p_1	M_E	δ_{995}	δ_1^*	δ_2^*	θ_{11}	θ_{21}	θ_{12}	θ_{22}	δ_1^*/θ_{11}	$R_{\theta_{11}} \times 10^{-4}$
25101	T2	-0.09	1.330	1.951	0.2616	0.0929	-0.0071	0.0276	-0.0043	0.0028	-0.0006	3.37	2.41
2	T2	0.12	1.375	1.899	0.2624	0.0951	-0.0120	0.0289	-0.0078	0.0042	-0.0012	3.29	2.46
3	T2	0.32	1.409	1.873	0.2663	0.0964	-0.0136	0.0297	-0.0089	0.0047	-0.0015	3.25	2.51
4	T2	0.42	1.422	1.860	0.2651	0.0954	-0.0137	0.0296	-0.0090	0.0047	-0.0015	3.22	2.49
5	T2	-0.79	1.020	2.017	0.2222	0.0589	-0.0016	0.0183	-0.0014	0.0002	-0.0000	3.22	1.31
25201	T1	-0.26	1.283	1.935	0.2277	0.0772	-0.0077	0.0235	-0.0054	0.0023	-0.0005	3.29	1.92
2	T1	-0.06	1.338	1.937	0.2560	0.0918	-0.0065	0.0270	-0.0038	0.0026	-0.0006	3.40	2.30
3	T1	0.14	1.382	1.898	0.2532	0.0906	-0.0113	0.0276	-0.0074	0.0039	-0.0011	3.29	2.32
4	T1	0.34	1.410	1.871	0.2578	0.0900	-0.0126	0.0281	-0.0082	0.0043	-0.0014	3.21	2.34
25301	T1	0.54	1.431	1.824	0.2573	0.0869	-0.0126	0.0281	-0.0086	0.0041	-0.0014	3.10	2.29
2	T1	0.74	1.449	1.829	0.2416	0.0812	-0.0162	0.0266	-0.0115	0.0047	-0.0020	3.05	2.23
3	T1	-0.46	1.200	1.917	0.1914	0.0627	-0.0037	0.0195	-0.0026	0.0011	-0.0002	3.22	1.50
4	T1	-0.66	1.080	1.957	0.2143	0.0567	-0.0032	0.0176	-0.0026	0.0006	-0.0001	3.22	1.29
5	T1	-1.46	1.005	2.041	0.2172	0.0596	-0.0007	0.0179	-0.0006	0.0000	-0.0000	3.34	1.34
6	T1	-0.96	1.005	2.041	0.2180	0.0596	-0.0004	0.0178	-0.0004	0.0000	-0.0000	3.35	1.33
25401	T1(0°)		0.991	2.049	0.2156	0.0574	-0.0004	0.0174	-0.0004	0.0000	-0.0000	3.30	1.27
2	T1(0°)		1.033	2.024	0.2213	0.0618	-0.0010	0.0188	-0.0008	0.0002	-0.0000	3.29	1.39
3	T1	0.54	1.432	1.849	0.2508	0.0866	-0.0170	0.0278	-0.0117	0.0052	-0.0022	3.12	2.37
---	---	in.	---	from p/P_p	in.	in.	in.	in.	in.	in.	in.	---	---

TABLE 7.3

LOCAL SKIN FRICTION COEFFICIENTS FROM COBRA PROBE MEASUREMENTS AT MACH 2

Run No.	Traverse Station	XT-XSWINV	C_{pp}	M_E	C_{FHKTAW}	$C_{FHKT'}$	C_{FSS}	M_E	C_{FHKTAW}	C_{FBRAD}
24501	T4(0°)		0.281	1.998	0.00151	0.00167	0.00179	2.010	0.00131	0.00145
24601	T4	0.71	0.186	1.824	0.00099	0.00119	0.00169	1.787	0.00106	0.00125
2	T4	0.21	0.150	1.882	0.00082	0.00099	0.00165	1.810	0.00093	0.00112
3	T4	-0.30	0.157	1.942	0.00087	0.00104	0.00168	1.870	0.00093	0.00111
4	T4	-0.80	0.235	2.021	0.00129	0.00146	0.00177	2.014	0.00125	0.00139
5	T4	-1.30	0.223	2.035	0.00124	0.00140	0.00177	2.021	0.00125	0.00139
24701	T4	1.21	0.218	1.785	0.00113	0.00135	0.00174	1.771	0.00115	0.00135
2	T4	0.91	0.192	1.808	0.00101	0.00121	0.00170	1.777	0.00111	0.00130
3	T4	0.51	0.164	1.840	0.00088	0.00107	0.00167	1.786	0.00096	0.00116
4	T4	0.01	0.147	1.918	0.00080	0.00097	0.00163	1.827	0.00091	0.00109
24801	T3	-0.70	0.214	1.983	0.00118	0.00135	0.00180	1.988	0.00122	0.00137
2	T3	-1.00	0.234	2.042	0.00128	0.00144	0.00177	2.021	0.00131	0.00145
3	T3	-0.40	0.178	1.933	0.00097	0.00115	0.00174	1.891	0.00095	0.00112
4	T3	-0.30	0.145	1.937	0.00081	0.00097	0.00170	1.871	0.00092	0.00109
5	T3	0.0	0.177	1.918	0.00095	0.00113	0.00165	1.829	0.00090	0.00108
6	T3	0.20	0.149	1.887	0.00081	0.00098	0.00166	1.810	0.00092	0.00111
24901	T3	0.0	0.143	1.926	0.00079	0.00096	0.00165	1.830	0.00091	0.00109
2	T3	-0.5	0.183	1.904	0.00103	0.00121	0.00181	1.921	0.00102	0.00119
25001	T2(0°)		0.228	2.026	0.00127	0.00143	0.00180	2.023	0.00131	0.00145
2	T2	-0.59	0.199	1.910	0.00112	0.00130	0.00186	1.955	0.00106	0.00123
3	T2	-0.39	0.156	1.941	0.00088	0.00104	0.00175	1.892	0.00094	0.00112
4	T2	-0.29	0.172	1.956	0.00094	0.00111	0.00169	1.868	0.00090	0.00108
5	T2	-0.19	0.142	1.931	0.00079	0.00096	0.00170	1.854	0.00091	0.00109
---	---	in.	---		Hopkins & Keener:		Sommer & Short:		Hopkins & Keener:	Bradshaw:
					TAW	T'	$R_{\theta_{11}}$		TAW	TAW
					M_E from p/P_p				M_E from p/P_o	
					d_c = 0.012-in.				d_c = 0.012-in.	

TABLE 7.3 (Cont'd)

Run No.	Traverse Station	XT-XSWINV	C_{pp}	M_E	C_{FHKTAW}	$C_{FHKT'}$	C_{FSS}	M_E	C_{FHKTAW}	C_{FBRAD}
25101	T2	-0.09	0.142	1.951	0.00079	0.00095	0.00165	1.840	0.00089	0.00107
2	T2	0.12	0.146	1.899	0.00081	0.00097	0.00167	1.818	0.00088	0.00107
3	T2	0.32	0.158	1.873	0.00086	0.00104	0.00167	1.803	0.00095	0.00104
4	T2	0.42	0.146	1.860	0.00081	0.00098	0.00168	1.796	0.00095	0.00114
5	T2	-0.79	0.257	2.017	0.00141	0.00156	0.00181	2.013	0.00128	0.00142
25201	T1	-0.26	0.170	1.935	0.00094	0.00111	0.00173	1.864	0.00094	0.00112
2	T1	-0.06	0.138	1.937	0.00077	0.00093	0.00167	1.834	0.00091	0.00109
3	T1	0.14	0.154	1.898	0.00085	0.00102	0.00169	1.815	0.00095	0.00114
4	T1	0.34	0.165	1.871	0.00090	0.00108	0.00170	1.802	0.00097	0.00116
25301	T1	0.54	0.185	1.824	0.00099	0.00119	0.00172	1.793	0.00103	0.00122
2	T1	0.74	0.201	1.829	0.00106	0.00126	0.00173	1.782	0.00113	0.00132
3	T1	-0.46	0.177	1.917	0.00098	0.00116	0.00182	1.909	0.00101	0.00118
4	T1	-0.66	0.214	1.957	0.00118	0.00136	0.00185	1.973	0.00114	0.00130
5	T1	-1.46	0.237	2.041	0.00130	0.00146	0.00180	2.018	0.00134	0.00147
6	T1	-0.96	0.237	2.041	0.00130	0.00146	0.00180	2.019	0.00134	0.00147
25401	T1(0°)		0.242	2.049	0.00133	0.00149	0.00181	2.030	0.00138	0.00151
2	T1(0°)		0.229	2.024	0.00126	0.00142	0.00179	2.005	0.00131	0.00144
3	T1	0.54	0.179	1.849	0.00096	0.00115	0.00170	1.790	0.00104	0.00124
---	---	in.	---		Hopkins & Keener:		Sommer & Short:		Hopkins & Keener:	Bradshaw:
					TAW	T'	$R_{\theta_{11}}$		TAW	TAW
					M_E from p/P_p				M_E from p/P_o	
					d_c = 0.012-in.				d_c = 0.012-in.	

TABLE 7.4

REFERENCE MAINSTREAM CONDITIONS AT STATION 1 FOR COBRA PROFILES MEASURED AT MACH 4

Run No.	Traverse STN	; XT	δ_W	ε	XWLE	XT-XSWINV	P_o	T_o	p_1	M_{E1}	u_{E1}	q_{E1}	$\mu_{E1} \times 10^6$	$R_{FT1} \times 10^{-6}$	T_{AW1}
22600	T1	-0.16	0	14.7	0.0		171.47	552.0	1.24	3.931	2237.6	13.40	0.1067	16.16	505.9
22700	T1	-0.16	0	14.7	-2.5		171.49	552.0	1.22	3.940	2238.8	13.31	0.1063	16.10	505.9
22901	T1	-0.16	0	14.7	1.0		171.42	543.0	1.24	3.931	2219.2	13.40	0.1048	16.59	497.7
2	T1	-0.16	14	26.3	-2.5	0.34	171.42	540.0	1.24	3.931	2213.1	13.40	0.1042	16.74	494.9
23000	T1	-0.16	12	24.4	-2.5	0.15	171.38	549.0	1.25	3.922	2230.3	13.49	0.1064	16.36	502.2
23100	T1	-0.16	0	14.8	-2.5		171.46	547.7	1.25	3.923	2227.8	13.49	0.1061	16.42	502.0
23201	T1	-0.16	0	14.7	0.0		171.50	538.5	1.24	3.932	2210.2	13.39	0.1038	16.81	493.5
2	T1	-0.16	8	20.7	0.0	-2.76	171.50	538.0	1.24	3.932	2209.2	13.39	0.1037	16.83	493.1
23301	T1	-0.16	0	14.7	-1.0		171.48	540.0	1.24	3.931	2213.1	13.40	0.1041	16.74	494.9
2	T1	-0.16	8	20.7	-1.0	-1.76	171.48	540.0	1.24	3.931	2213.1	13.40	0.1041	16.74	494.9
23401	T1	-0.16	0	14.7	-1.5		171.48	538.3	1.24	3.930	2209.5	13.41	0.1038	16.83	493.4
2	T1	-0.16	8	20.7	-1.5	-1.26	171.48	537.8	1.24	3.930	2208.4	13.41	0.1037	16.86	492.9
23501	T1	-0.16	0	14.7	-2.0		171.52	537.7	1.23	3.936	2209.1	13.35	0.1034	16.82	492.8
2	T1	-0.16	8	20.7	-2.0	-0.76	171.52	536.0	1.23	3.936	2205.6	13.35	0.1031	16.90	491.2
23600	T1	-0.16	8	20.7	-2.5	-0.26	171.47	534.5	1.23	3.936	2202.5	13.35	0.1028	16.98	489.8
23700	T1	-0.16	8	20.7	-2.5	-0.26	171.43	548.8	1.22	3.945	2233.0	13.24	0.1054	16.20	502.9
23801	T1	-0.16	16	28.2	0.0	-2.00	171.55	552.0	1.15	3.984	2244.9	12.82	0.1043	15.76	505.6
2	T1	-0.16	16	27.8	-1.0	-1.00	171.55	552.5	1.02	4.075	2257.9	11.89	0.1005	15.08	505.6
23901	T1	-0.16	16	28.2	-1.5	-0.50	171.58	553.0	1.15	3.986	2247.2	12.80	0.1044	15.70	506.5
2	T1	-0.16	16	27.8	-2.0	0.0	171.58	553.0	1.01	4.085	2260.1	11.79	0.1002	14.99	506.0
24000	T1	-0.16	16	28.1	-2.0	0.0	171.57	545.5	1.14	3.990	2232.4	12.76	0.1027	16.02	499.6
24100	T1	-0.16	16	28.1	-2.25	0.25	171.55	541.6	1.15	3.988	2224.2	12.78	0.1020	16.22	496.1
24200	T1	-0.16	16	28.4	-1.75	-0.25	171.59	539.9	1.25	3.927	2212.4	13.45	0.1043	16.78	494.8
24300	T1	-0.16	16	28.1	-1.75	-0.25	171.51	536.9	1.14	3.993	2215.1	12.73	0.1008	16.41	491.7
24400	T1	-0.16	16	28.1	-1.25	-0.75	171.56	536.5	1.14	3.996	2214.7	12.70	0.1006	16.41	491.3
---	---	in.	deg.	deg.	in.	in.	psia	°R.	psia	from p_1/P_o	ft/sec	psi	slugs/ ft.sec.	---	°R.

TABLE 7.5

INTEGRAL PARAMETERS FROM COBRA PROBE PROFILES MEASURED AT MACH 4

Run	Traverse Station	XT-XSWINV	p/p_1	M_E	δ_{995}	δ_1^*	δ_2^*	θ_{11}	θ_{21}	θ_{12}	θ_{22}	δ_1^*/θ_{11}	$R\theta_{11} \times 10^{-4}$
22600	T1(0°)		1.008	3.879	0.1821	0.0642	-0.0037	0.0083	-0.0033	0.0004	-0.0001	7.76	1.07
22700	T1(0°)		1.130	3.629	0.1840	0.0632	-0.0030	0.0089	-0.0026	0.0004	-0.0001	7.07	1.05
22901	T1(0°)		1.008	3.859	0.1797	0.0616	-0.0031	0.0080	-0.0028	0.0003	-0.0001	7.66	1.05
2	T1(14°)	0.34	2.135	3.509	0.3920	0.1598	-0.0172	0.0262	-0.0122	0.0050	-0.0052	6.10	5.35
23000	T1(12°)	0.15	1.837	3.796	0.3989	0.1615	-0.0020	0.0216	0.0012	0.0032	-0.0028	7.48	4.88
23100	T1(0°)		1.008	3.848	0.1864	0.0650	-0.0033	0.0085	-0.0030	0.0003	-0.0001	7.67	1.09
23201	T1(0°)		1.008	3.887	0.1815	0.0638	-0.0034	0.0081	-0.0031	0.0004	-0.0001	7.87	1.10
2	T1(8°)	-2.76	1.008	3.875	0.1784	0.0626	-0.0035	0.0079	-0.0032	0.0004	-0.0001	7.89	1.06
23301	T1(0°)		1.008	3.876	0.1897	0.0657	-0.0040	0.0085	-0.0036	0.0004	-0.0001	7.73	1.13
2	T1(8°)	-1.76	1.009	3.870	0.1814	0.0637	-0.0040	0.0082	-0.0036	0.0004	-0.0001	7.76	1.09
23401	T1(0°)		1.008	3.824	0.1828	0.0649	-0.0032	0.0084	-0.0028	0.0004	-0.0001	7.70	1.08
2	T1(8°)	-1.26	1.270	3.446	0.1817	0.0588	-0.0063	0.0091	-0.0055	0.0008	-0.0004	6.45	1.05
23501	T1(8°)		1.008	3.892	0.1845	0.0647	-0.0039	0.0083	-0.0035	0.0004	-0.0001	7.84	1.12
2	T1(8°)	-0.76	1.477	3.567	0.2099	0.0772	-0.0069	0.0107	-0.0055	0.0014	-0.0005	7.19	1.60
23600	T1(16°)	-0.26	1.580	3.454	0.2216	0.0832	-0.0059	0.0115	-0.0043	0.0016	-0.0005	7.21	1.67
23700	T1(16°)	-0.26	1.580	3.460	0.2319	0.0849	-0.0054	0.0118	-0.0038	0.0016	-0.0005	7.18	1.64
23801	T1(16°)	-2.00	1.022	3.917	0.1833	0.0649	-0.0044	0.0082	-0.0040	0.0004	-0.0001	7.92	1.03
2	T1(1y°)	-1.00	1.400	3.599	0.1839	0.0586	-0.0106	0.0085	-0.0086	0.0019	-0.0015	6.88	0.98
23901	T1(16°)	-0.50	1.943	3.552	0.1968	0.0999	-0.0137	0.0132	-0.0082	0.0055	-0.0035	7.57	2.27
2	T1(16°)	0.0	2.045	4.323	0.3695	0.1716	-0.0053	0.0190	-0.0005	0.0048	-0.0053	9.03	5.89
24000	T1(16°)	0.0	2.045	4.073	0.3760	0.1685	-0.0025	0.0205	0.0019	0.0043	-0.0050	8.22	6.00
24100	T1(16°)	0.25	2.230	3.708	0.3963	0.1698	-0.0162	0.0245	-0.0108	0.0054	-0.0063	6.92	6.22
24200	T1(16°)	-0.25	1.987	3.440	0.2833	0.1209	-0.0130	0.0179	-0.0066	0.0064	-0.0050	6.77	3.17
24300	T1(16°)	-0.25	1.987	3.609	0.2790	0.1202	-0.0111	0.0167	-0.0055	0.0056	-0.0046	7.18	3.20
24400	T1(16°)	-0.75	1.860	3.610	0.1498	0.0815	-0.0033	0.0094	-0.0010	0.0023	-0.0009	8.72	1.70
---	---	in.	---	from p/P_p	in.	in.	in.	in.	in.	in.	in.	---	---

TABLE 7.6

LOCAL SKIN FRICTION COEFFICIENTS FROM COBRA PROBE MEASUREMENTS AT MACH 4

Run No.	Traverse Station	XT-XSWINV	M_E	C_{FHKTAW}	$C_{FHKT'}$	C_{FSS}	M_E	C_{FHKTAW}	C_{FBRAD}
22600	T1		3.879	0.00103	0.00093	0.00115	3.937	0.00102	0.00093
22700	T1		3.629	0.00094	0.00088	0.00123	3.937	0.00100	0.00092
22901	T1		3.859	0.00106	0.00095	0.00116	3.936	0.00103	0.00093
2	T1	0.34	3.509	0.00117	0.00107	0.00094	3.397	0.00128	0.00112
23000	T1	0.15	3.796	0.00098	0.00090	0.00088	3.502	0.00121	0.00107
23100	T1		3.848	0.00103	0.00093	0.00115	3.937	0.00102	0.00093
23201	T1		3.887	0.00107	0.00095	0.00114	3.937	0.00102	0.00093
2	T1	-2.76	3.875	0.00105	0.00094	0.00115	3.937	0.00106	0.00095
23301	T1		3.876	0.00103	0.00093	0.00114	3.937	0.00101	0.00092
2	T1	-1.76	3.870	0.00096	0.00088	0.00115	3.936	0.00098	0.00090
23401	T1		3.824	0.00098	0.00090	0.00116	3.937	0.00098	0.00090
2	T1	-1.26	3.446	0.00094	0.00090	0.00129	3.767	0.00082	0.00079
23501	T1		3.892	0.00098	0.00089	0.00114	3.937	0.00099	0.00090
2	T1	-0.76	3.567	0.00066	0.00066	0.00115	3.658	0.00062	0.00065
23600	T1	-0.26	3.454	0.00053	0.00056	0.00118	3.609	0.00050	0.00054
23700	T1	-0.26	3.460	0.00057	0.00059	0.00118	3.609	0.00051	0.00055
23801	T1	-2.00	3.917	0.00093	0.00085	0.00115	3.927	0.00088	0.00084
2	T1	-1.00	3.599	0.00104	0.00097	0.00125	3.696	0.00071	0.00072
23901	T1	-0.50	3.552	0.00058	0.00059	0.00108	3.463	0.00053	0.00058
2	T1	0.0	4.323	0.00090	0.00079	0.00075	3.428	0.00105	0.00097
24000	T1	0.0	4.073	0.00080	0.00074	0.00079	3.428	0.00105	0.00097
24100	T1	0.25	3.708	0.00115	0.00103	0.00085	3.368	0.00133	0.00116
24200	T1	-0.25	3.440	0.00074	0.00074	0.00105	3.448	0.00076	0.00076
24300	T1	-0.25	3.609	0.00077	0.00075	0.00100	3.448	0.00074	0.00075
24400	T1	-0.75	3.610	0.00041	0.00044	0.00112	3.494	0.00036	0.00042
---	---	in.		Hopkins & Keener:	----	Sommer & Short:		Hopkins & Kenner:	Bradshaw
				TAW	T'	$R_{\theta_{11}}$		TAW	TAW
				M_E from p/P_p				M_E from p/P_o	
				d_c = 0.012-in.				d_c = 0.012-in.	

TABLE 8
AIR INJECTION TESTS

Run No.	δ_w	XWLE	P_o	T_o	p_1	M_{E1}	P_{o_j}	T_{o_j}	θ_j	Comments
260		OUT	34.10	536.4	4.59	1.966	167.89	538.8	0	Repeatability and Uniformity
261		OUT	34.24	528.7	4.59	1.969	166.22	524.6	0	of jet flow in empty tunnel.
262		OUT	34.05	525.8	4.59	1.966	166.99	529.4	0	Obstacle blocks on Line 17.
263		OUT	34.18	530.0	4.61	1.965			0	Blocks on Line 17, No jet.
265		OUT	34.20	529.3	4.65	1.960			0	New Blocks on Lines 17, $\alpha 2$.
266		OUT	34.24	529.0	4.59	1.970			0	Different Blocks on Line 17, Same Blocks on Line $\alpha 2$.
267		OUT	34.15	530.0	4.58	1.969			0	Blocks Pitched $\cong \pm 10$ degrees.
268		OUT	Mainstream Flow Conditions Same as for Run 267						0	Oil Flow Visualization; Blocks Pitched on Line $\alpha 2$.
269		OUT	34.26	535.0	4.59	1.970	170.98	533.4	0	Oil Flow Visualization.
270		OUT	34.23	535.0	4.59	1.969	114.31	530.0	0	Oil Flow Visualization.
271		OUT	34.37	536.5	4.67	1.960	209.91	535.2	0	Oil Flow Visualization.
272	0→11	2.0	34.30	533.0	4.59	1.971			0	Check Wedge Static Pressures versus δ_w
273	11.5	3.0	Flow Conditions Same as for Run 290 ($P_{o_j} \cong 167$ psia)						0	Oil Flow Visualization.
274	11.5	1.0	Flow Conditions Same as for Run 288 (XWLE=1.5-in.) ($P_{o_j} \cong 167$ psia)						0	Oil Flow Visualization.
275	11.5	3.0	Flow Conditions Same as for Run 271 ($P_{o_j} \cong 210$ psia)						0	Oil Flow Visualization.
276	11.7	2.125	Flow Conditions Same as for Run 269 ($P_{o_j} \cong 171$ psia)						0	Oil Flow Visualization.
277	11.5	3.00	Flow Conditions Same as for Run 270 ($P_{o_j} \cong 114$ psia)						0	Oil Flow Visualization.
278	11.5	3.00	Flow Conditions Same as for Run 289 ($P_{o_j} \cong 167$ psia)						30	Oil Flow Visualization.
279	11.5	1.5	Flow Conditions Same as for Run 269 ($P_{o_j} \cong 171$ psia)						-30	Oil Flow Visualization
---	Degrees	in.	psia	°R	psia	---	psia	°R	Degrees	----------

TABLE 8 (Cont'd)

Run No.	δ_w	XWLE	P_o	T_o	p_1	M_{E1}	P_{o_j}	T_{o_j}	θ_j	Comments
280	11.5	1.5	Flow Conditions Same as for Run 291 ($P_{o_j} \cong 167$ psia)						-20	Oil Flow Visualization.
281	11.5	1.5	Flow Conditions Same as for Run 292 ($P_{o_j} \cong 168$ psia)						-12	Oil Flow Visualization.
282	11.2	1.64	Flow Conditions Same as for Run 269 ($P_{o_j} \cong 171$ psia)						-40	Oil Flow Visualization.
283	11.5	1.5	Flow Conditions Same as for Run 269 ($P_{o_j} \cong 171$ psia)						-35	Oil Flow Visualization.
284	11.5	1.5	Flow Conditions Same as for Run 287 ($P_{o_j} \cong 167$ psia)						-25	Oil Flow Visualization.
285	11.5	1.5	Flow Conditions Same as for Run 269 ($P_{o_j} \cong 171$ psia)						-15	Oil Flow Visualization.
286	11.5	1.5	Flow Conditions Sames as for Run 270 ($P_{o_j} \cong 114$ psia)						-25	Oil Flow Visualization.
287	11.5	1.5	34.49	531.0	4.68	1.962	166.95	533.0	-25	Static Pressures.
			(See Flow viz. Run 284)							
288	11.5	1.5	34.55	536.0	4.60	1.974	167.01	537.5	0	Static Pressures.
			(See Flow viz. Run 274)							
289	11.5	3.0	34.65	537.0	4.61	1.974	166.58	539.2	30	Static Pressures.
			(See Flow viz. Run 278)							
290	11.5	3.0	34.67	537.2	4.61	1.975	167.13	538.3	0	Static Pressures.
			(See Flow viz. Run 273)							
291	11.5	1.5	34.34	534.2	4.63	1.966	166.97	533.0	-20	Static Pressures.
			(See Flow viz. Run 280)							
292	11.5	1.5	34.33	531.3	4.51	1.982	167.70	531.6	-12	Static Pressures.
			(See Flow viz. Run 281)							
293		OUT	34.40	529.0	4.53	1.981	166.87	530.3	-12	Static Pressures.
294		OUT	Flow Conditions Same as for Run 293						-12	Oil Flow Visualization.
295	8	1.5	34.35	533.3	4.51	1.983	166.81	533.8	-12	Pressures and Oil Flow Visualization.
---	Degrees	in.	psia	°R	psia	---	psia	°R	Degrees	----------

TABLE 8 (Cont'd)

Run No.	δ_w	XWLE	P_o	T_o	p_1	M_{El}	P_{o_j}	T_{o_j}	θ_j	Comments
296	8	1.5	34.38	533.3	4.50	1.985	167.22	533.0	-20	Pressures and Oil Flow Visualization.
297	8	1.5	34.38	534.7	4.67	1.961	166.85	533.4	30	Pressures and Oil Flow Visualization.
298	8	1.5	34.37	531.3	4.66	1.962	166.99	532.2	20	Pressures and Oil Flow Visualization.
299	0	1.5	34.44	537.2	4.56	1.977	167.44	535.2	0	Obstacle Blocks on Line 10.
300	0	1.5	34.44	538.3	4.56	1.977			0	Obstacle Blocks on Line 10.
301	8	1.5	34.39	535.0	4.55	1.977	167.22	537.1	0	Obstacle Blocks on Line 10; Oil Flow Visualization.
302	11.5	-3.63	34.49	535.3	4.58	1.975	166.74	537.9	0	2D Wedge Flow with $M_j \cong 3$.
303	8	-3.63	34.42	534.3	4.61	1.969	166.72	535.7	0	2D Wedge Flow with $M_j \cong 3$.
304		OUT	34.38	536.2	4.61	1.968	167.38	535.5	0	New Obstacle Blocks on Line 10. Compare with Run 299.
305		OUT	34.38	535.8	4.61	1.968	167.53		0	Obstacle Blocks on Line 10 T_{o_j} Thermometer Removed.
306		OUT	34.38	535.7	4.62	1.967	166.85		0	Obstacle Blocks on Line 10 T_{o_j} Thermometer + Screen Removed.
307	8	-3.63	34.36	532.9	4.60	1.970	75.68	530.9	0	2D Wedge Flow with $M_j \cong 2.5$.
---	Degrees	in.	psia	°R	psia	---	psia	°R	Degrees	----------

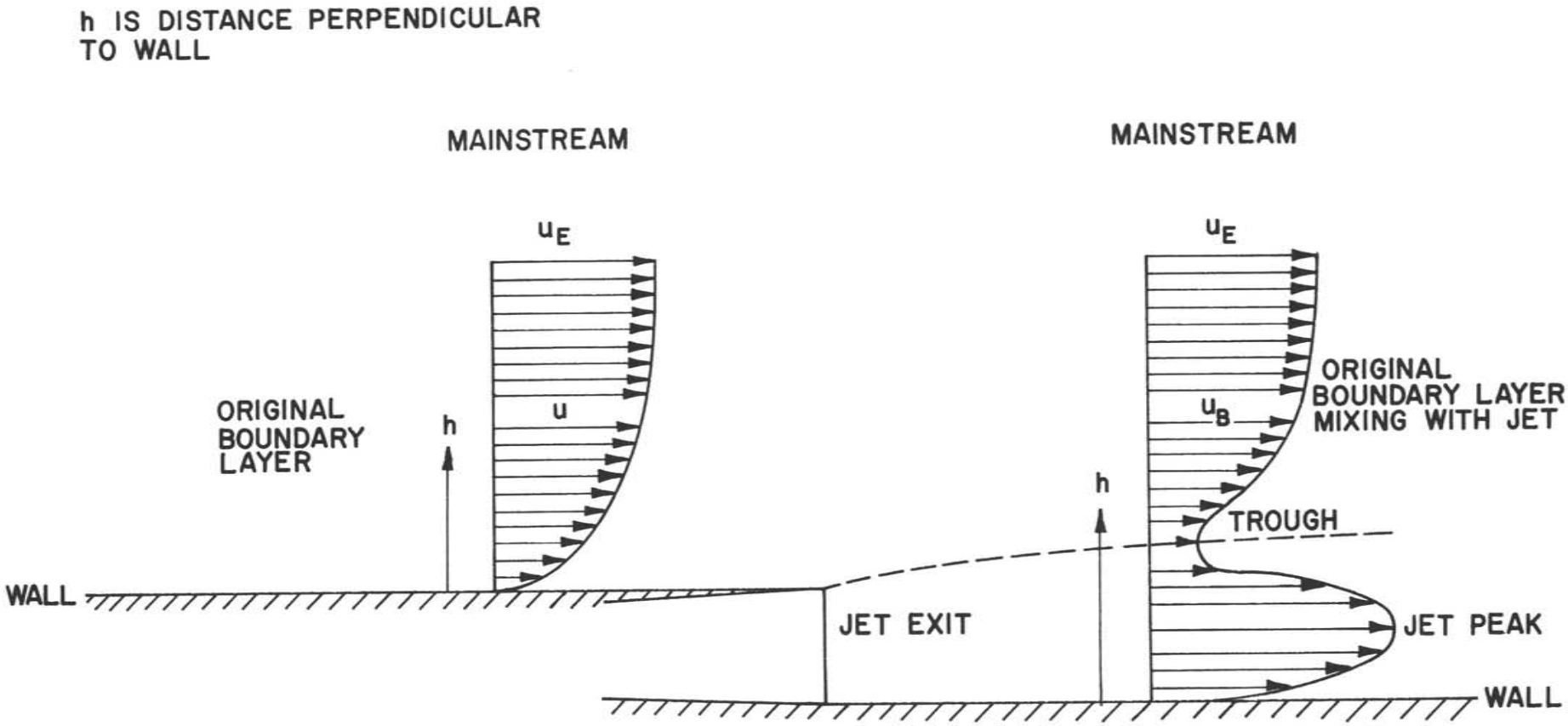

FIG. 1: DEFINITION OF JET PEAK AND WAKE TROUGH

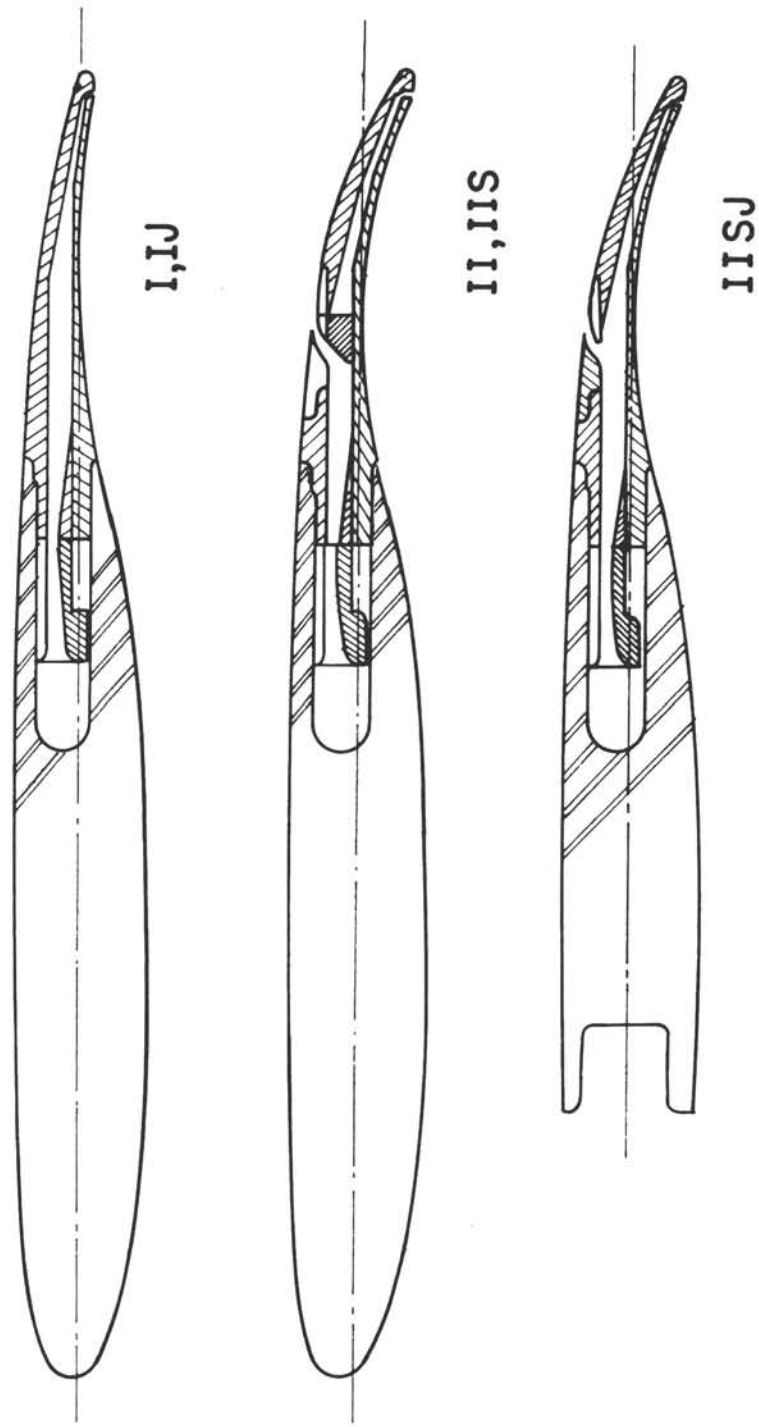

FIG. 2(a): SUPERCRITICAL AEROFOILS WITH SLOT BLOWING AND JET FLAP

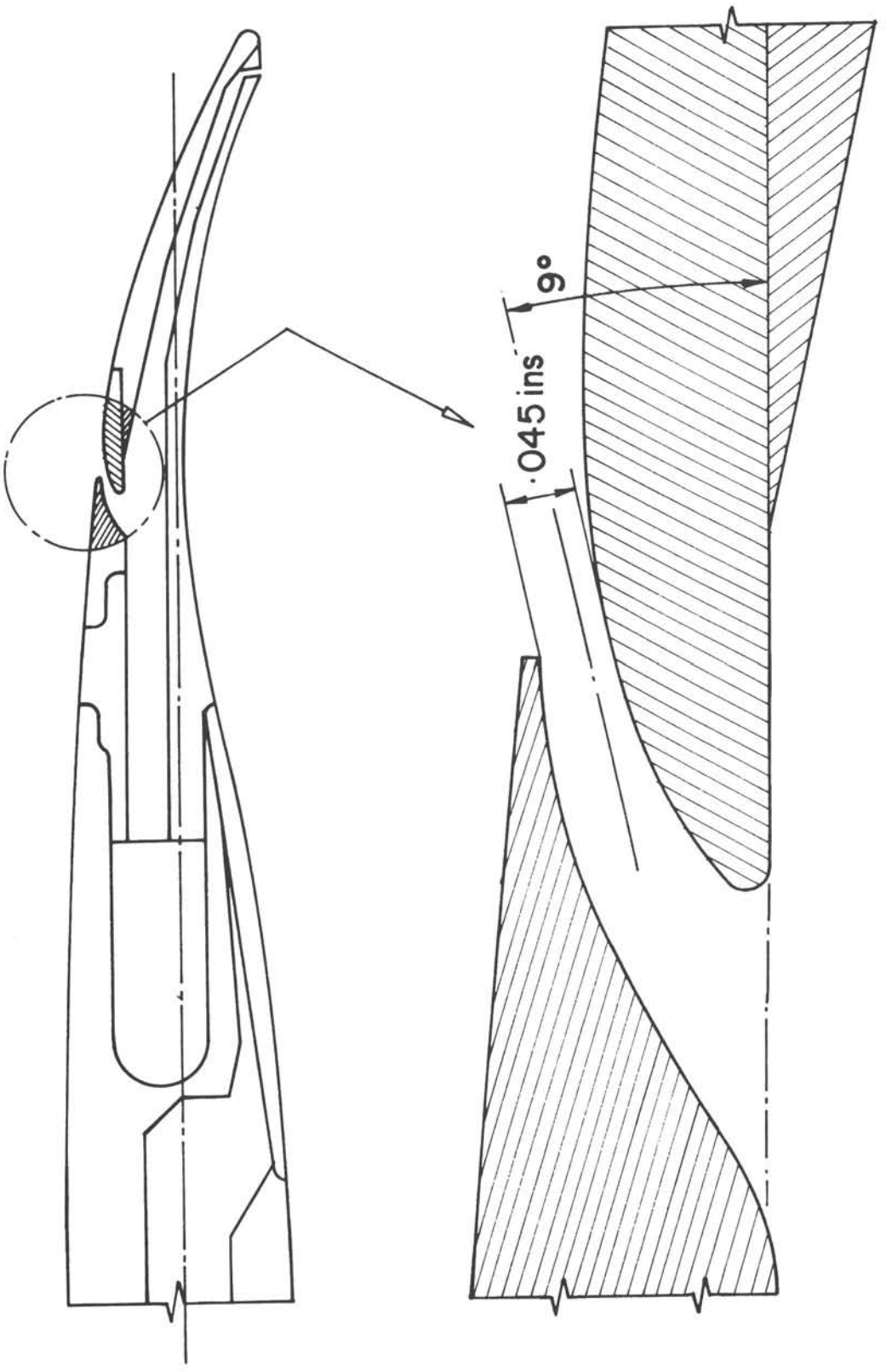

FIG. 2(b): SLOT BLOWING NOZZLE ON AEROFOIL II

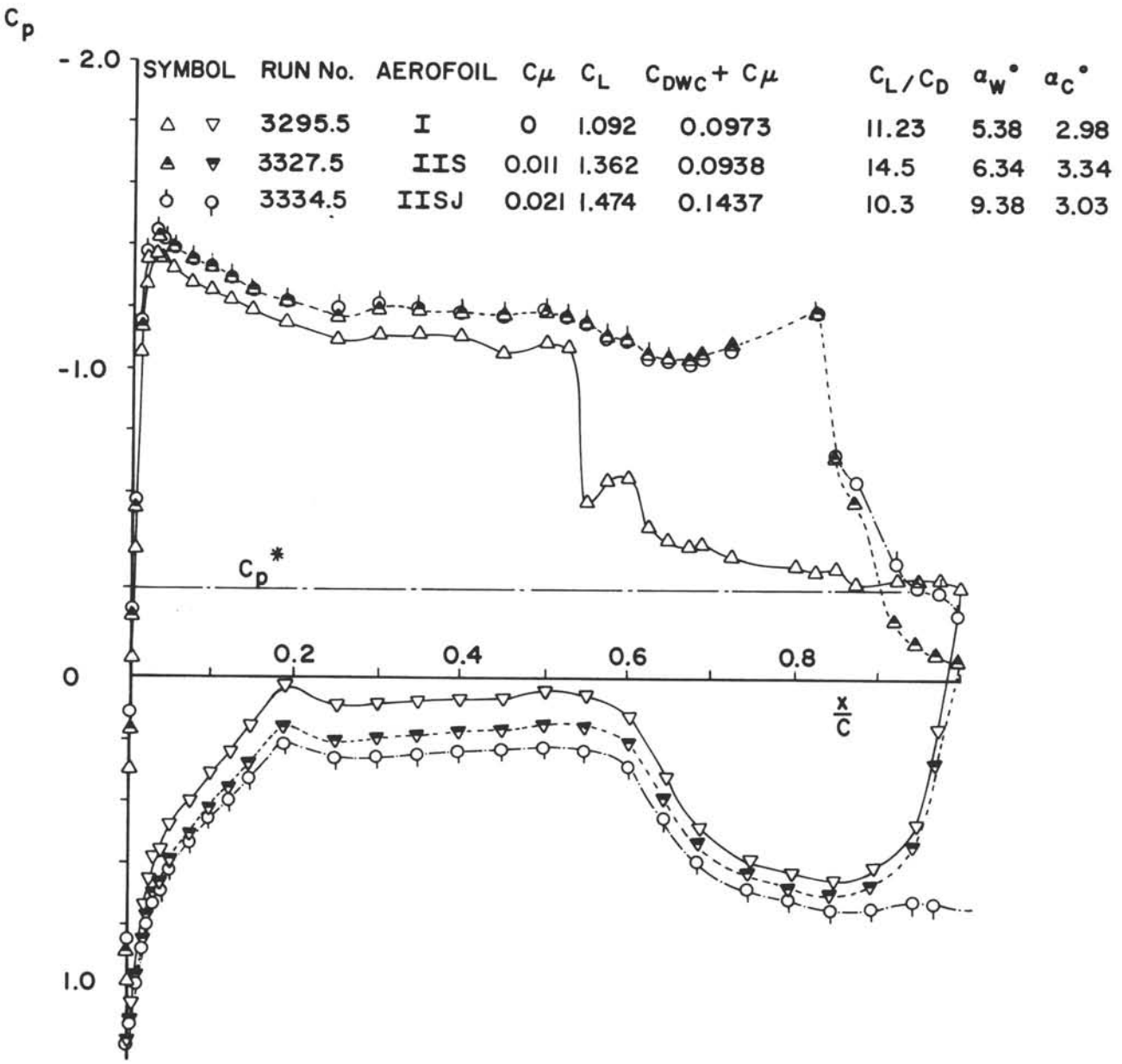

FIG. 3: PRESSURES AROUND SUPERCRITICAL AEROFOIL SHOWING EFFECT OF SLOT BLOWING AND JET FLAP ON AEROFOIL II AT MACH 0.85 AND CHORD REYNOLDS NUMBER OF 30 MILLION

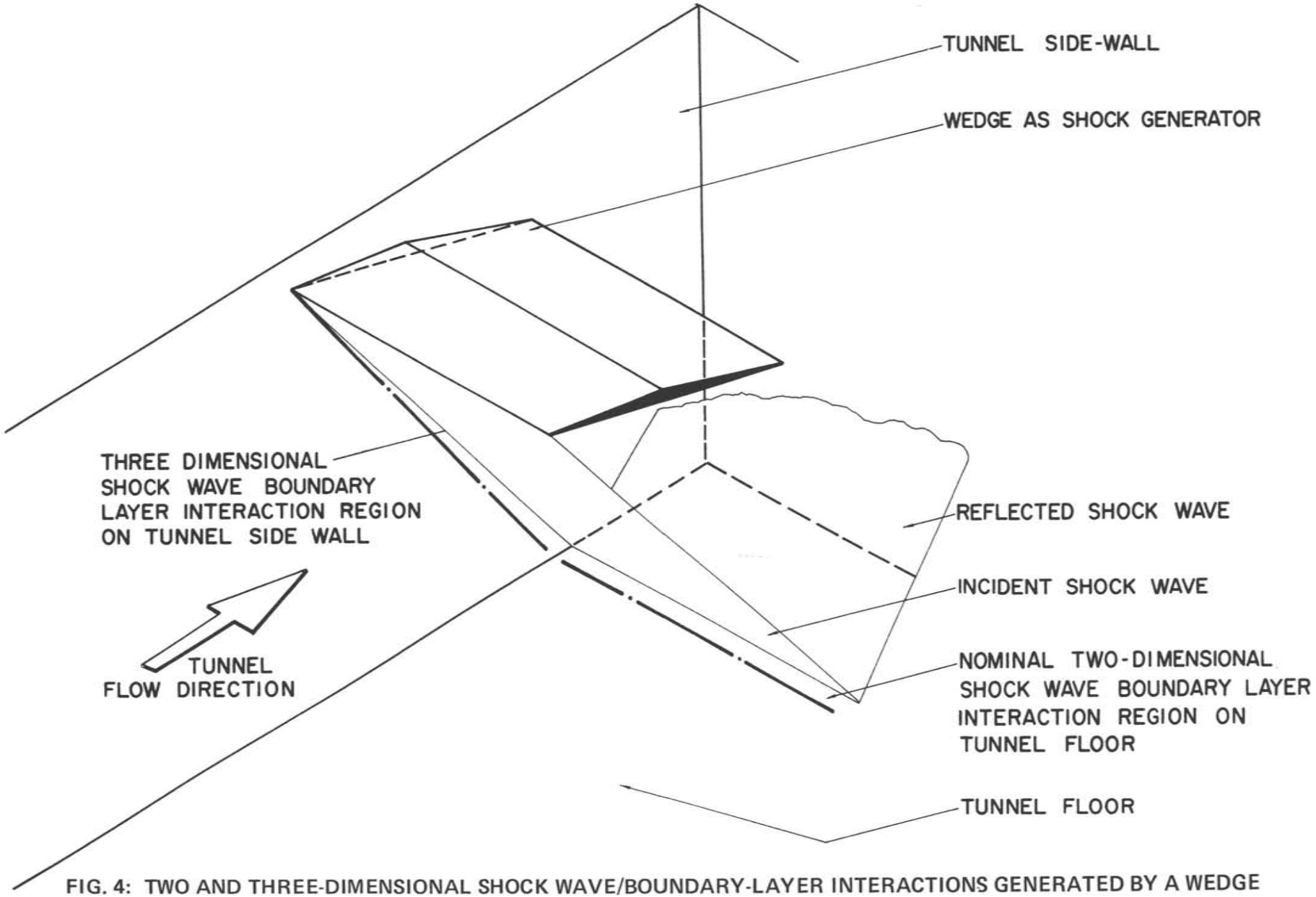

FIG. 4: TWO AND THREE-DIMENSIONAL SHOCK WAVE/BOUNDARY-LAYER INTERACTIONS GENERATED BY A WEDGE IN A RECTANGULAR DUCT

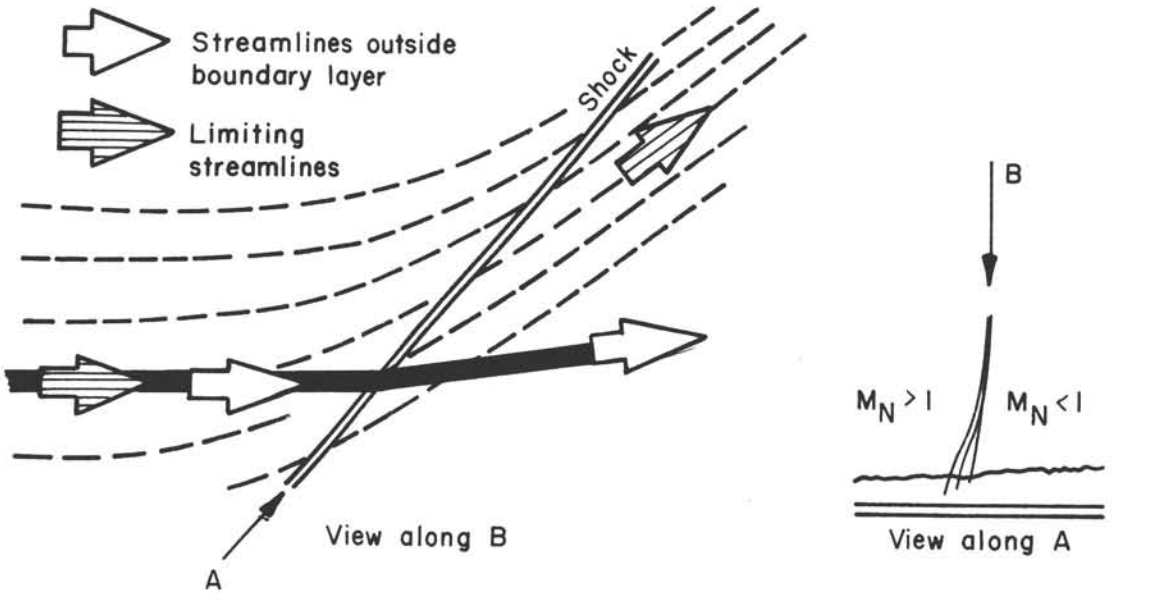

(a) Attached flow

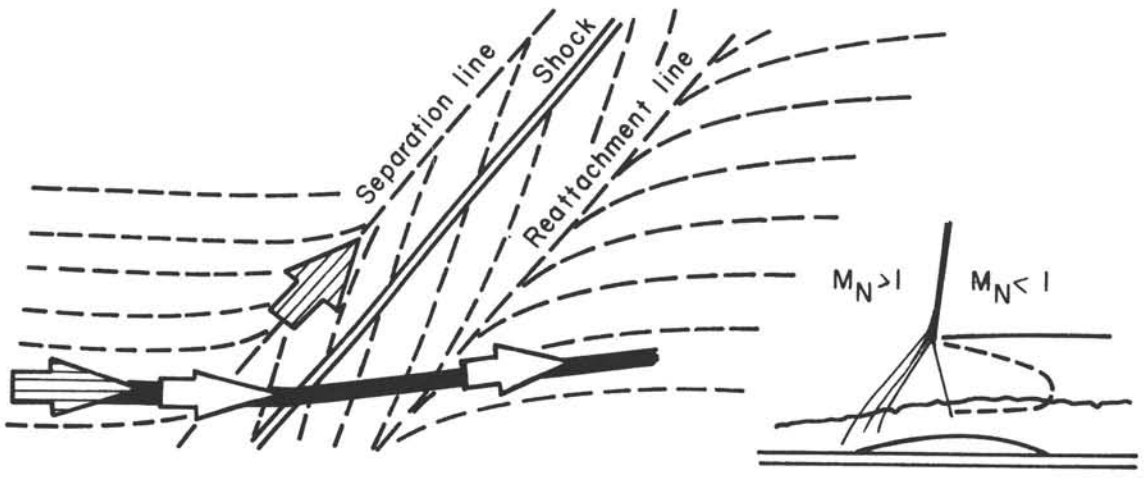

(b) Separated flow

FIG. 5: SCHEMATIC DIAGRAM OF SURFACE FLOW BENEATH SWEPT SHOCKS, REFERENCE 30

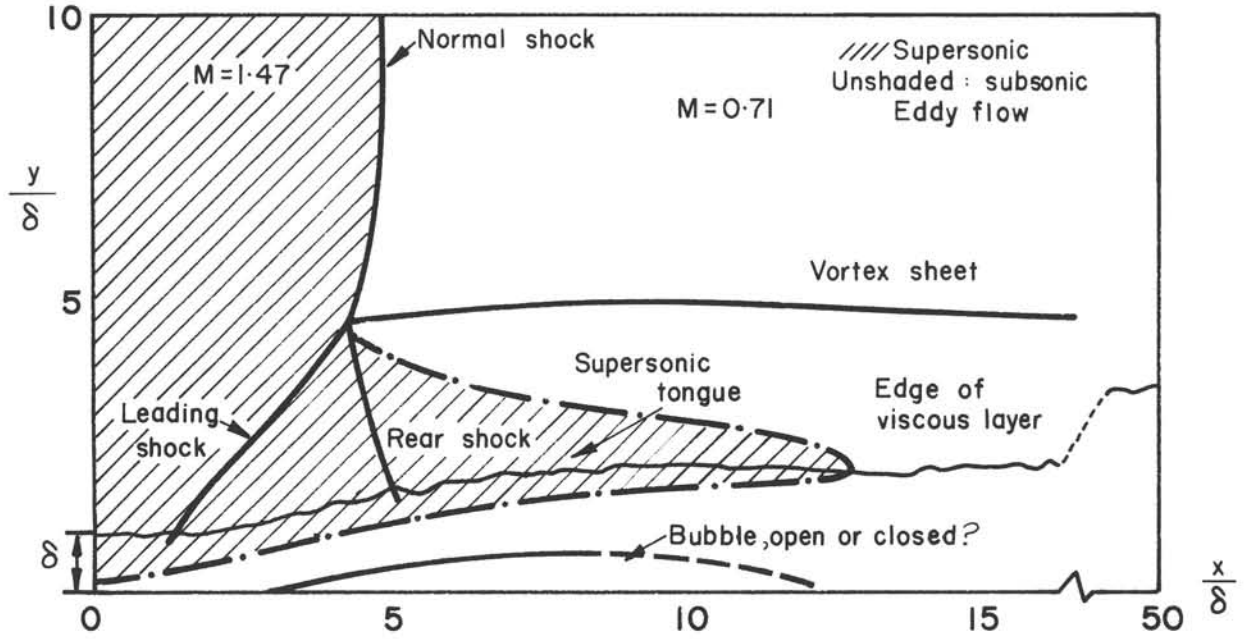

Flow field through the interaction

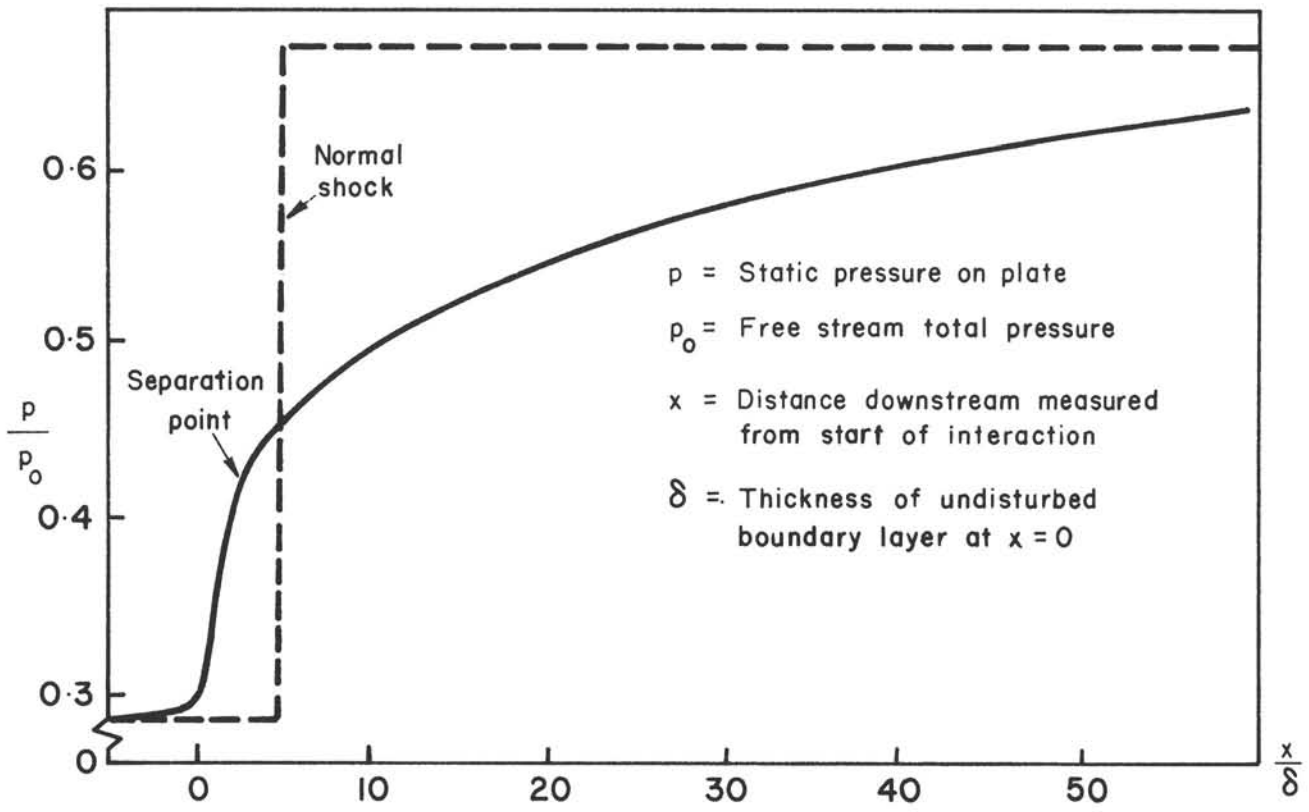

Surface pressure distribution

FIG. 6: POSSIBLE INTERPRETATION OF SWEPT NORMAL SHOCK/TURBULENT BOUNDARY-LAYER INTERACTION WHEN VIEWED ALONG SHOCK, AFTER SEDDON, REFERENCE 52

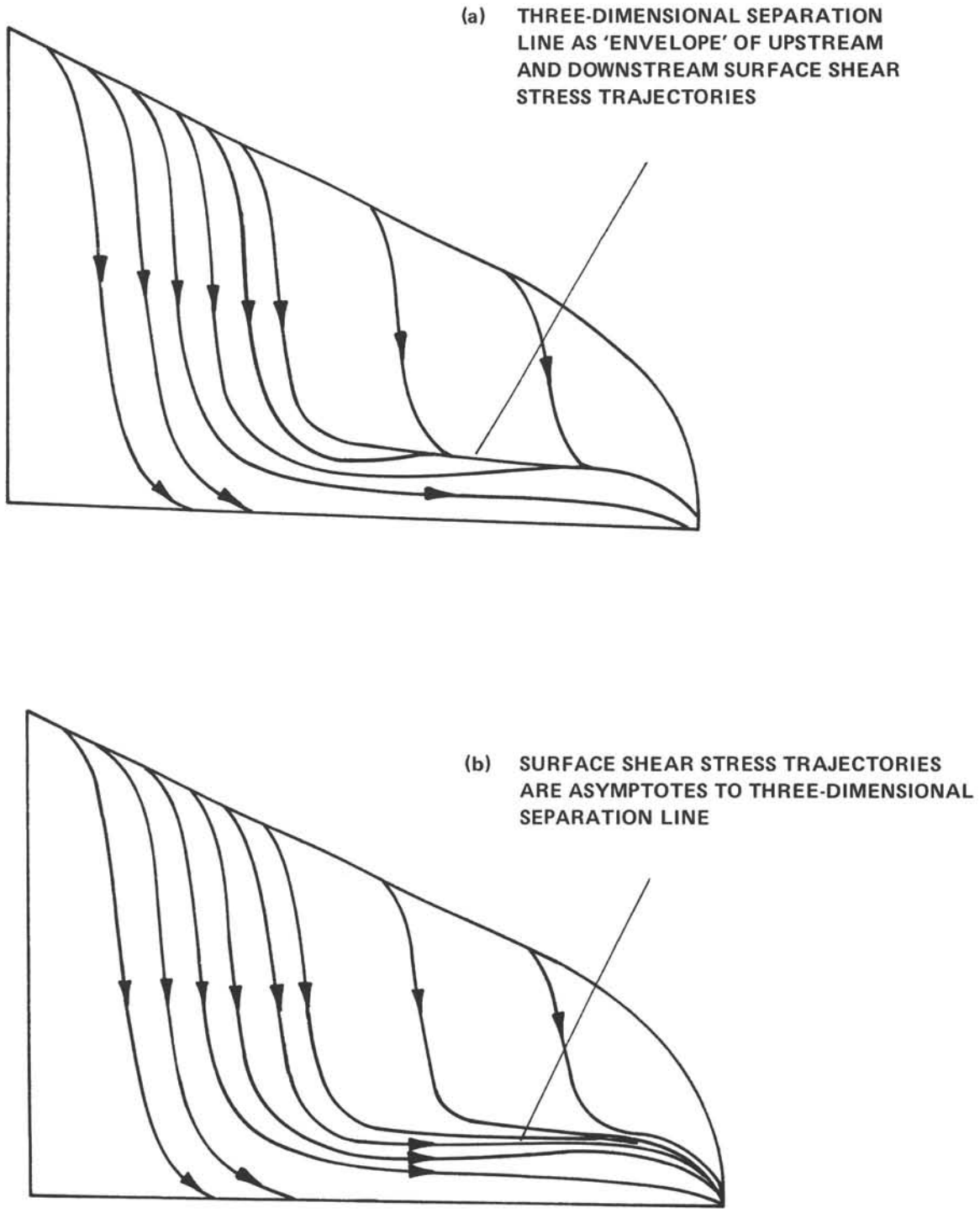

FIG. 7: PLAUSIBLE PATTERNS OF SURFACE SHEAR STRESS TRAJECTORIES FOR A 3D SEPARATION BENEATH A SWEPT SHOCK WAVE

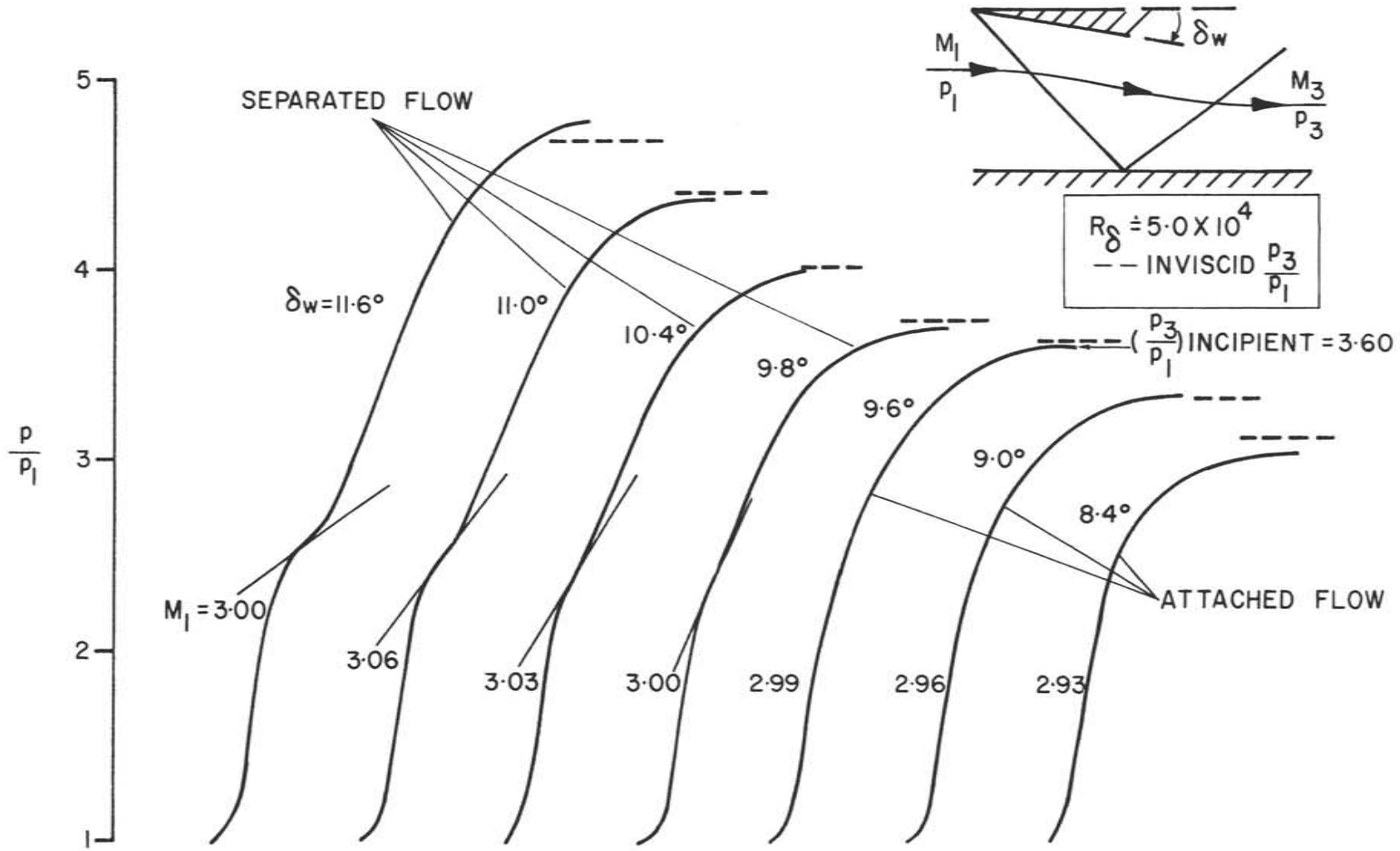

FIG. 8: INCIPIENT SEPARATION FROM WALL PRESSURES FOR AN INCIDENT SHOCK MODEL, REFERENCE 51

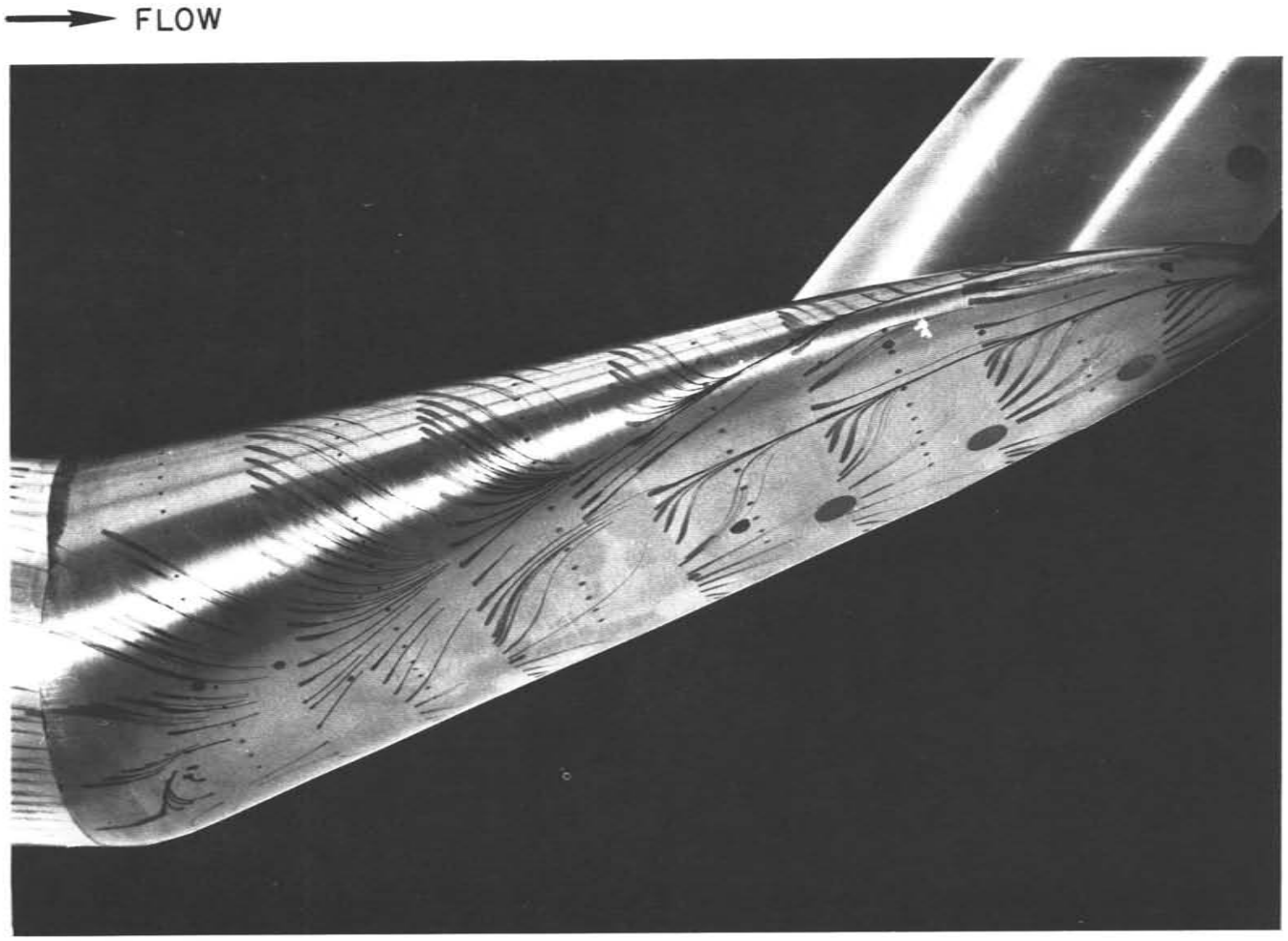

$M_\infty \doteq 0.72$; $q \doteq 8$ psi; $R_{\#} \doteq 10^7$ per foot; AFTERBODY LENGTH = 1.5 ft;
ANGLE OF UPSWEEP OF AFTERBODY $\mathcal{L}$ = 20° ; TURBULENT BOUNDARY LAYER

FIG. 9: LIMITING STREAMLINES ON UPSWEPT FUSELAGE

UNDISTURBED TURBULENT B/L THICKNESS $\begin{cases} \delta \cong 0{\cdot}2\,\text{in};\ R_\delta = 1{\cdot}5 \times 10^5 \text{ AT MACH 2} \\ \delta \cong 0{\cdot}18\,\text{in};\ R_\delta = 2{\cdot}5 \times 10^5 \text{ AT MACH 4} \end{cases}$

β° IS MEASURED WITH RESPECT TO DEFLECTION AT B/L EDGE

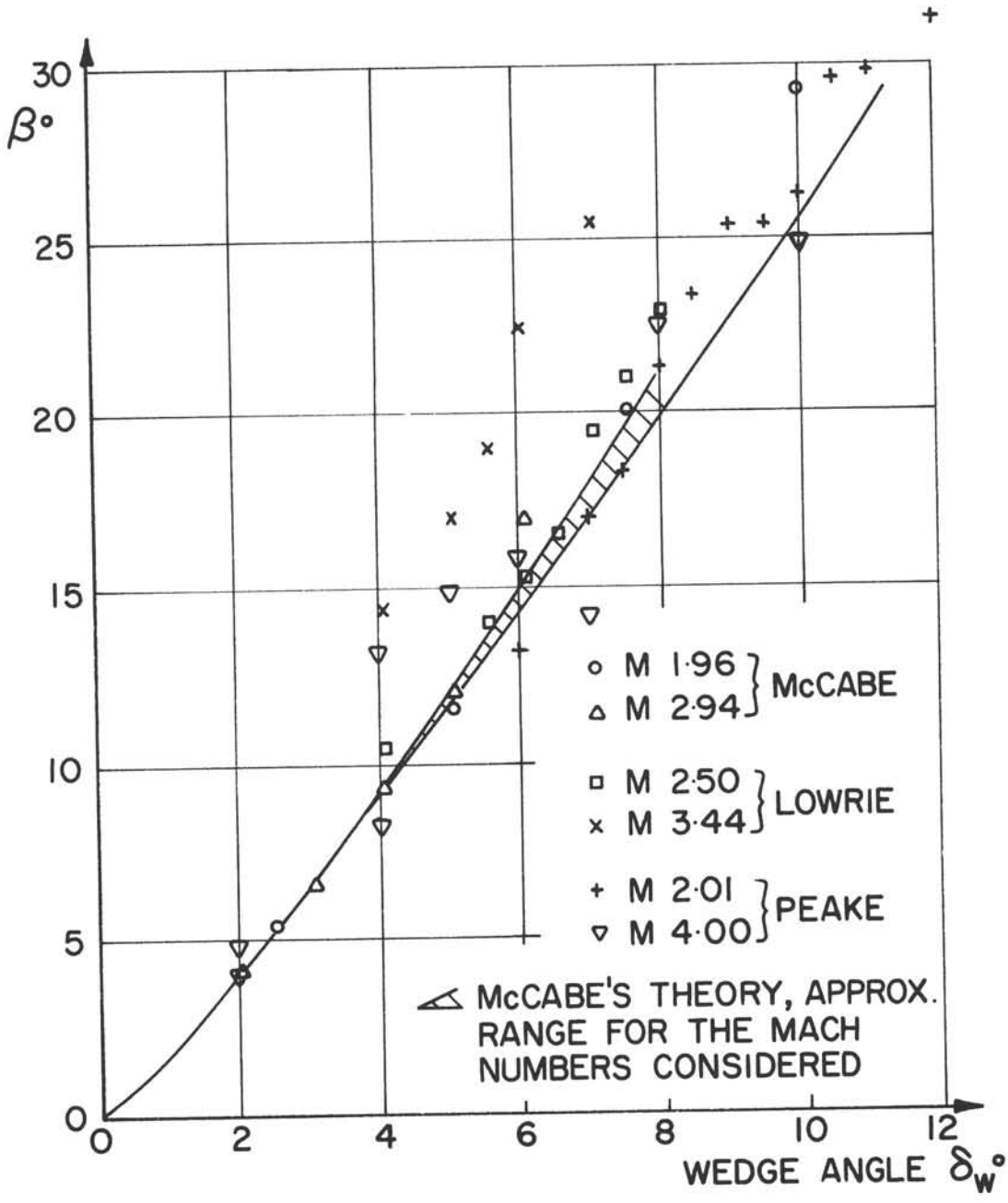

FIG. 10: COMPARISON OF MEASURED "WALL STREAMLINE" DEFLECTION (MAX) AND McCABE'S THEORY

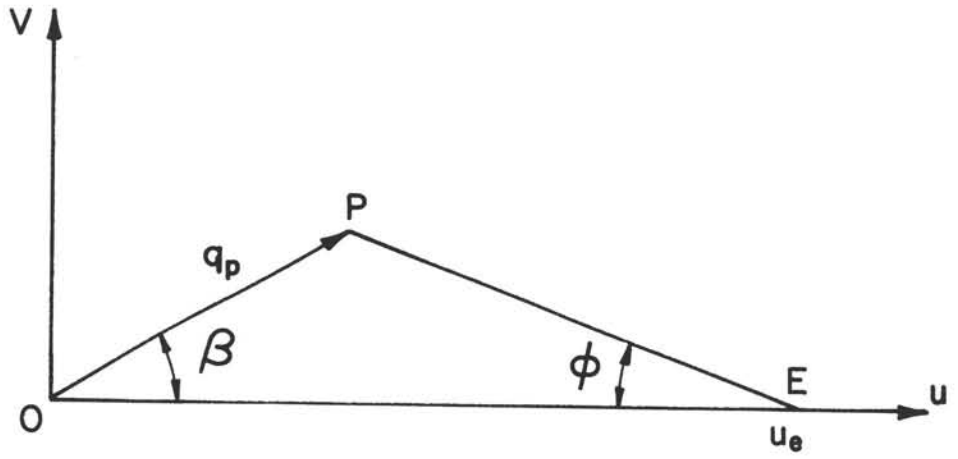

FIG. 11(a): JOHNSTON'S TRIANGULAR MODEL FOR CROSSFLOW

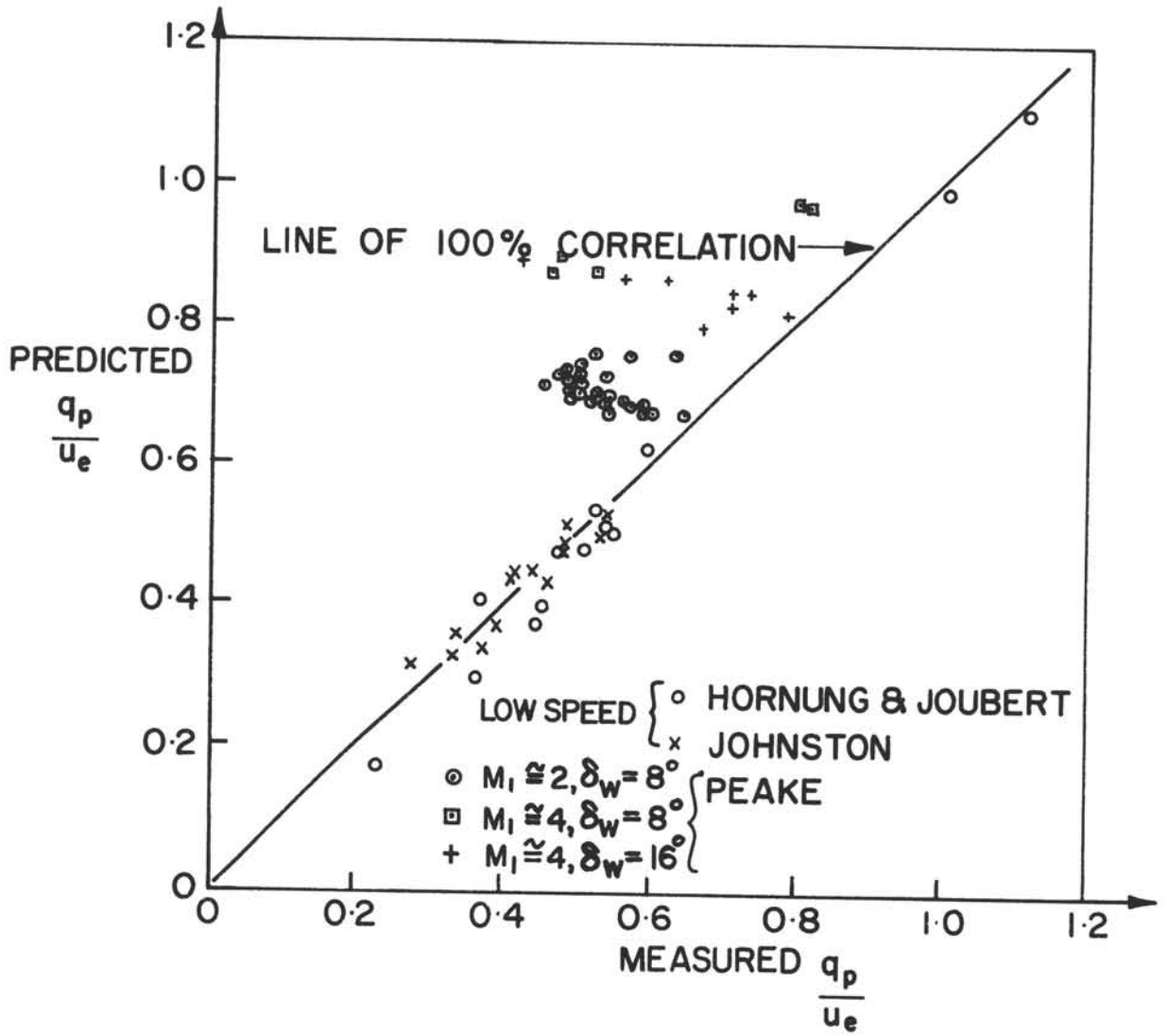

FIG. 11(b): EXPERIMENTAL TEST OF LOWRIE'S JUNCTION POINT CRITERION

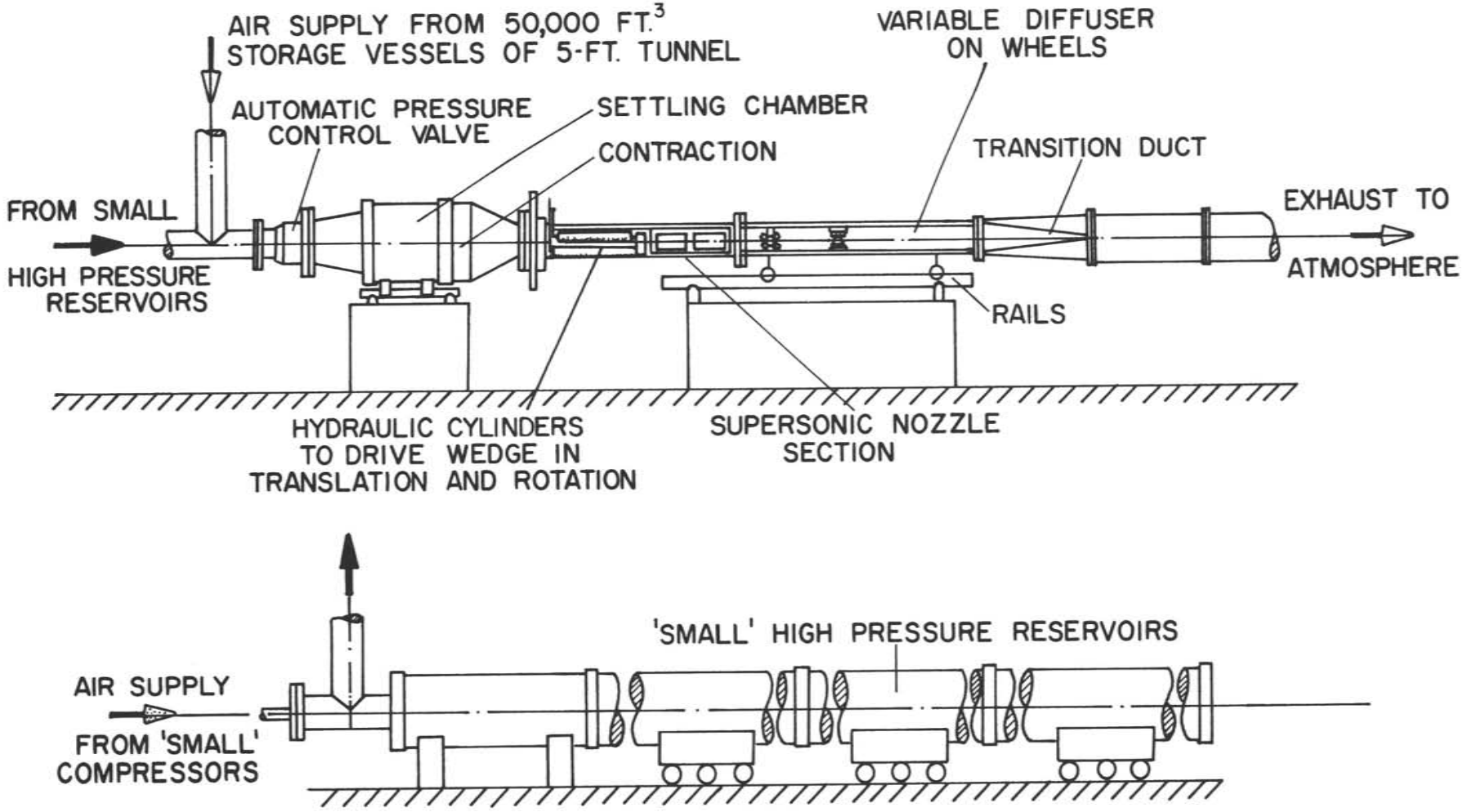

FIG. 12: SCHEMATIC ARRANGEMENT OF 5 X 5-IN. BLOWDOWN WIND TUNNEL

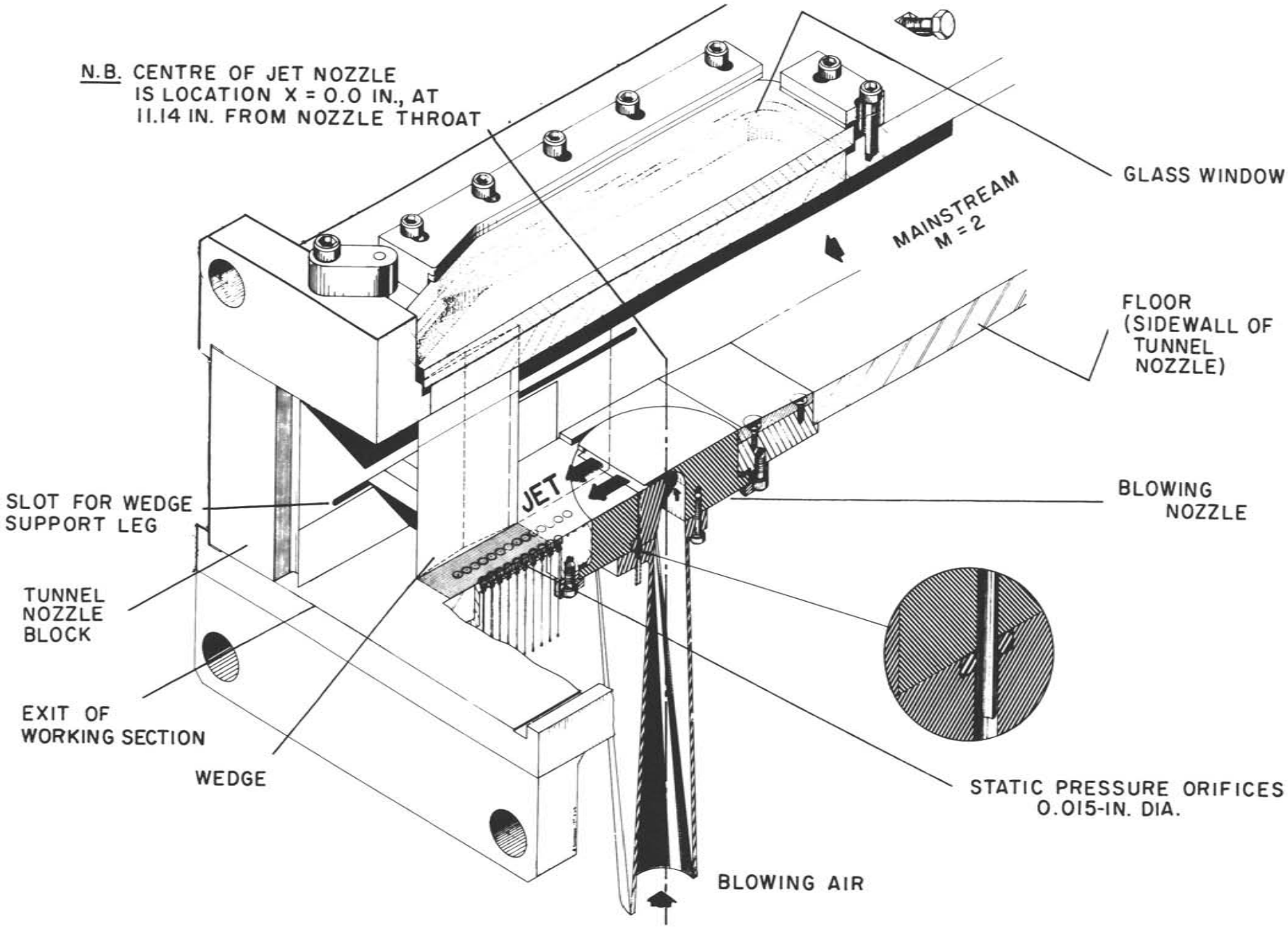

FIG. 13: TYPICAL ASSEMBLY OF WORKING SECTION OF 5 X 5-IN. WIND TUNNEL FOR BLC

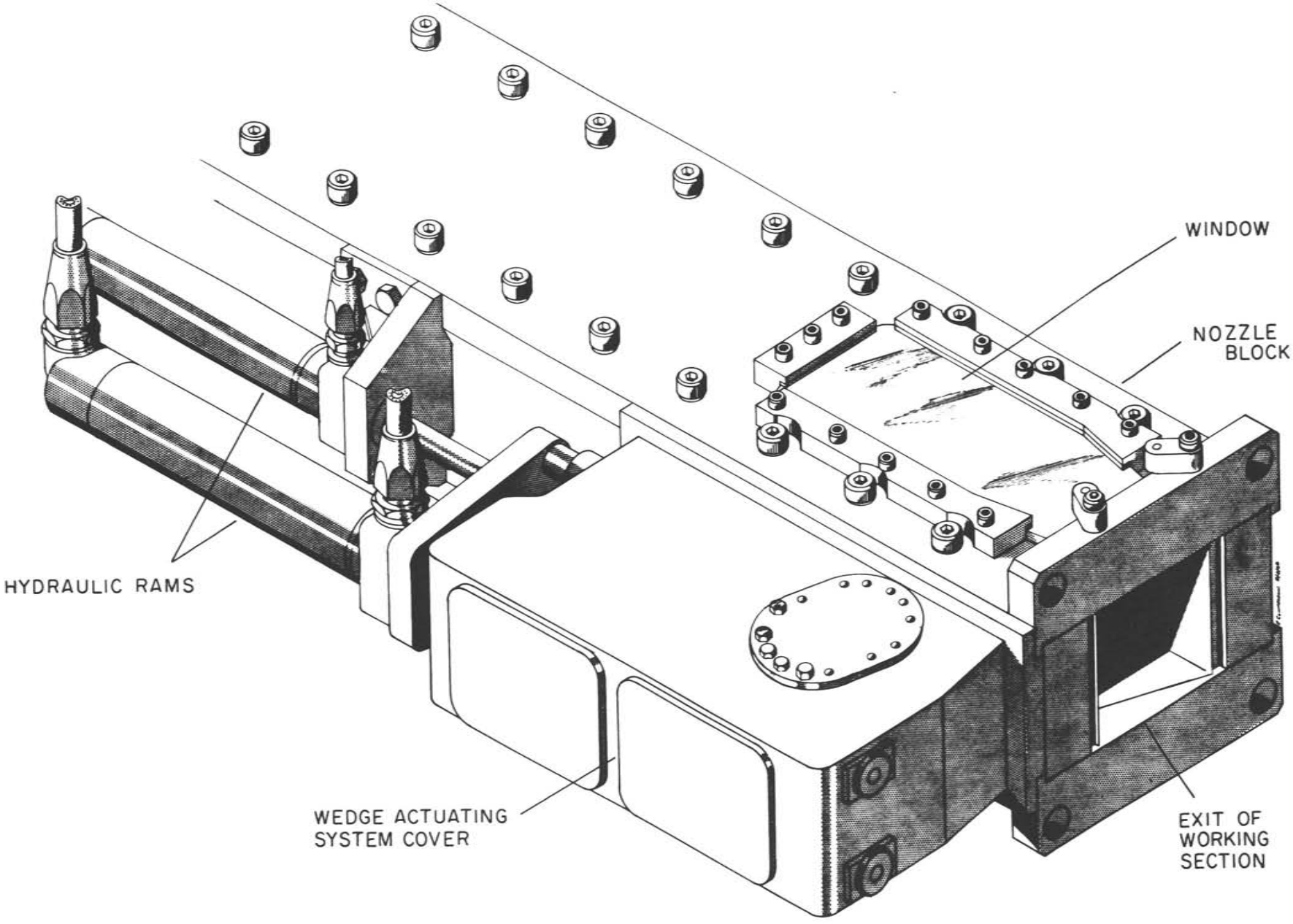

FIG. 14: HYDRAULIC RAMS TO ACTUATE WEDGE MOVEMENT

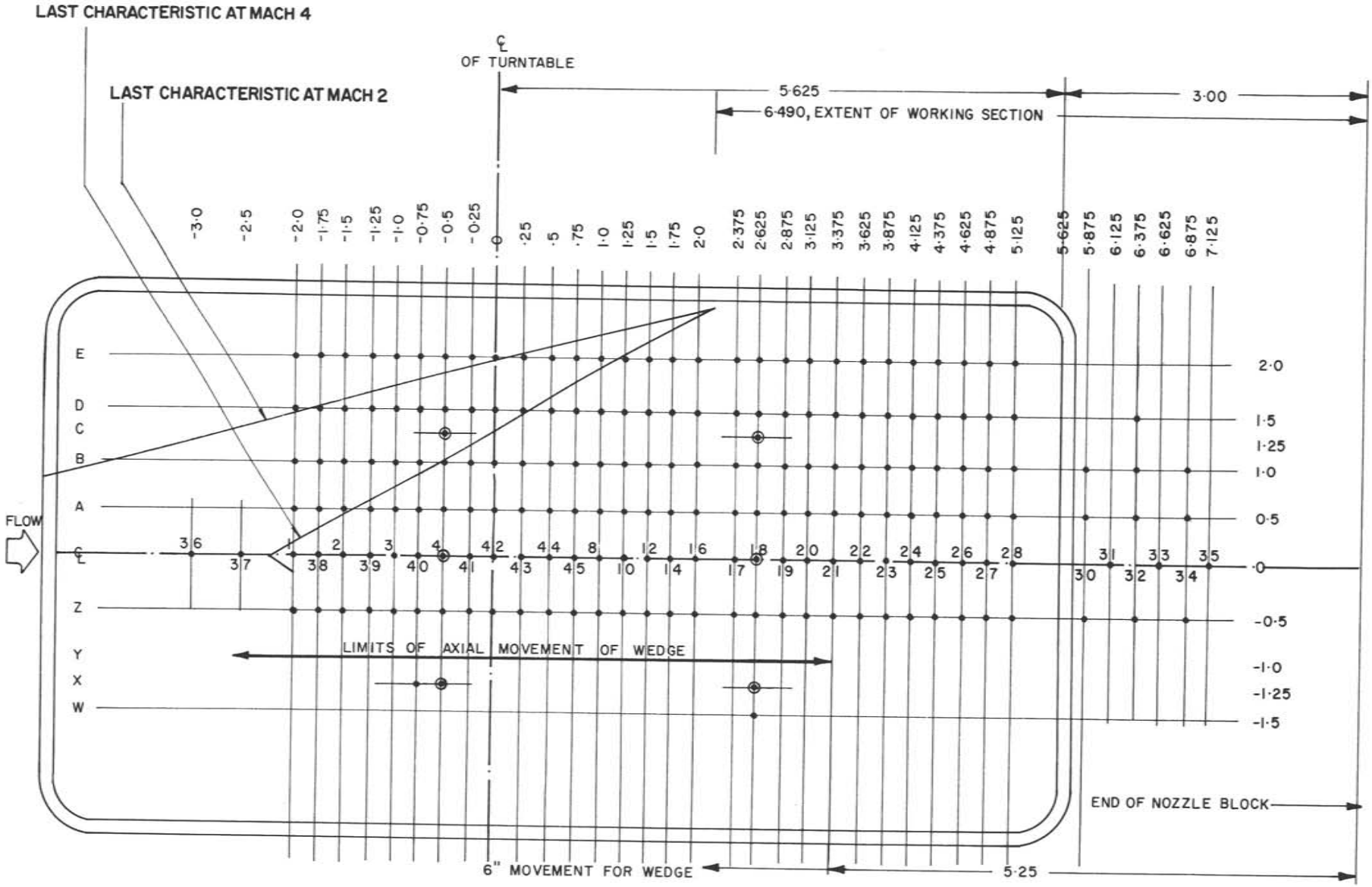

NOTES:

(1) • ARE STATIC PRESSURE ORIFICES, 0·015-IN. DIA.
(2) NO. 1 IS REFERENCE STATIC ORIFICE
(3) 4,4C,4X, AND 18,18C,18X ARE PITOT TRAVERSE LOCATIONS, ◉
(4) ALL DIMENSIONS ARE IN INCHES
(5) APEX OF VORTEX GENERATOR ON TUNNEL FLOOR IN MACH 4 TESTS IS AT X = -9·3 In, SEMI-APEX ANGLE = 30°
(6) SIDEWALL VORTEX GENERATOR (SINGLE) SITUATED WITH L.E. AT X = 0·0, OR -6·25 In, INCLINED AT 20° TO TUNNEL FLOOR, FOR SOME MACH 2 TESTS

FIG. 15: LAYOUT OF STATIC PRESSURE ORIFICES IN PLAIN TUNNEL FLOOR

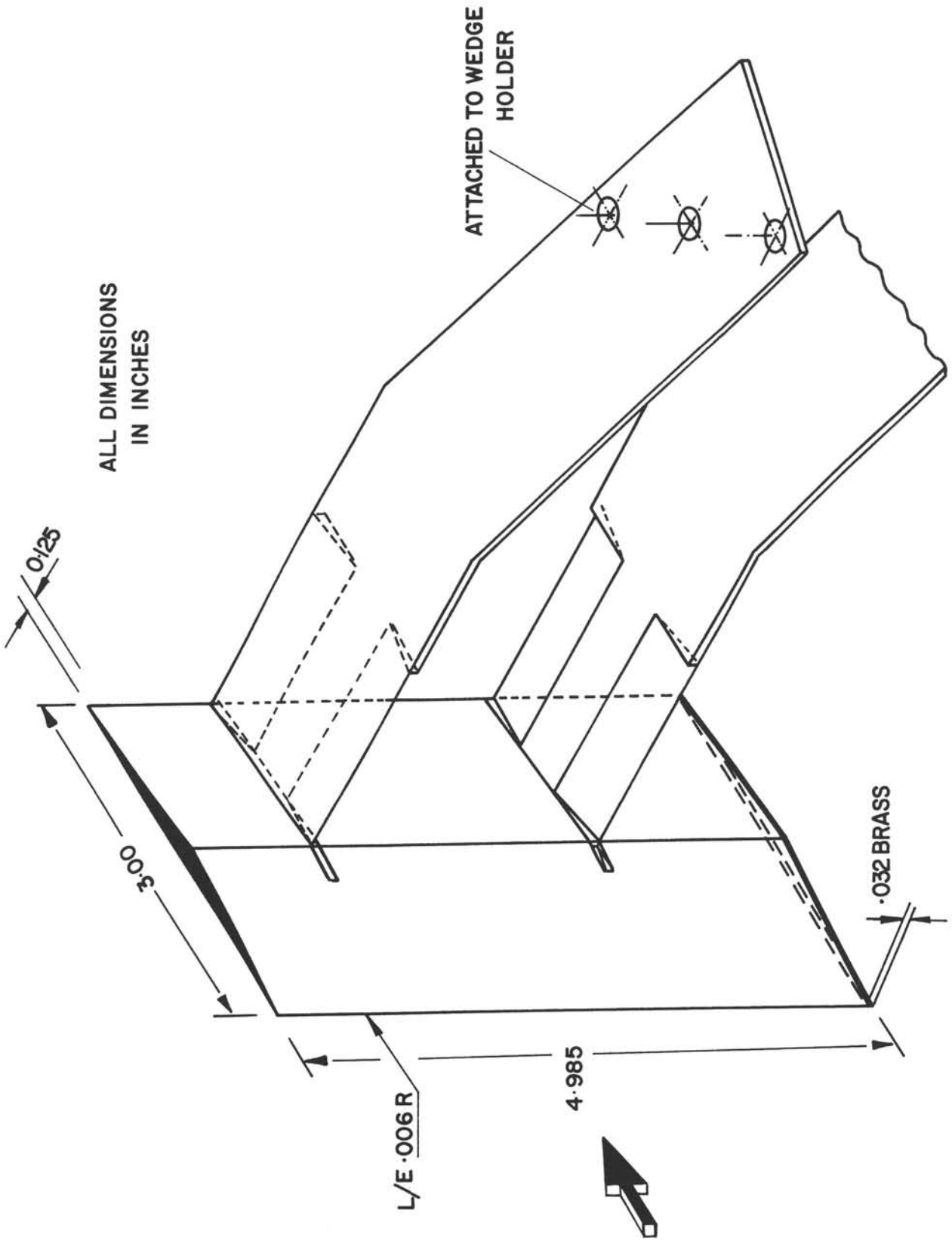

FIG. 16: ISOMETRIC VIEW OF WEDGE ASSEMBLY

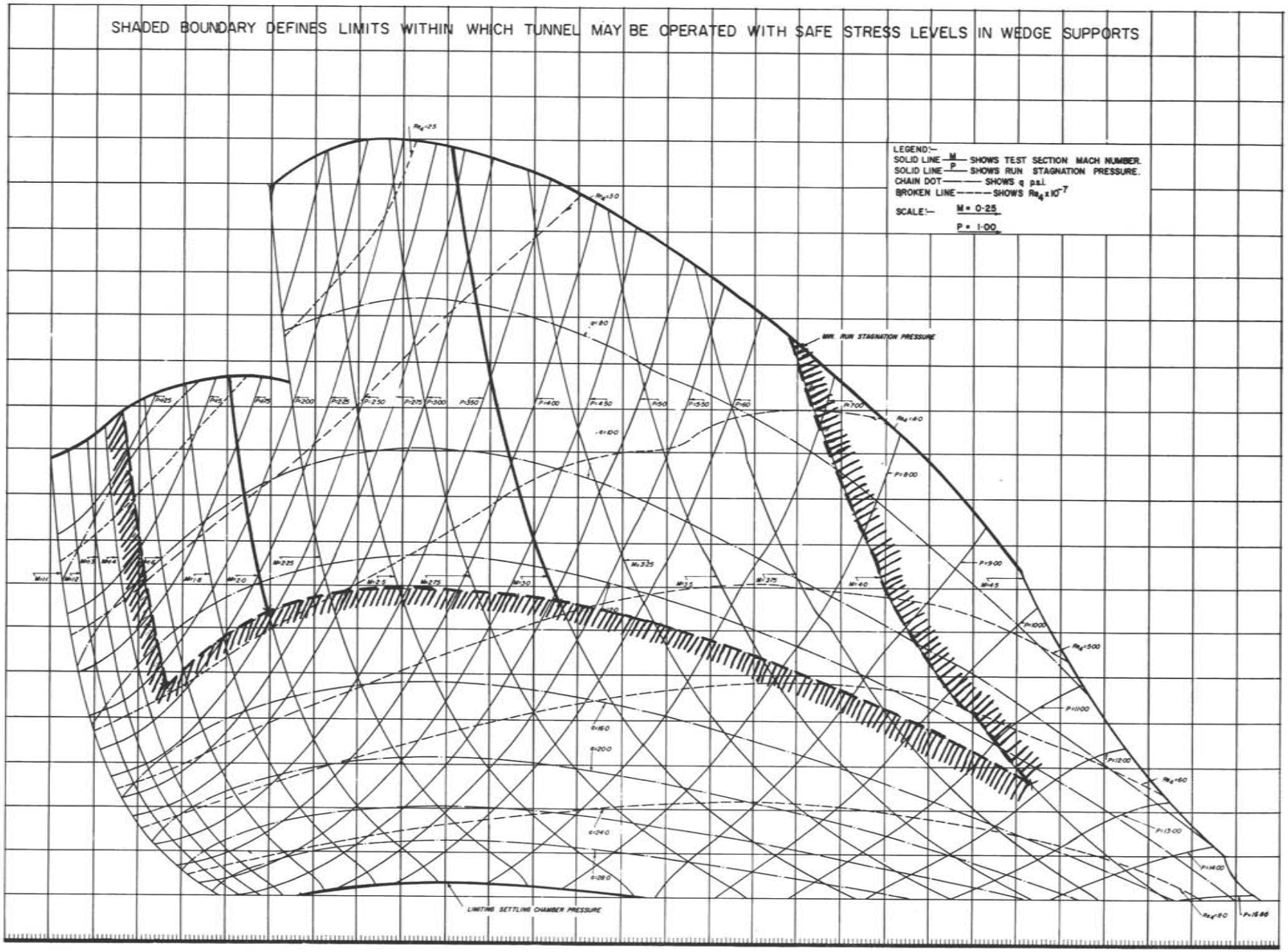

FIG. 17: TUNNEL PERFORMANCE CHART

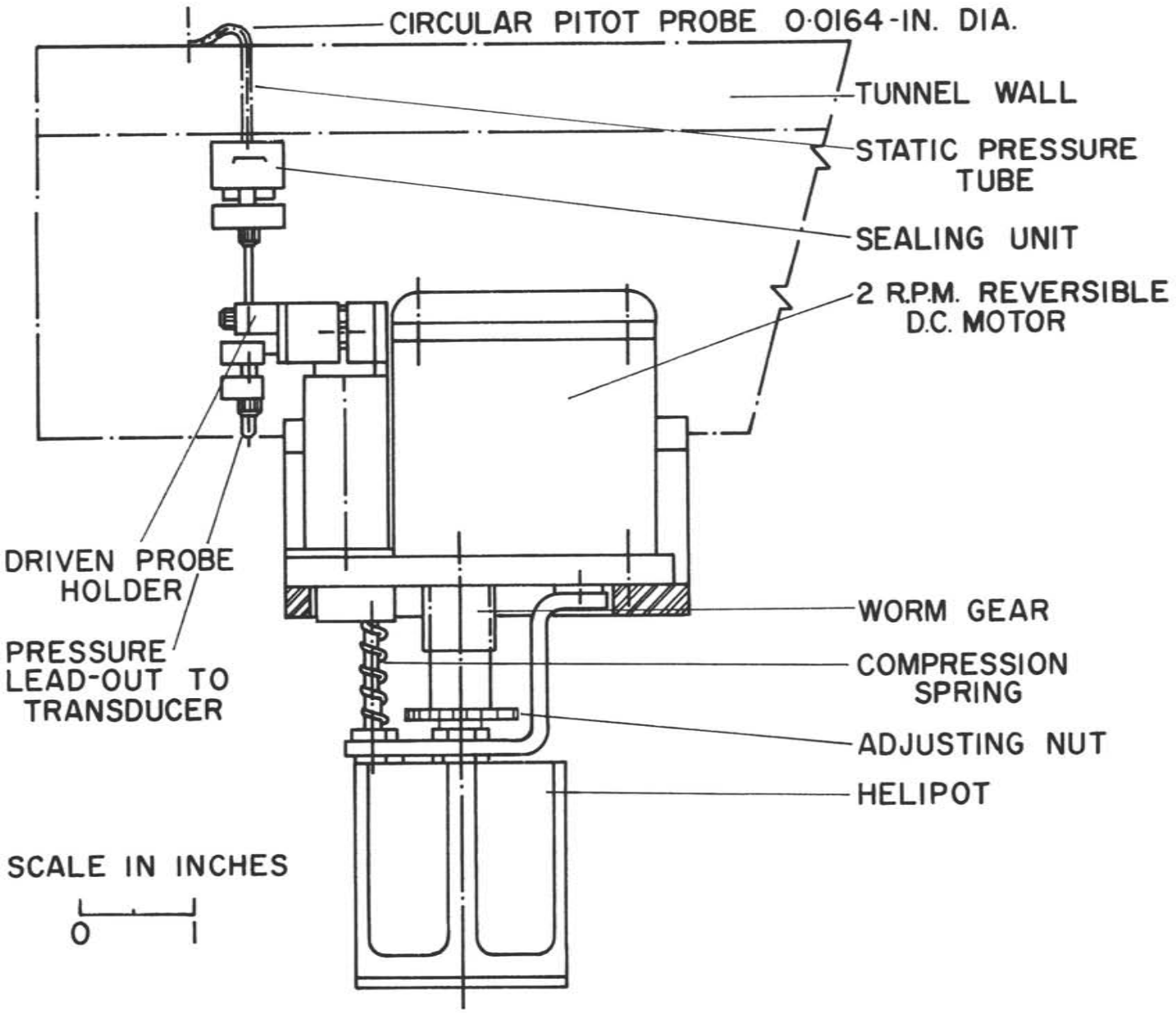

FIG. 18(a): PITOT PROBE UNIT FOR TRAVERSE OF 2D BOUNDARY LAYER, SIDE VIEW

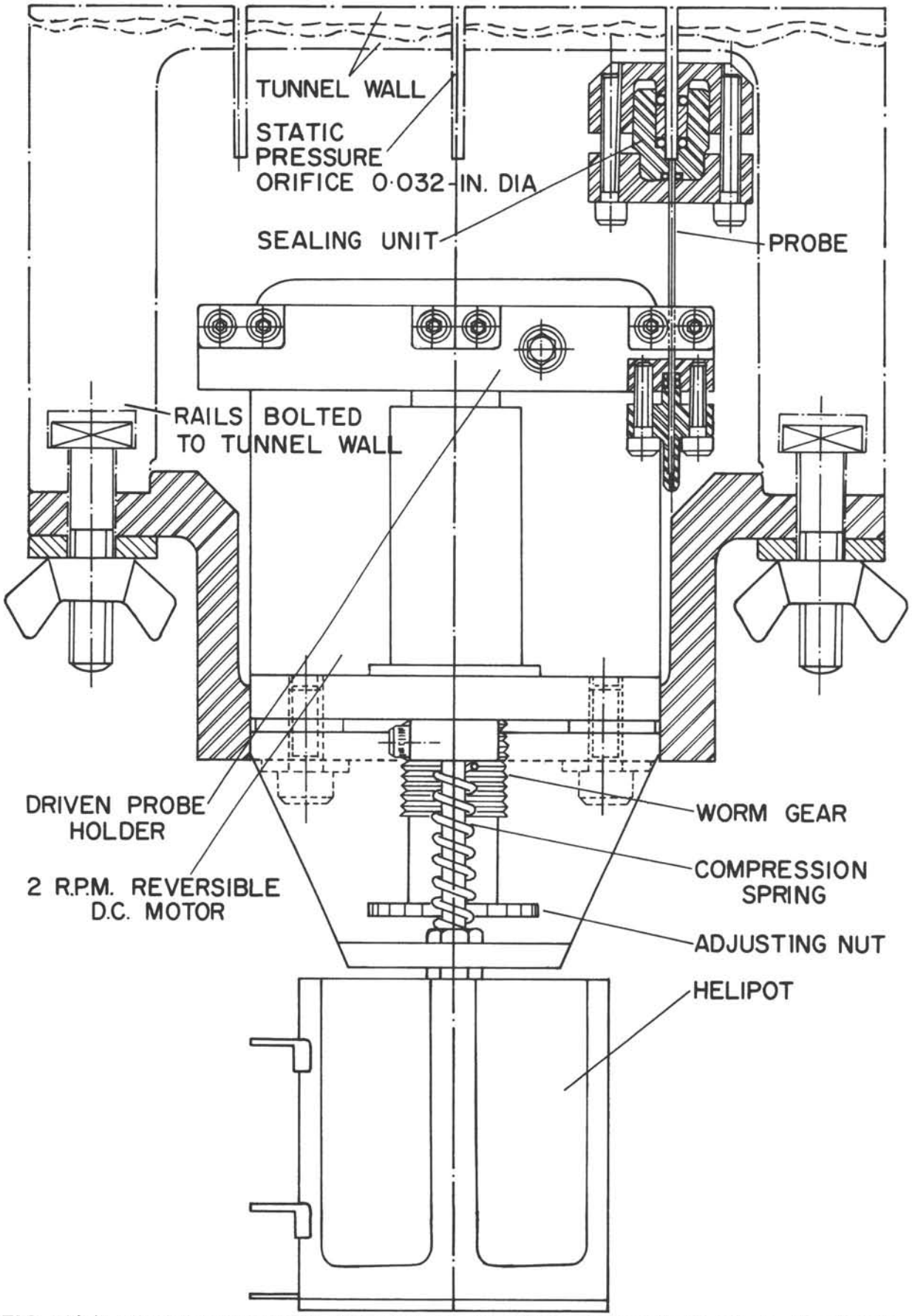

FIG. 18(b): PITOT PROBE UNIT FOR TRAVERSE OF 2D BOUNDARY LAYER, END VIEW

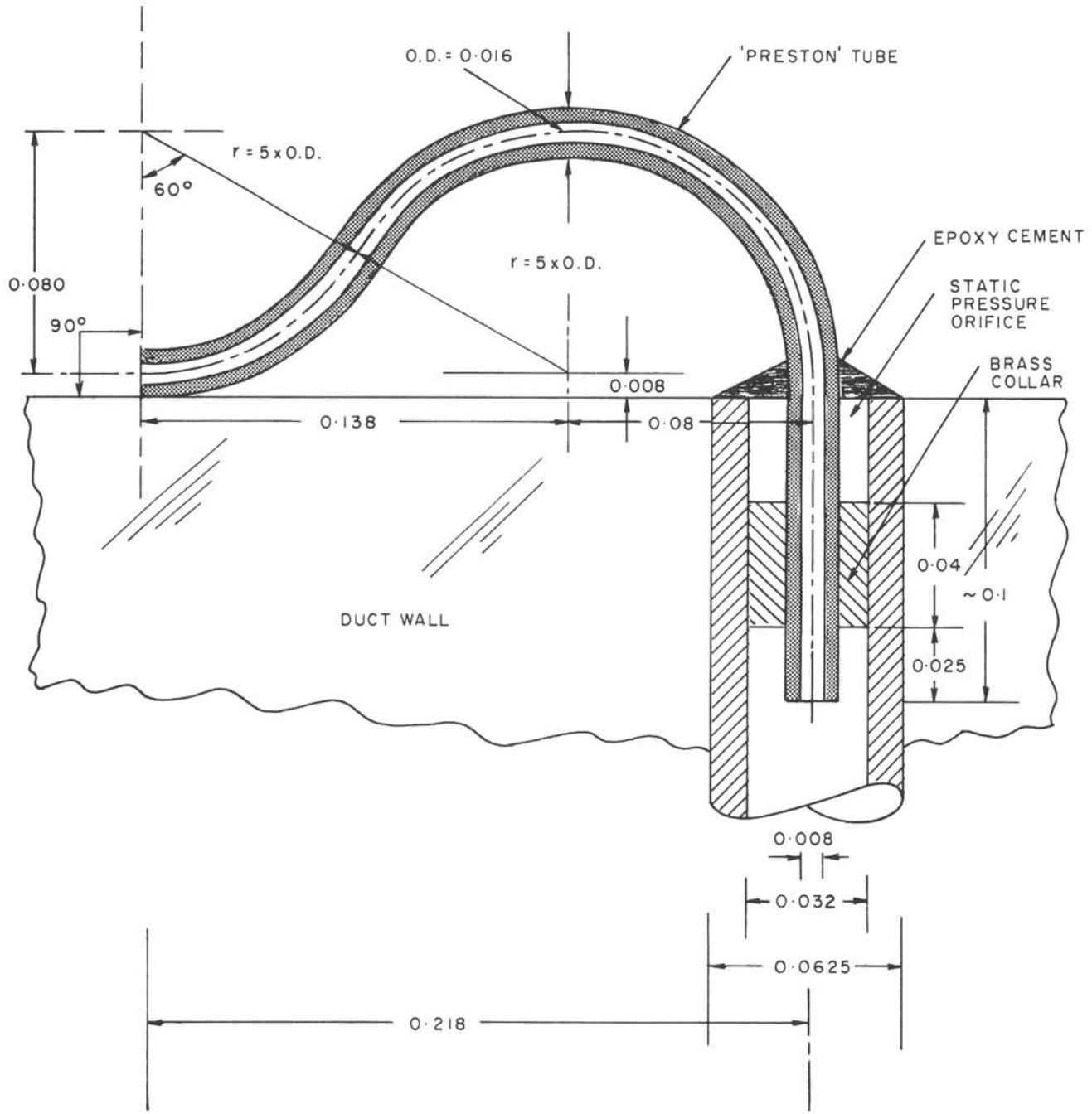

NOTE: ALL DIMENSIONS ARE IN INCHES

FIG. 18(c): PRESTON TUBE

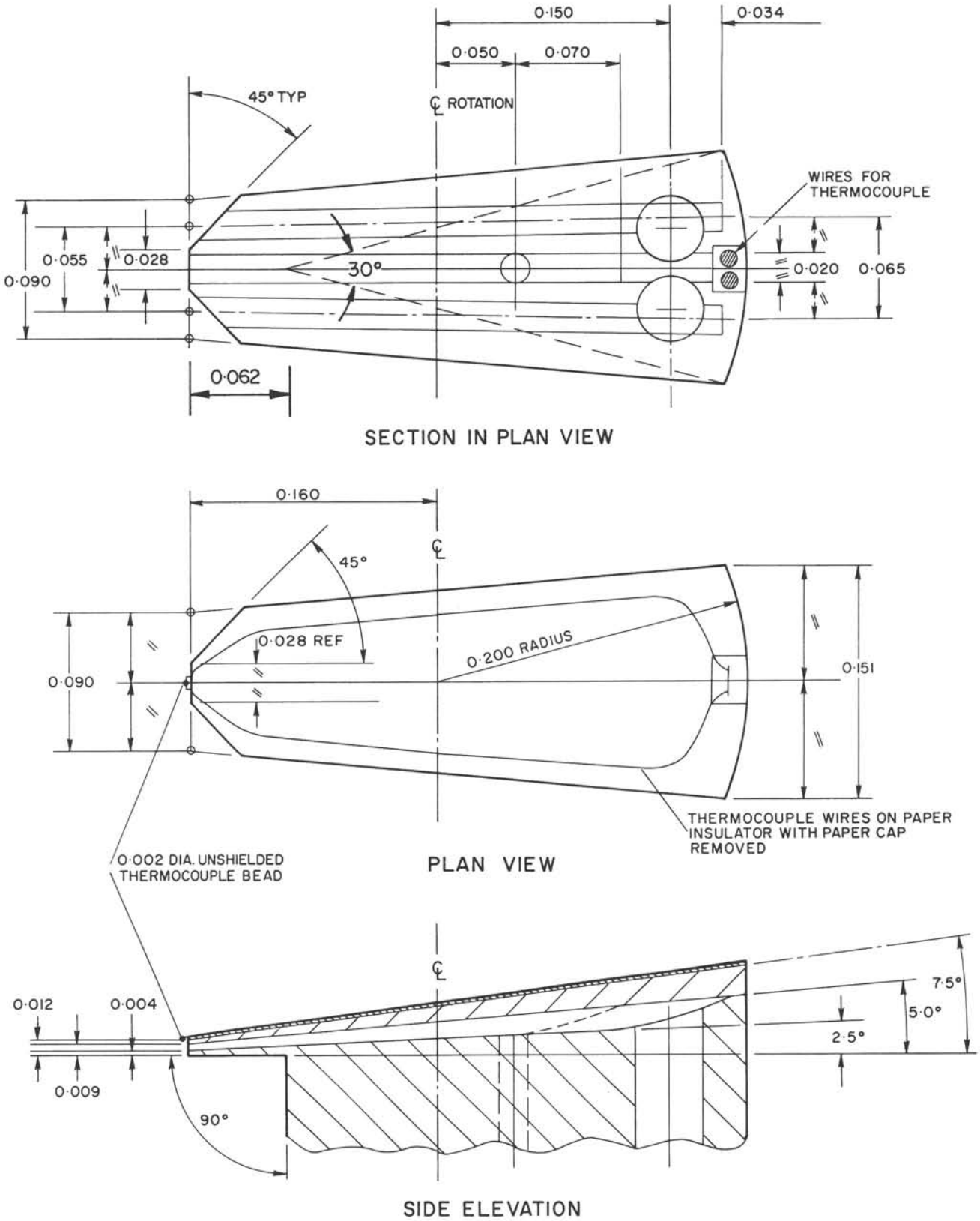

FIG. 19: HEAD OF COBRA PROBE, DESIGN DIMENSIONS

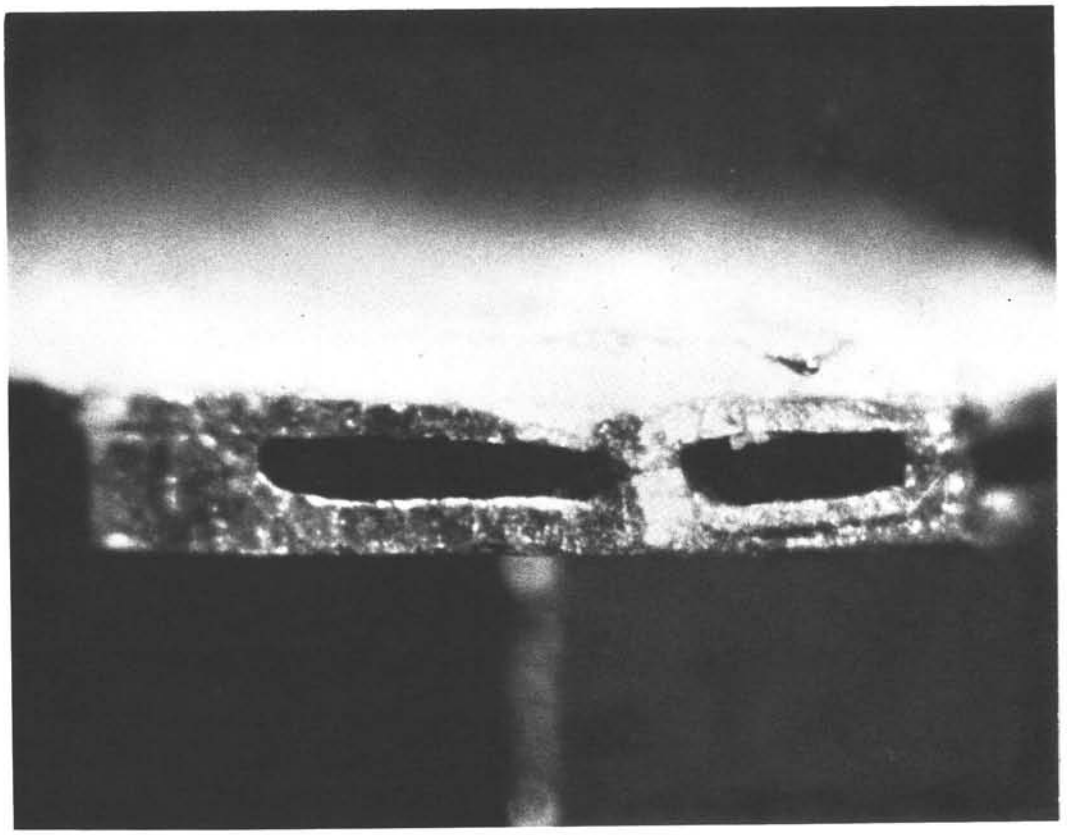

FRONTAL VIEW FROM STARBOARD SIDE OF PROBE SHOWING THERMOCOUPLE BEAD ABOVE CENTRE PITOT ORIFICE

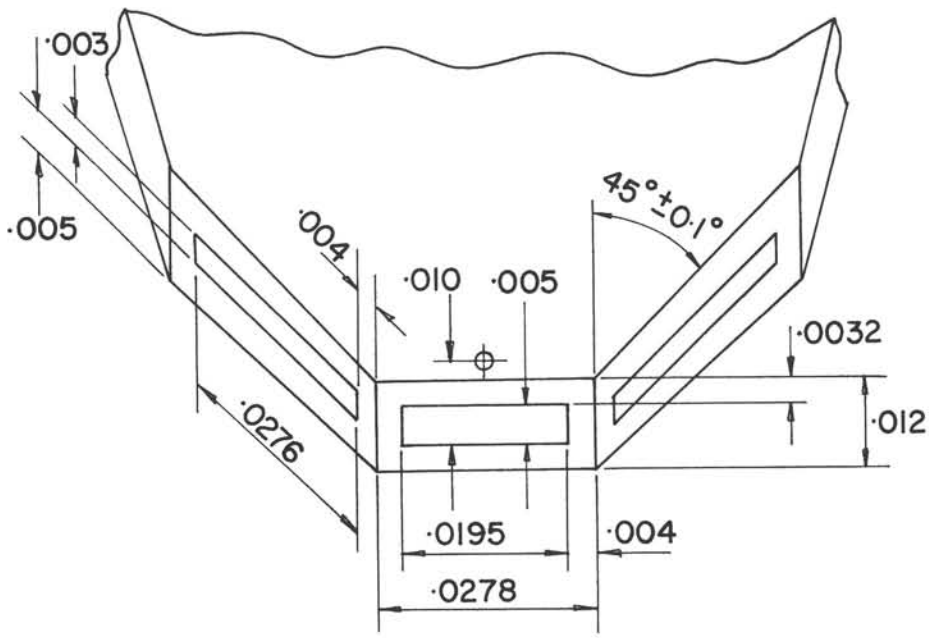

DIMENSIONED FRONTAL VIEW

FIG. 20: MAGNIFIED VIEW OF COBRA PROBE HEAD AS MANUFACTURED

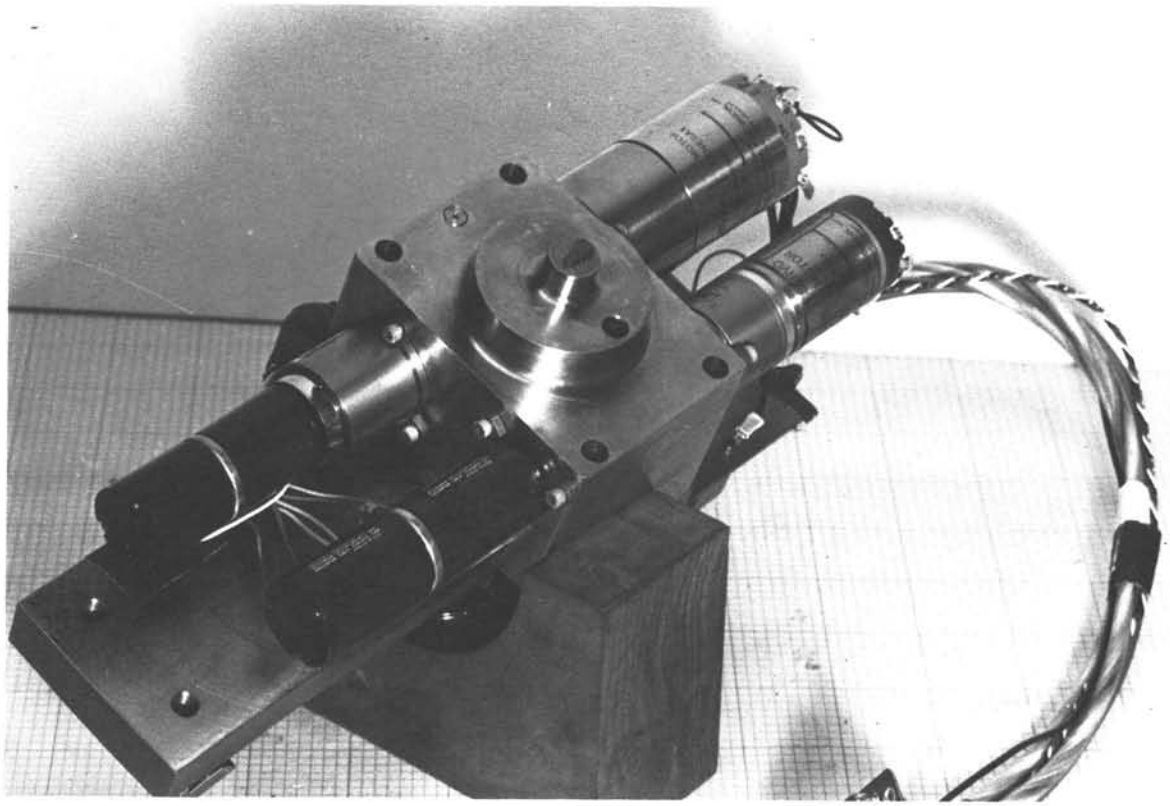

YAW AND TRAVERSING MECHANISM

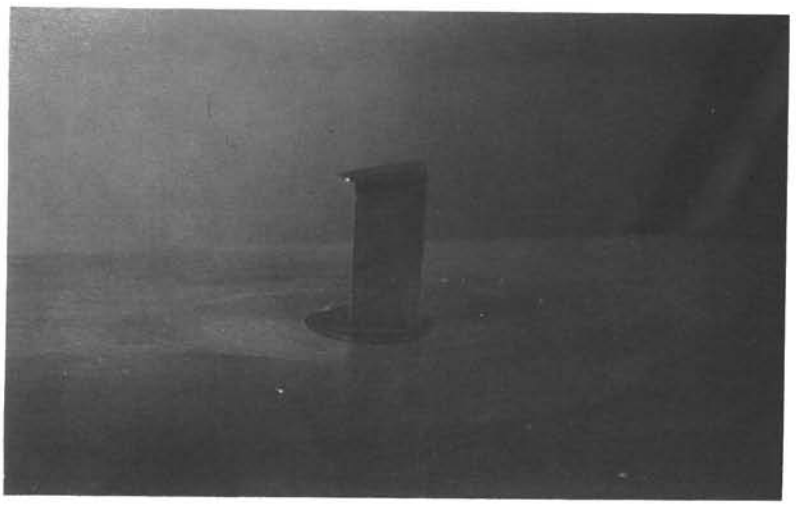

SIDE VIEW OF HEAD AND STEM SUPPORT

FIG. 21(a): ASSEMBLY OF COBRA YAW PROBE, PHOTOGRAPHIC VIEWS

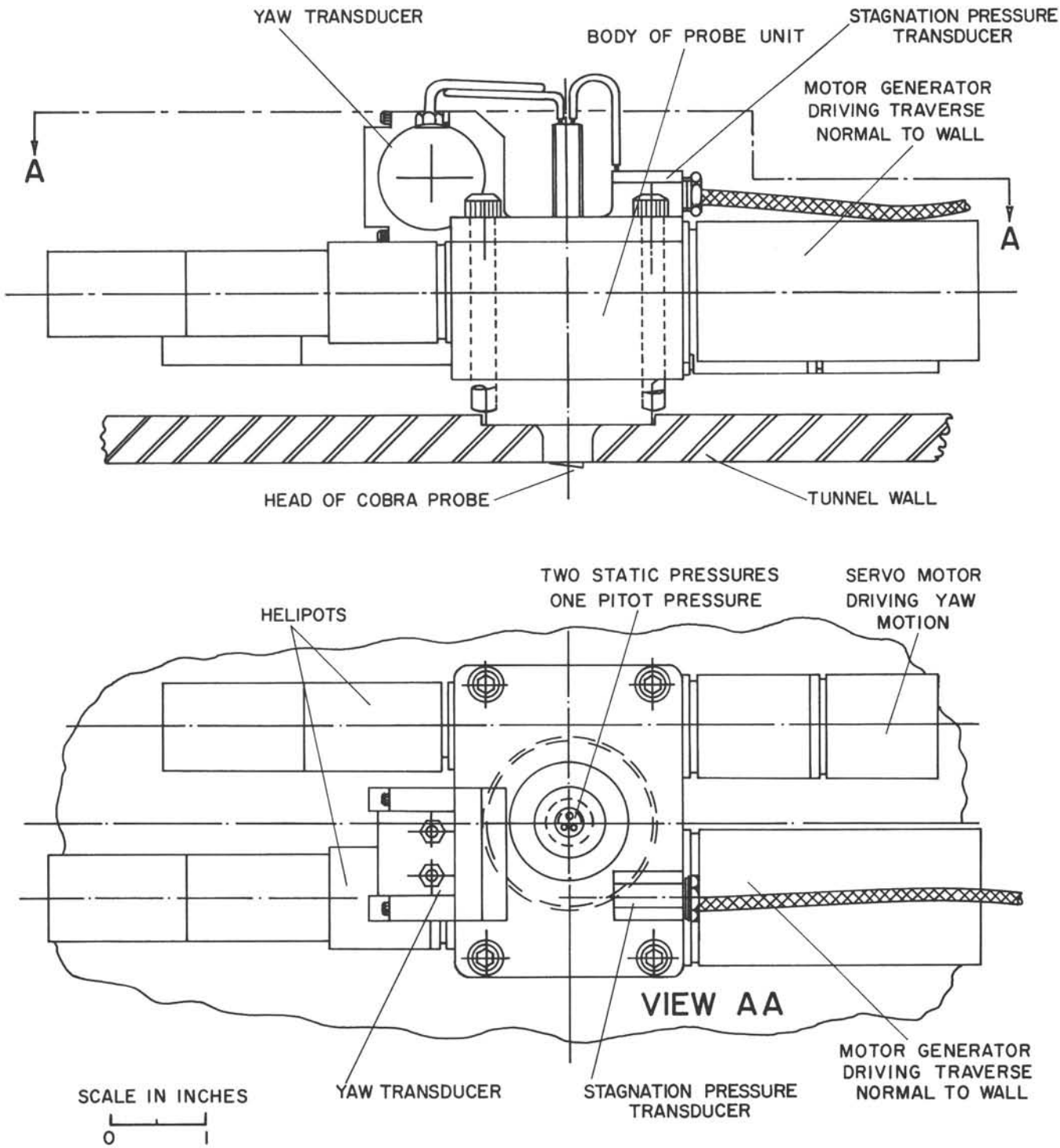

FIG. 21(b): ASSEMBLY OF COBRA YAW PROBE, ELEVATION VIEWS

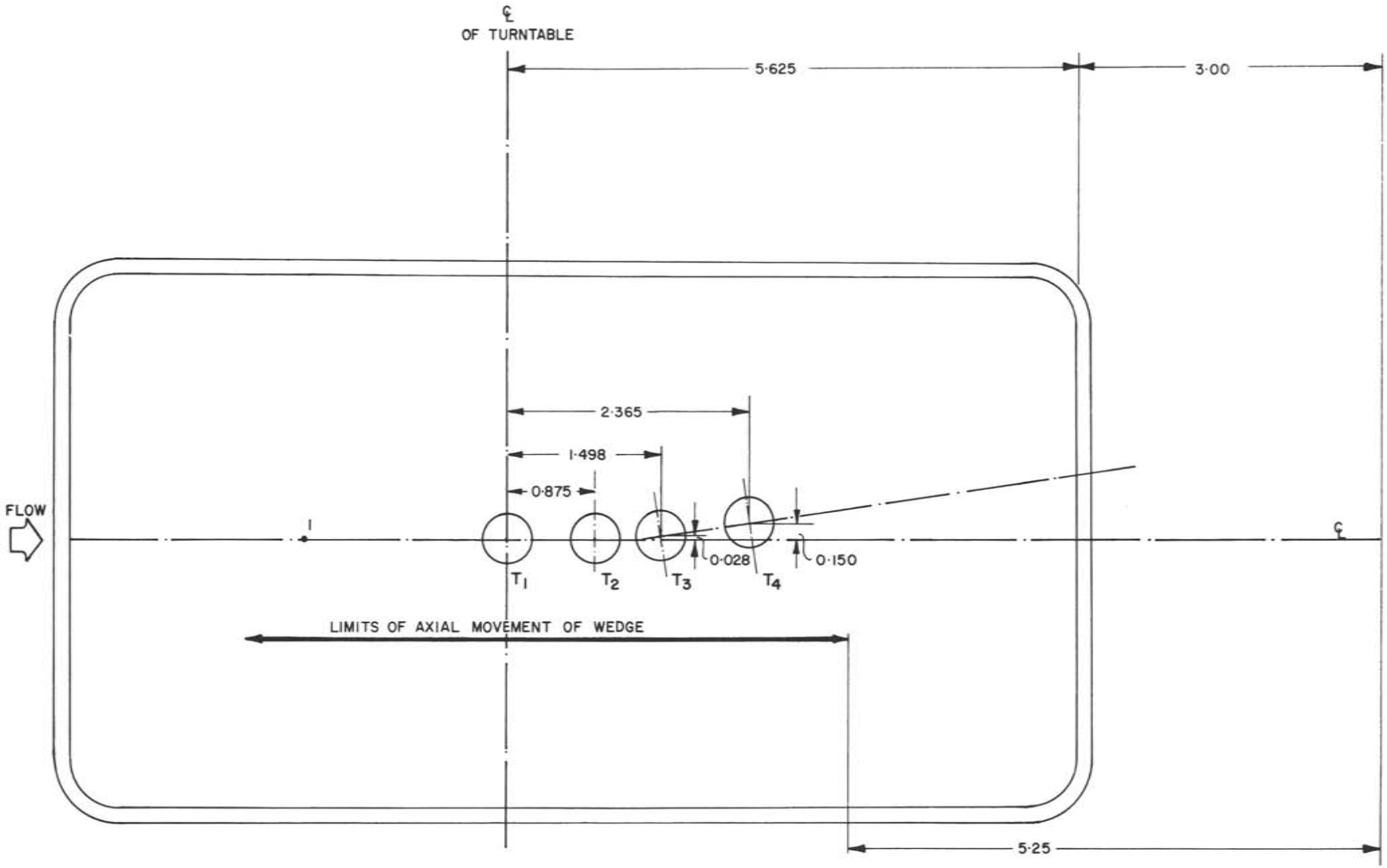

NOTES:

(1) • NO.1 IS REFERENCE STATIC PRESSURE ORIFICE
(2) ⊕ IS COBRA PROBE TRAVERSE STATION
(3) PITOT ORIFICE OF COBRA PROBE IS SITUATED 0·160 IN. AHEAD OF CENTRE OF CIRCULAR INSERT

FIG. 22: FLOOR INSERT TO SUPPORT COBRA PROBE

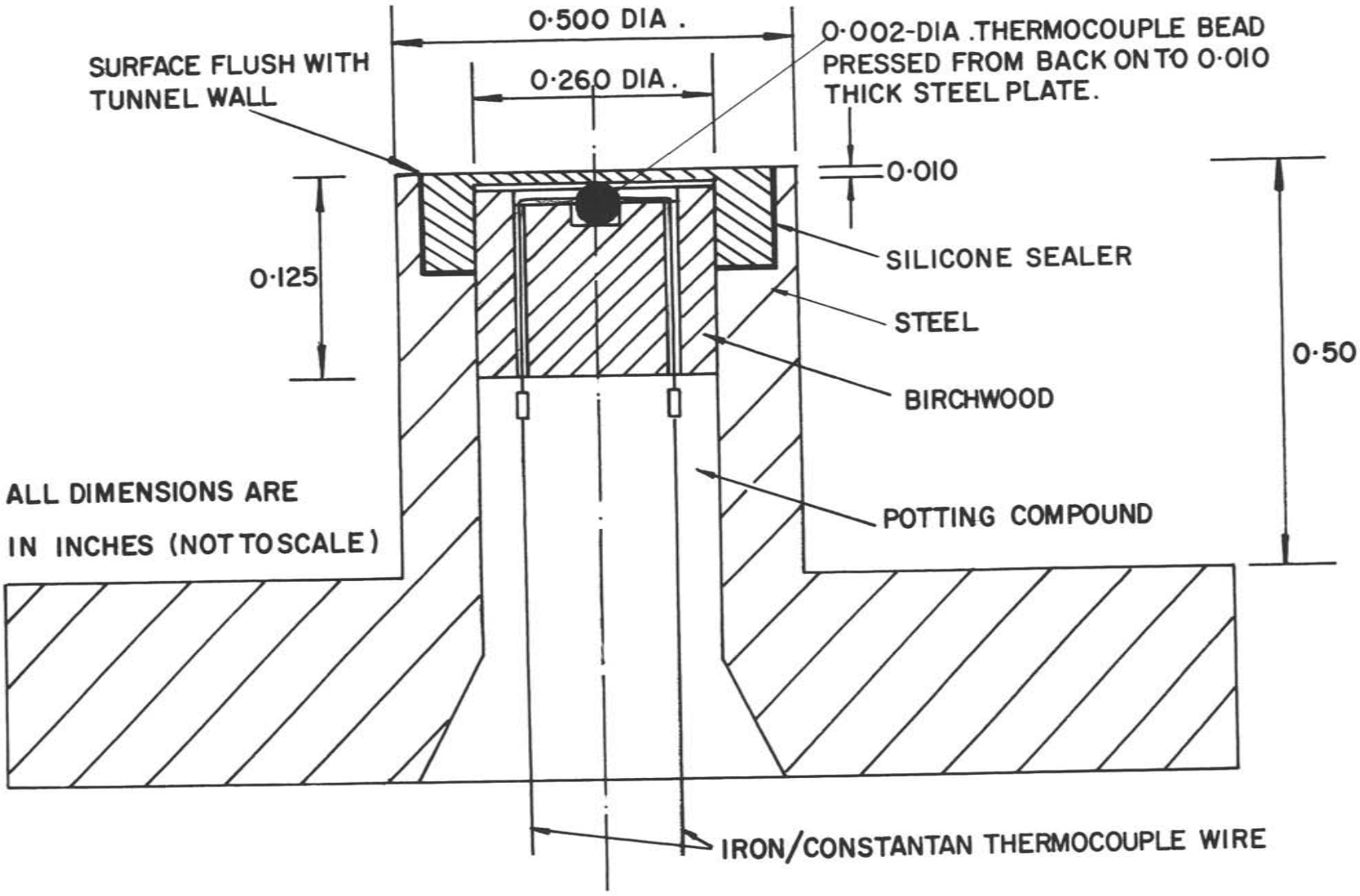

FIG. 23: WALL TEMPERATURE THERMOCOUPLE PLUG

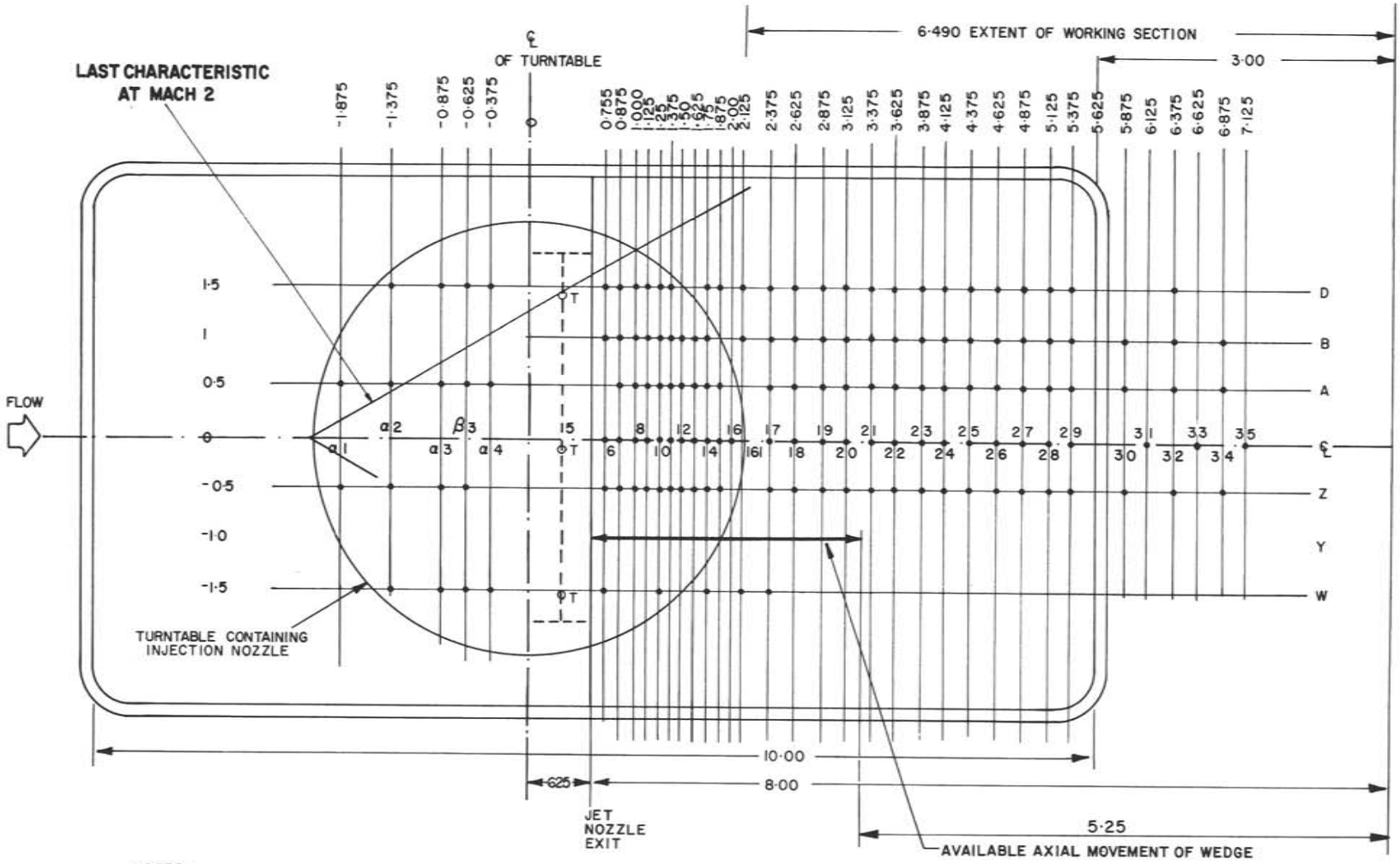

NOTES:

(1) • ARE STATIC PRESSURE ORIFICES, 0·015-IN. DIA.
(2) α IZ IS REFERENCE STATIC ORIFICE
(3) o ARE STATIC PRESSURE ORIFICES AT INJECTION NOZZLE THROAT
(4) ALL DIMENSIONS ARE IN INCHES

LAYOUT OF STATIC PRESSURE ORIFICES ABOUT INJECTION SLOT

FIG. 24: LAYOUT OF STATIC PRESSURE ORIFICES ABOUT INJECTION SLOT

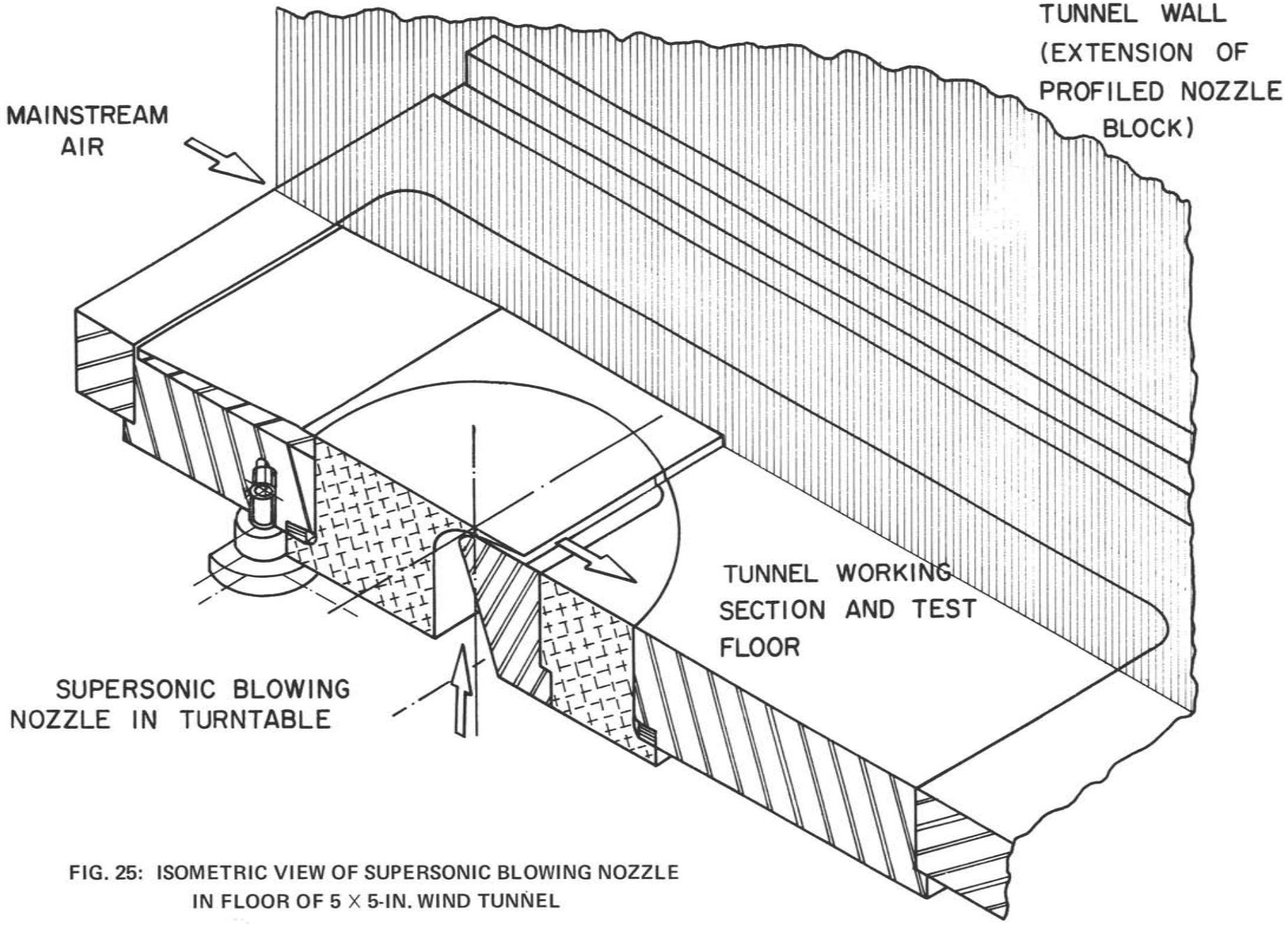

FIG. 25: ISOMETRIC VIEW OF SUPERSONIC BLOWING NOZZLE IN FLOOR OF 5 × 5-IN. WIND TUNNEL

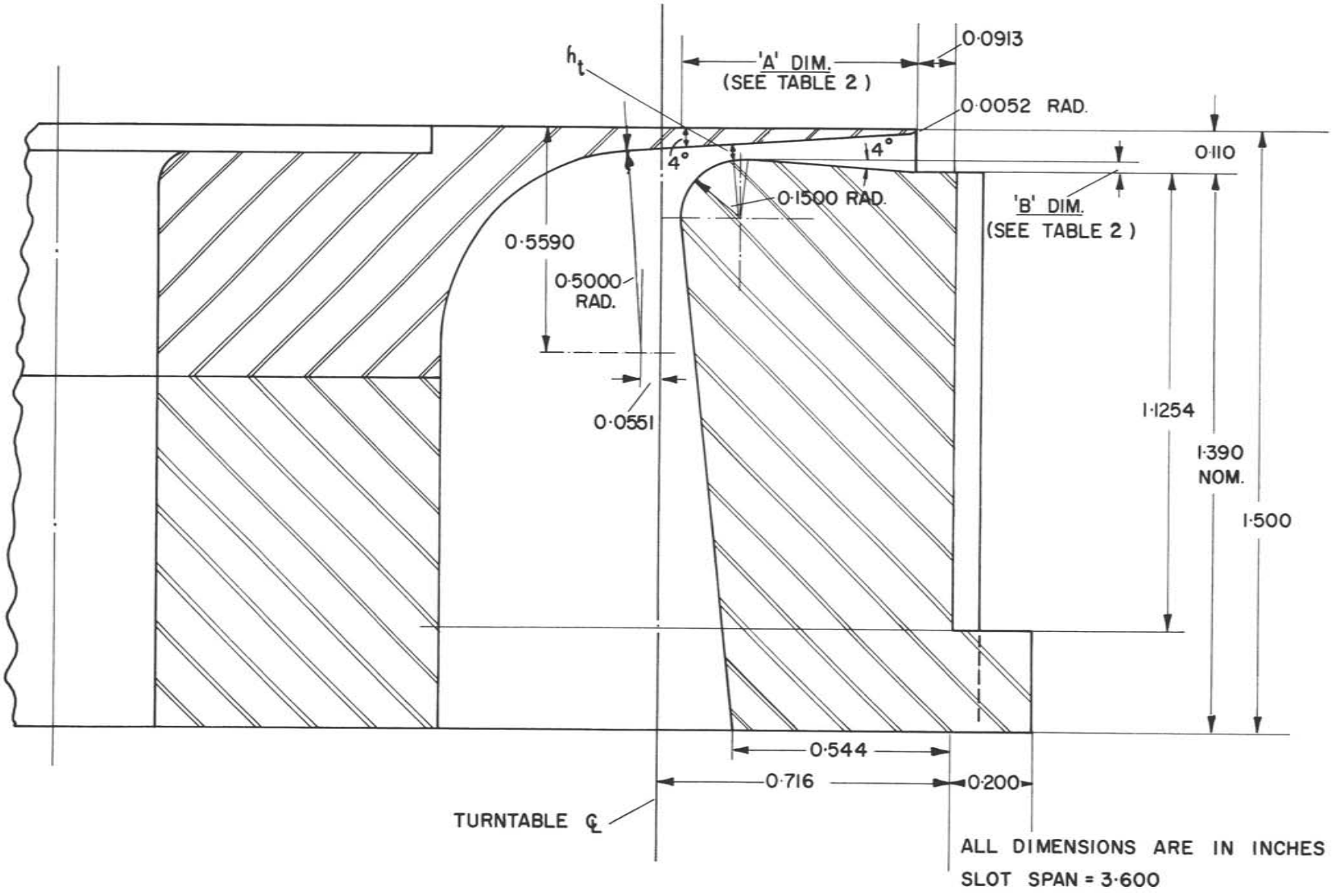

FIG. 26: INJECTION NOZZLE PROFILE

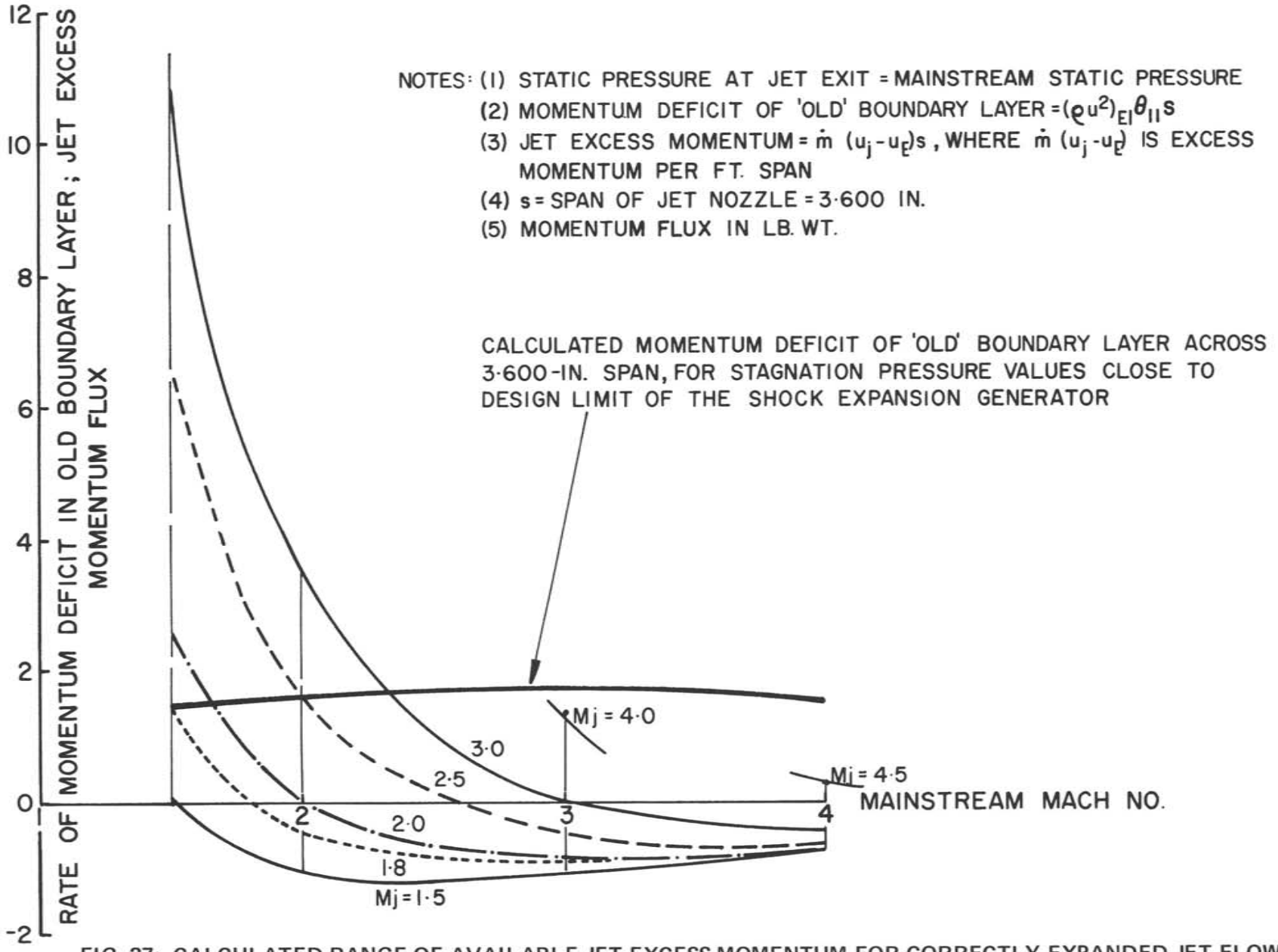

FIG. 27: CALCULATED RANGE OF AVAILABLE JET EXCESS MOMENTUM FOR CORRECTLY EXPANDED JET FLOW

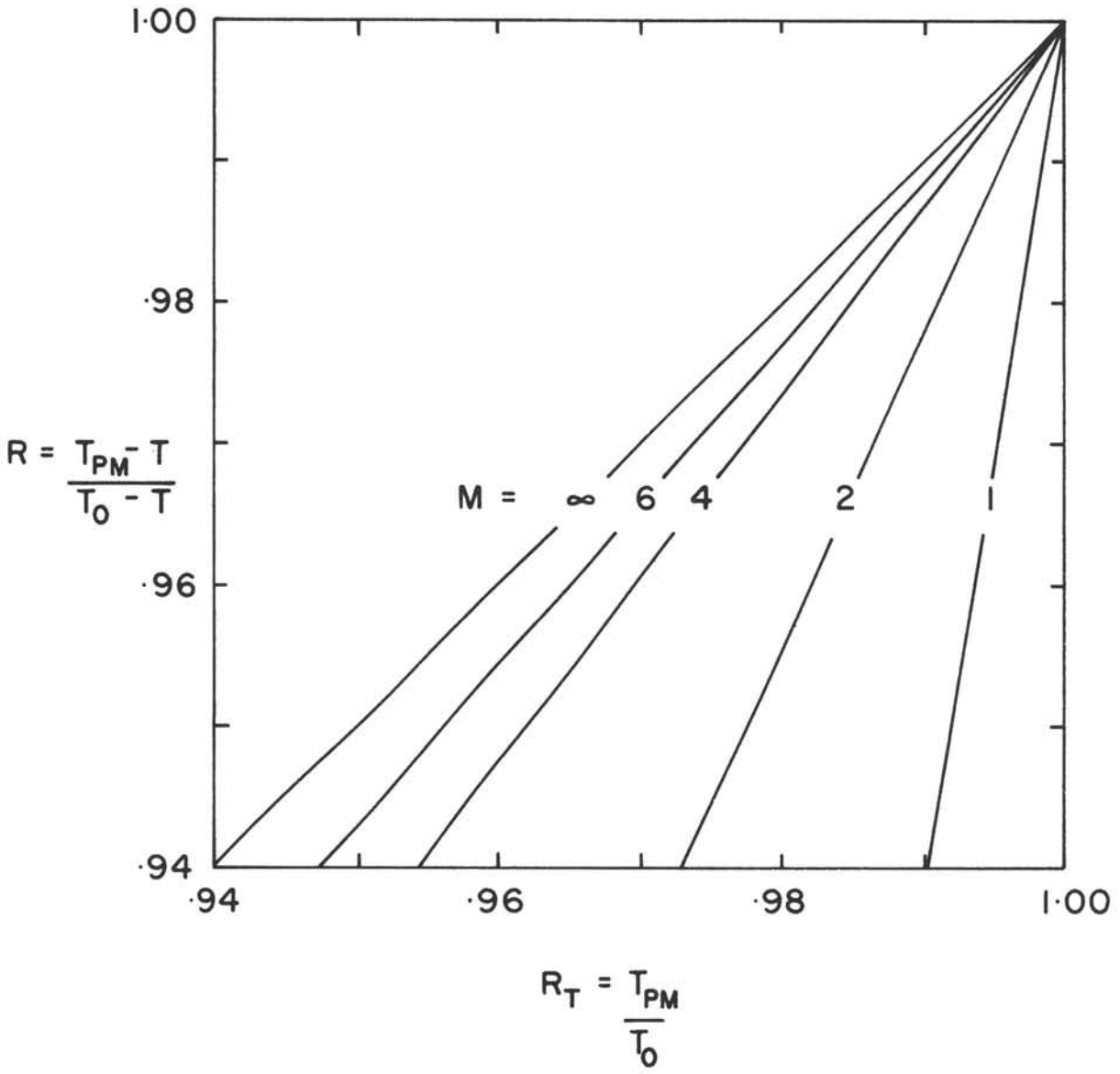

FIG. 28: RECOVERY FACTOR R, AND TEMPERATURE RATIO, R_T, RELATED TO MAINSTREAM MACH NUMBER

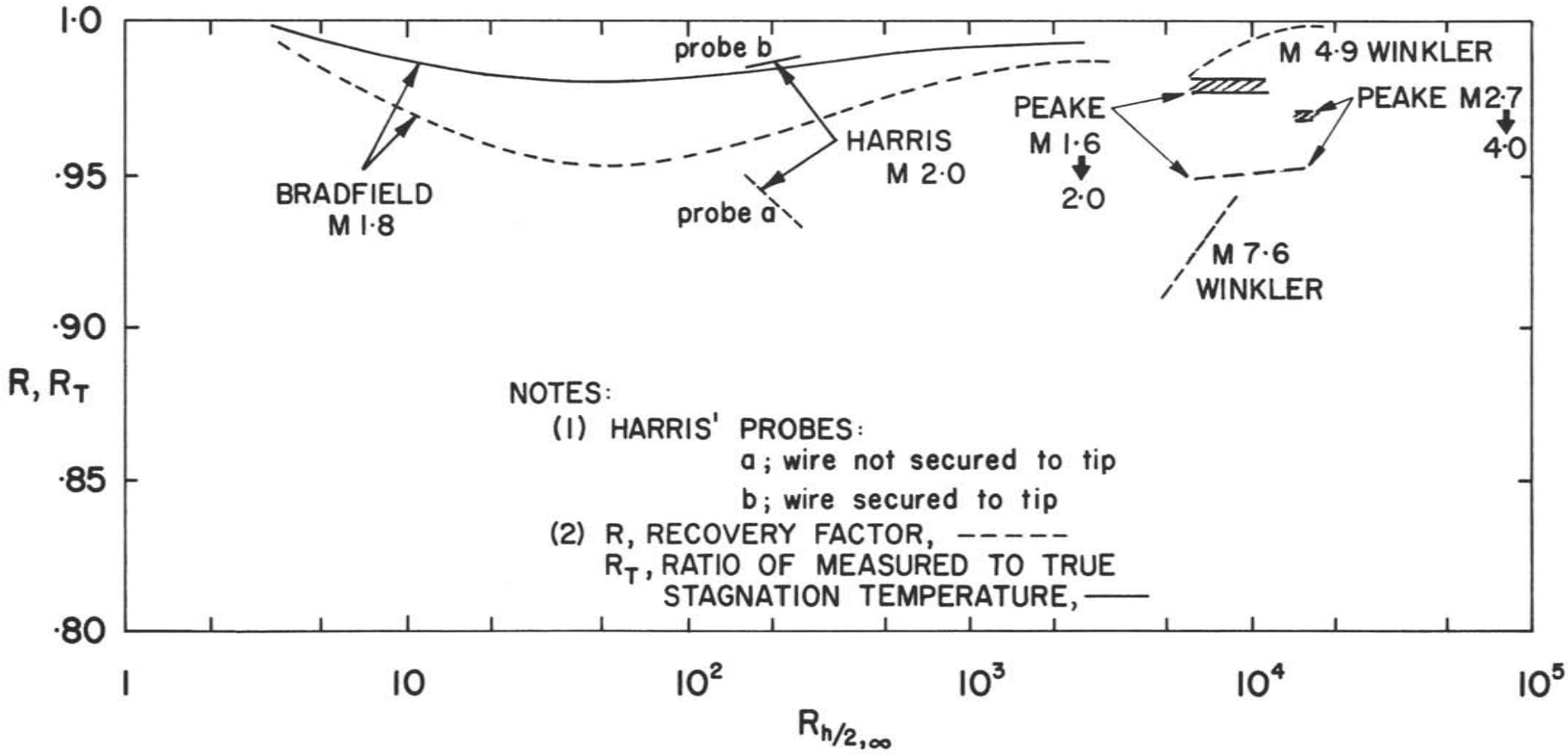

FIG. 29: RECOVERY FACTOR OF COBRA PROBE THERMOCOUPLE

PRESSURE DISTRIBUTIONS

FLOW VISUALIZATION

RUN 106

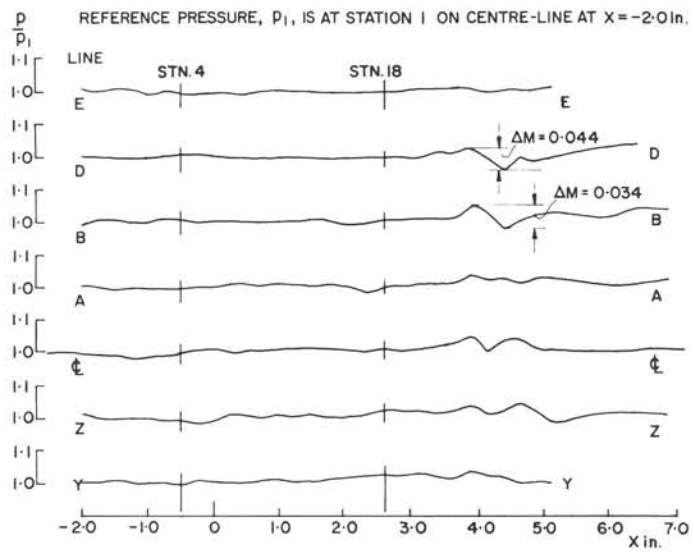

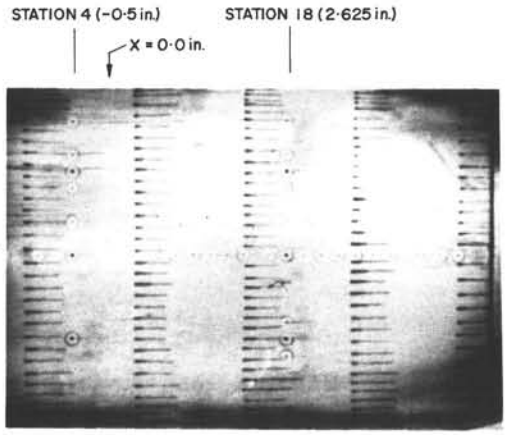

SIDEWALL VORTEX GENERATOR OUT

UNDISTURBED BOUNDARY LAYER THICKNESS, $\delta \cong 0{\cdot}2$ in., $R_\delta = 1{\cdot}5 \times 10^5$

RUN 107

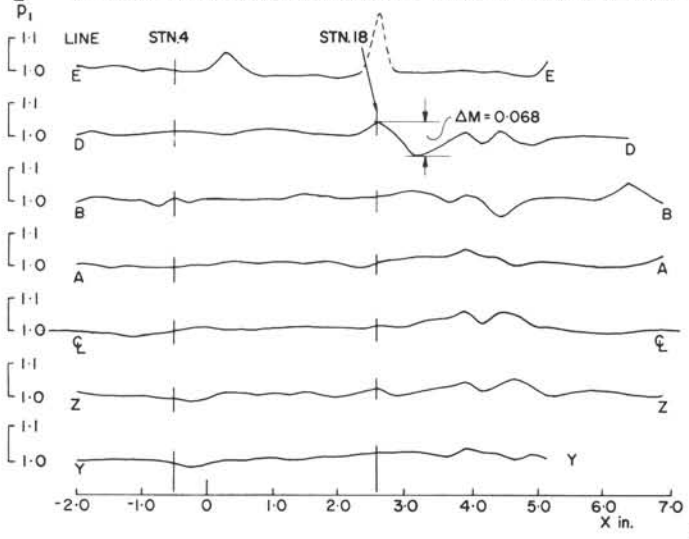

SIDEWALL V.G. AT XVGLE = -6·25 in.

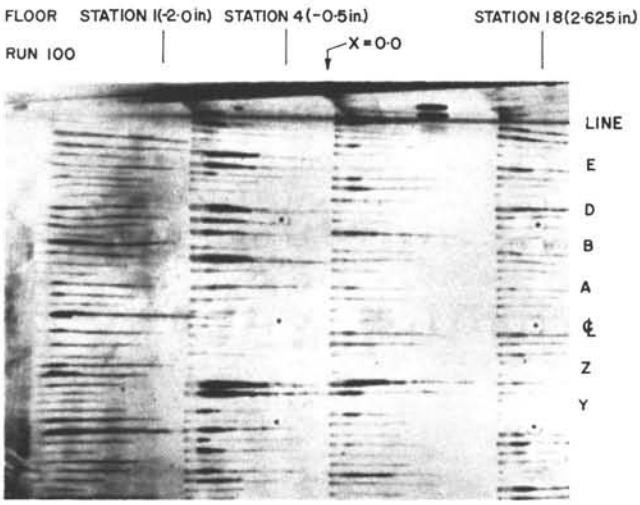

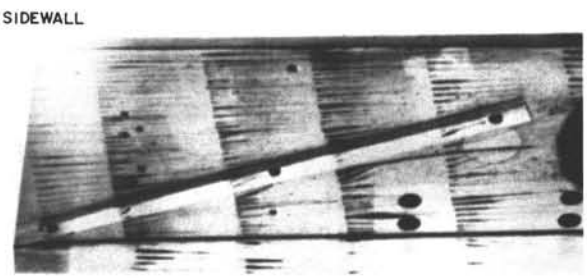

SIDEWALL VORTEX GENERATOR IN

FIG. 30: EFFECT OF SIDEWALL VORTEX GENERATOR ON EMPTY TUNNEL FLOW AT MACH 2

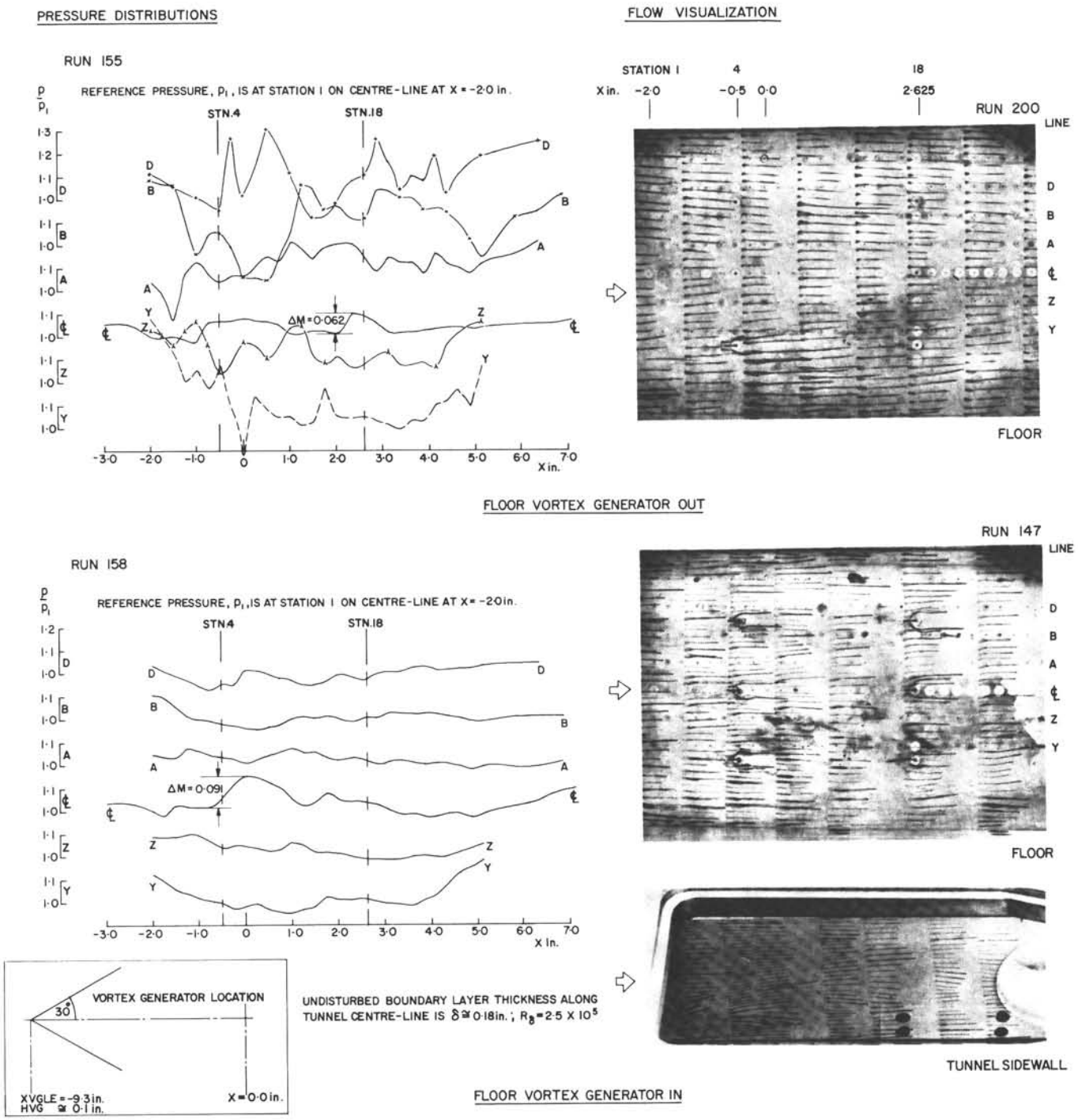

FIG. 31: SURFACE PRESSURE DISTRIBUTIONS AND FLOW VISUALIZATION IN EMPTY TUNNEL AT MACH 4

STATION	SYMBOL	RUN NO.	δ_{995} in.	δ_1^* in.	θ_{11} in.	$H = \delta_1^*/\theta_{11}$
4, ℄	⊙	66	0·217	0·051	0·015	3·4
4c	X	72	0·193	0·046	0·014	3·3
4x	+	73	0·223	0·053	0·016	3·3

STATION	SYMBOL	RUN NO.	δ_{995} in.	δ_1^* in.	θ_{11} in.	$H = \delta_1^*/\theta_{11}$
18, ℄	⊙	78	0·231	0·059	0·018	3·3
18c	X	83	0·241	0·061	0·018	3·4
18x	+	79	0·242	0·063	0·019	3·3

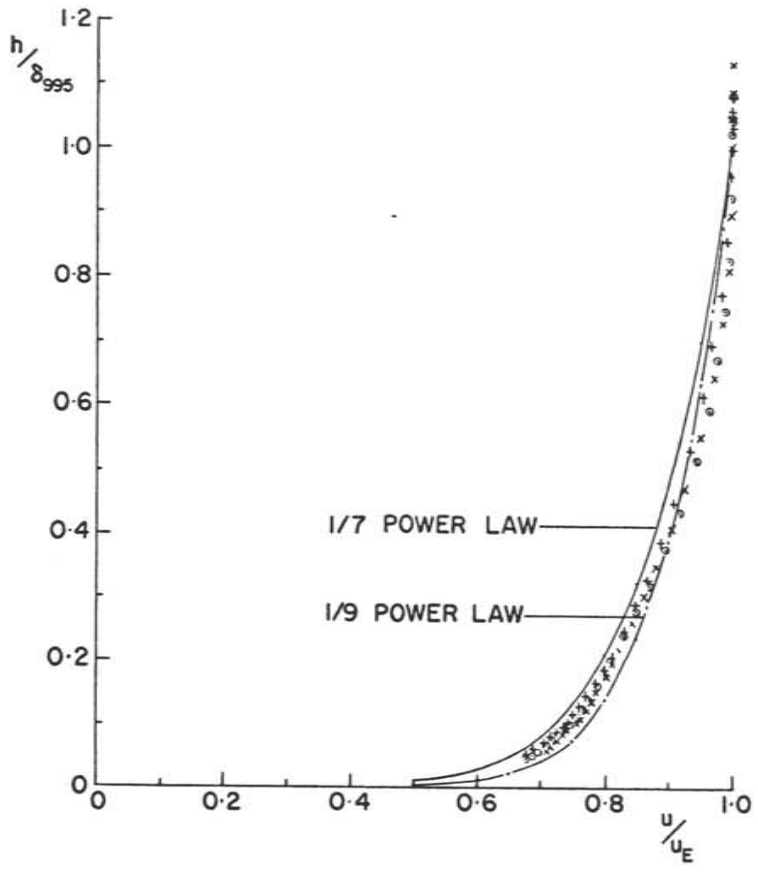

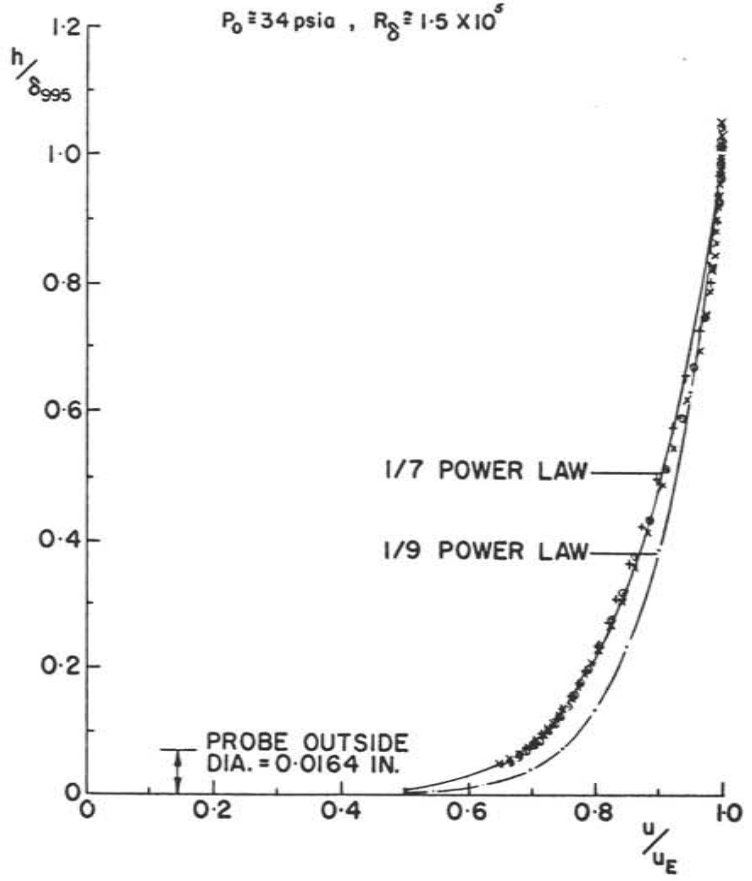

FIG. 32: SPANWISE SYMMETRY: VELOCITY PROFILES IN EMPTY TUNNEL AT MACH 2 MEASURED WITH CIRCULAR PITOT TUBE

LINE 4

STATION	SYMBOL	RUN NO.	δ_{995} in.	δ_1^* in.	θ_{11} in.	$H = \delta_1^*/\theta_{11}$
4, ℄	□	66	0·217	0·051	0·015	3·4
	∨	88	0·203	0·051	0·015	3·4
4c	□	72	0·193	0·046	0·014	3·3
	∨	90	0·199	0·050	0·015	3·3
4x	□	73	0·223	0·053	0·016	3·3
	∨	89	0·207	0·051	0·015	3·4

LINE 18

STATION	SYMBOL	RUN NO.	δ_{995} in.	δ_1^* in.	θ_{11} in.	$H = \delta_1^*/\theta_{11}$
18x	□	79	0·242	0·063	0·019	3·3
	∨	80	0·238	0·060	0·018	3·3

$P_0 \cong 34$ psia, $R_\delta \cong 1{\cdot}5 \times 10^5$

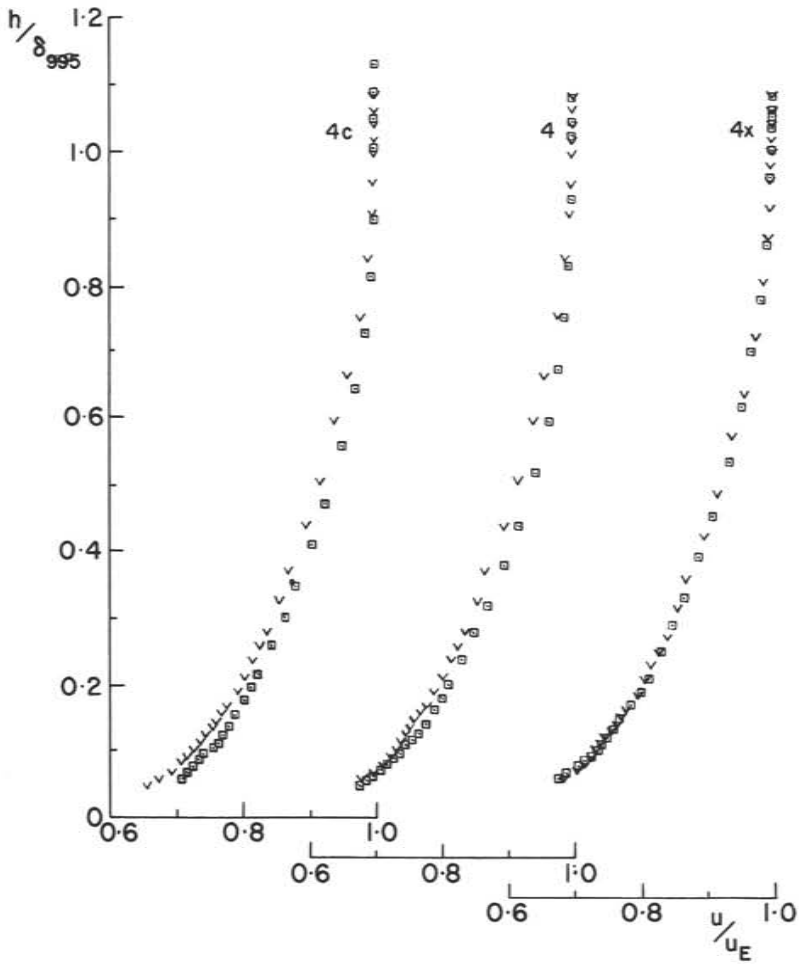

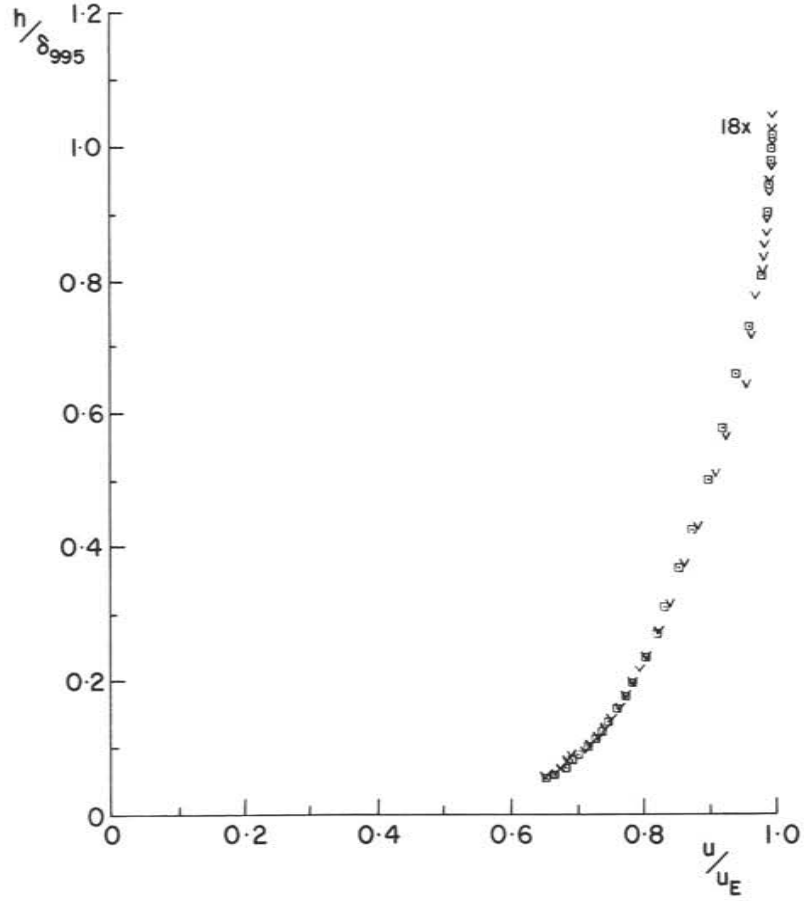

FIG. 33: REPEATABILITY OF VELOCITY PROFILES IN EMPTY TUNNEL AT MACH 2 MEASURED WITH CIRCULAR PITOT

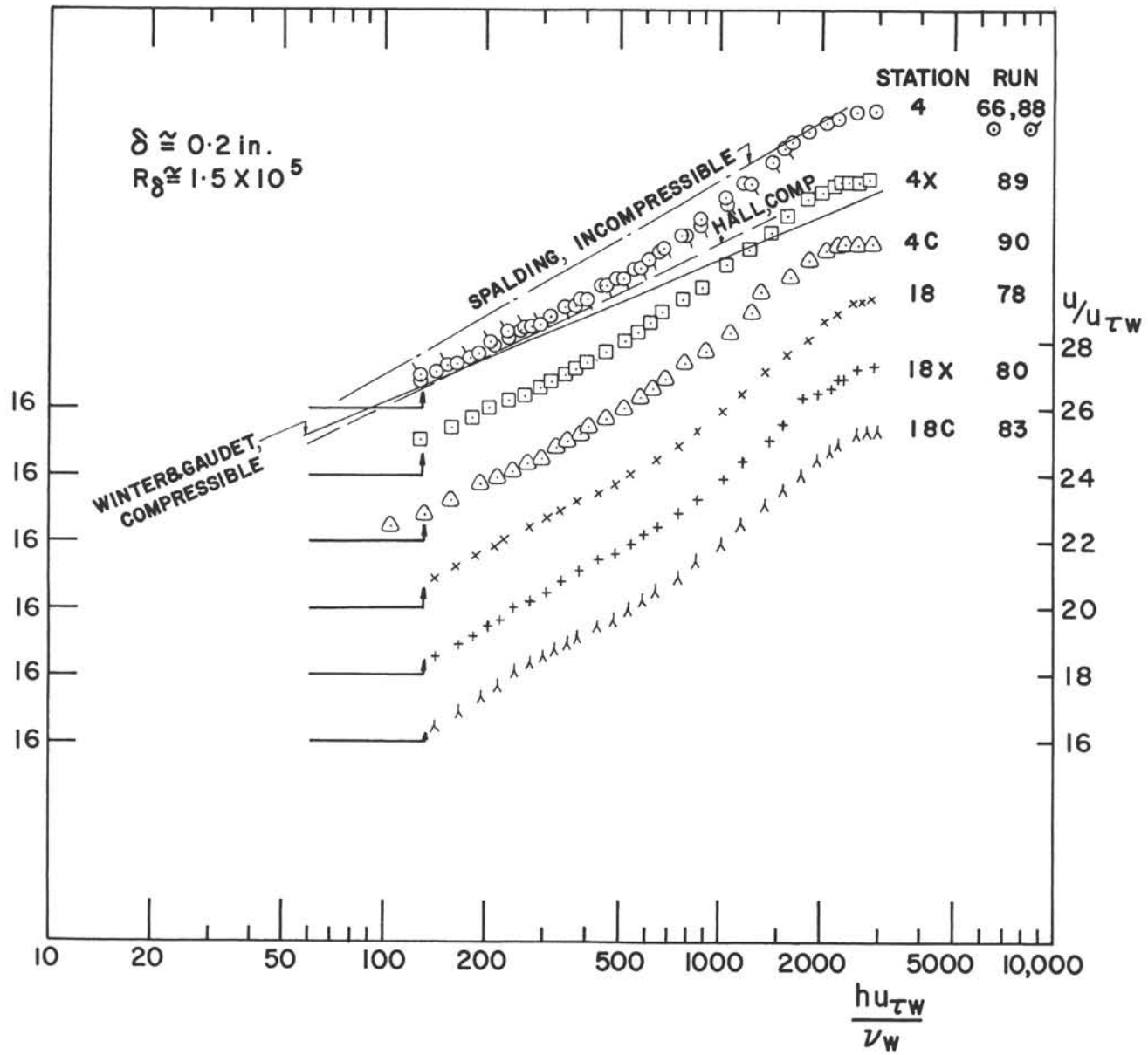

FIG. 34: SEMI-LOGARITHMIC VELOCITY PROFILES IN EMPTY TUNNEL FROM CIRCULAR PITOT TUBE AT MACH 2

STATION	SYMBOL	RUN NO.	δ_{995} in.	δ_1^* in.	θ_{11} in.
18	○	142	0·441	0·216	0·026
18c	×	145	0·235	0·085	0·011
18x	+	144	0·241	0·087	0·011

STATION	SYMBOL	RUN NO.	δ_{995} in.	δ_1^* in.	θ_{11} in.
4	○	197	0·208	0·070	0·009
4c	×	198	0·325	0·126	0·016
4x	+	199	0·332	0·128	0·017
18	○	195	0·241	0·069	0·009
18c	×	196	0·365	0·137	0·018
18x	+	194	0·353	0·138	0·018
18	○	148	0·229	0·072	0·009
18c	×	146	0·365	0·142	0·017

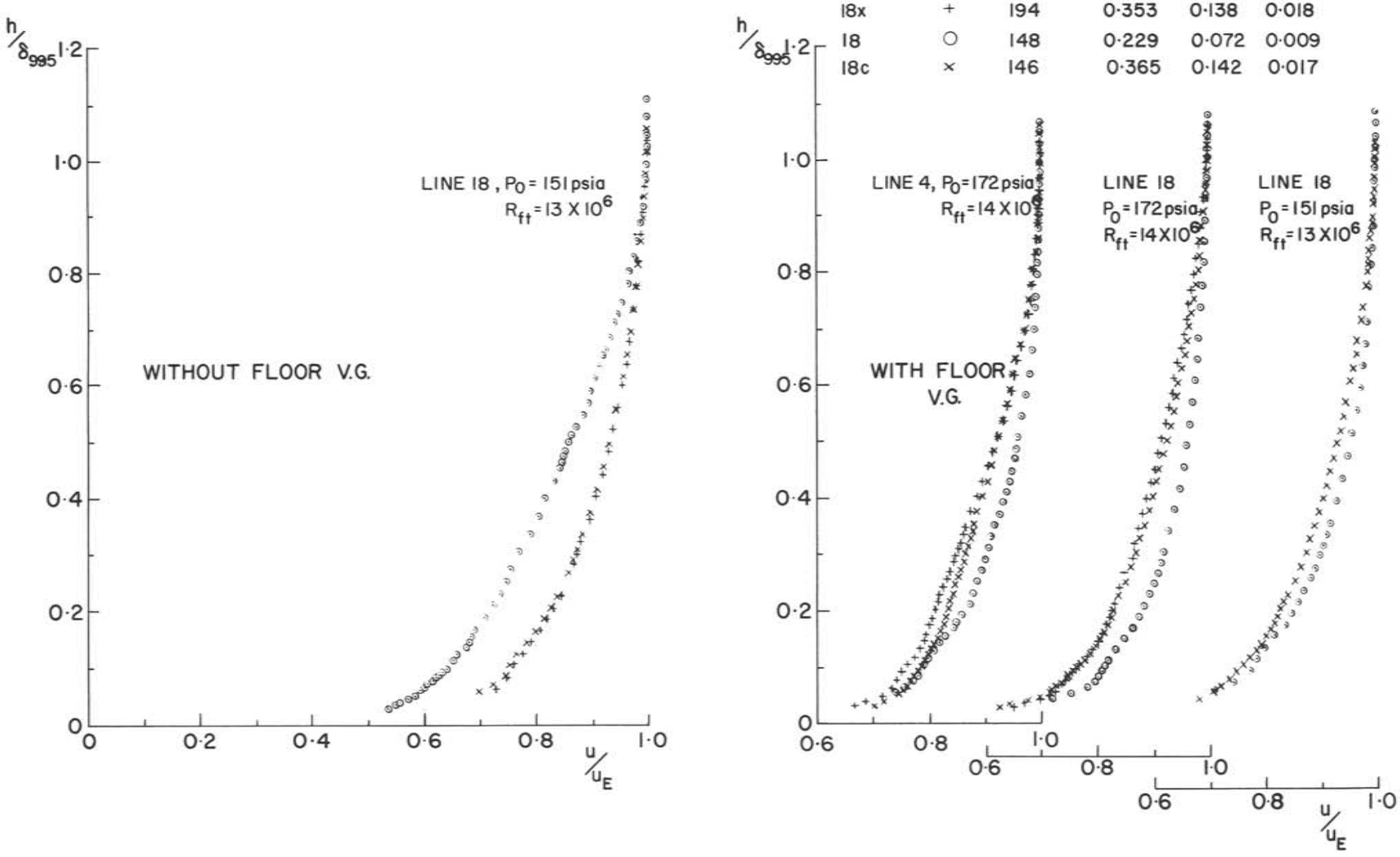

FIG. 35: SPANWISE SYMMETRY: VELOCITY PROFILES IN EMPTY TUNNEL AT MACH 4 MEASURED WITH CIRCULAR PITOT WITHOUT AND WITH FLOOR VORTEX GENERATOR

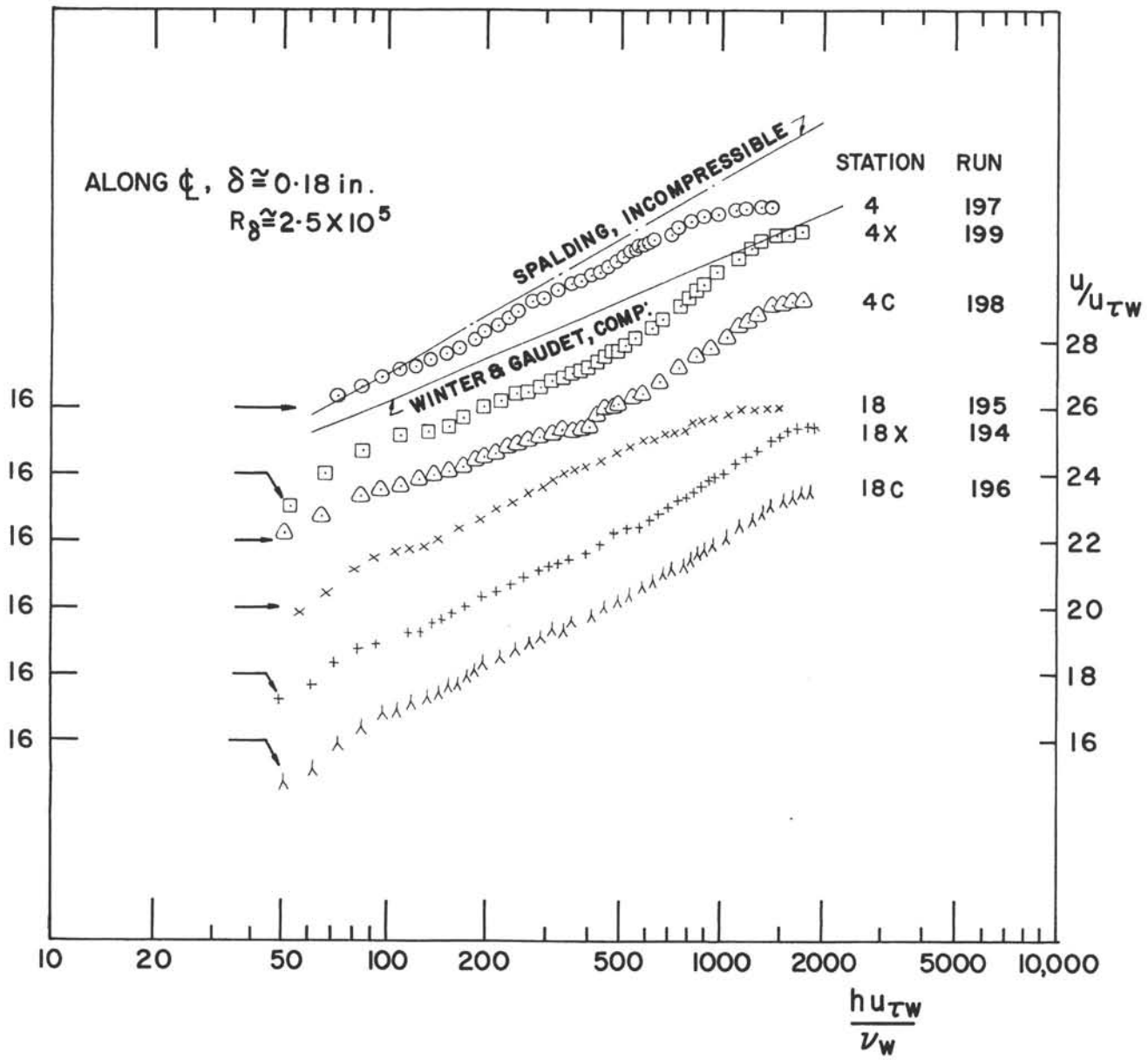

FIG. 36: SEMI-LOGARITHMIC VELOCITY PROFILES IN EMPTY TUNNEL FROM CIRCULAR PITOT TUBE AT MACH 4 WITH V.G. ON FLOOR

STATION	SYMBOL	RUN NO.	δ_{995} in.	δ_1^* in.	θ_{11} in.	$H = \delta_1^*/\theta_{11}$	$R_{ft} \times 10^{-6}$
4	⊙	66	0·217	0·051	0·015	3·4	8·9
	∧	67	0·210	0·049	0·014	3·5	10·2
	T	68	0·205	0·047	0·014	3·4	14·0
18	⊙	78	0·231	0·059	0·018	3·3	8·8
	∧	77	0·230	0·058	0·017	3·4	10·1
	T	76	0·225	0·055	0·016	3·4	13·8

STATION	SYMBOL	RUN NO.	δ_{995} in.	δ_1^* in.	θ_{11} in.	$H = \delta_1^*/\theta_{11}$	$R_{ft} \times 10^{-6}$
18	⊙	148	0·229	0·072	0·009	8·0	12·3
	▽	195	0·241	0·069	0·009	7·7	14·1

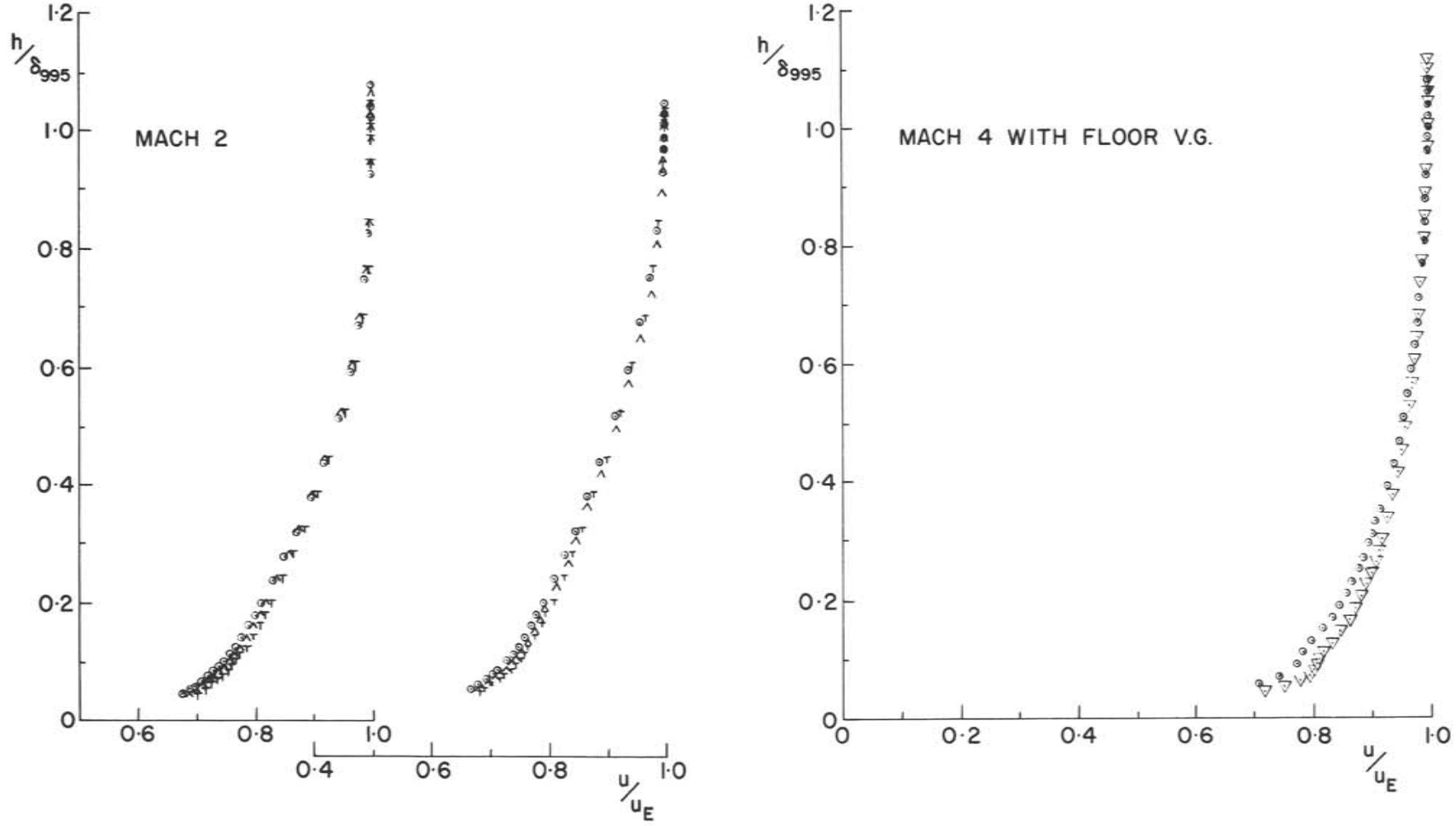

FIG. 37: EFFECT OF REYNOLDS NUMBER ON VELOCITY PROFILES IN EMPTY TUNNEL AT MACH 2 AND 4, MEASURED WITH CIRCULAR PITOT

PROBE	SYMBOL	RUN NO.	STATION	X in.	δ_{995} in.	δ_1^* in.	θ_{11} in.	$R_{\theta_{11}} \times 10^{-4}$
O'R PITOT	⊙	88	4	-0·5	0·203	0·051	0·015	1·1
COBRA	⊡	24501	T1	0·0	0·237	0·062	0·019	1·4

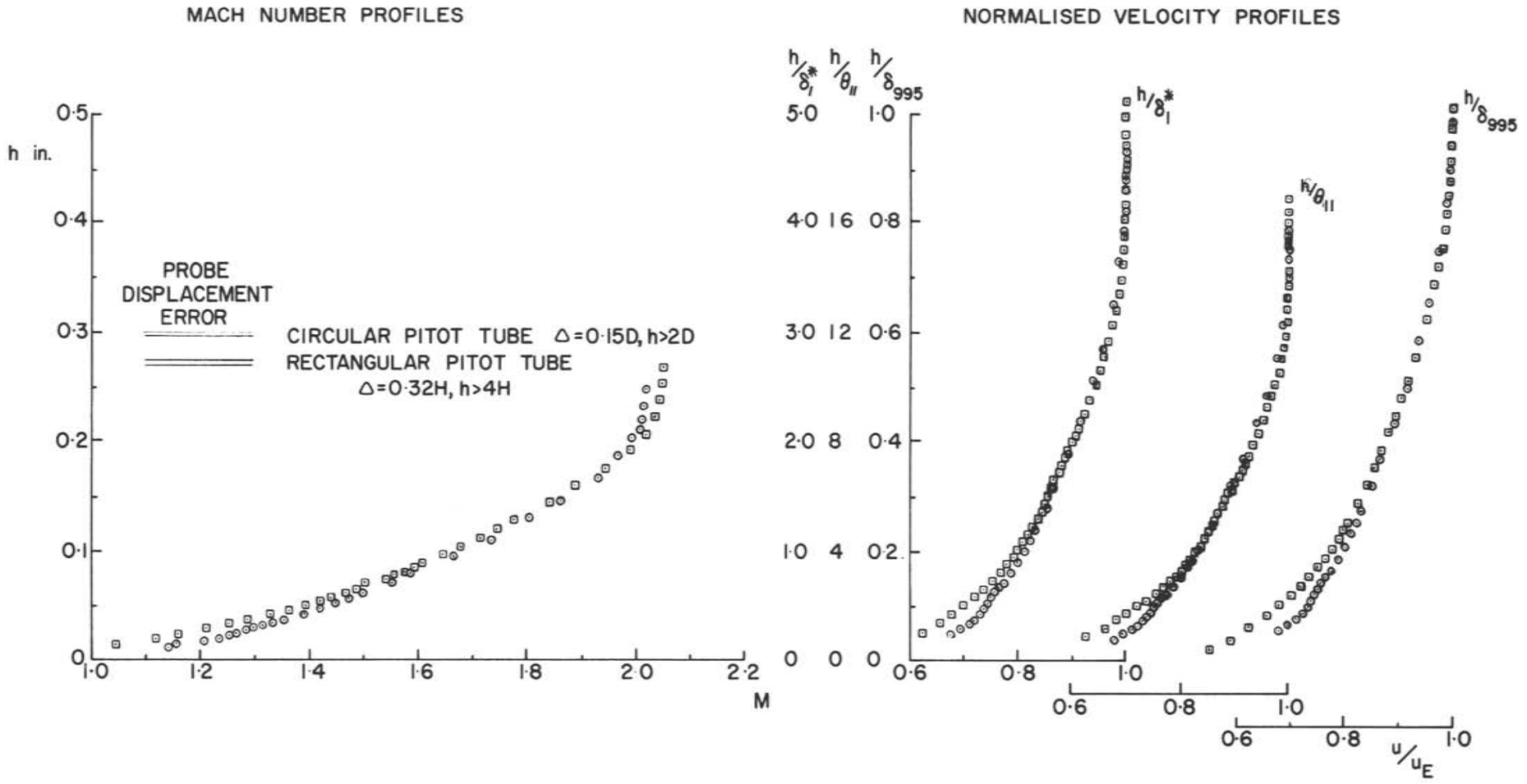

FIG. 38: COBRA AND CIRCULAR PITOT TUBE VELOCITY PROFILES ALONG $\mathcal{L}$ AT MACH 2 IN EMPTY TUNNEL

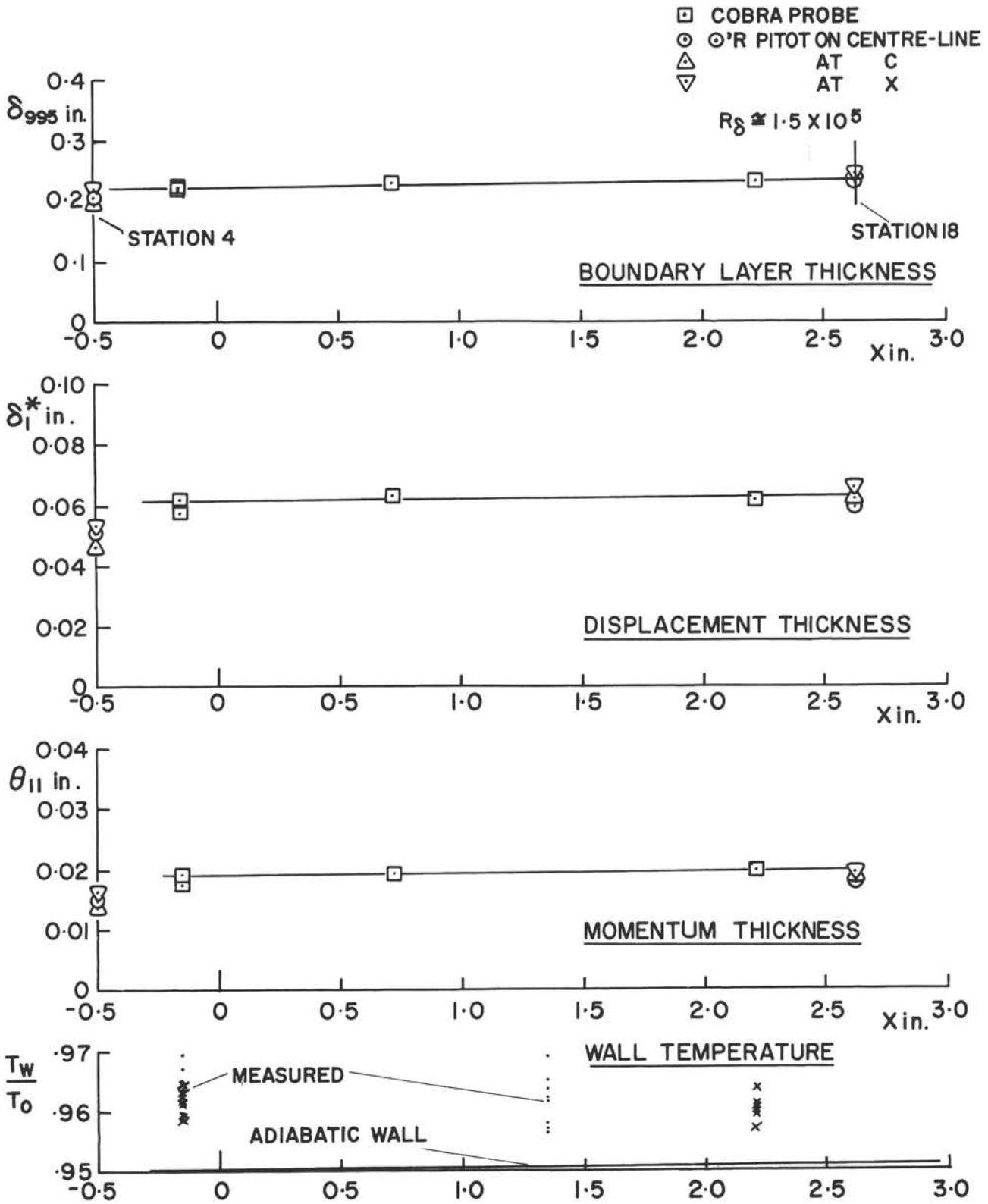

FIG. 39: INTEGRAL PARAMETERS AND WALL TEMPERATURES FOR FLOW IN EMPTY TUNNEL AT MACH 2

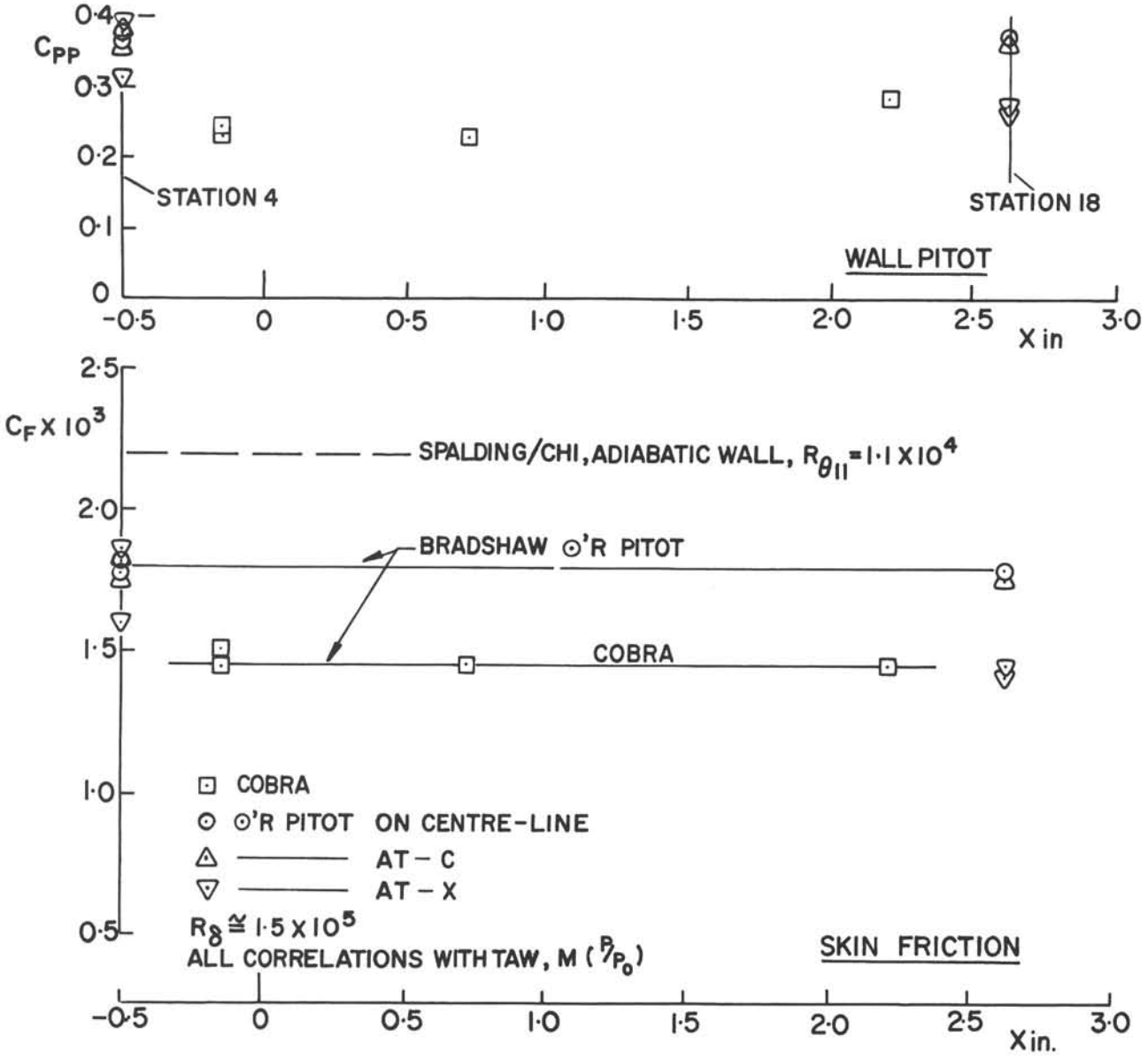

FIG. 40: LOCAL SKIN FRICTION FOR FLOW IN EMPTY TUNNEL AT MACH 2

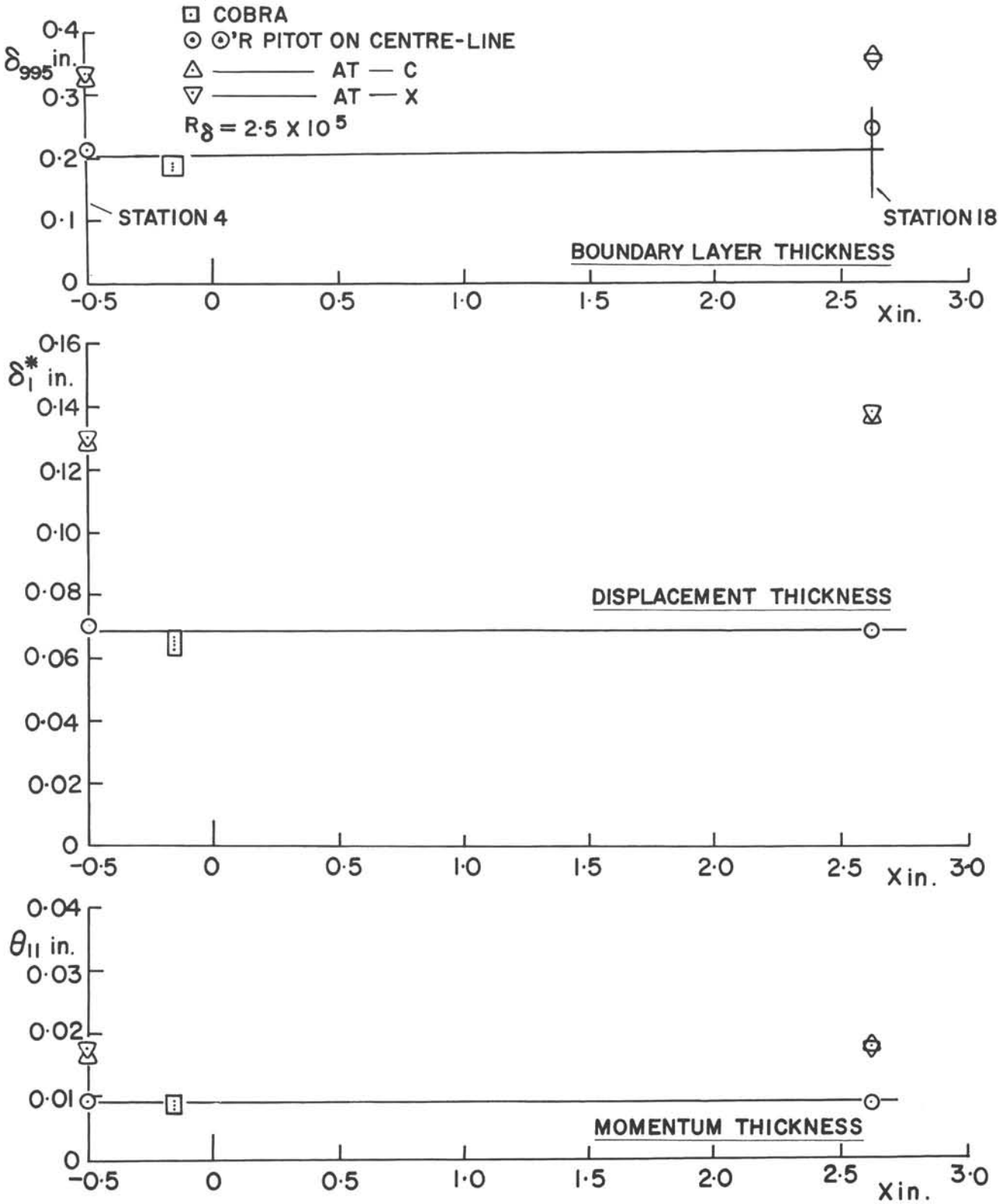

FIG. 41: INTEGRAL PARAMETERS FOR FLOW IN EMPTY TUNNEL AT MACH 4 WITH FLOOR V.G. IN

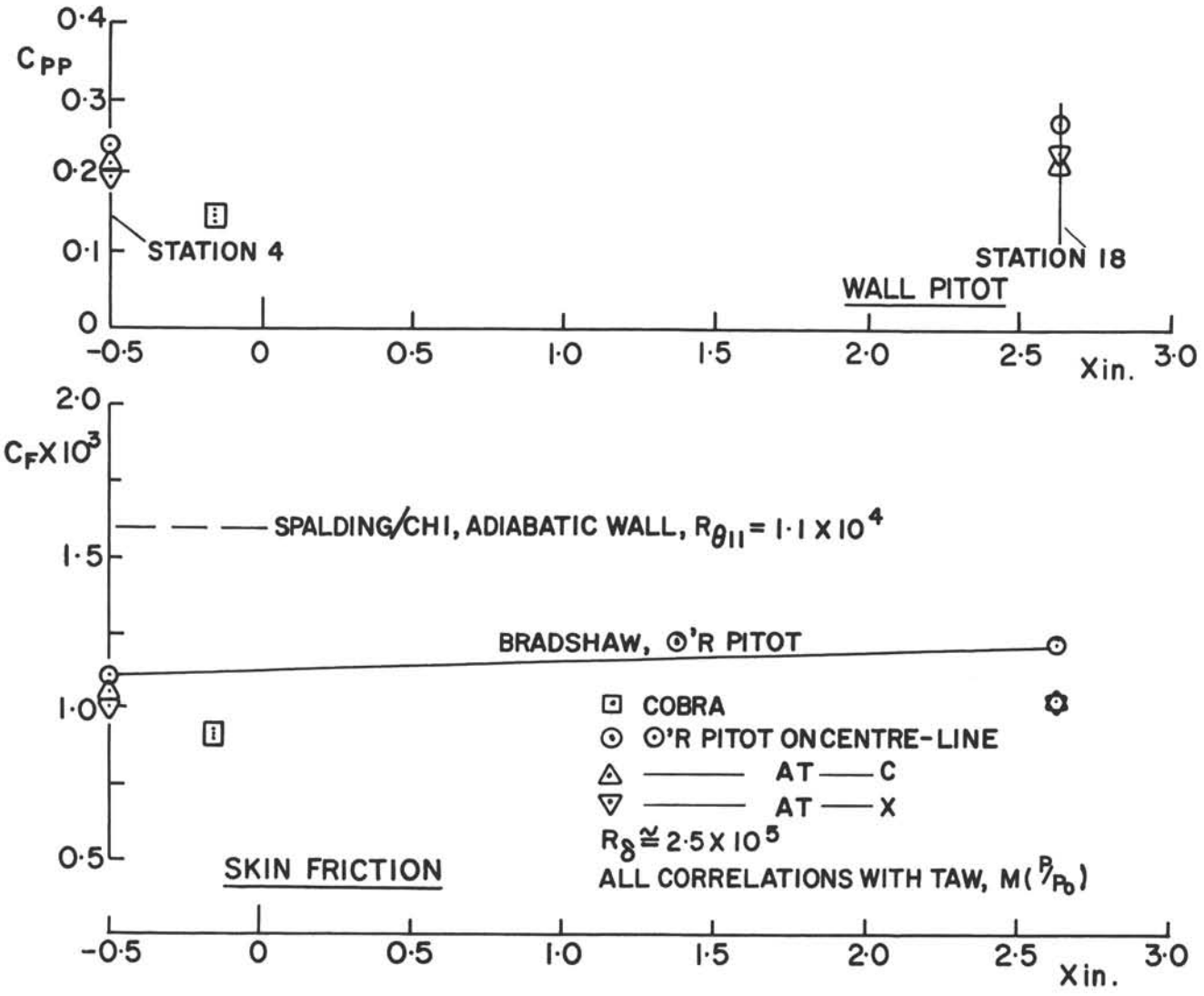

FIG. 42: LOCAL SKIN FRICTION FOR FLOW IN EMPTY TUNNEL AT MACH 4 WITH FLOOR V.G. IN

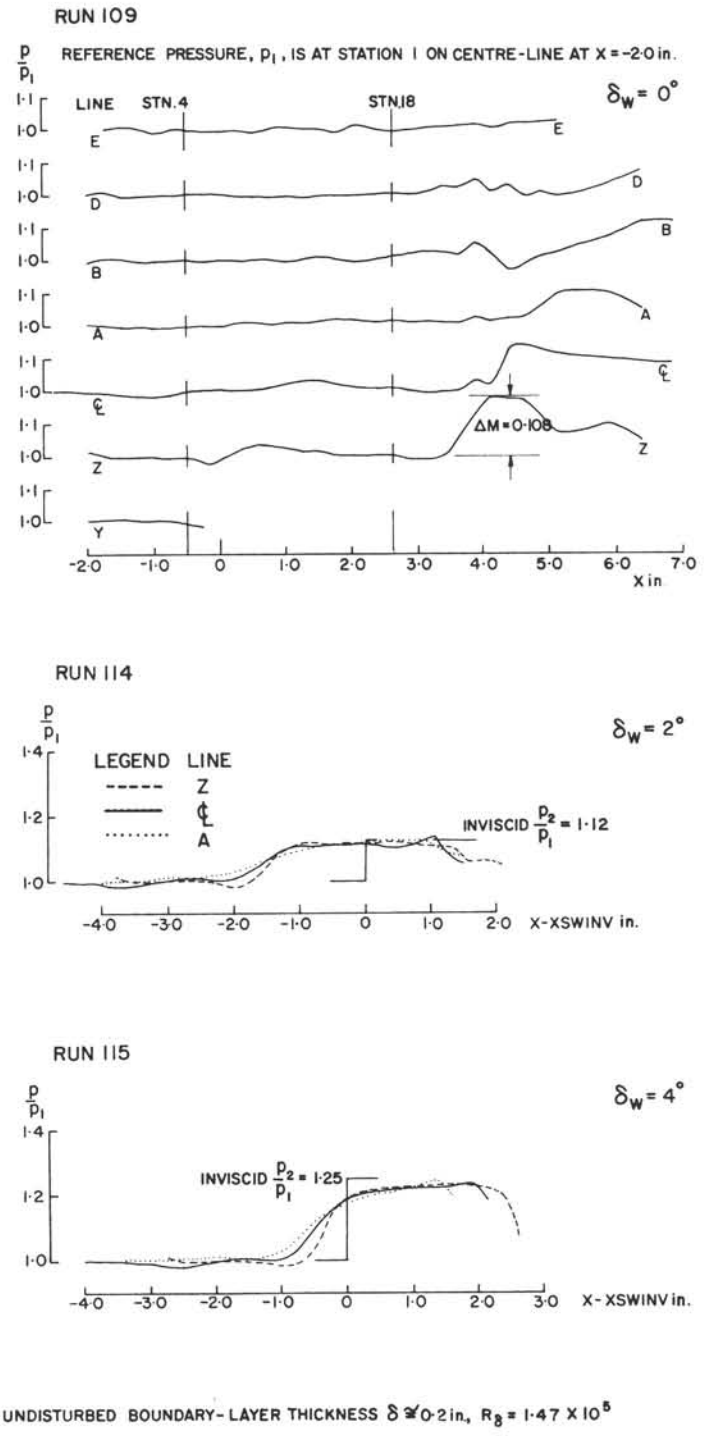

UNDISTURBED BOUNDARY-LAYER THICKNESS $\delta \approx 0.2$ in., $R_\delta = 1.47 \times 10^5$

FIG. 43: SURFACE PRESSURE DISTRIBUTIONS AT SMALL WEDGE DEFLECTION ANGLES AT MACH 2 (XWLE = 0.0 in.)

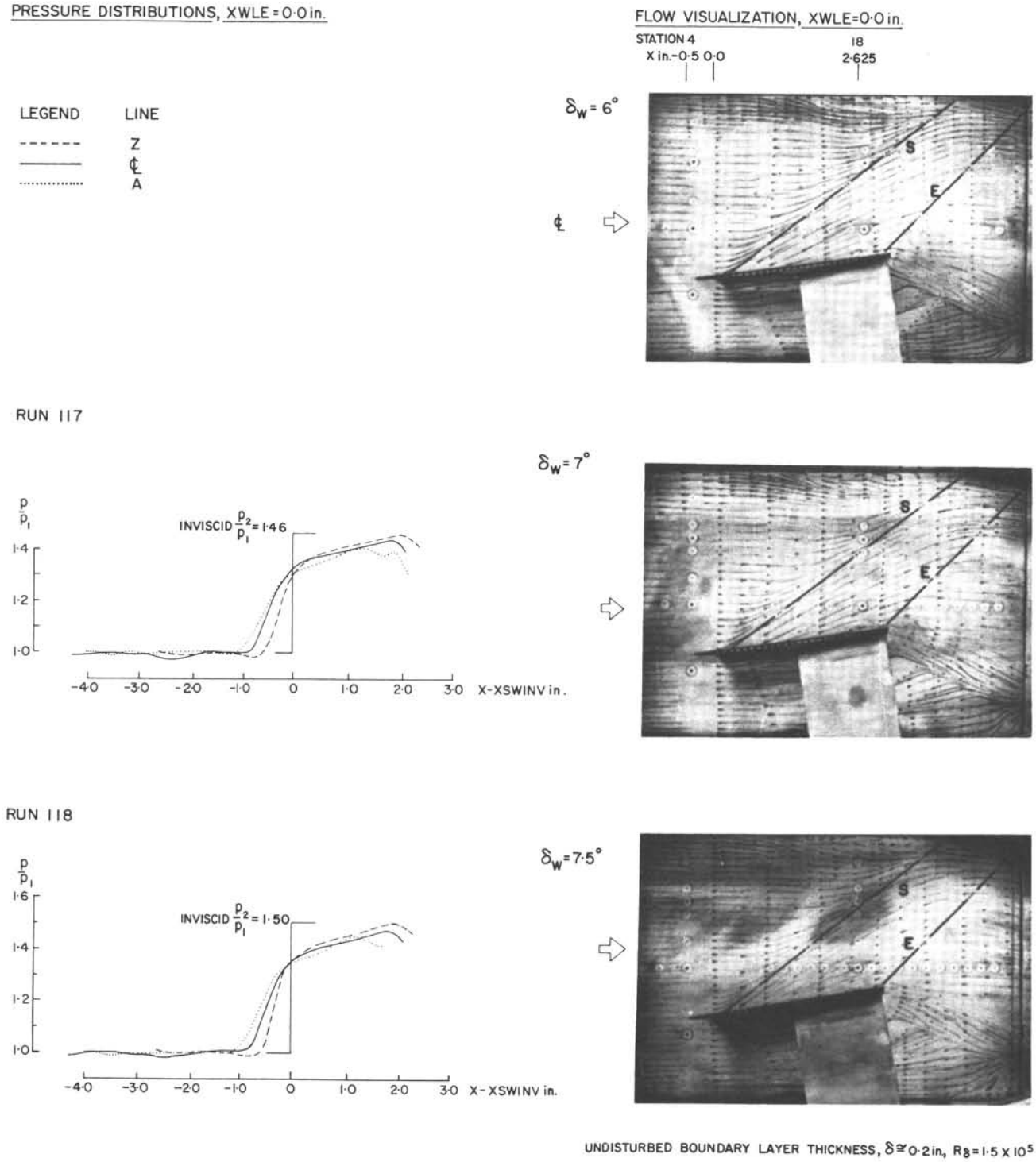

FIG. 44: SURFACE PRESSURE DISTRIBUTIONS AND FLOW VISUALIZATION FOR δ_w = 6, 7 AND 7.5-DEGREES AT MACH 2

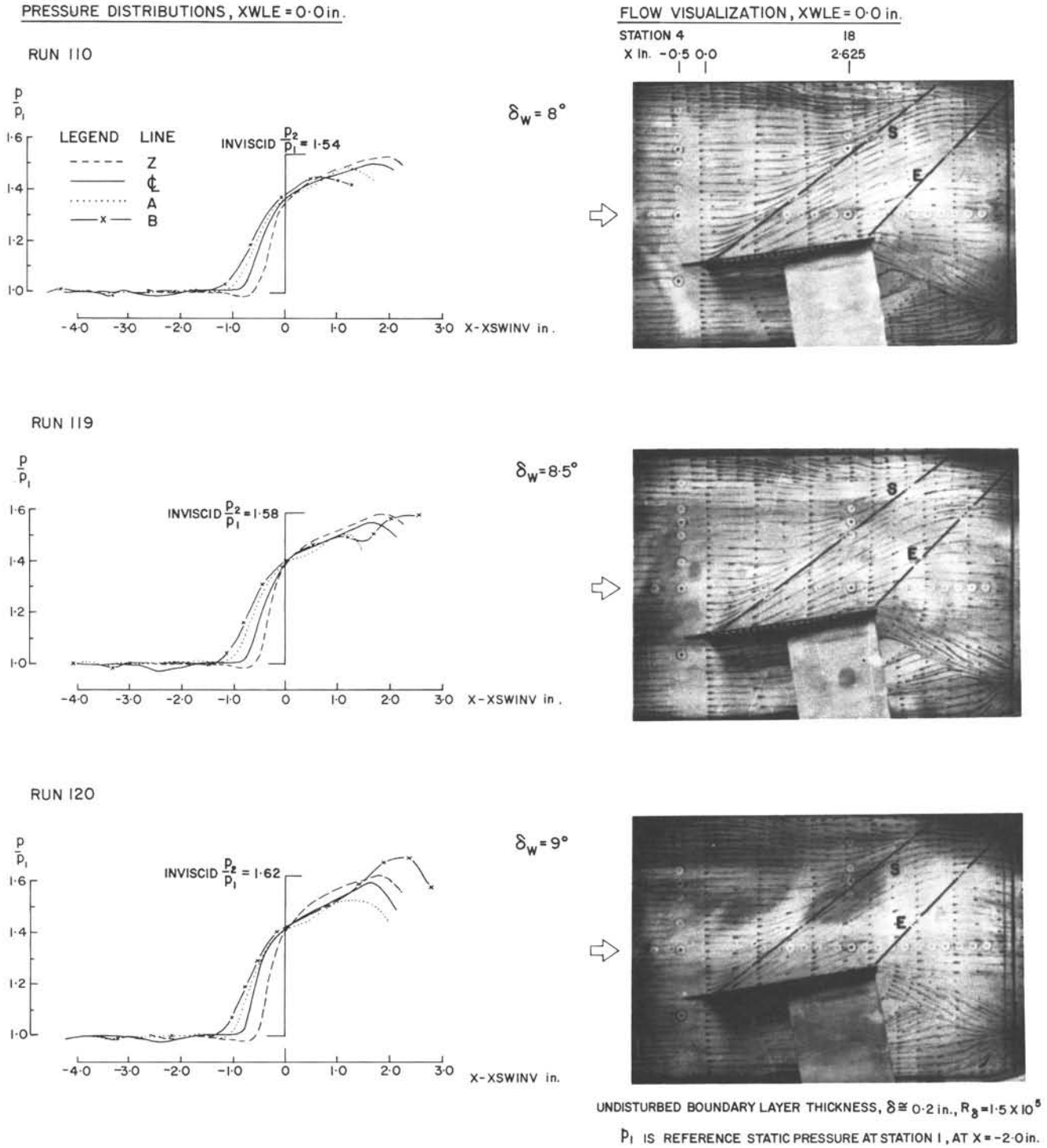

FIG. 45: SURFACE PRESSURE DISTRIBUTIONS AND FLOW VISUALIZATION FOR δ_w = 8, 8.5 AND 9-DEGREES AT MACH 2

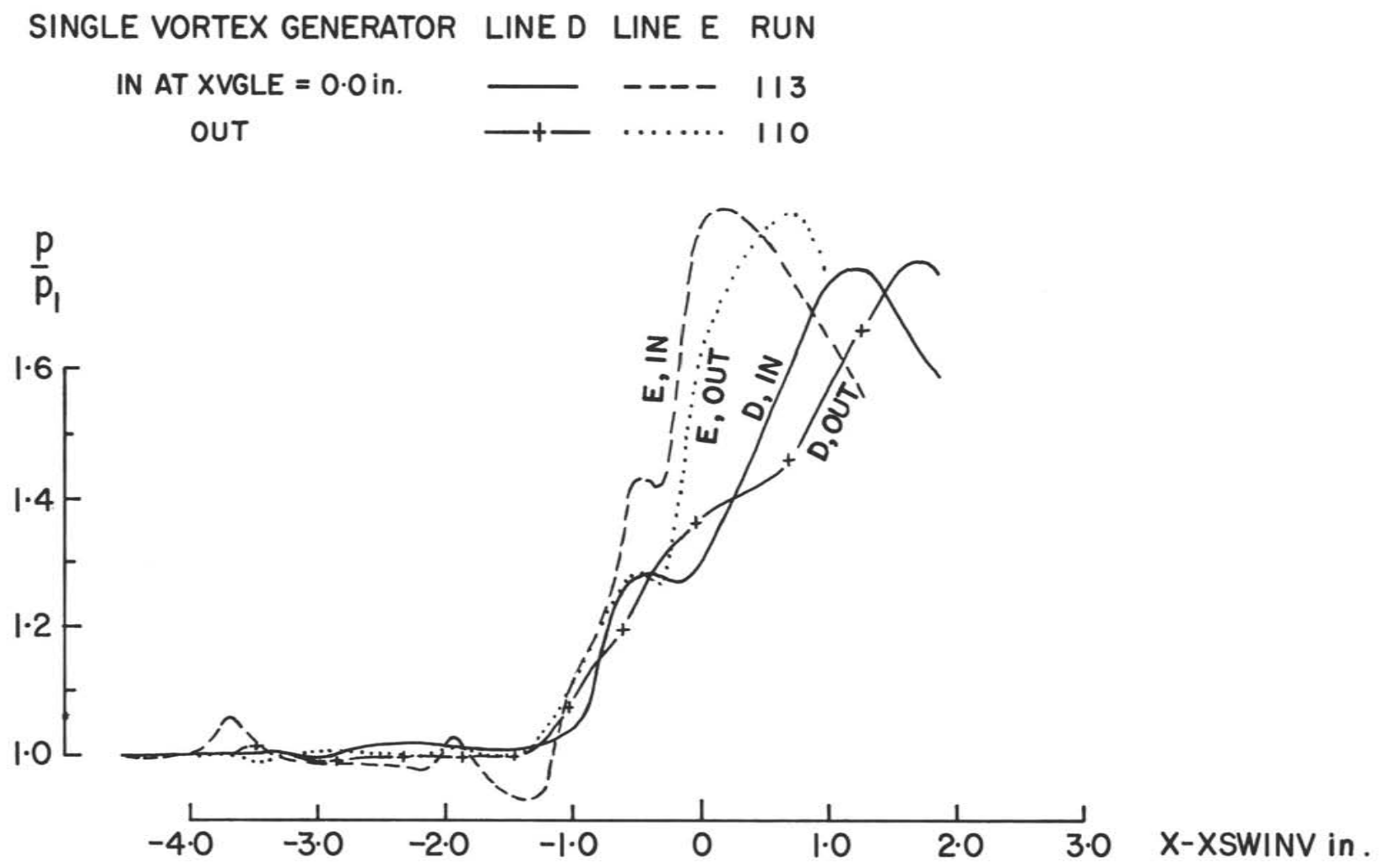

FIG. 46: EFFECT OF SIDEWALL VORTEX GENERATOR ON SURFACE PRESSURE DISTRIBUTIONS NEAREST THE SIDEWALL FOR δ_w = 8-DEGREES AT MACH 2

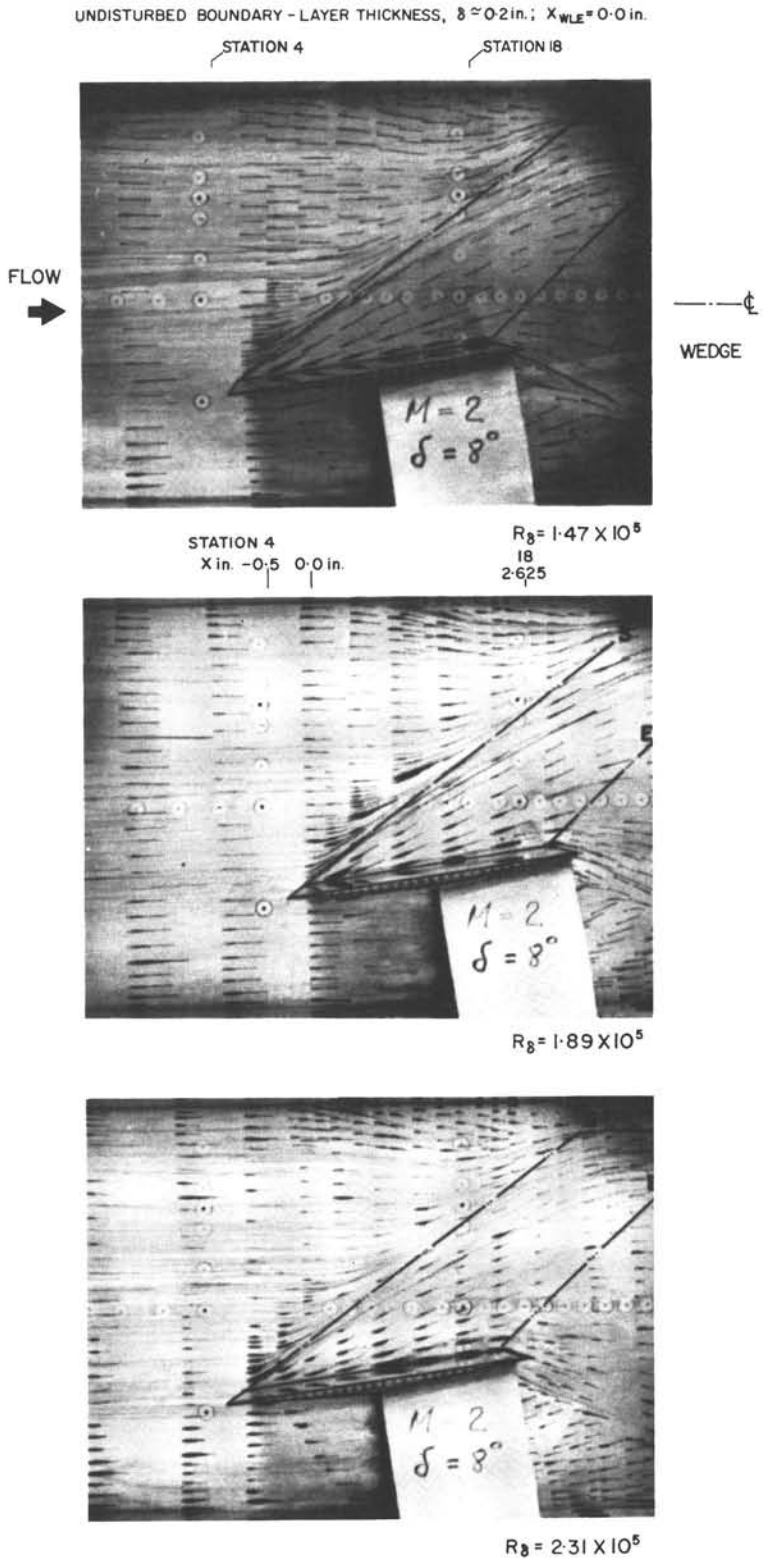

FIG. 47: SURFACE FLOW VISUALIZATION WITH CHANGE OF REYNOLDS NUMBER FOR δ_w = 8-DEGREES AT MACH 2

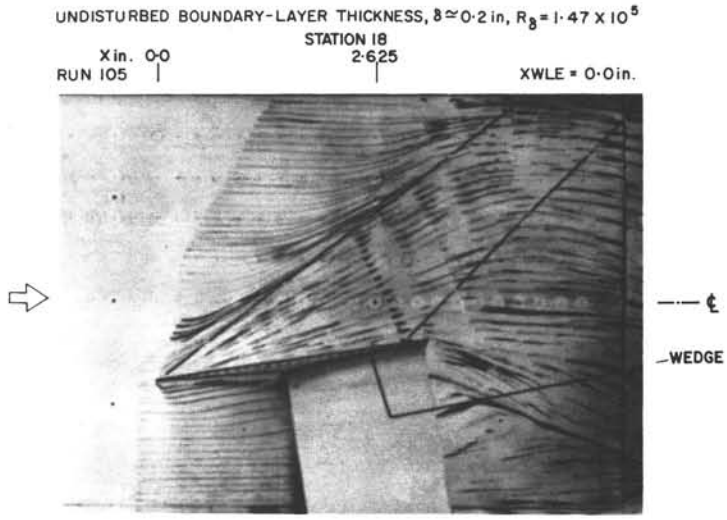

WITHOUT SIDEWALL VORTEX GENERATOR

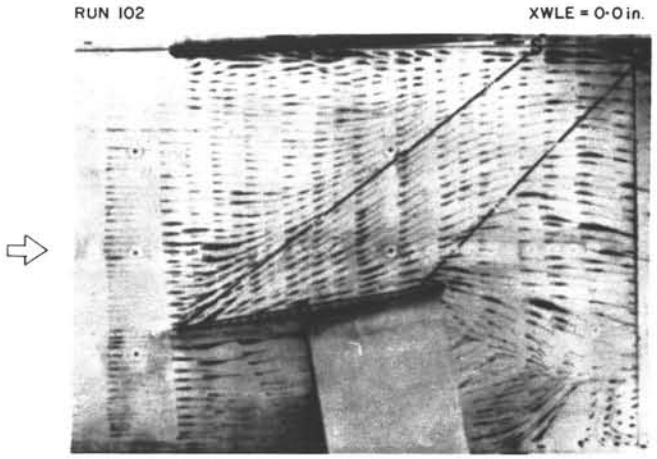

WITH SIDEWALL VORTEX GENERATOR AT XVGLE=0·0in.

IG. 48: EFFECT OF SIDEWALL VORTEX GENERATOR ON SURFACE FLOW VISUALIZATION FOR δ_w = 9-DEGREES AT MACH 2

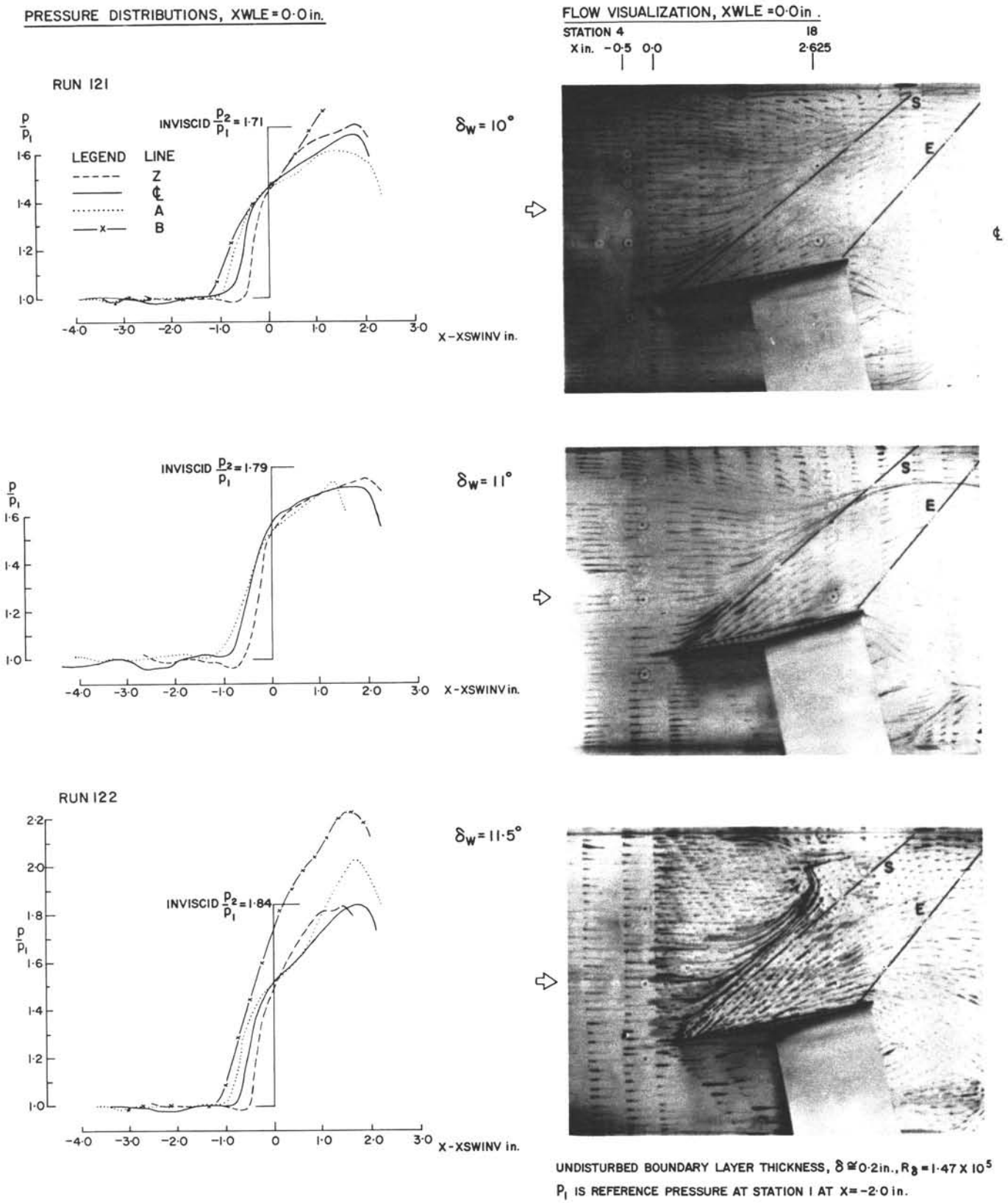

UNDISTURBED BOUNDARY LAYER THICKNESS, $\delta \cong 0{\cdot}2$ in., $R_\delta = 1{\cdot}47 \times 10^5$

P_1 IS REFERENCE PRESSURE AT STATION 1 AT X = -2·0 in.

FIG. 49: SURFACE PRESSURE DISTRIBUTIONS AND FLOW VISUALIZATION FOR δ_w = 10, 11 AND 11.5-DEGREES AT MACH 2

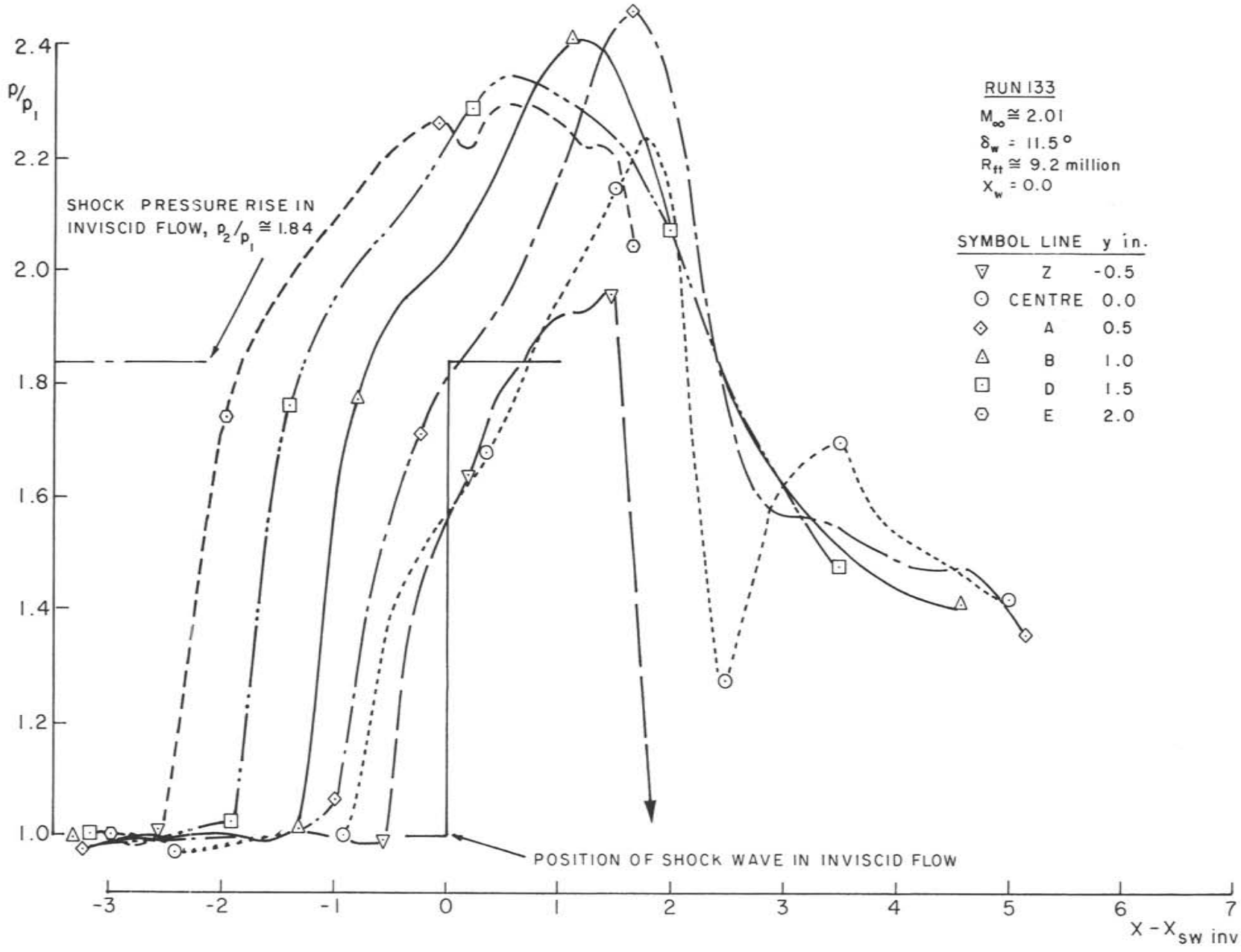

FIG. 50: PRESSURES ALONG TEST WALL AT MACH 2 AND WEDGE ANGLE OF 11.5-DEGREES AT A FIXED WEDGE POSITION, XWLE = 0.0-IN.; SIDEWALL V.G. IN AT XVGLE = 0.0-IN.

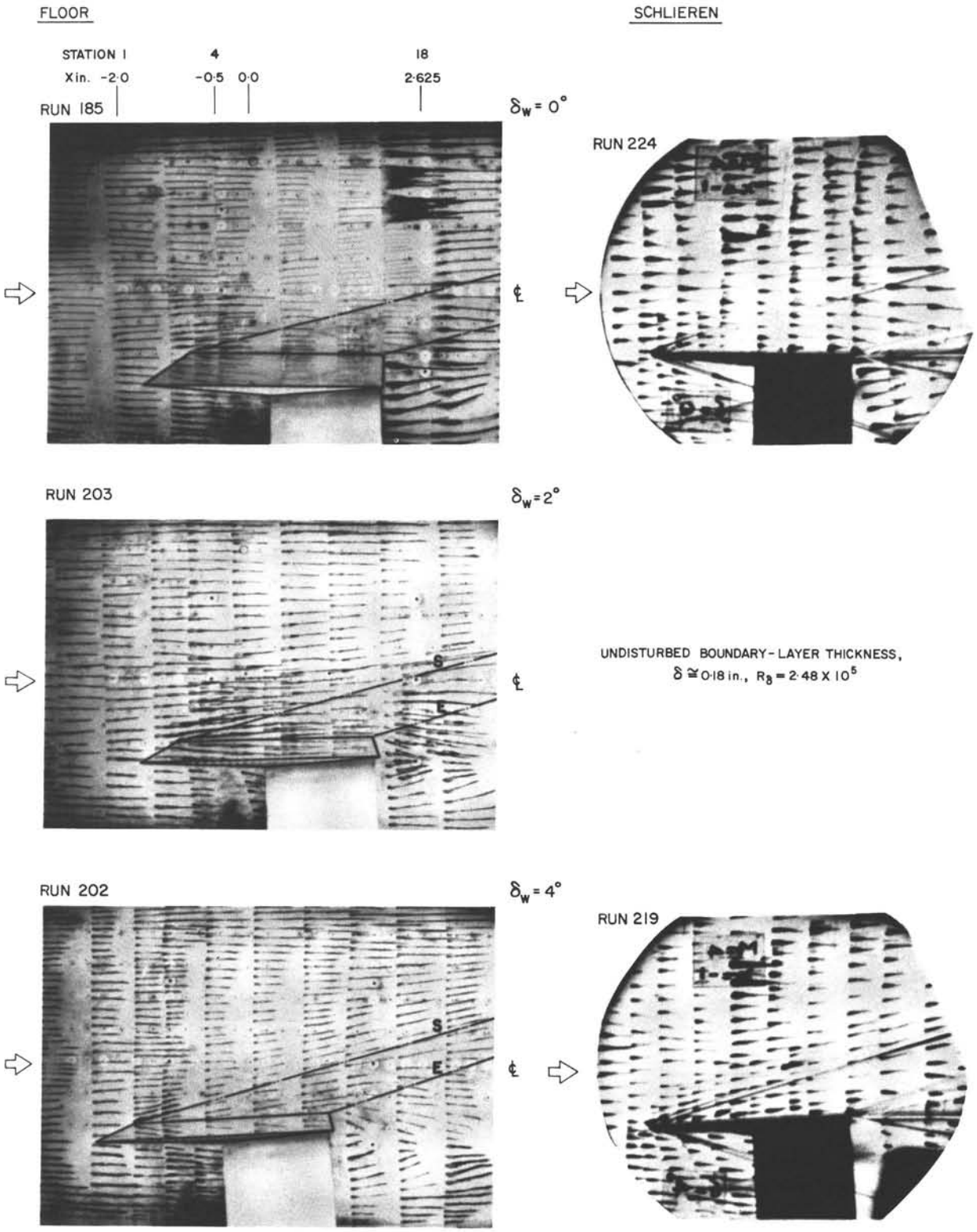

FIG. 51: SCHLIEREN AND SURFACE FLOW VISUALIZATION AT SMALL WEDGE ANGLES AT MACH 4 (FLOOR V.G. IN)

PRESSURE DISTRIBUTIONS, XWLE = 0·0 in.

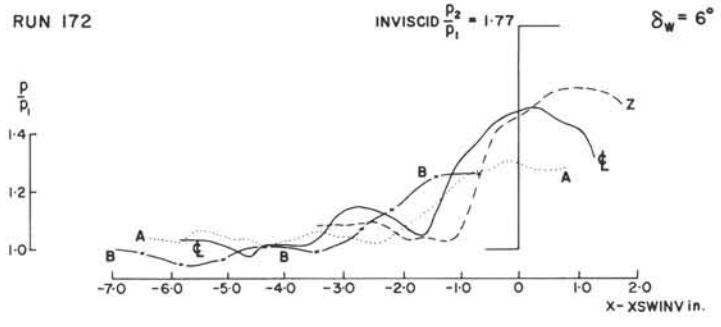

p_1 IS REFERENCE STATIC PRESSURE AT STATION 1 ON TUNNEL ℄ AT X = -2·0 in.

LEGEND	LINE
- - - - -	Z
———	℄
.....	A
—x—	B

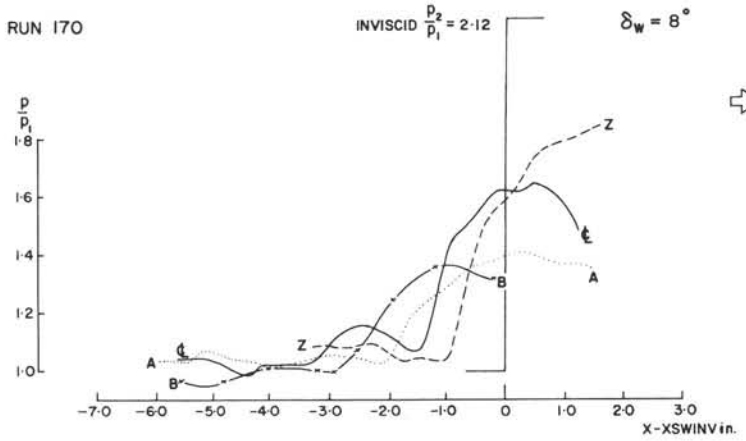

UNDISTURBED BOUNDARY LAYER THICKNESS, $\delta \cong 0{\cdot}18$ in., $R_\delta = 2{\cdot}5 \times 10^5$

FLOW VISUALIZATION, XWLE = -1·0 in.

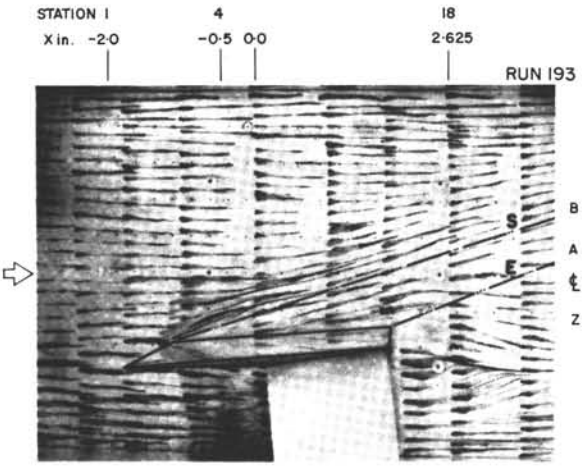

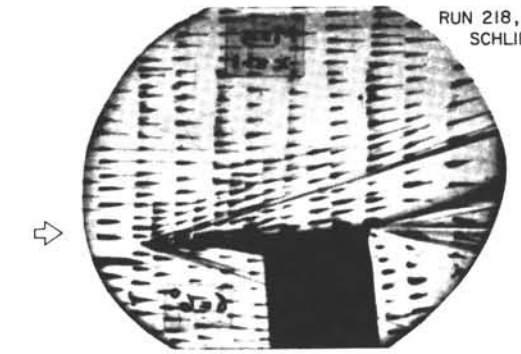

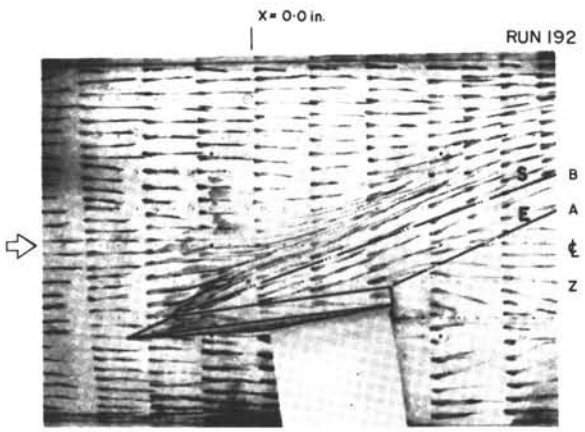

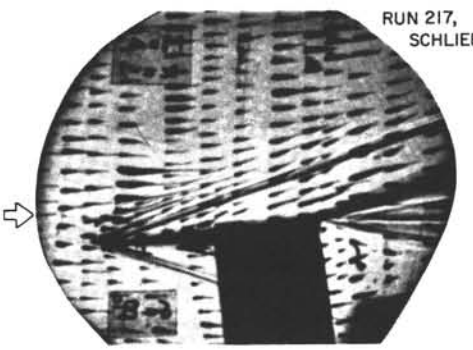

FIG. 52: SURFACE PRESSURE DISTRIBUTIONS AND FLOW VISUALIZATION FOR δ_w = 6 AND 8-DEGREES AT MACH 4 (FLOOR V.G. IN)

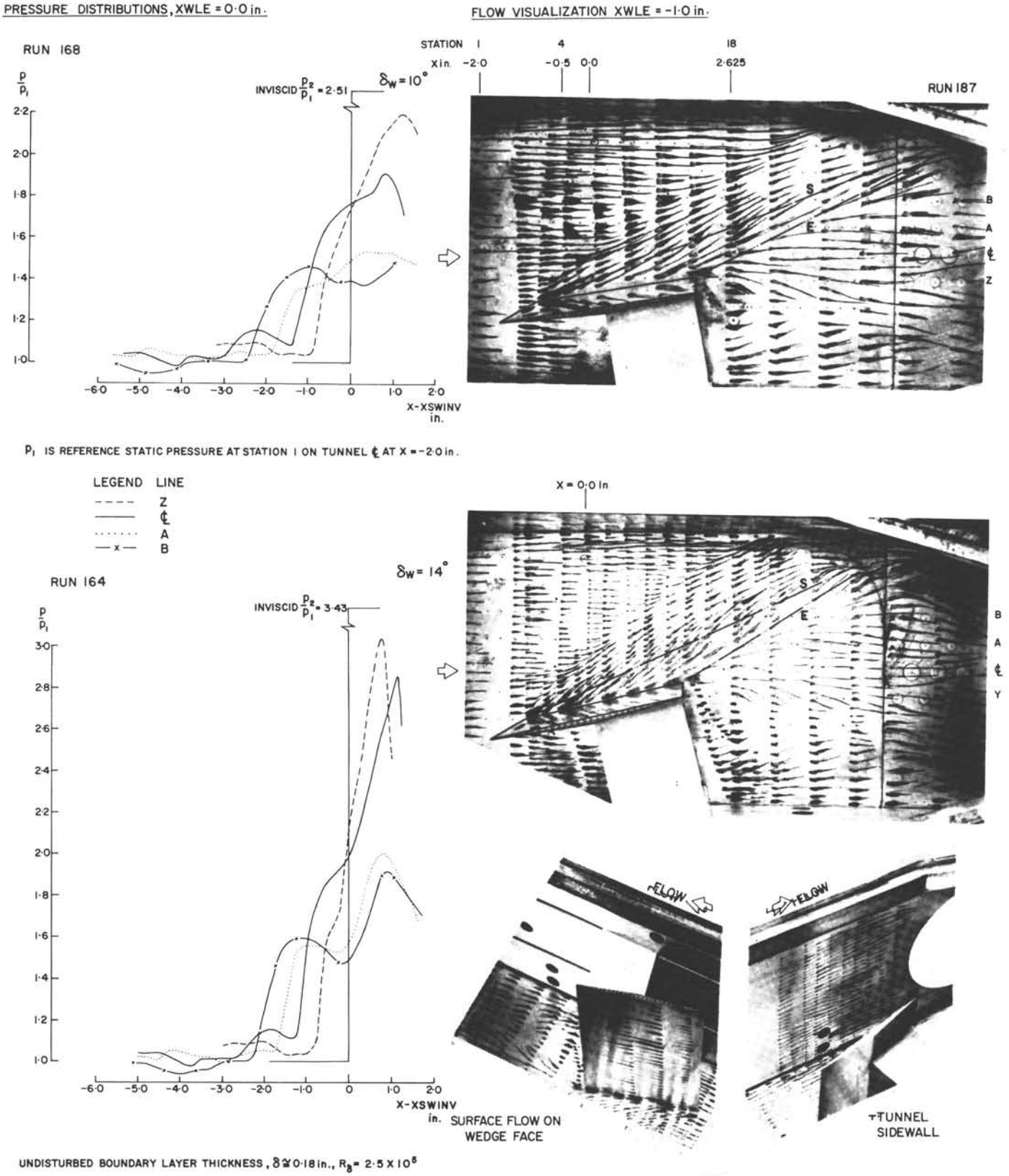

FIG. 53: SURFACE PRESSURE DISTRIBUTIONS AND FLOW VISUALIZATION FOR δ_w = 10 AND 14-DEGREES AT MACH 4 (FLOOR V.G. IN)

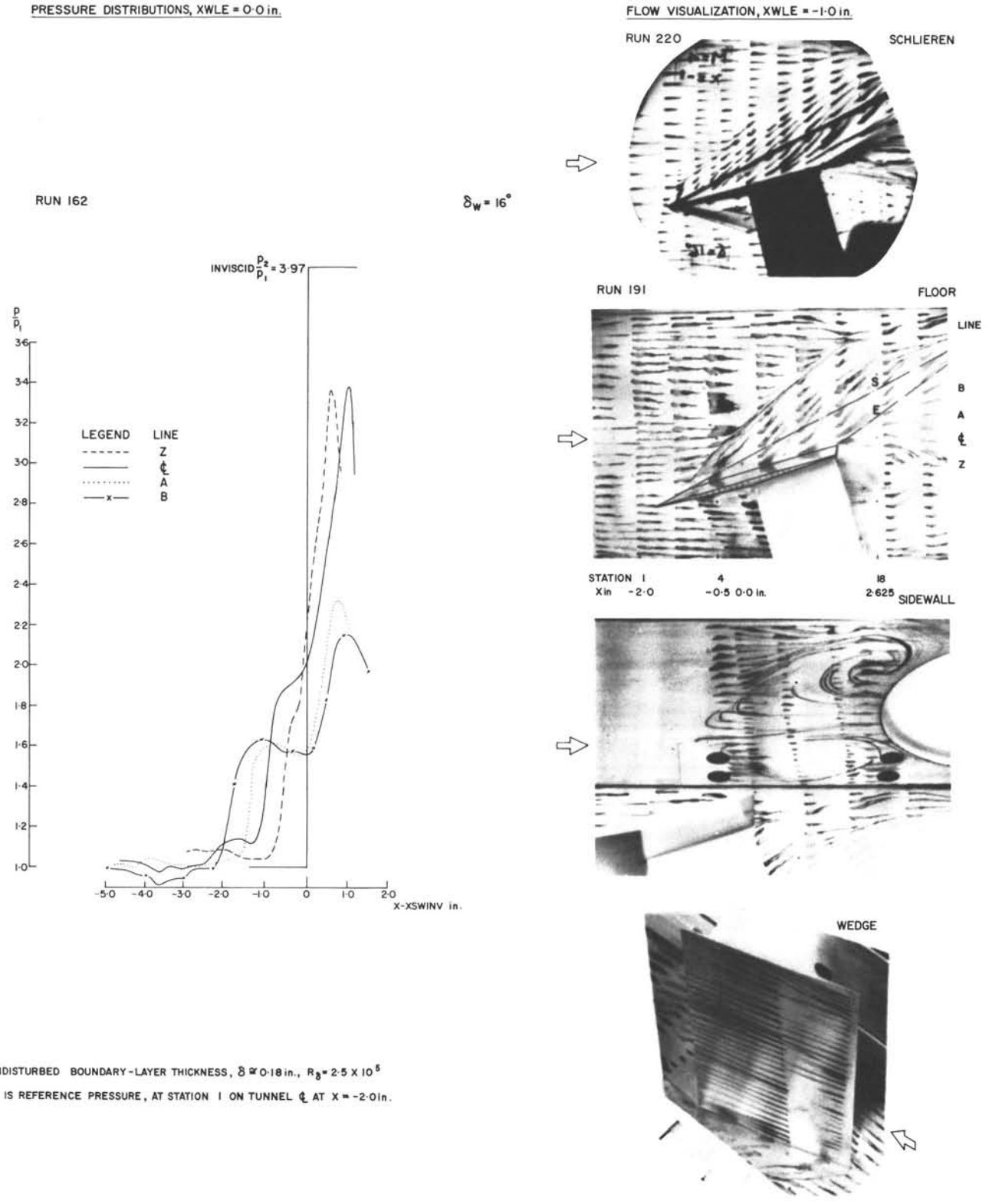

UNDISTURBED BOUNDARY-LAYER THICKNESS, $\delta \approx 0.18$ in., $R_\delta = 2.5 \times 10^5$

p_1 IS REFERENCE PRESSURE, AT STATION 1 ON TUNNEL ℄ AT X = -2·0 in.

FIG. 54: SURFACE PRESSURE DISTRIBUTIONS AND FLOW VISUALIZATION FOR STRONG 3D SWEPT INTERACTION, δ_w = 16-DEGREES AT MACH 4 (FLOOR V.G. IN)

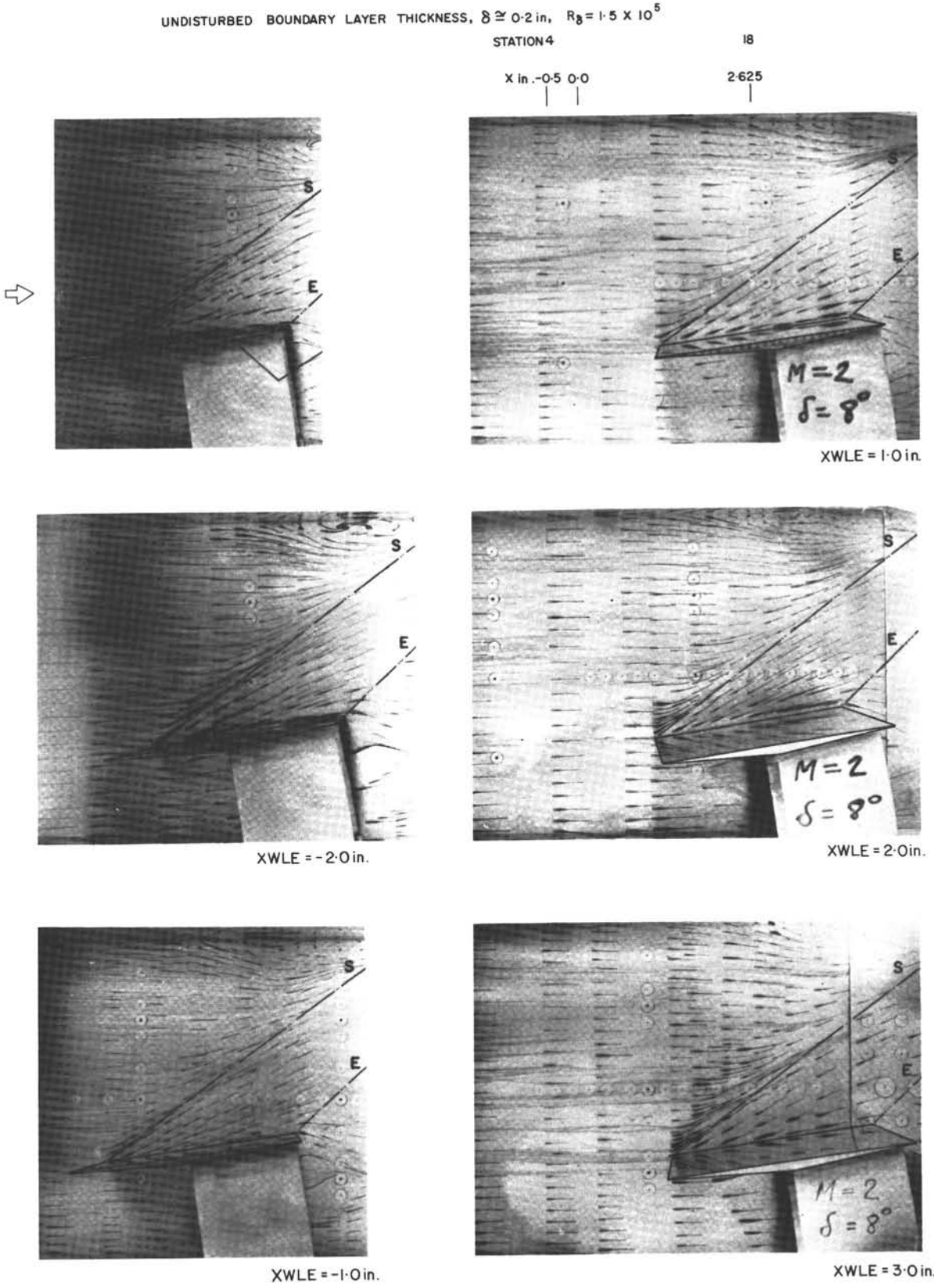

FIG. 55: SURFACE FLOW VISUALIZATION WITH CHANGE OF WEDGE AXIAL LOCATION FOR δ_w = 8-DEGREES AT MACH 2

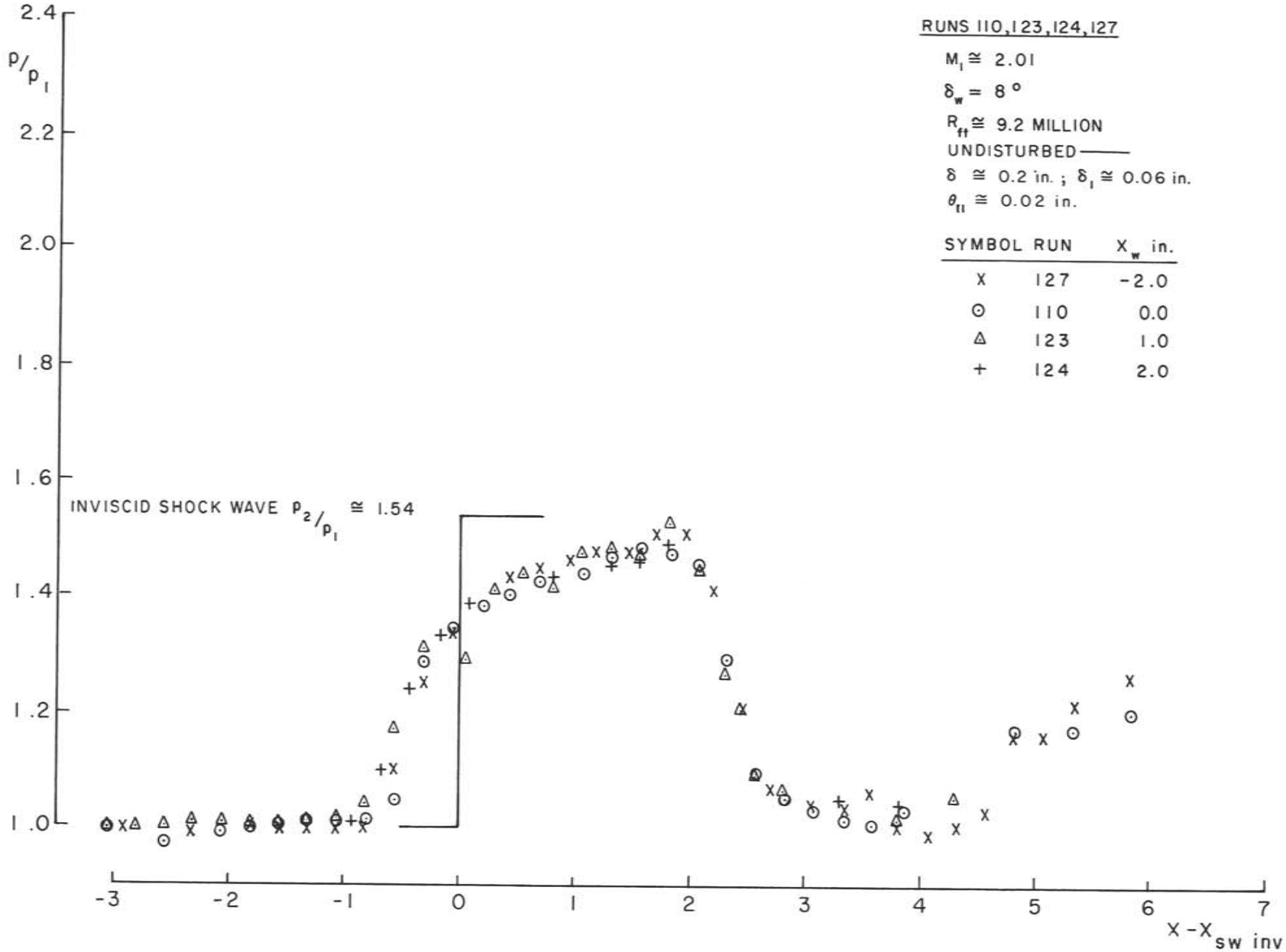

FIG. 56: CENTRE-LINE PRESSURES AT MACH 2 AND WEDGE ANGLE OF 8-DEGREES FOR VARIOUS LONGITUDINAL POSITIONS OF WEDGE

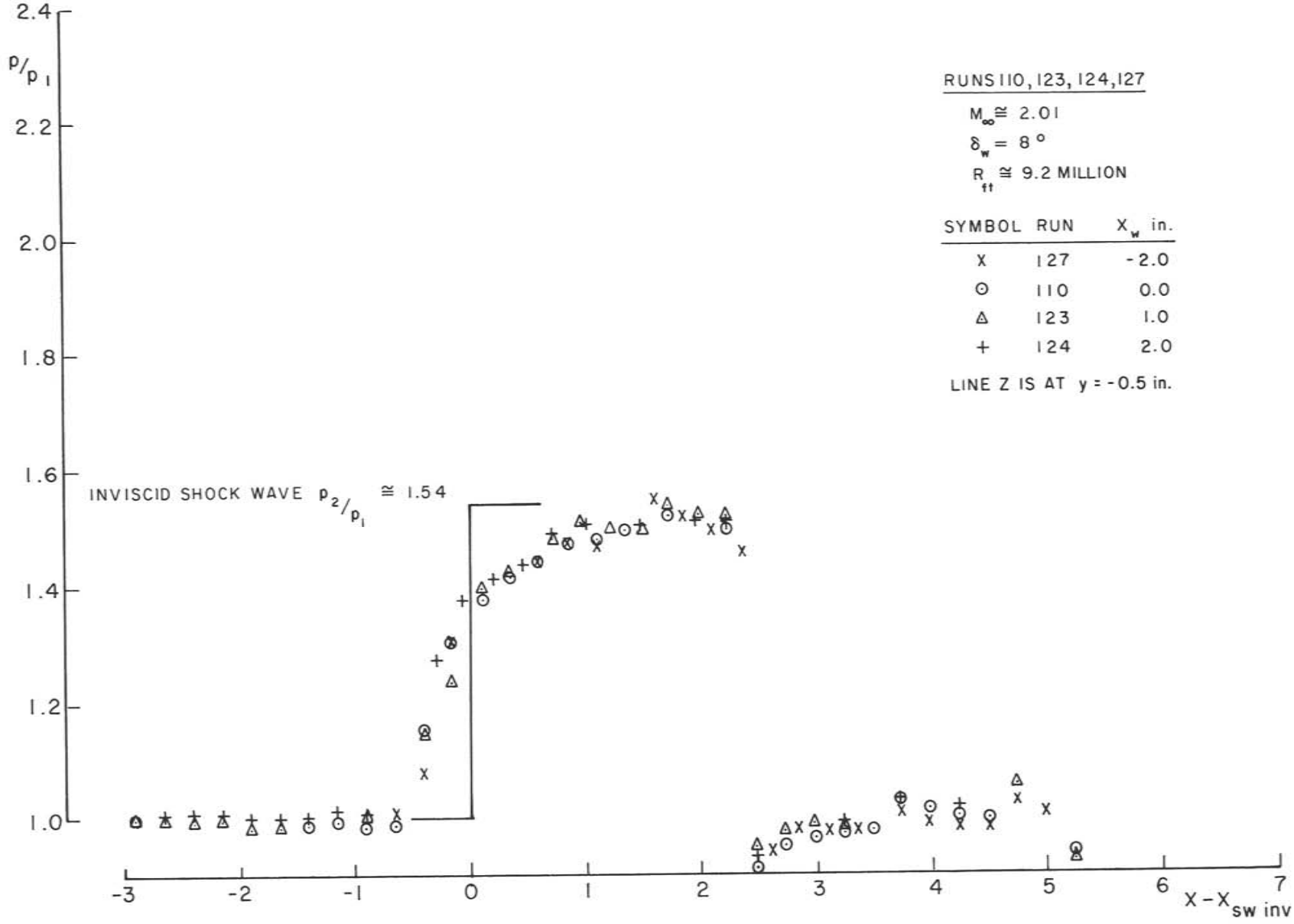

FIG. 57: PRESSURES ALONG LINE Z AT MACH 2 AND WEDGE ANGLE OF 8-DEGREES FOR VARIOUS LONGITUDINAL POSITIONS OF WEDGE

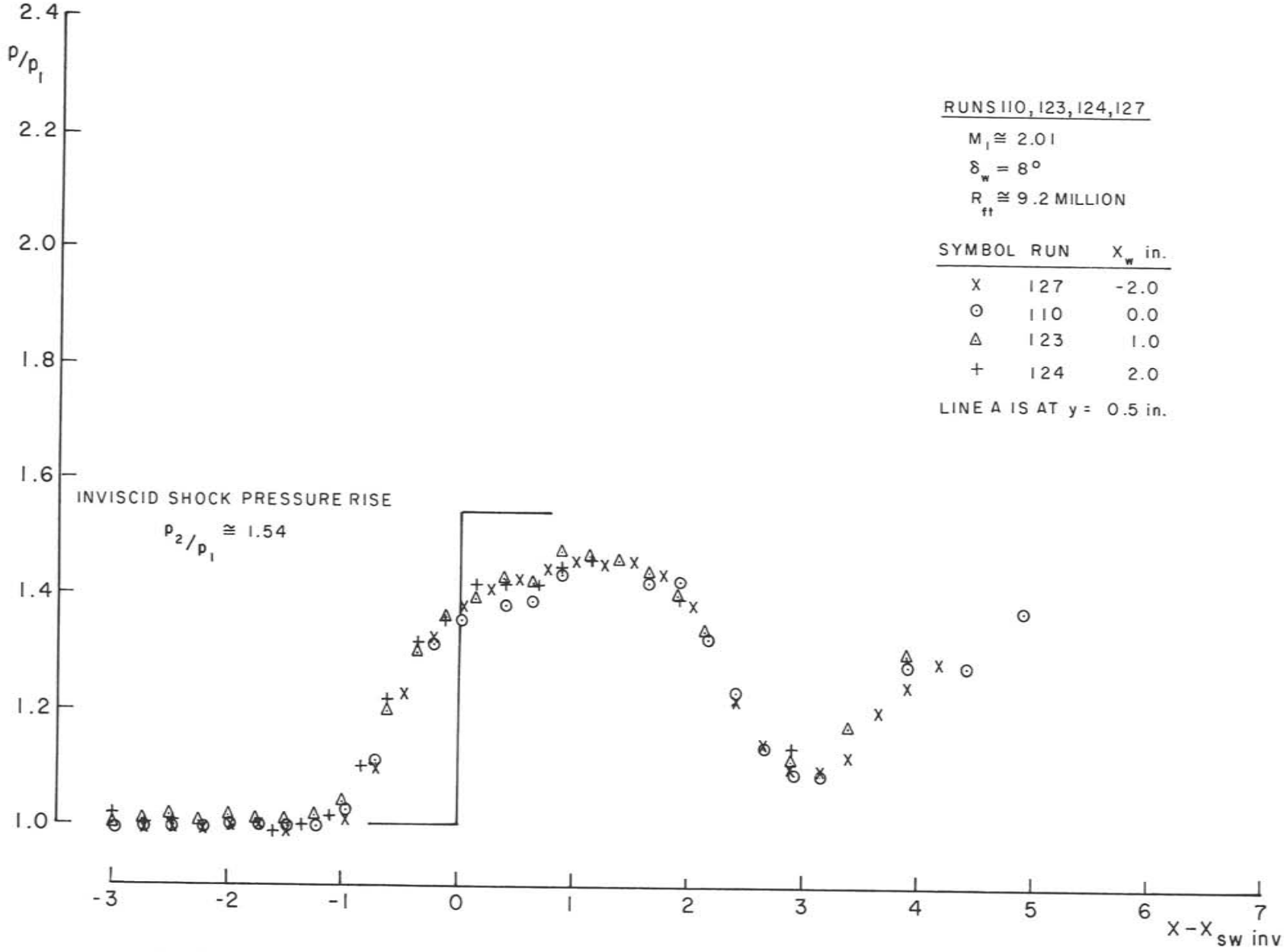

FIG. 58: PRESSURES ALONG LINE A AT MACH 2 AND WEDGE ANGLE OF 8-DEGREES FOR VARIOUS LONGITUDINAL POSITIONS OF WEDGE

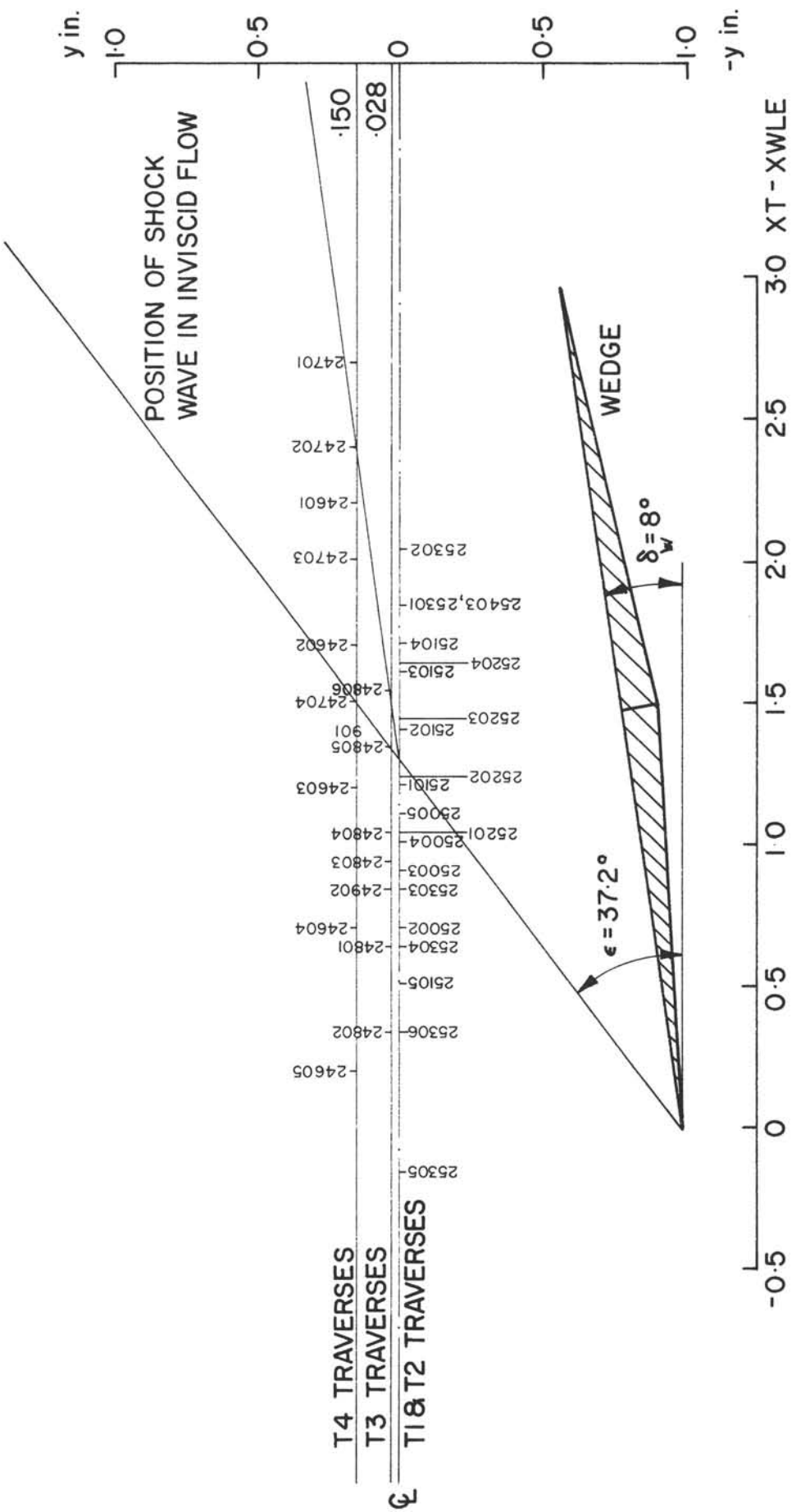

FIG. 59: MAP OF COBRA PROBE TRAVERSE LOCATIONS AT MACH 2, δ_w = 8-DEGREES

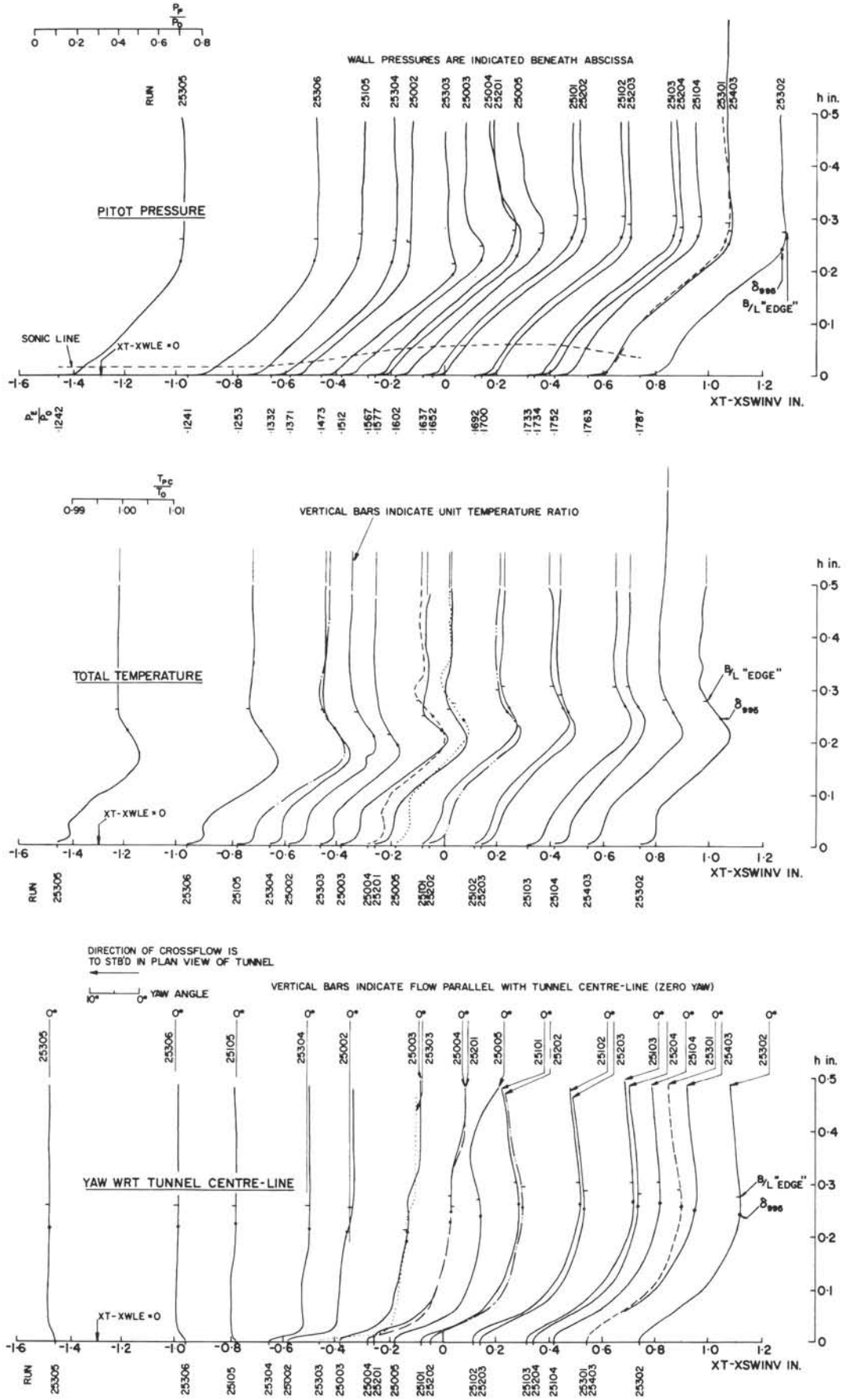

FIG. 60: COBRA PROBE MEASUREMENTS ALONG TUNNEL ℄ AT MACH 2 AND δ_w = 8-DEGREES

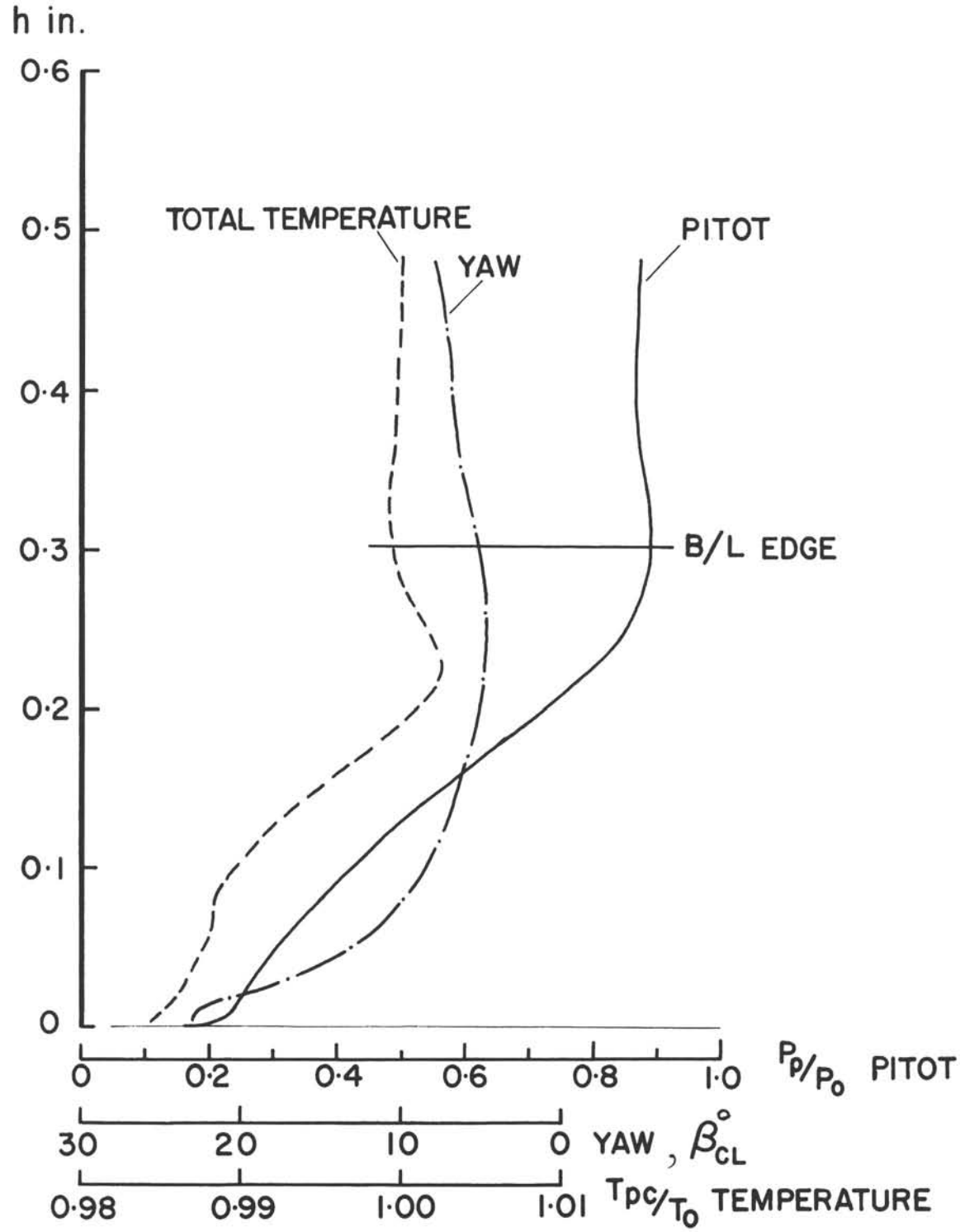

FIG. 61: PITOT, TOTAL TEMPERATURE AND YAW ANGLE DISTRIBUTIONS FOR RUN 25101 NEAR INVISCID SHOCK WAVE LOCATION; FOR δ_w = 8-DEGREES AT MACH 2

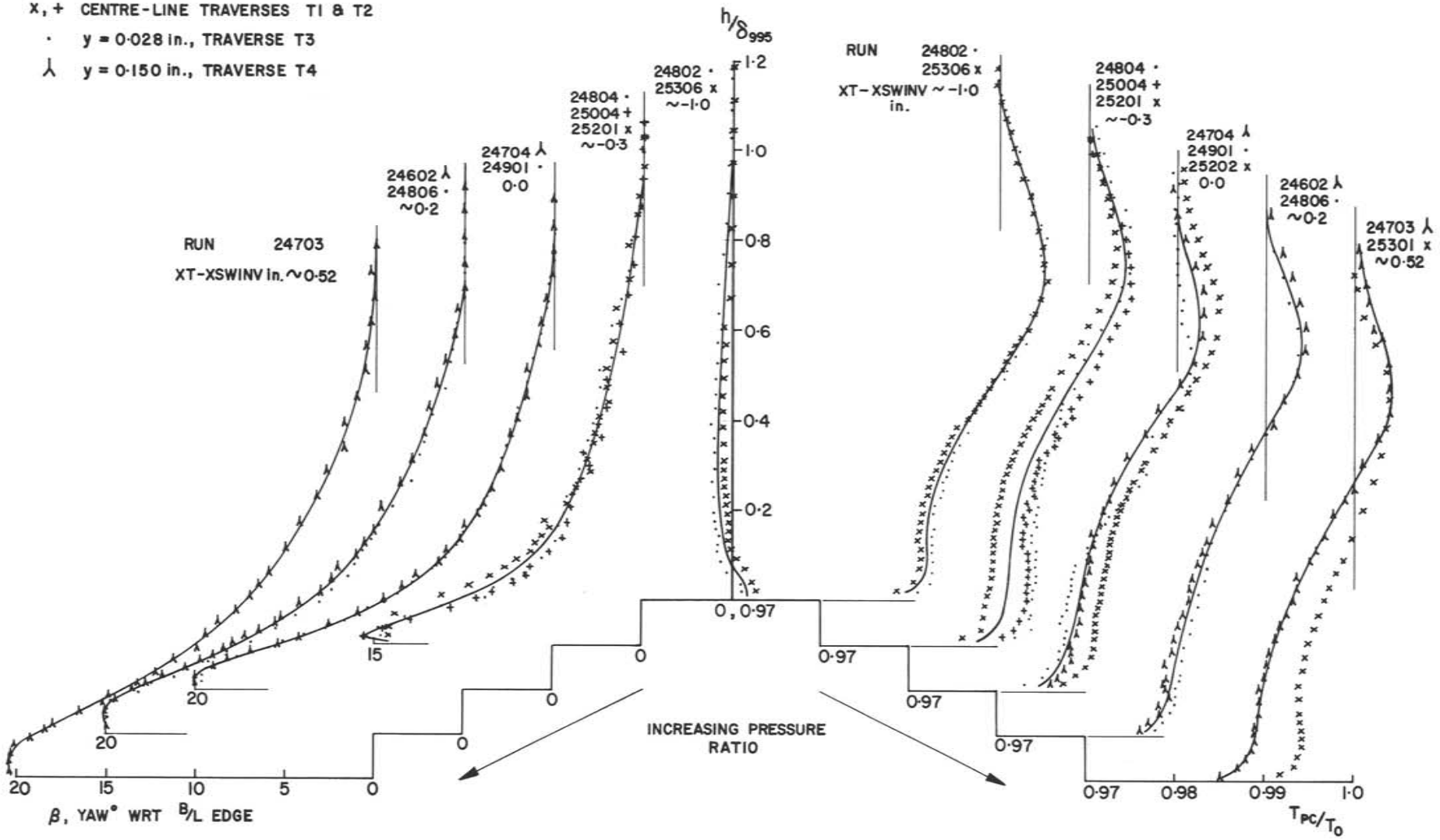

FIG. 62: YAW AND TOTAL TEMPERATURE DISTRIBUTIONS FOR δ_w = 8-DEGREES AT MACH 2

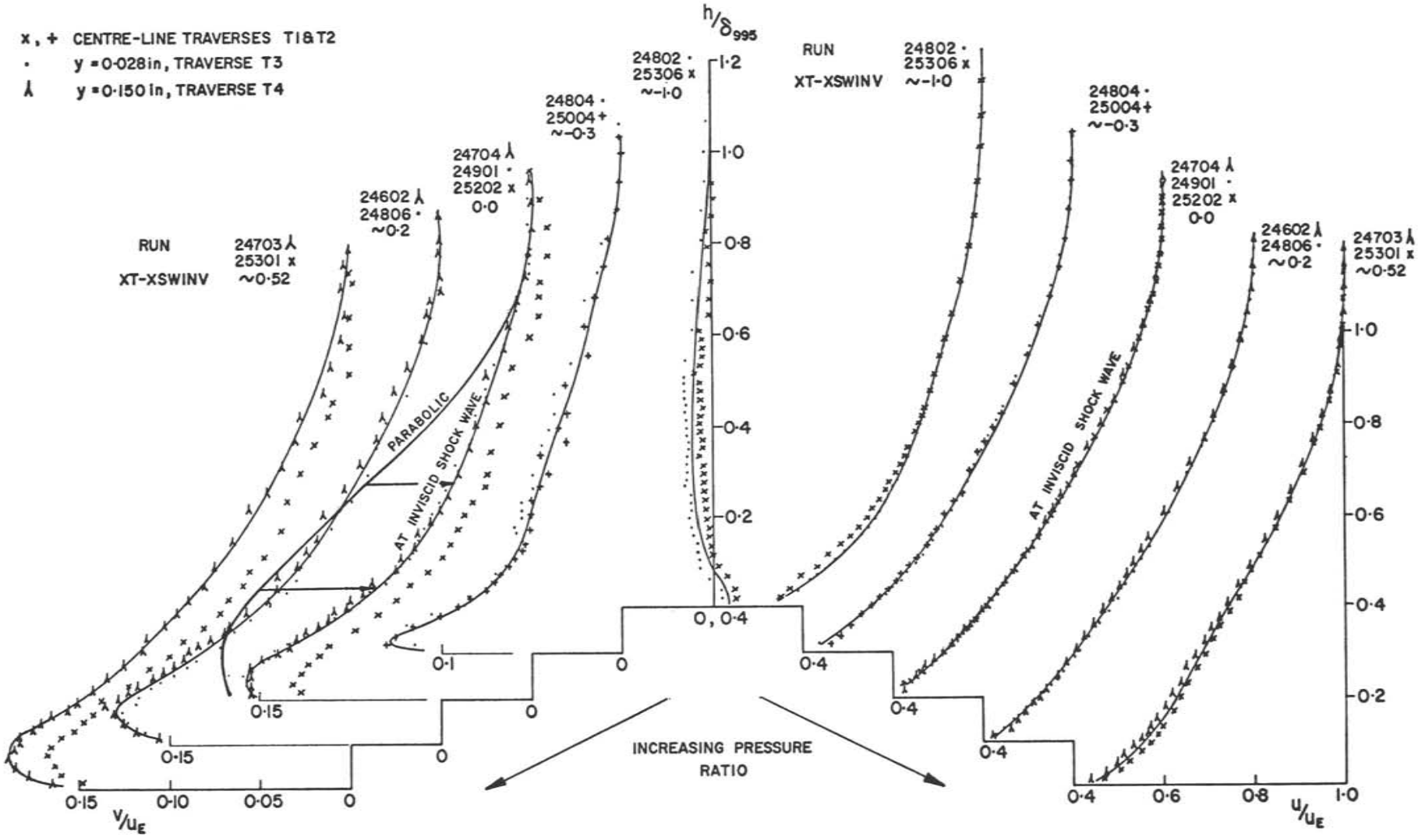

FIG. 63: CROSSFLOW AND STREAMWISE FLOW VELOCITY PROFILES FOR δ_w = 8-DEGREES AT MACH 2

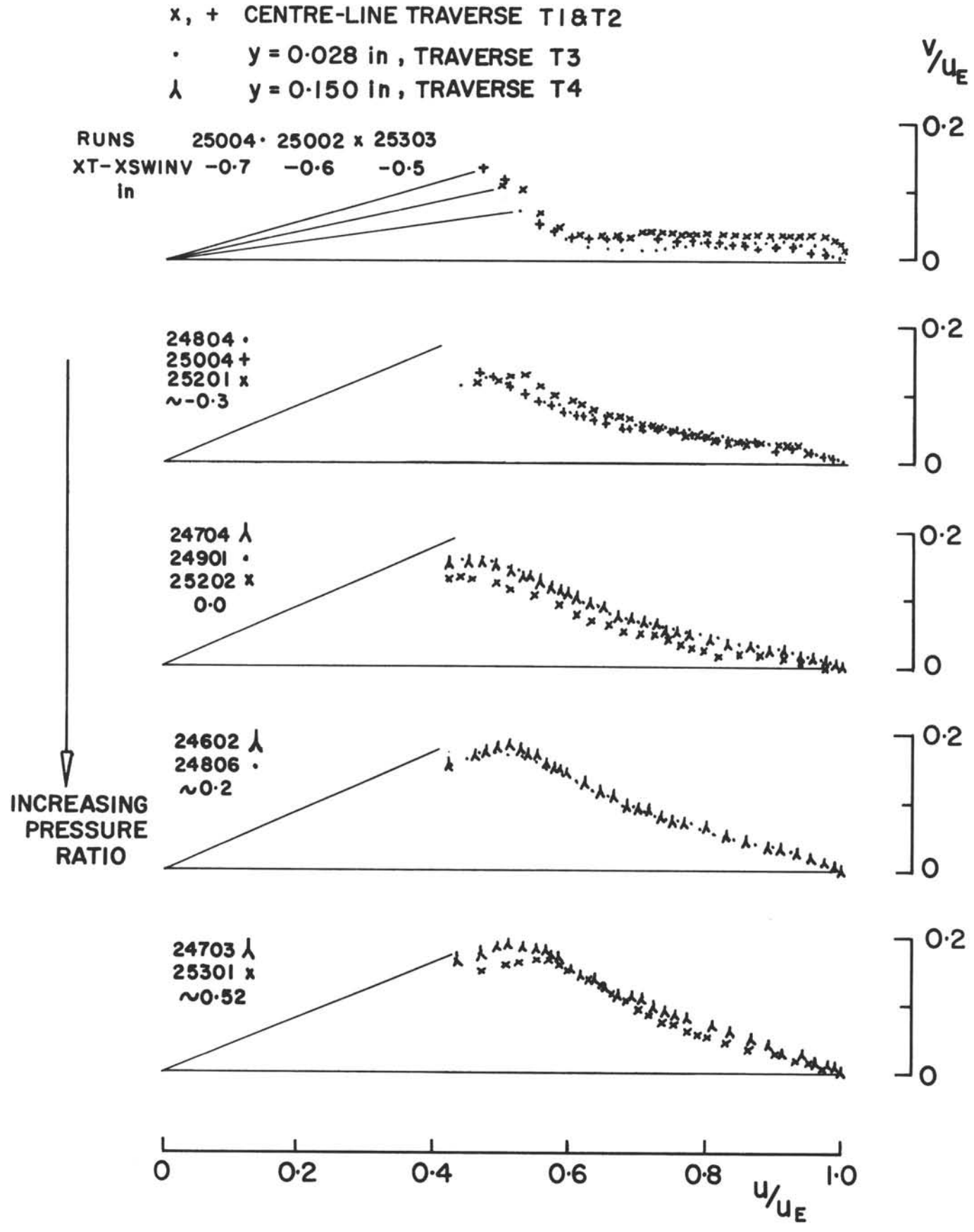

FIG. 64: POLAR PLOTS OF VELOCITY PROFILES FOR δ_w = 8-DEGREES AT MACH 2

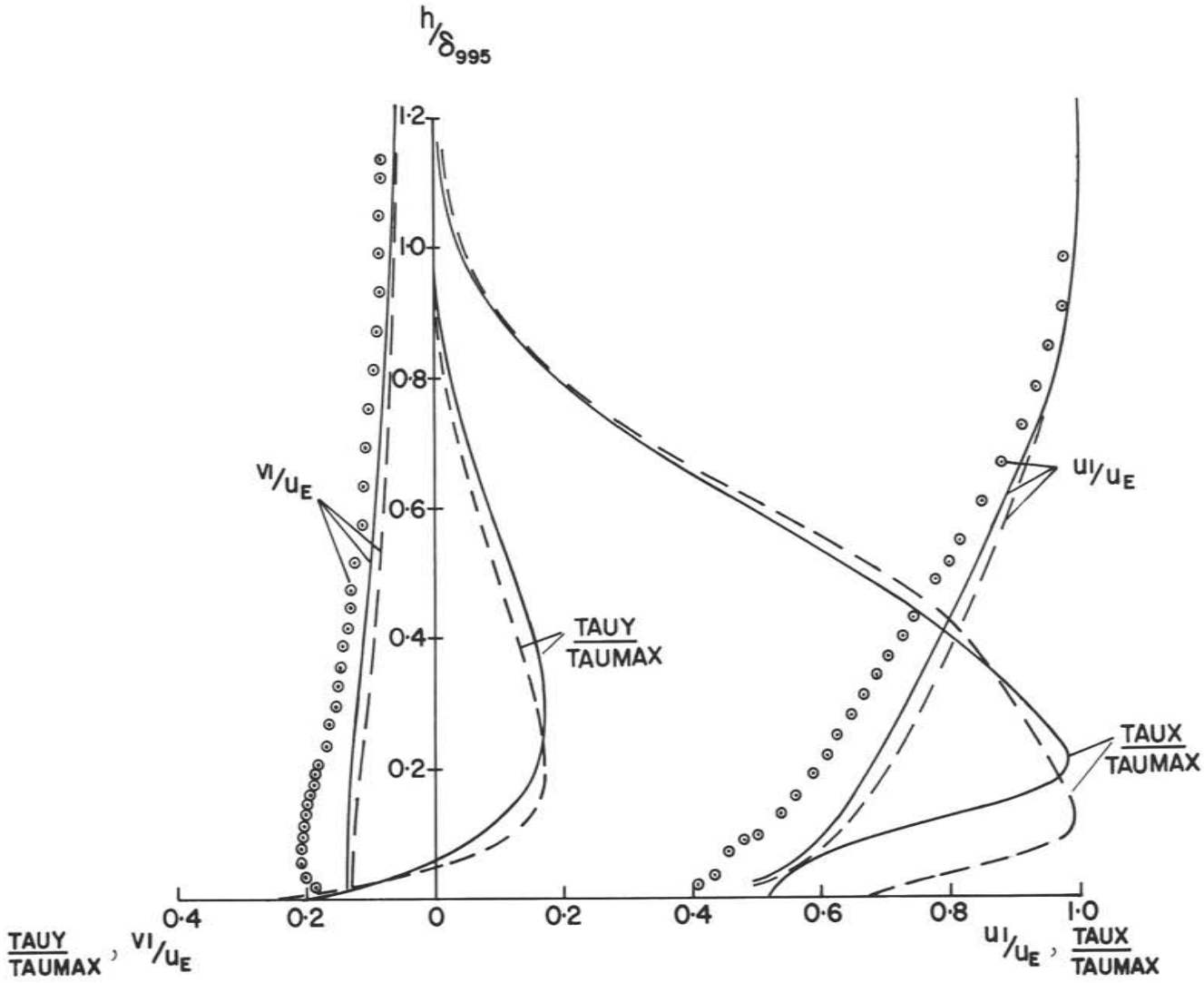

FIG. 65: COMPARISON BETWEEN EXPERIMENTAL AND CALCULATED VELOCITY PROFILES AT MACH 2

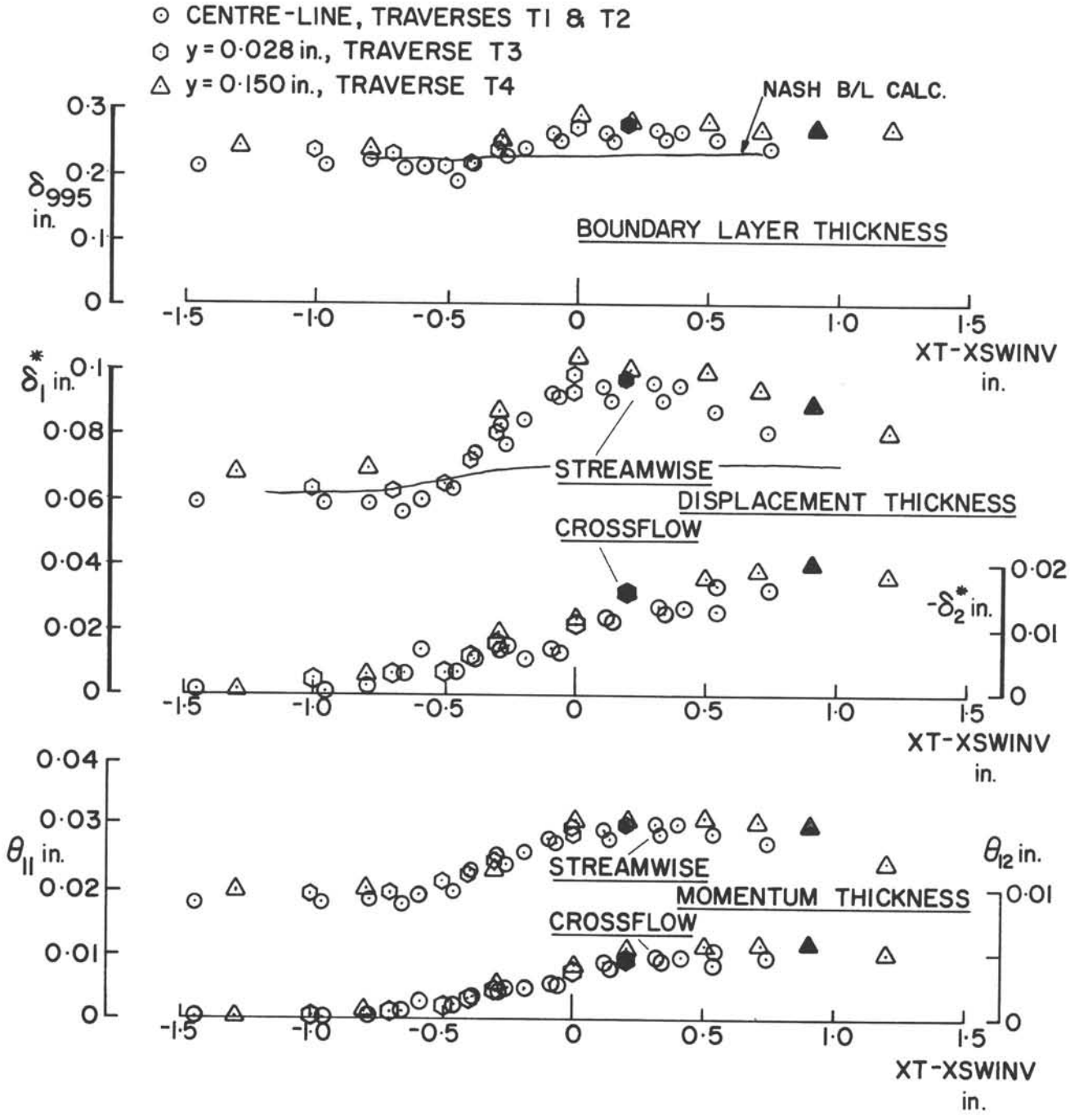

FIG. 66: INTEGRAL PARAMETERS FOR δ_w = 8-DEGREES AT MACH 2

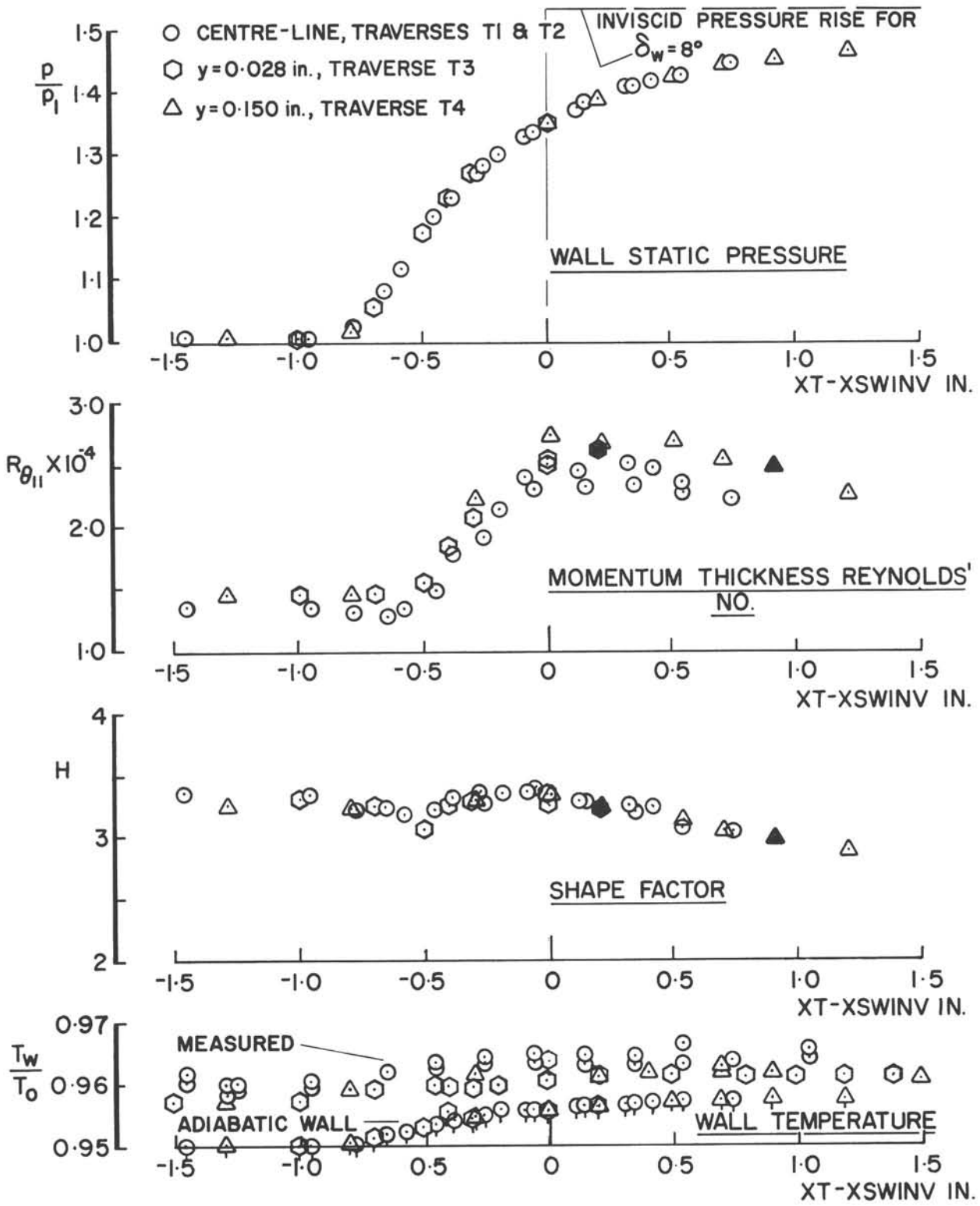

FIG. 67: STREAMWISE INTEGRAL PARAMETERS AND WALL CONDITIONS FOR δ_w = 8-DEGREES AT MACH 2

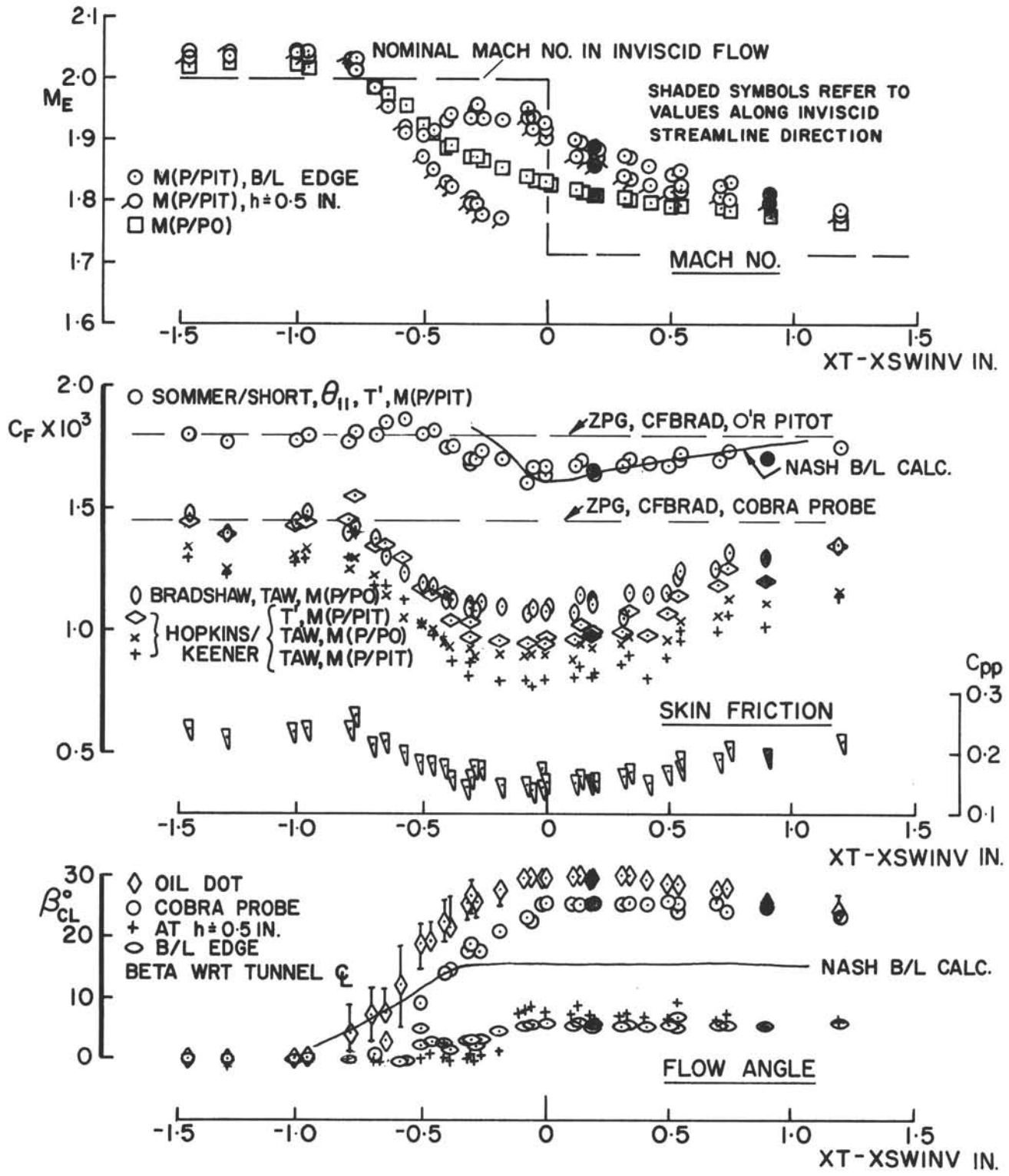

FIG. 68: LOCAL SKIN FRICTION AND FLOW DEFLECTIONS FOR δ_w = 8-DEGREES AT MACH 2

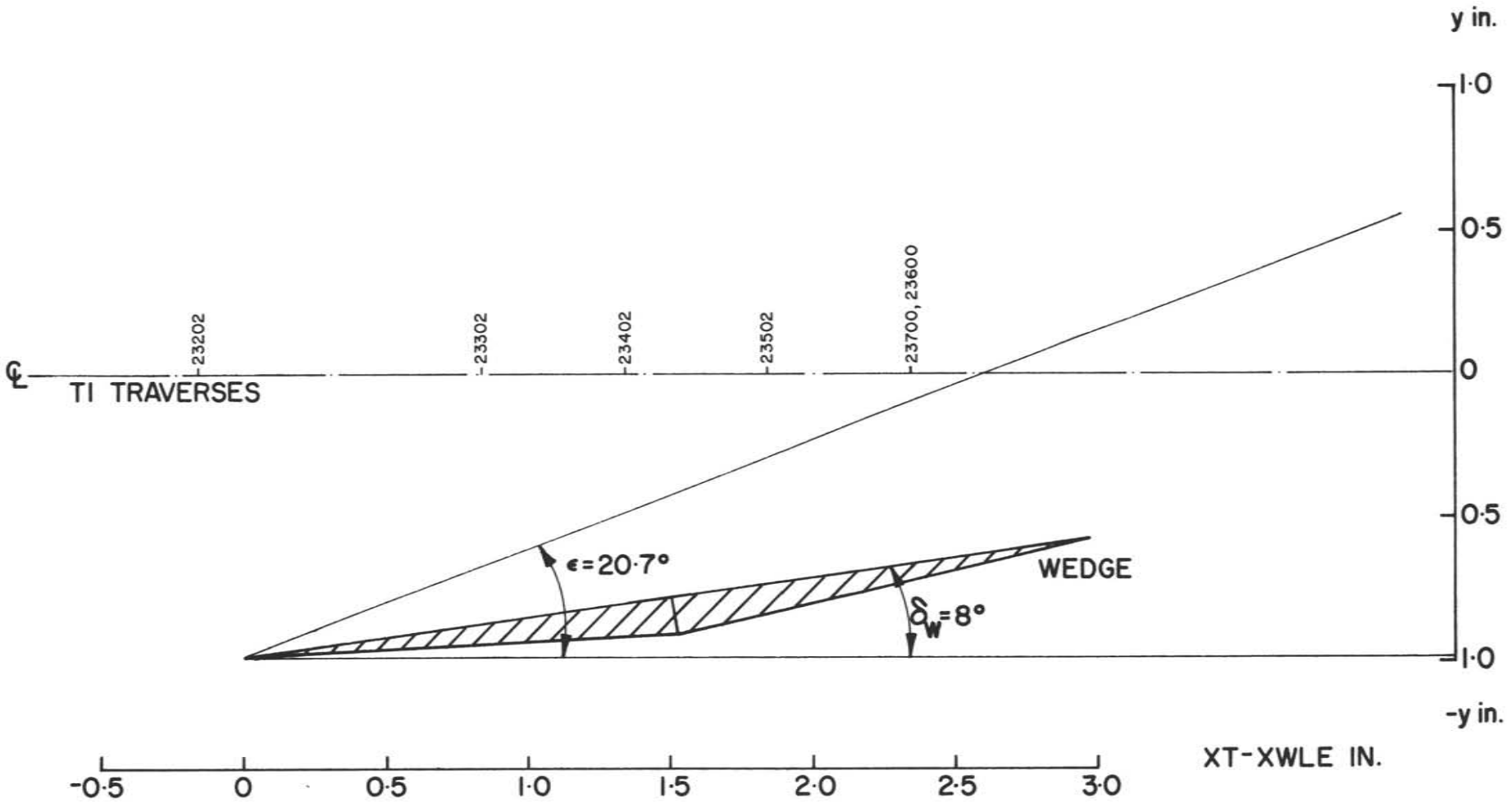

FIG. 69: MAP OF COBRA PROBE TRAVERSE LOCATIONS AT MACH 4, δ_w = 8-DEGREES

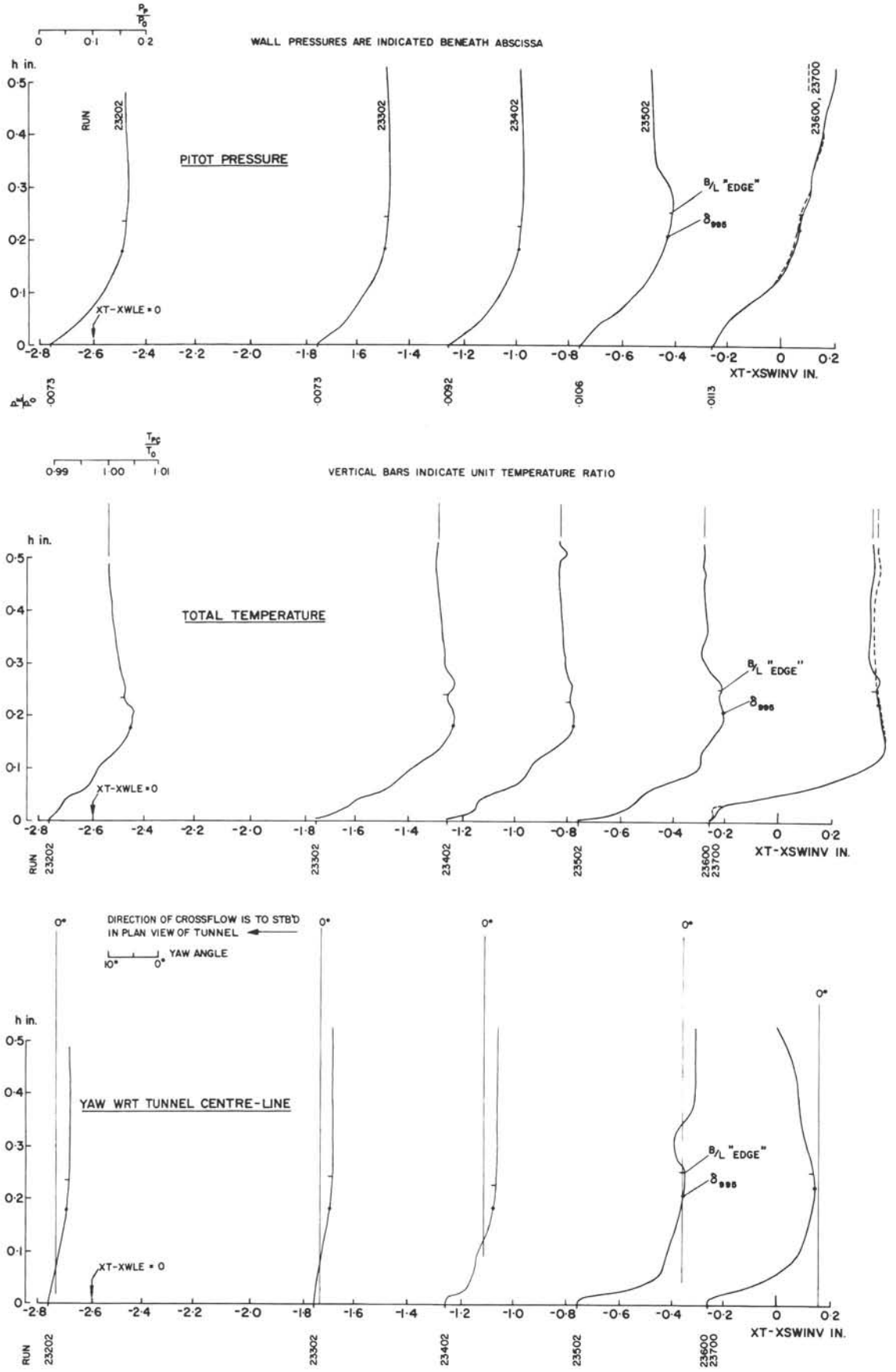

FIG. 70: COBRA PROBE MEASUREMENTS ALONG TUNNEL $\mathcal{L}$ AT MACH 4 AND δ_w = 8-DEGREES

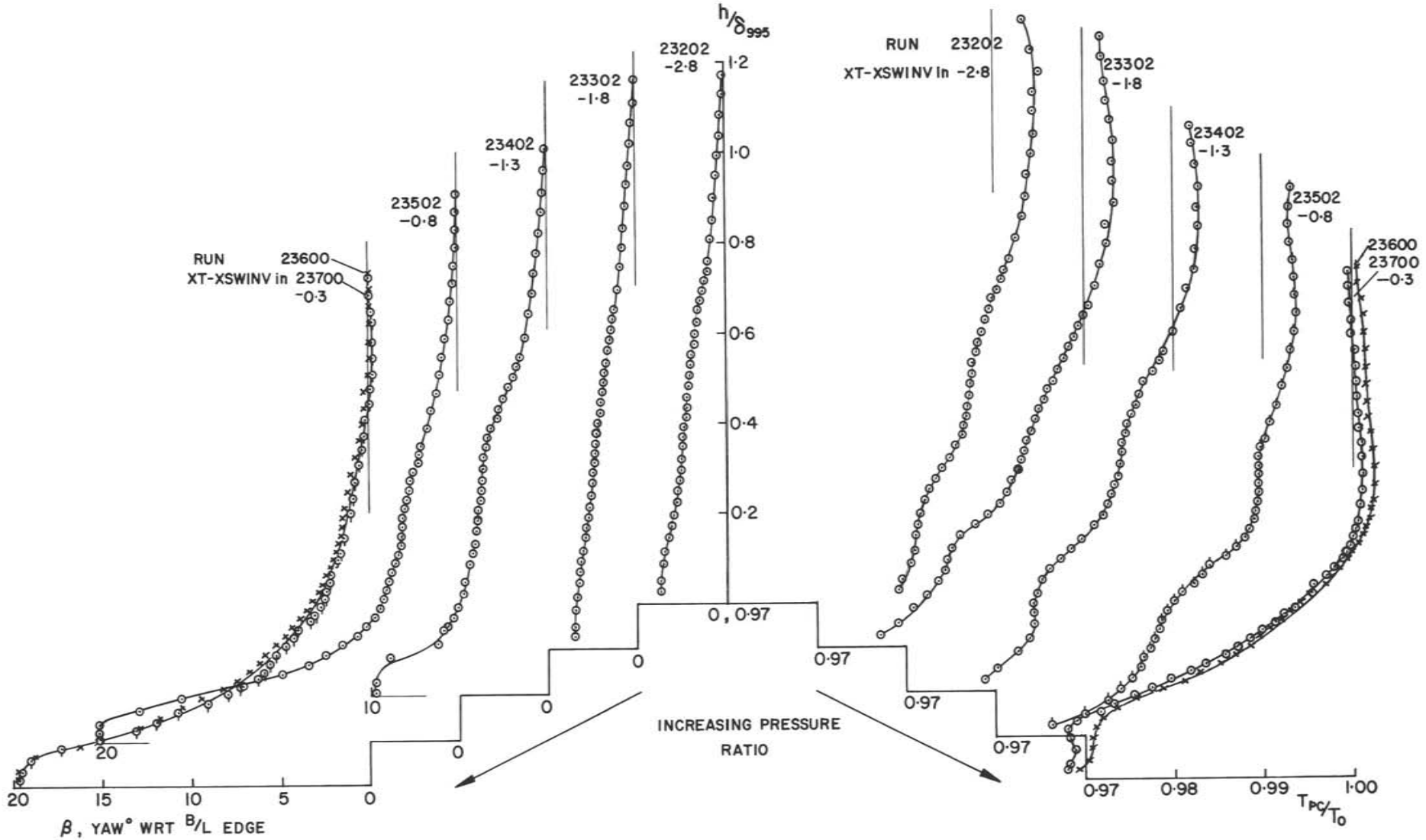

FIG. 71: YAW AND TOTAL TEMPERATURE DISTRIBUTIONS FOR δ_w = 8-DEGREES AT MACH 4

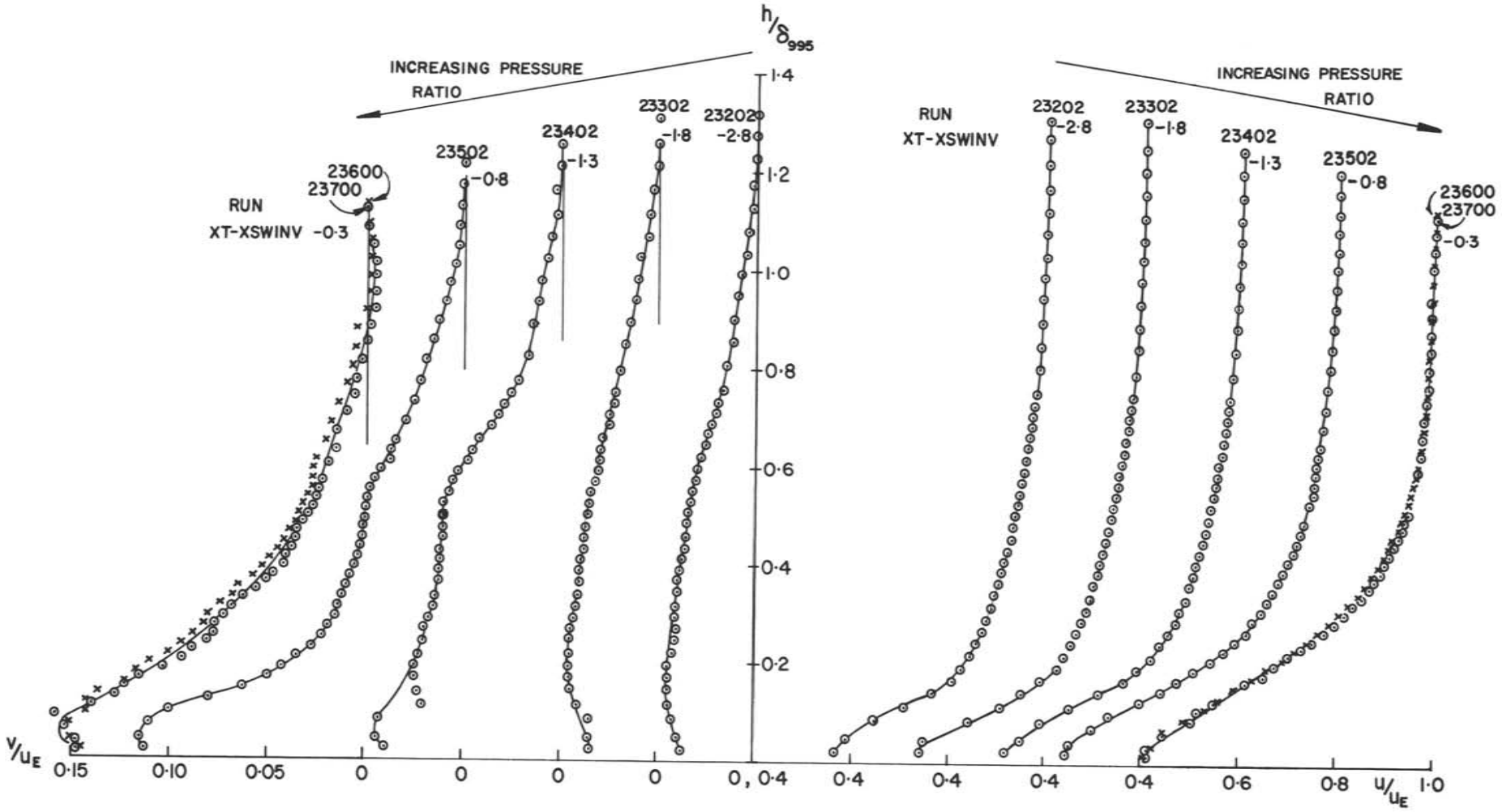

FIG. 72: CROSSFLOW AND STREAMWISE FLOW VELOCITY PROFILES FOR δ_w = 8-DEGREES AT MACH 4

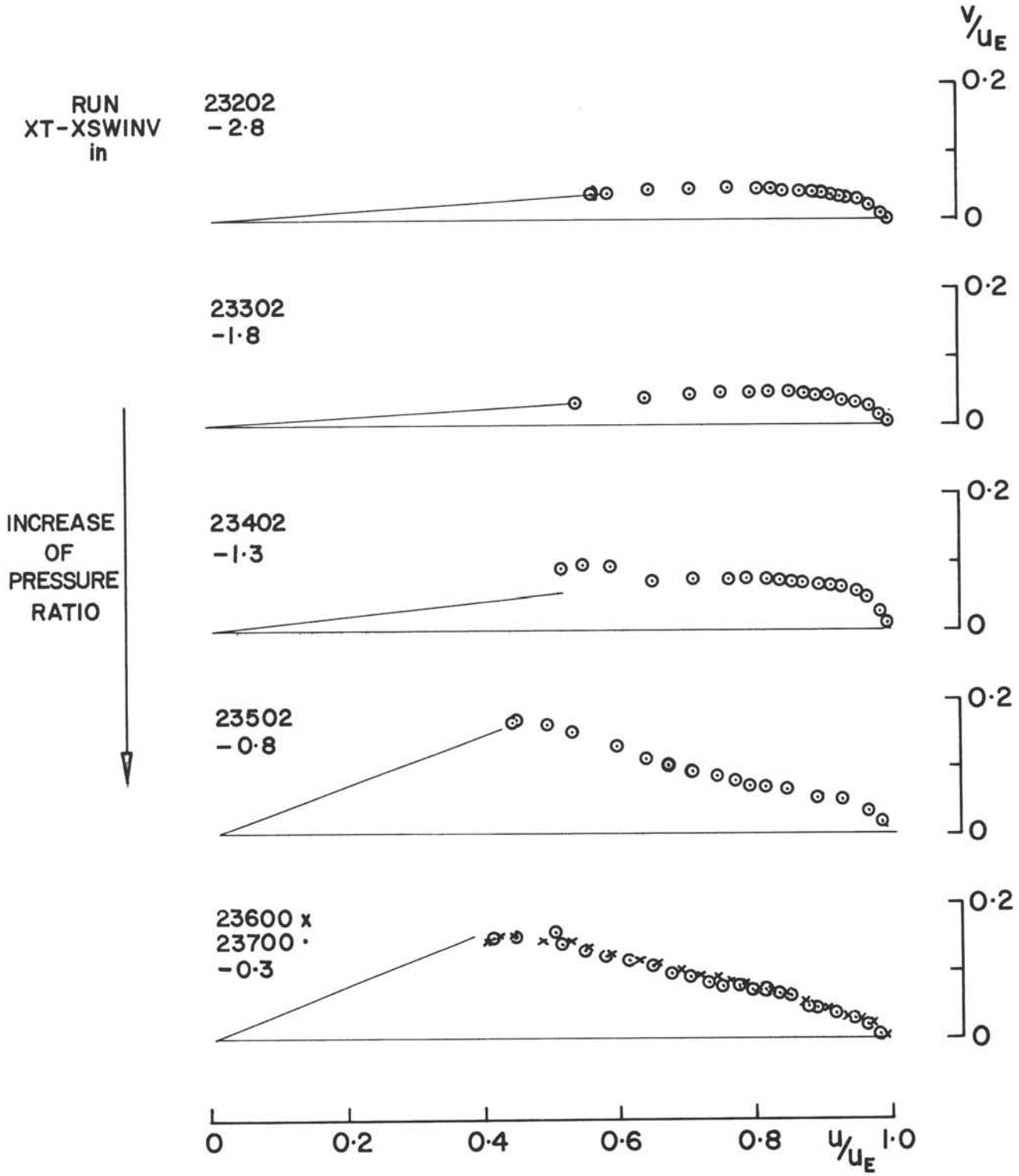

FIG. 73: POLAR PLOTS OF VELOCITY PROFILES FOR δ_w = 8-DEGREES AT MACH 4

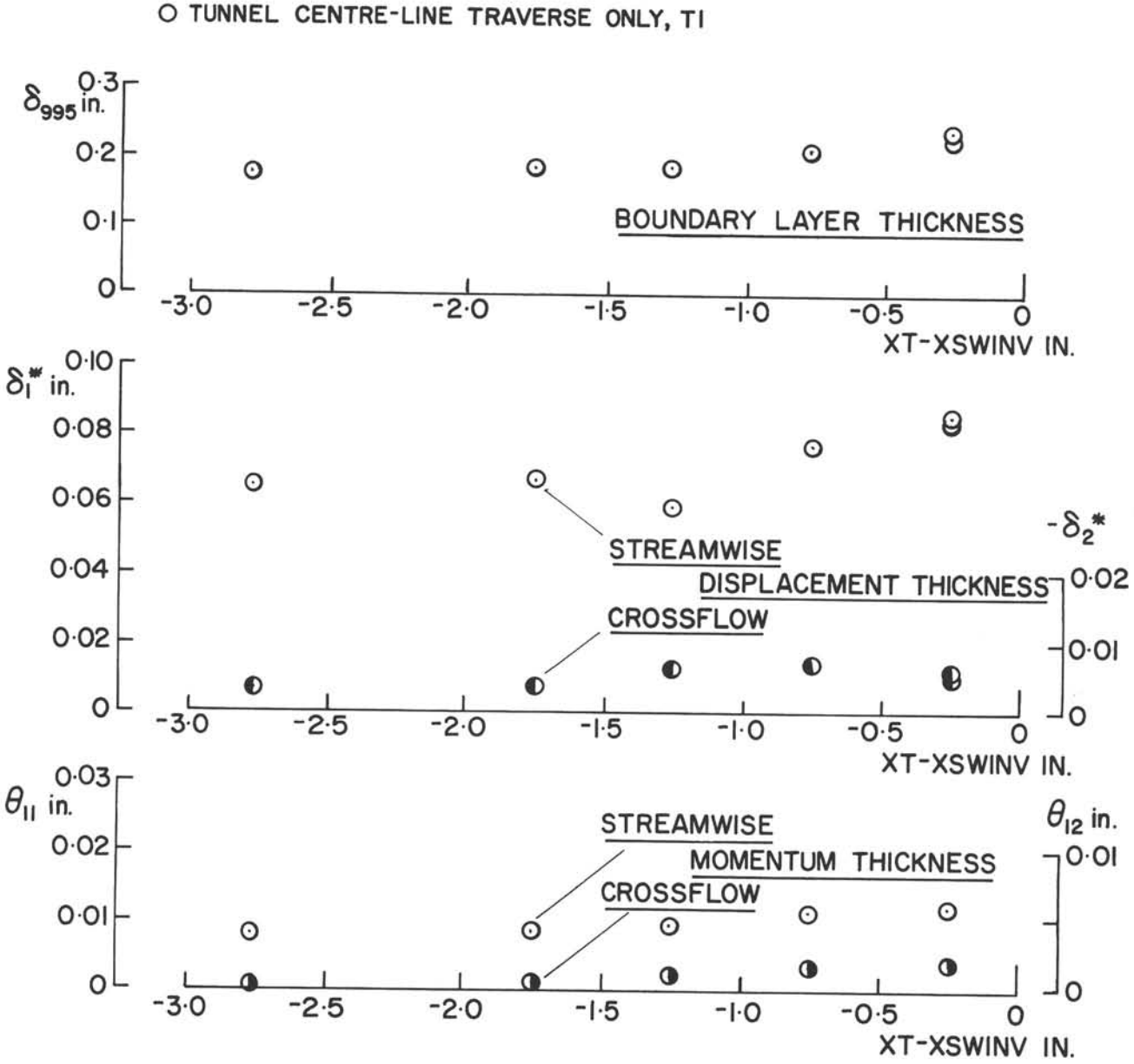

FIG. 74: INTEGRAL PARAMETERS FOR δ_w = 8-DEGREES AT MACH 4

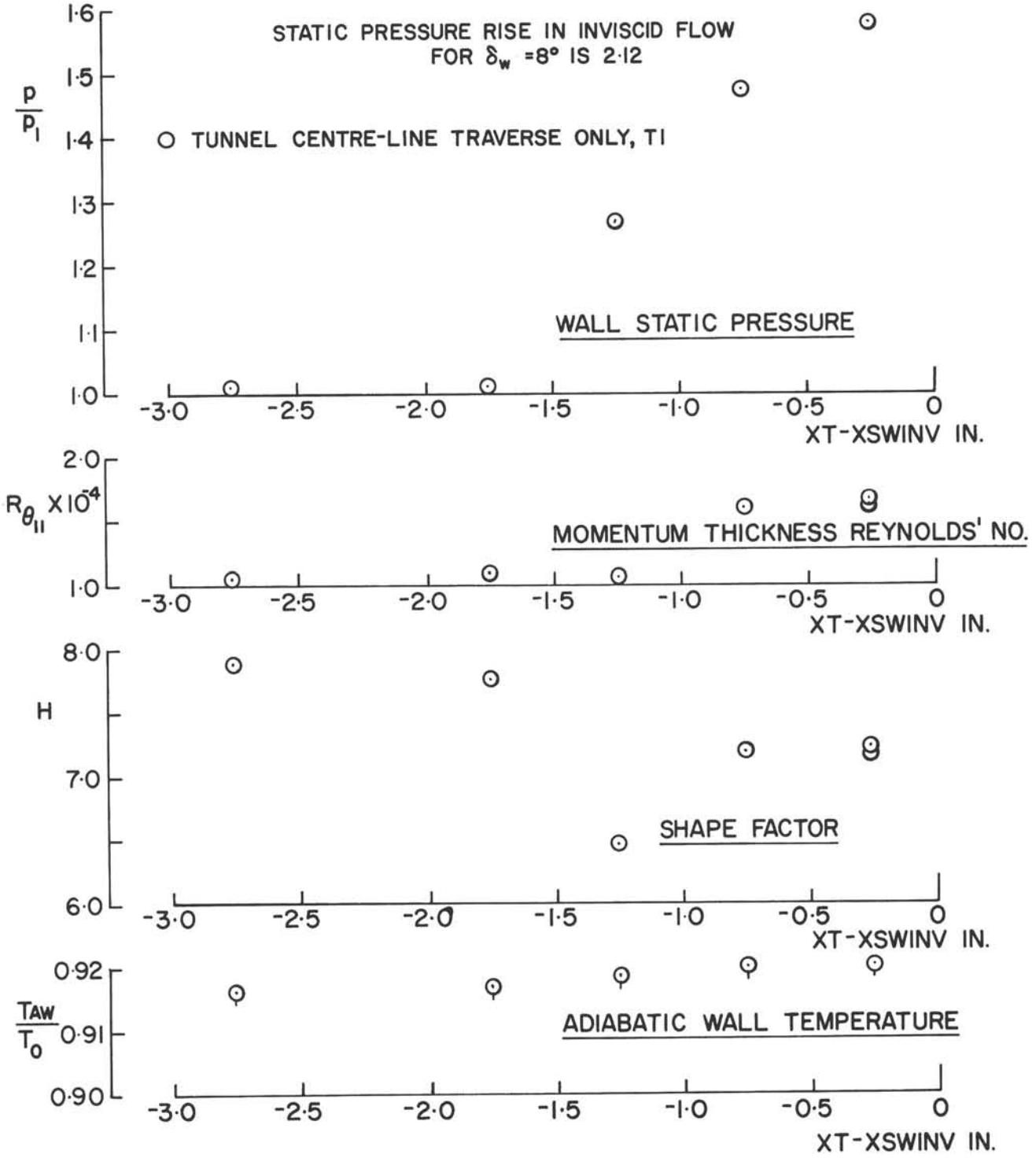

FIG. 75: STREAMWISE INTEGRAL PARAMETERS AND WALL CONDITIONS FOR δ_w = 8-DEGREES AT MACH 4

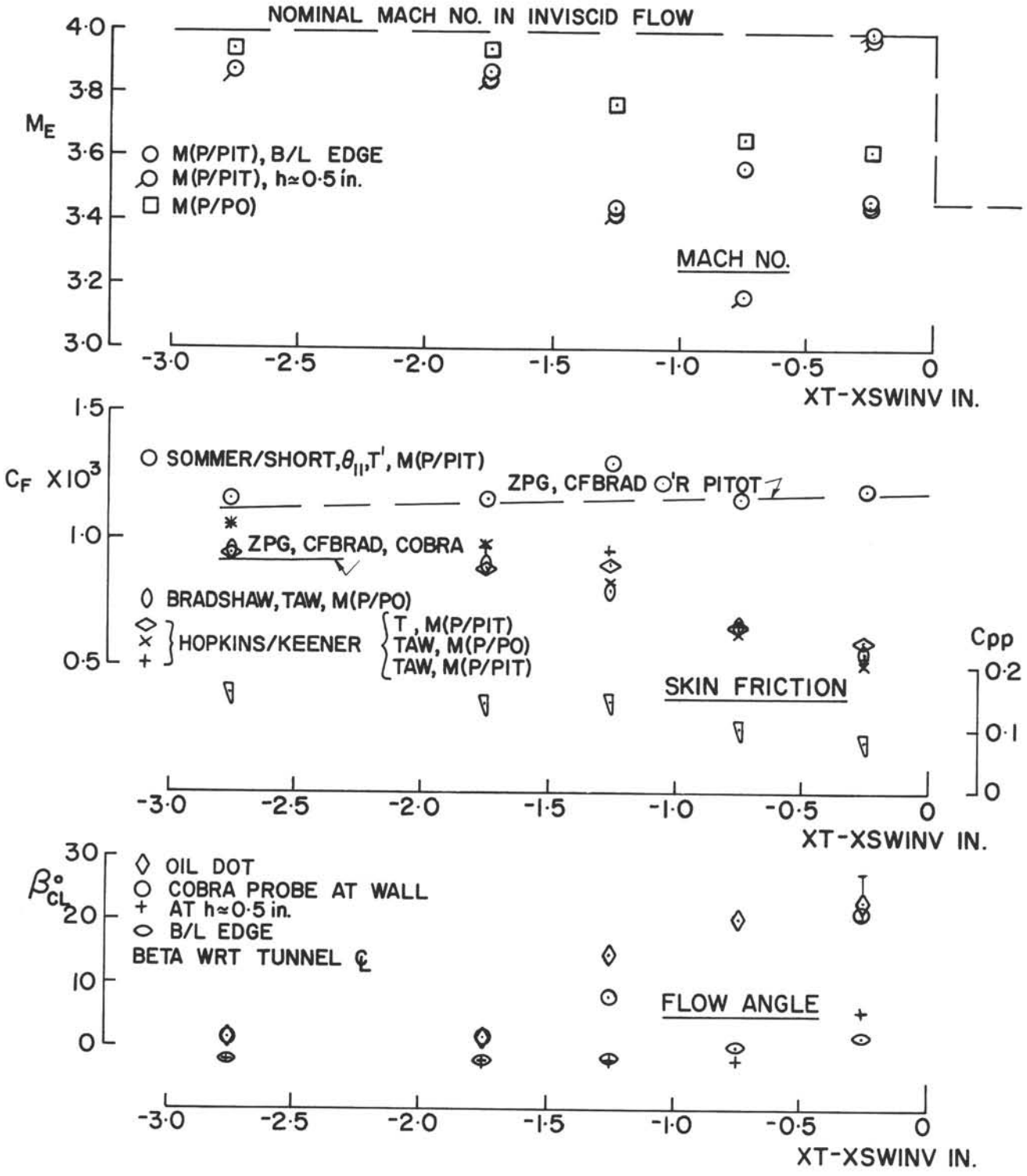

FIG. 76: LOCAL SKIN FRICTION AND FLOW DEFLECTIONS FOR δ_w = 8-DEGREES AT MACH 4

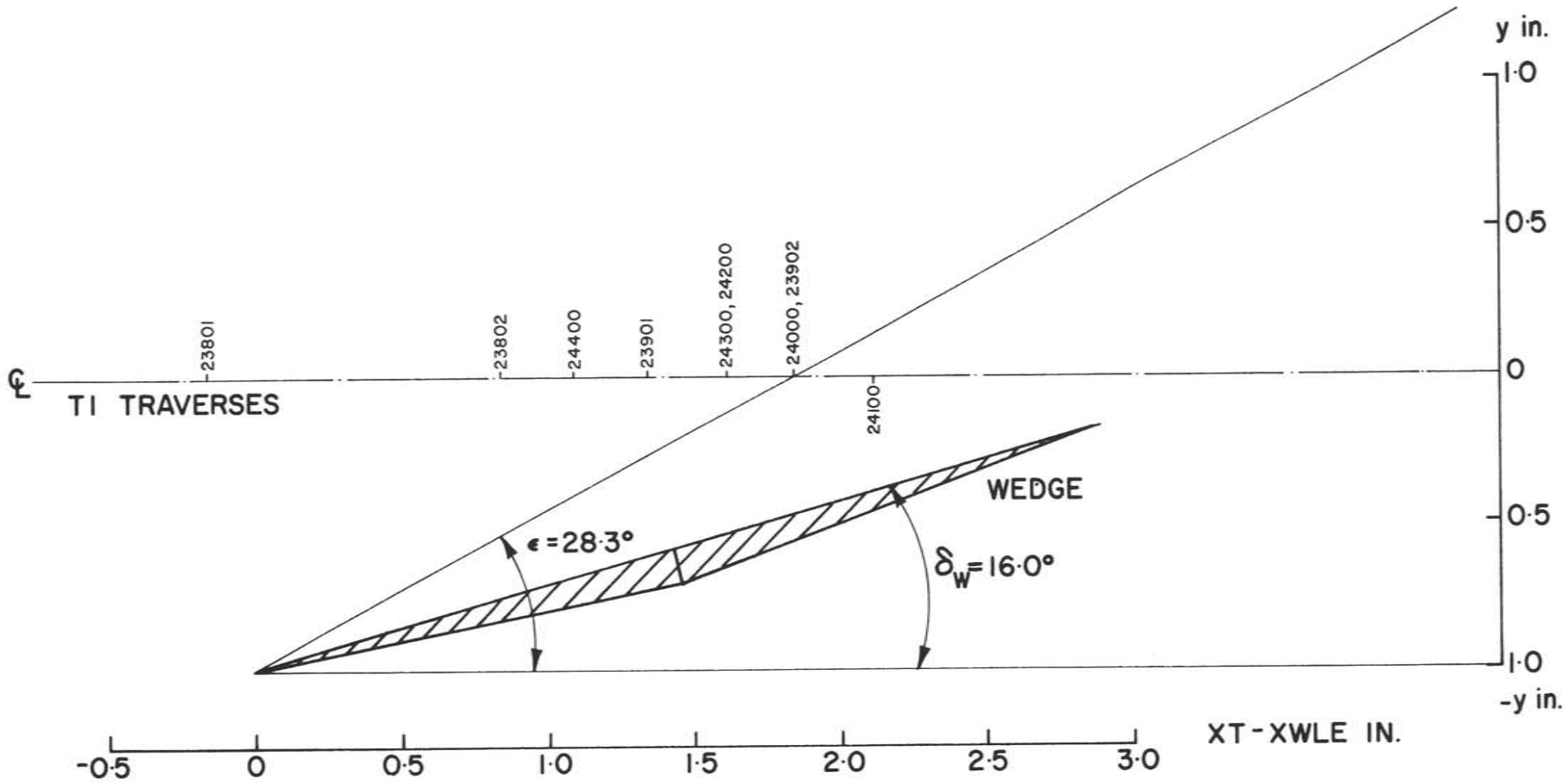

FIG. 77: MAP OF COBRA PROBE TRAVERSE LOCATIONS AT MACH 4, δ_w = 16-DEGREES

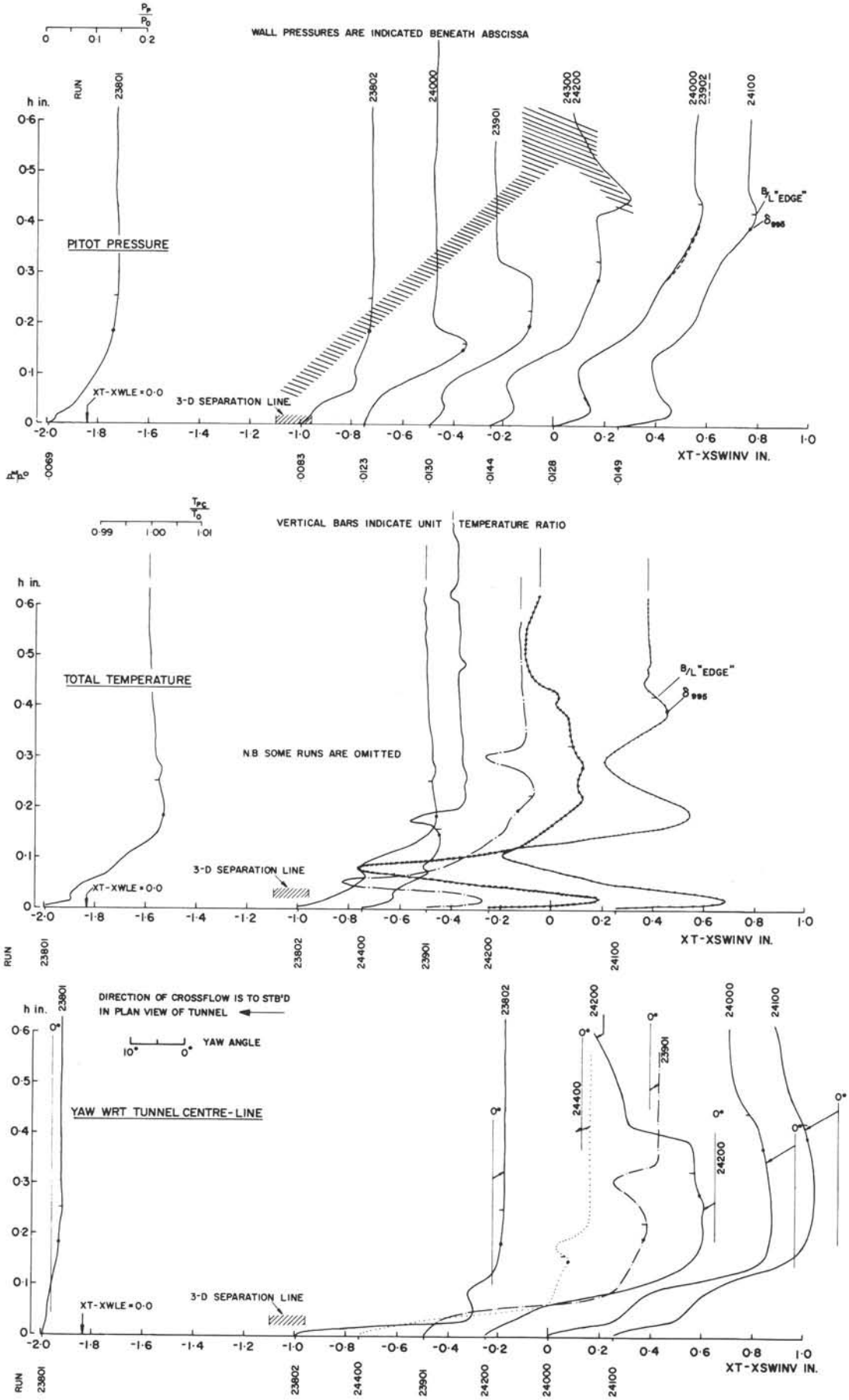

FIG. 78: COBRA PROBE MEASUREMENTS ALONG TUNNEL $\mathcal{L}$ AT MACH 4 AND δ_w = 16-DEGREES

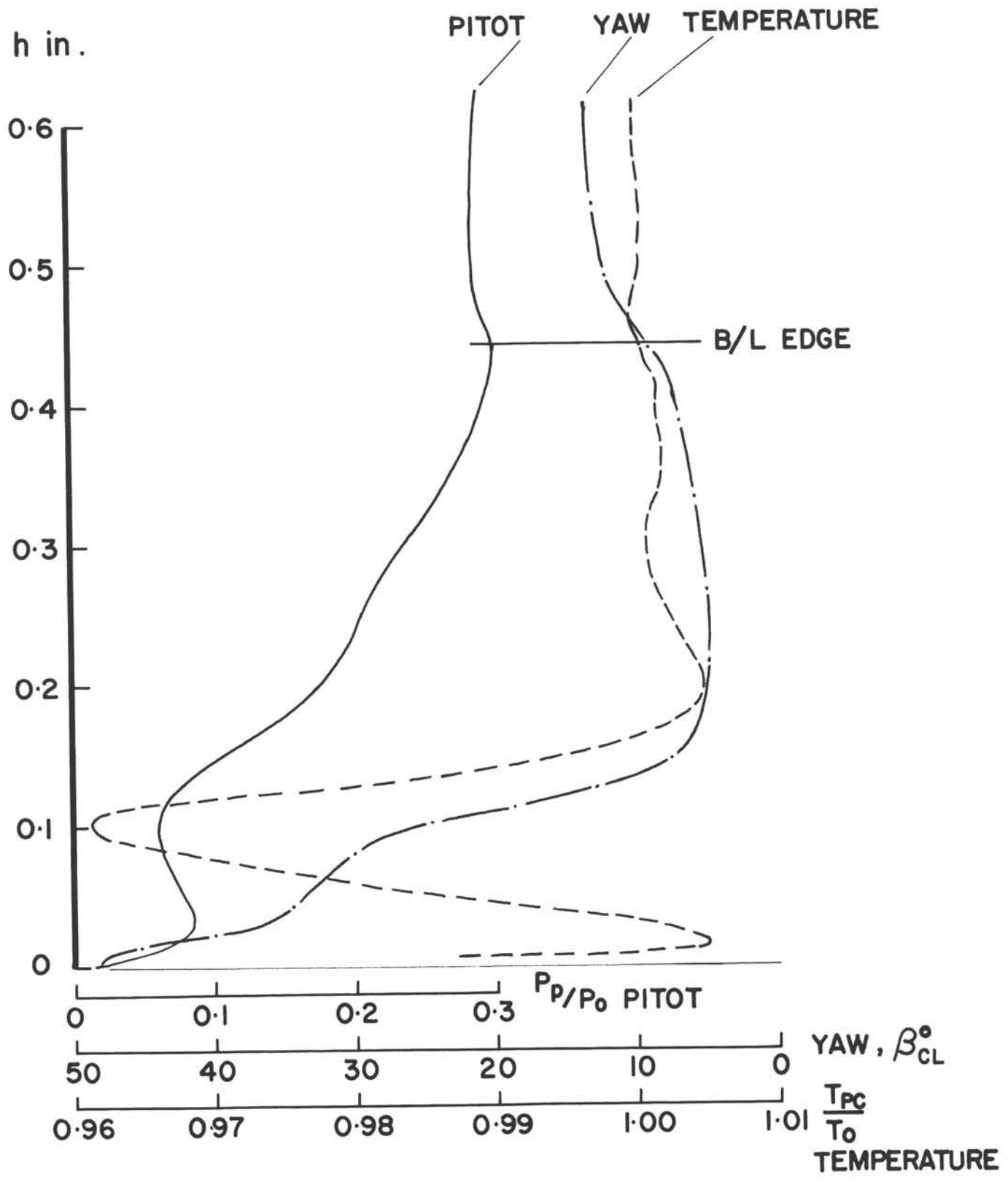

FIG. 79: PITOT, TOTAL TEMPERATURE AND YAW ANGLE DISTRIBUTIONS FOR RUN 24000 NEAR INVISCID SHOCK WAVE LOCATION; FOR δ_w = 16-DEGREES AT MACH 4

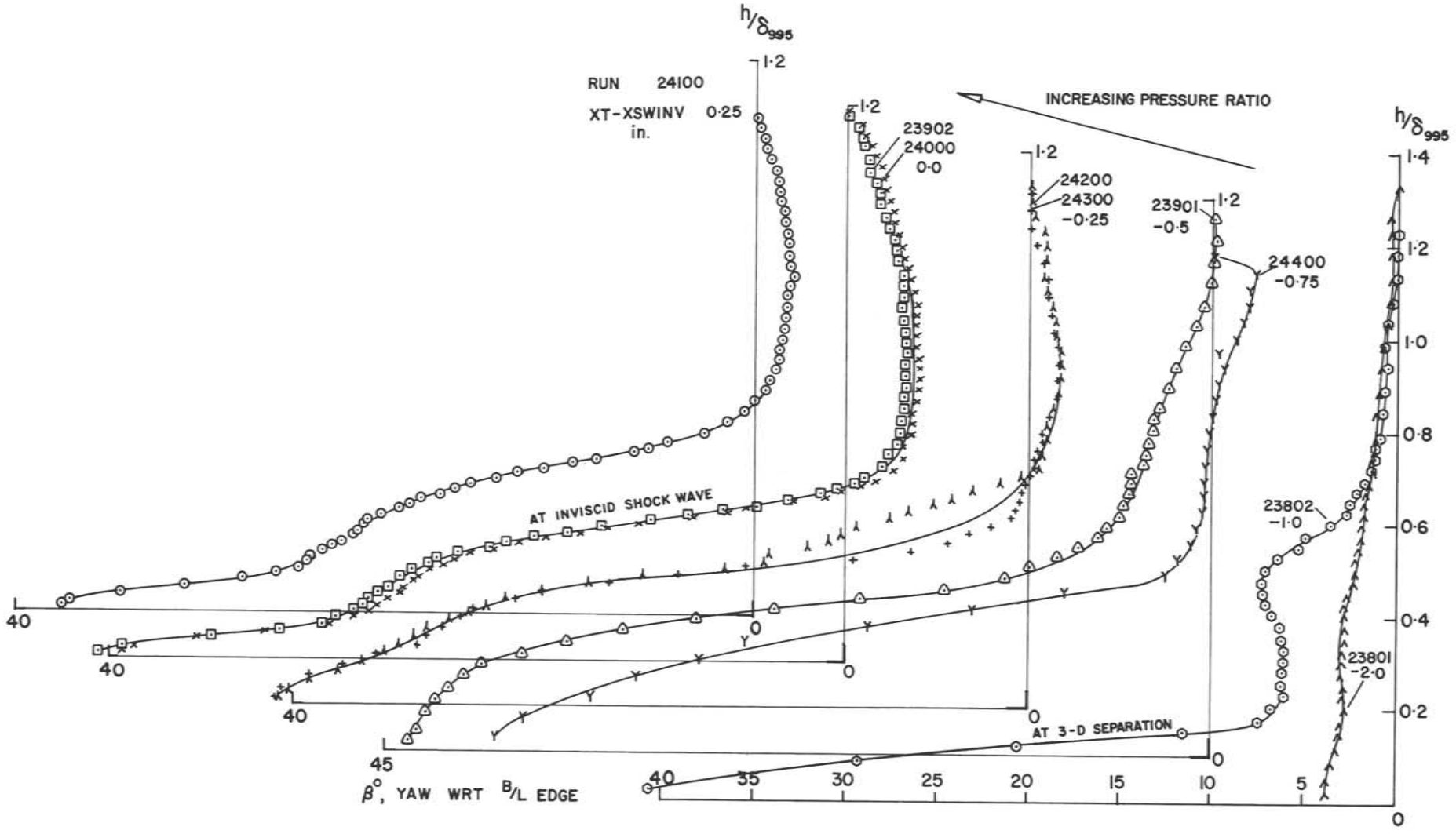

FIG. 80: YAW DISTRIBUTIONS FOR δ_w = 16-DEGREES AT MACH 4

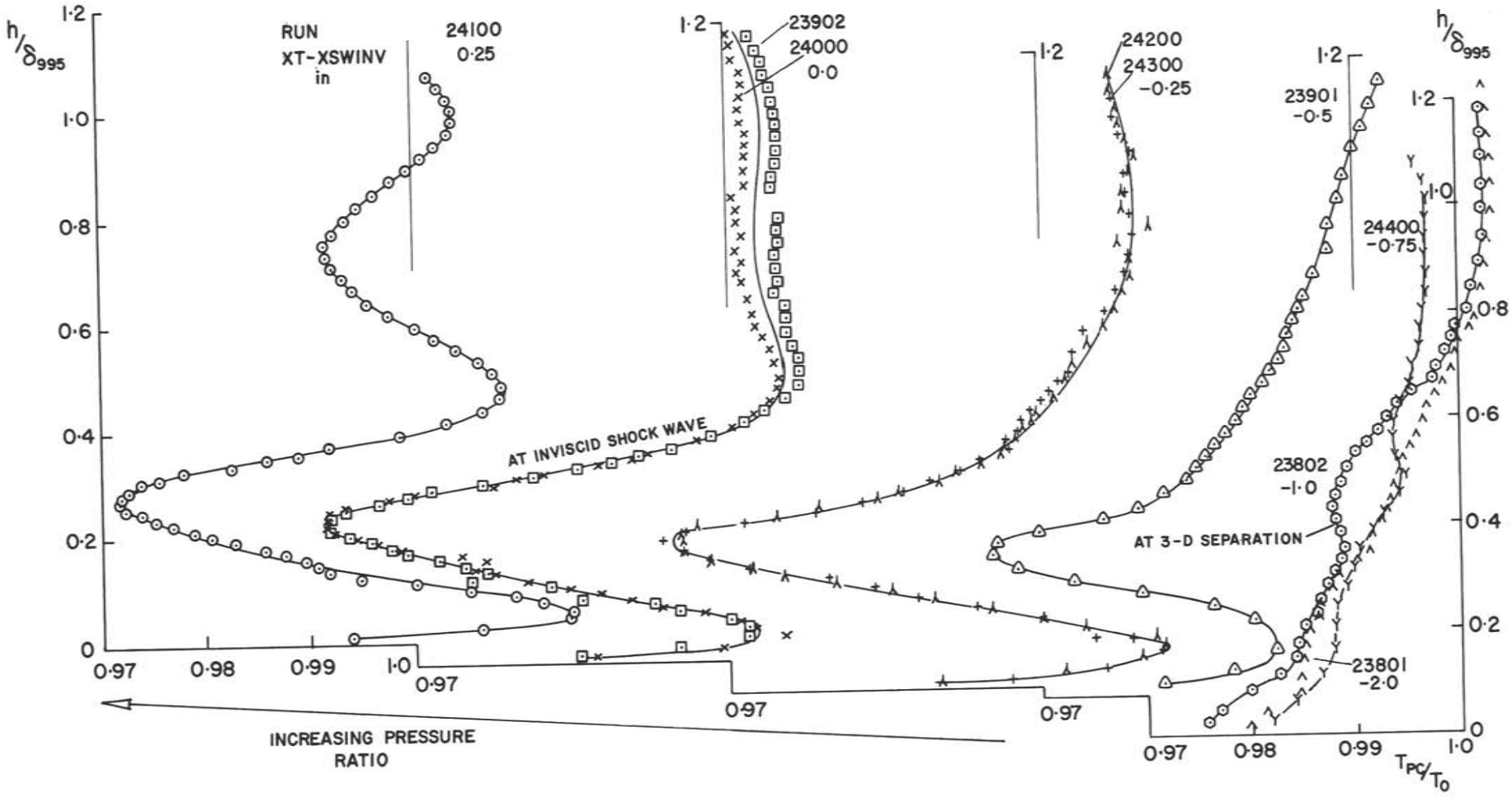

FIG. 81: TOTAL TEMPERATURE DISTRIBUTIONS FOR δ_w = 16-DEGREES AT MACH 4

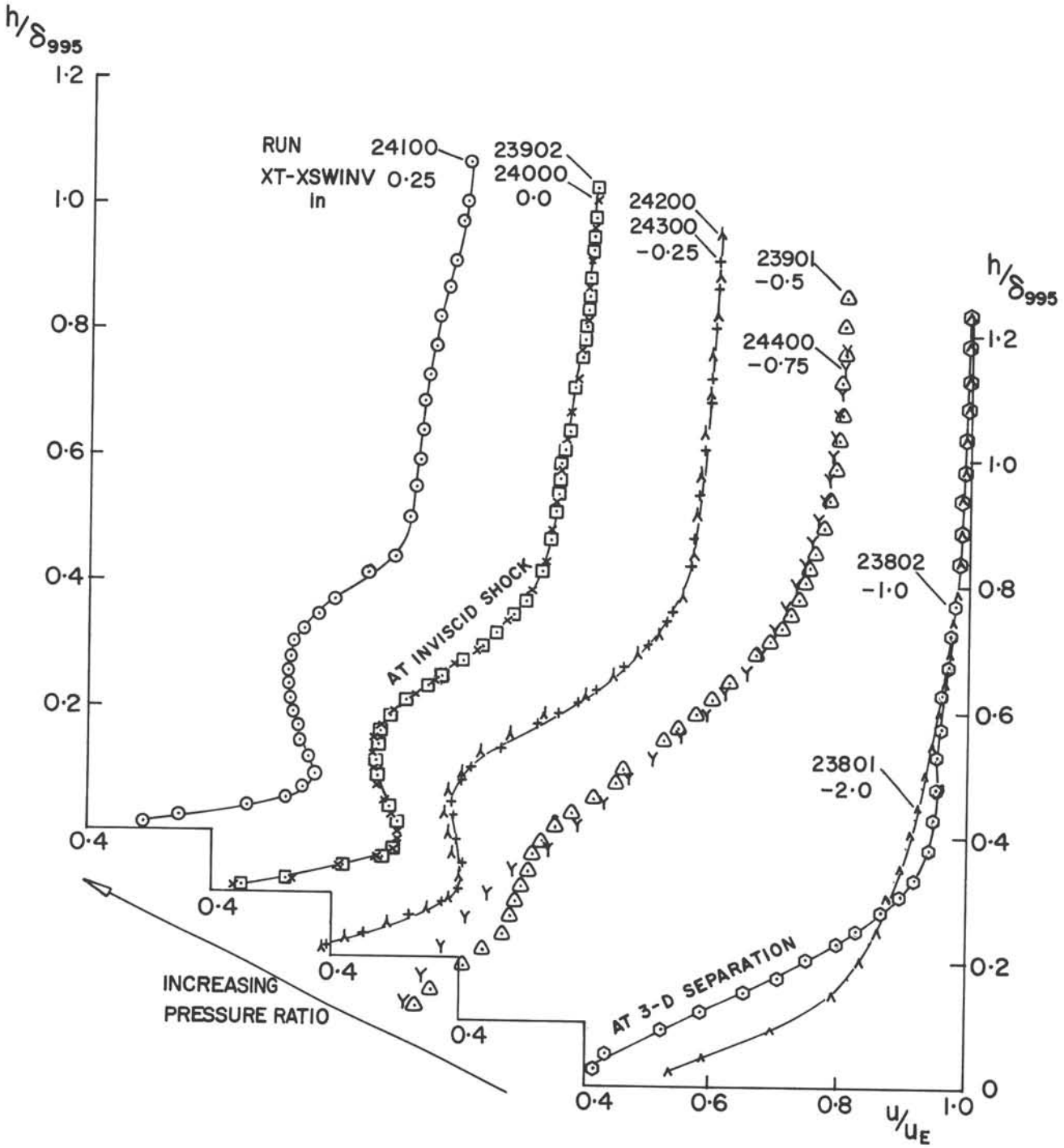

FIG. 82: STREAMWISE FLOW VELOCITY PROFILES FOR δ_w = 16-DEGREES AT MACH 4

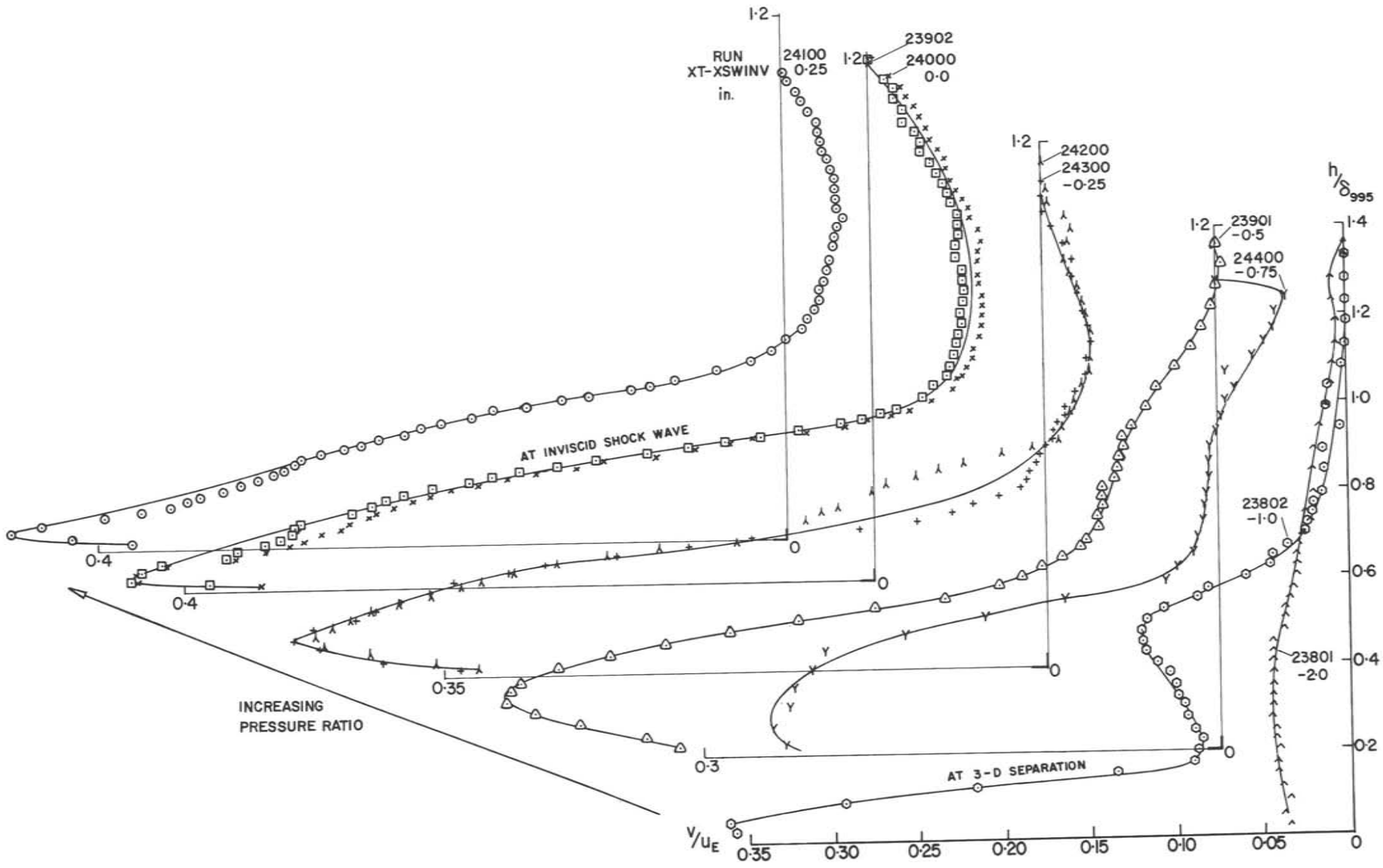

FIG. 83: CROSSFLOW VELOCITY PROFILES FOR δ_w = 16-DEGREES AT MACH 4

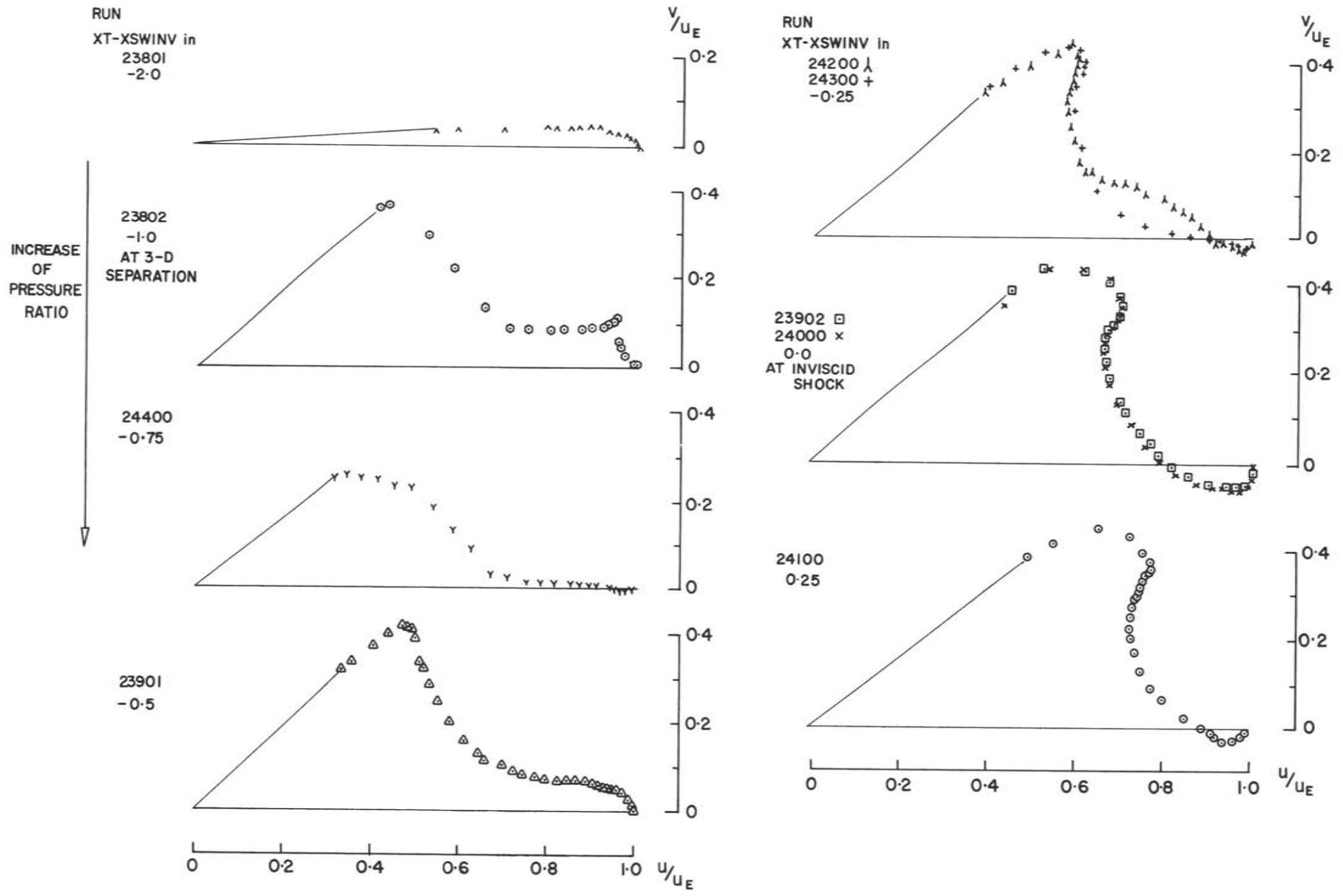

FIG. 84: POLAR PLOTS OF VELOCITY PROFILES FOR δ_w = 16-DEGREES AT MACH 4

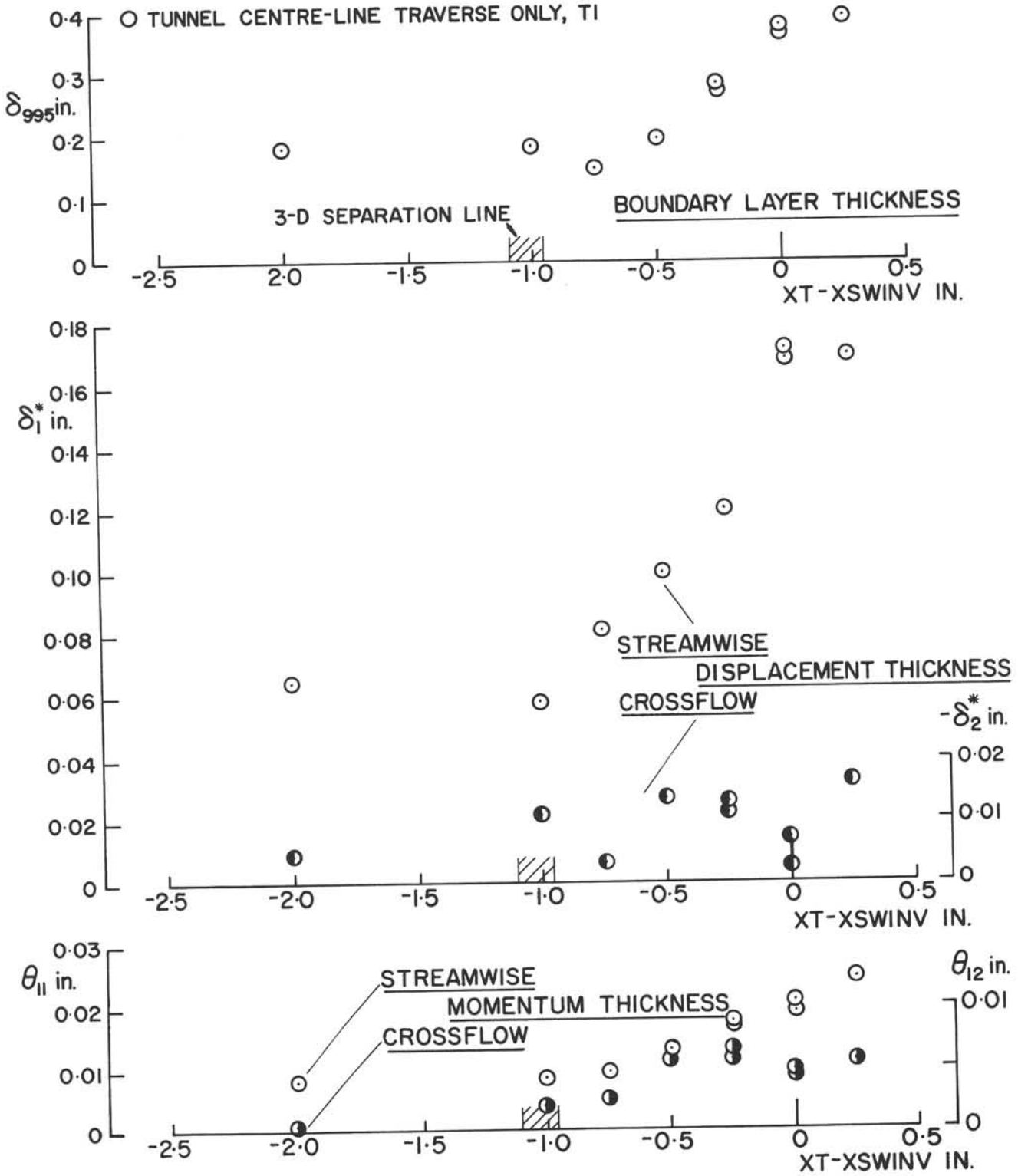

FIG. 85: INTEGRAL PARAMETERS FOR δ_w = 16-DEGREES AT MACH 4

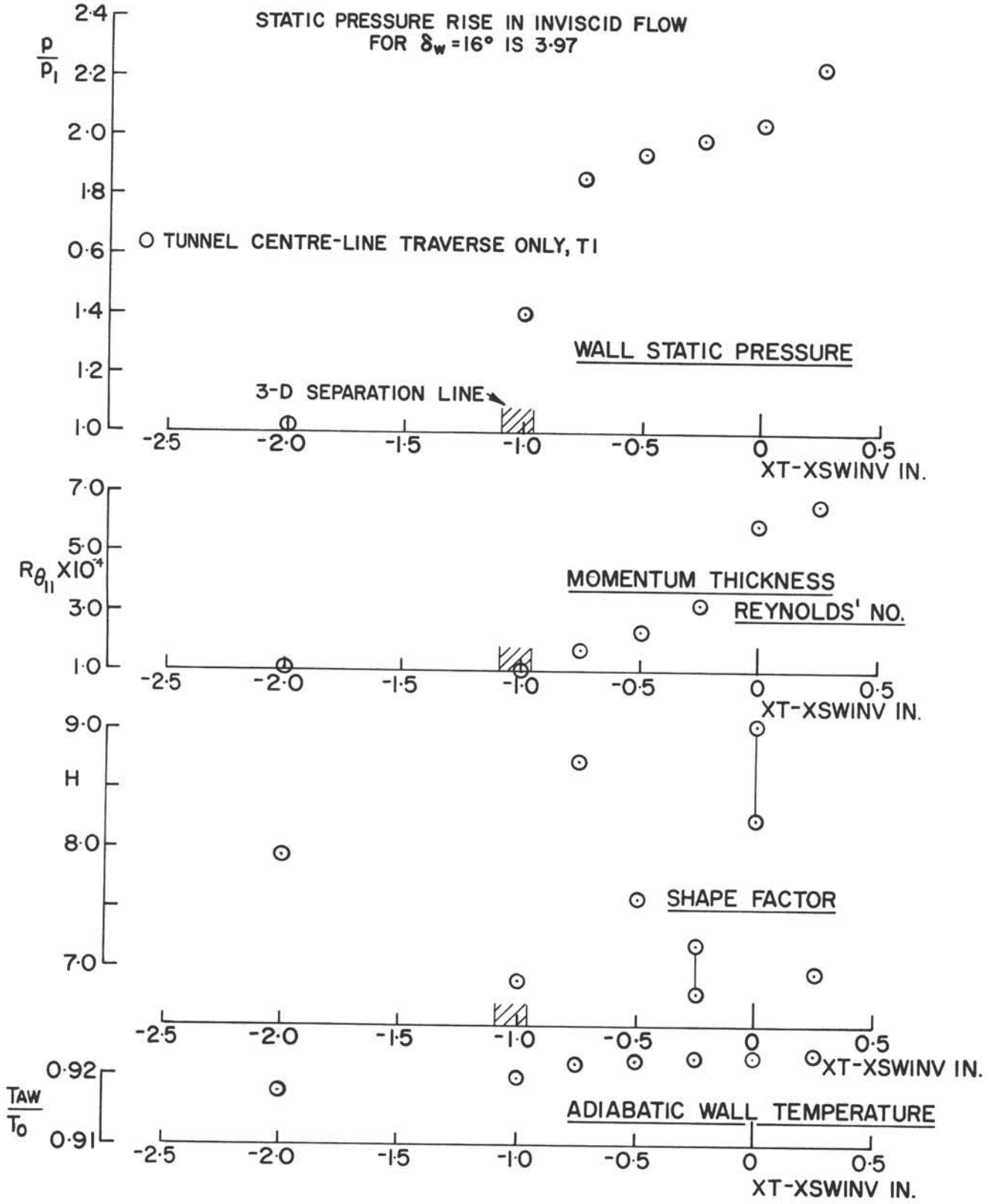

FIG. 86: STREAMWISE INTEGRAL PARAMETERS AND WALL CONDITIONS FOR δ_w = 16-DEGREES AT MACH 4

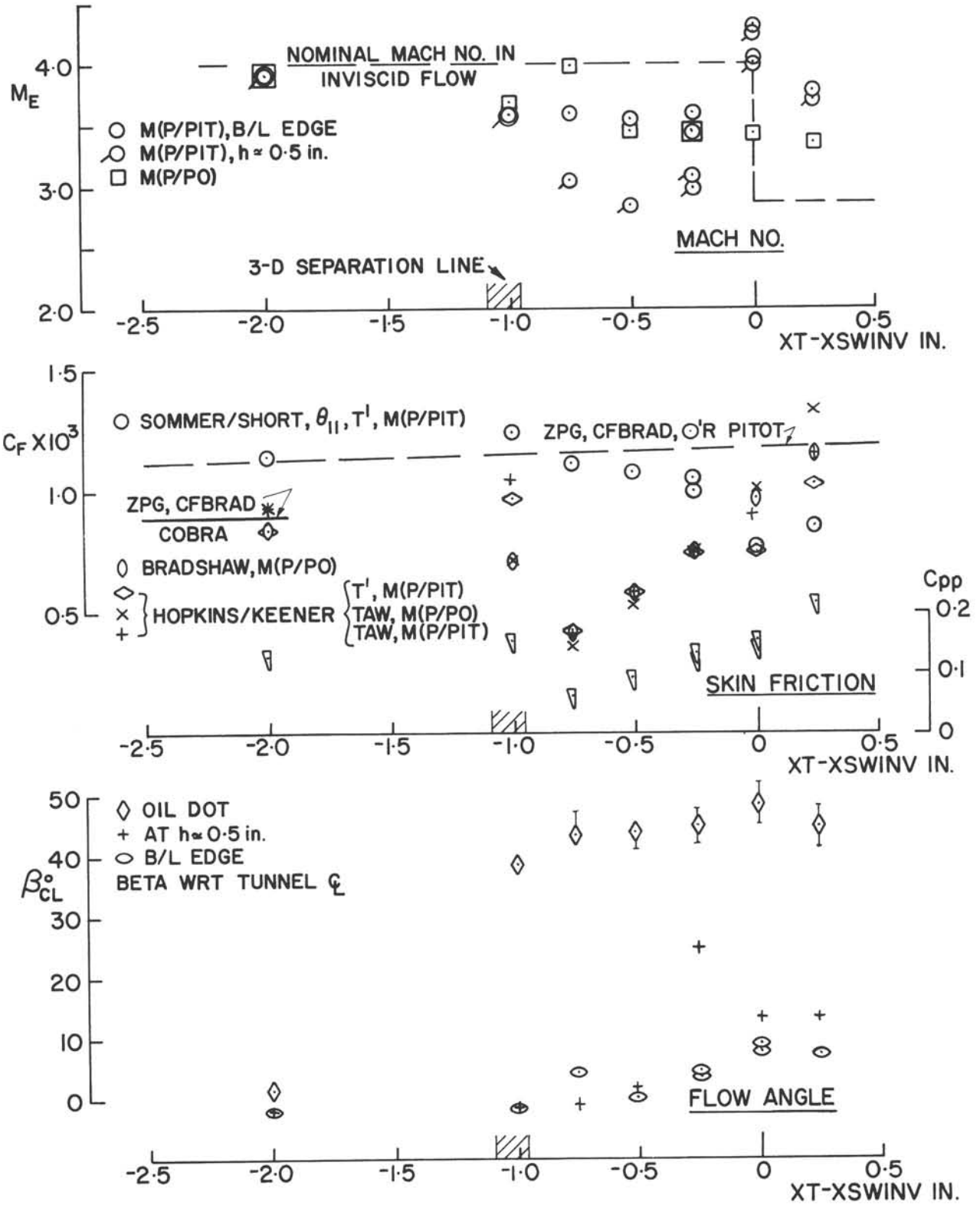

FIG. 87: LOCAL SKIN FRICTION AND FLOW DEFLECTIONS FOR δ_w = 16-DEGREES AT MACH 4

UNDISTURBED BOUNDARY-LAYER THICKNESS, $\delta \cong 0{\cdot}2$ in., $R_\delta = 1{\cdot}5 \times 10^5$

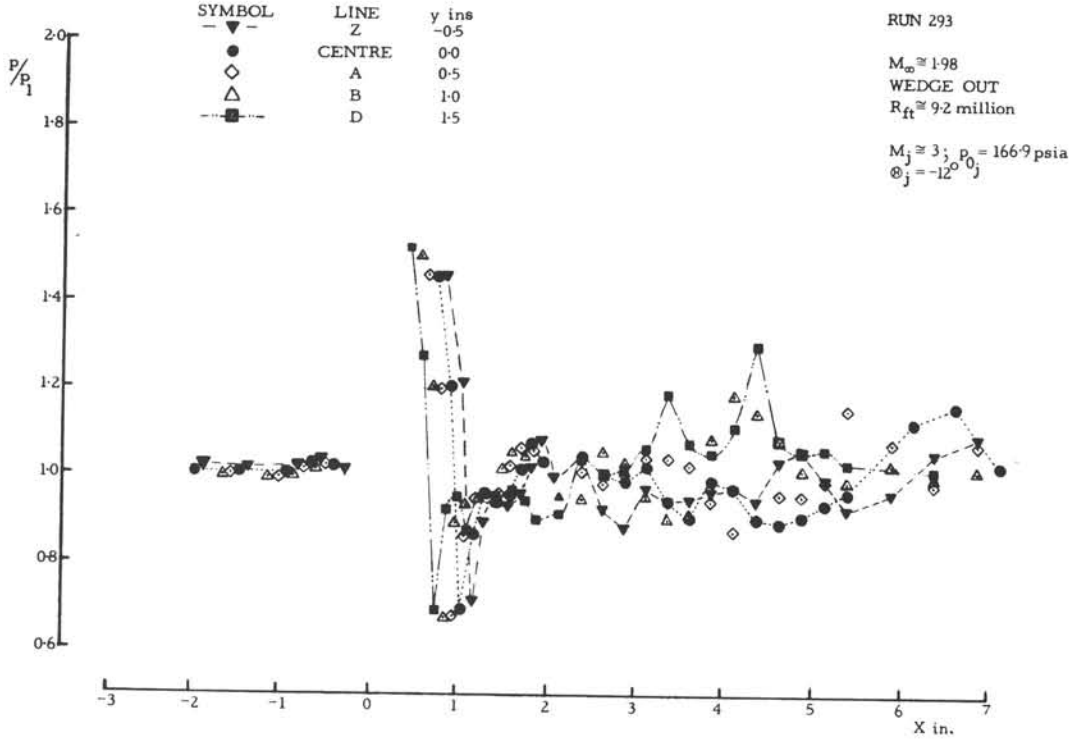

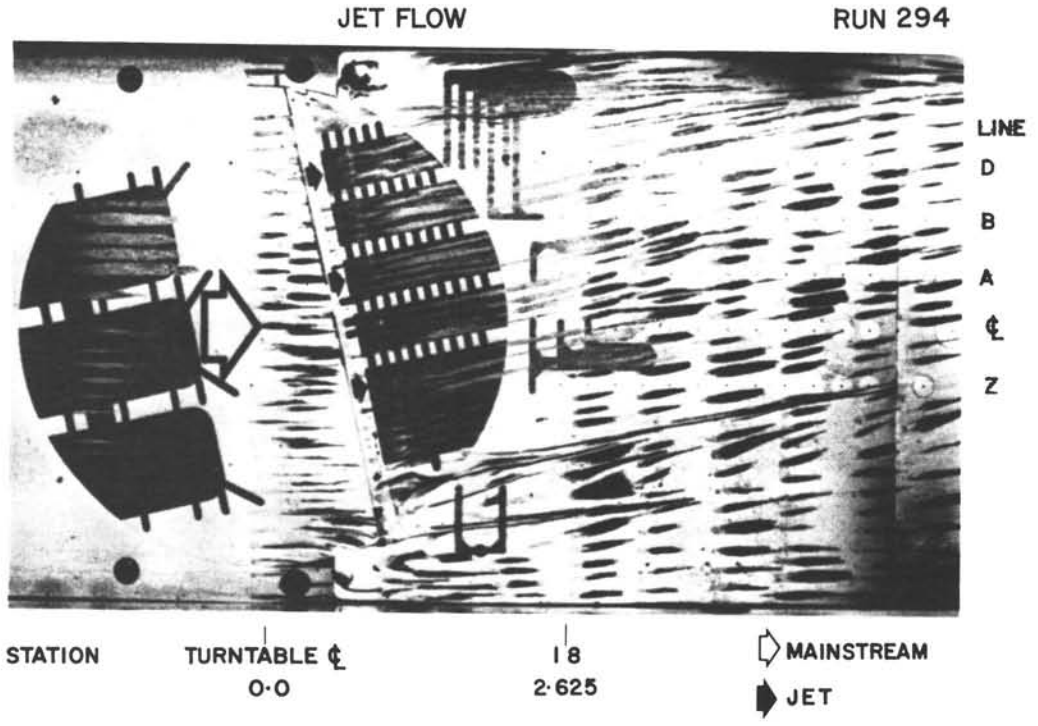

FIG. 88: DOWNSTREAM PENETRATION OF JET IN EMPTY TUNNEL: SURFACE PRESSURES AND FLOW VISUALIZATION AT $\theta_j = -12$-DEGREES AT $M_j \cong 3$

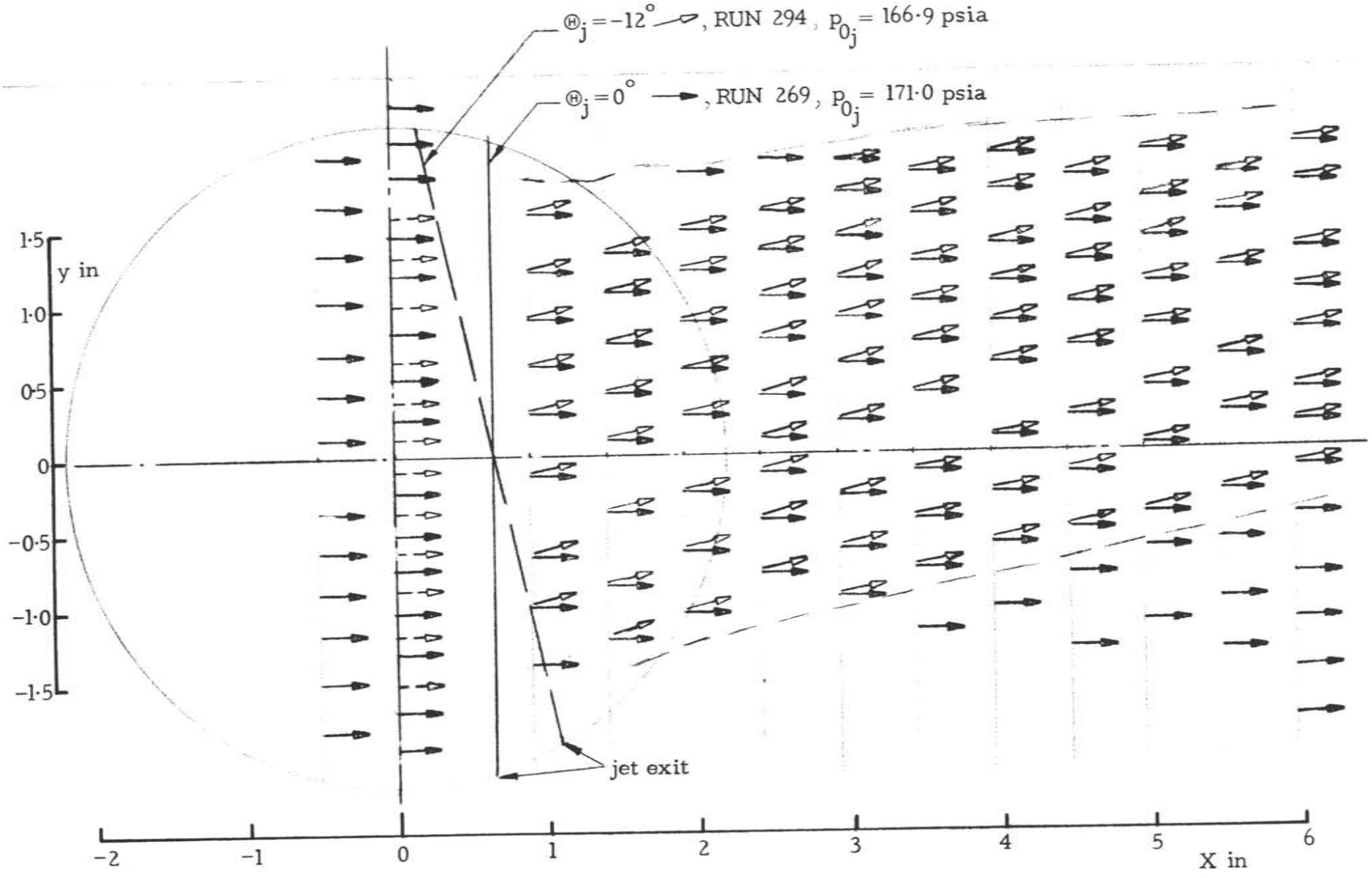

FIG. 89: DOWNSTREAM PENETRATION OF SKEWED JET SURFACE SHEAR STRESS TRAJECTORIES AT θ_j = −12-DEGREES, $M_j \cong 3$, AT MACH 2

SYMBOL	RUN	p_{0_j} psia	p_1 psia	REMARKS
—○—	260	167·9	4·59	static pressures in empty tunnel: jet on
- -△- -	261	166·2	4·59	repeat of run 260: jet on
—○—	265	---	4·65	block pressures in empty tunnel: jet off
—▽—	266	---	4·59	new blocks on ℄, A and B: jet off
-·-◇-·-	267	---	4·58	blocks yawed at approx. 10° to tunnel ℄: jet off

$M_\infty \cong 1{\cdot}97$; $R_{ft} \cong 9{\cdot}2$ million
$M_j \cong 3$; $\theta_j = 0°$

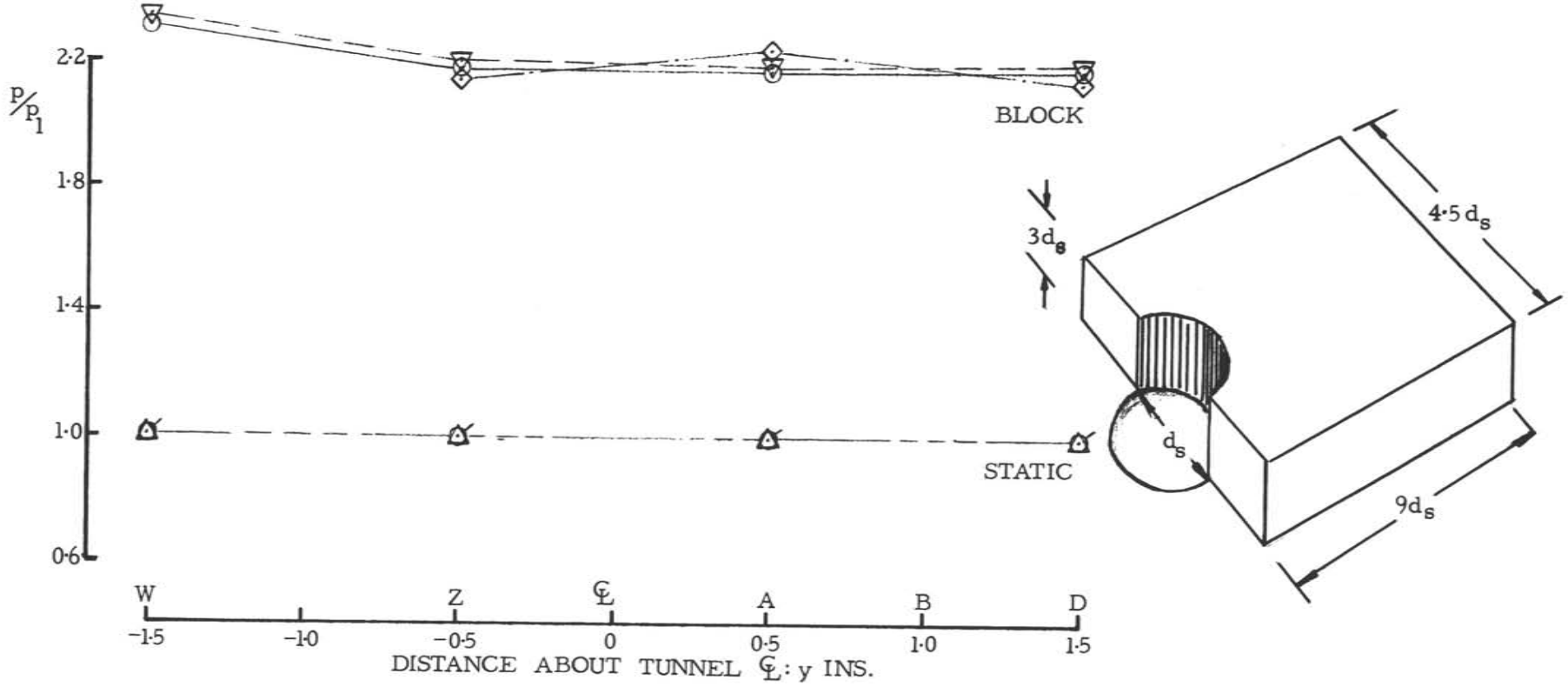

FIG. 90: STATIC AND OBSTACLE BLOCK PRESSURES ACROSS LINE A2 UPSTREAM OF JET SLOT

SYMBOL	RUN	p_{0_j} psia	p_1 psia	REMARKS
—○—	260	167·9	4·59	static pressures in empty tunnel: jet on
– △ –	261	166·2	4·59	repeat of run 260
···□···	290	167·1	4·61	statics ahead of wedge, X_w = 3 in.: jet on
—○—	299	167·4	4·56	blocks on: jet on
– ▽ –	301	167·2	4·55	blocks on ahead of wedge, X_w = 3 ins.
-···⬡···-	300	---	4·56	blocks on: jet off

$M_\infty \cong 1{\cdot}97$; $R_{ft} \cong 9{\cdot}2$ million
$M_j \cong 3$; $\theta_j = 0°$

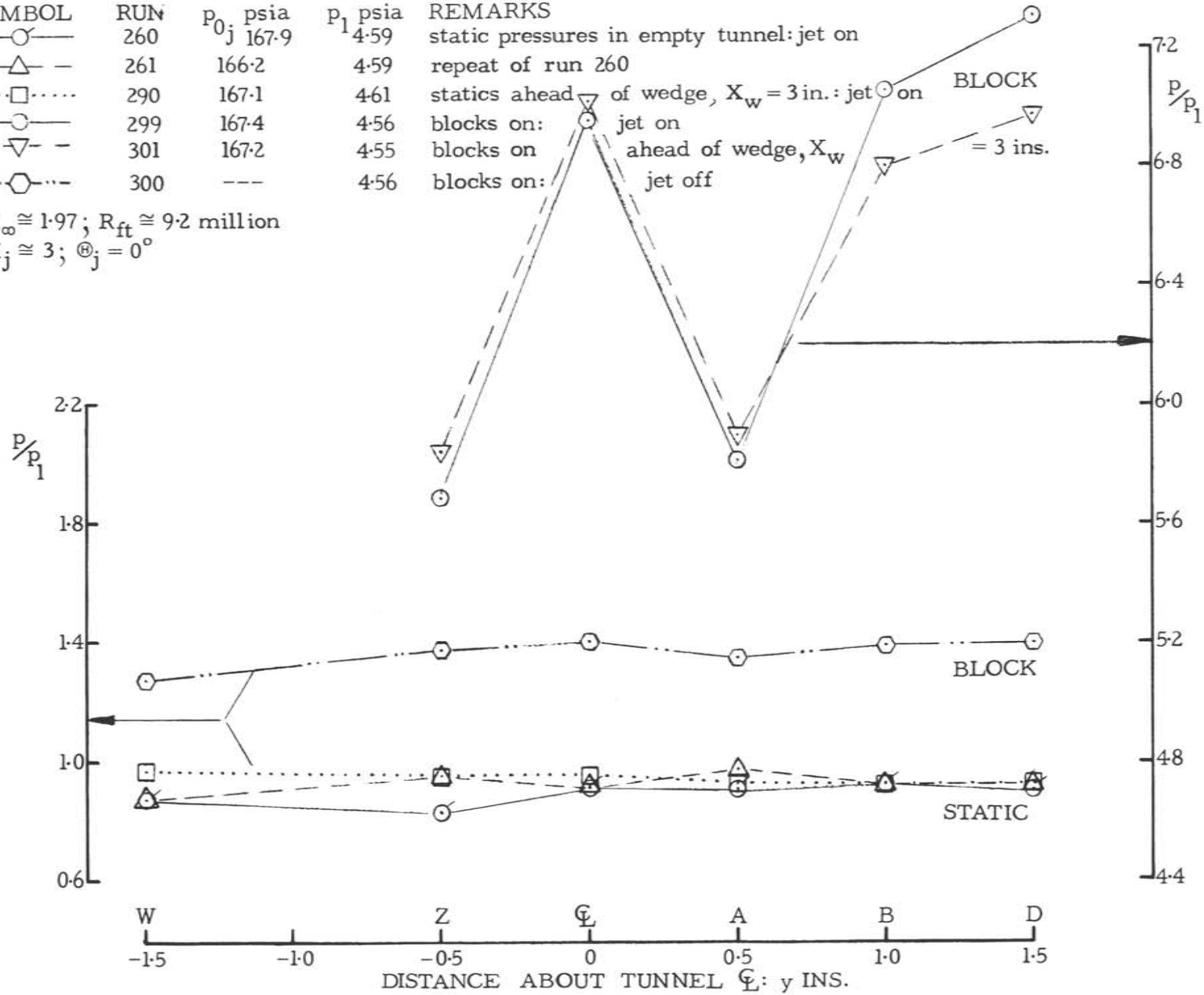

FIG. 91: STATIC AND OBSTACLE BLOCK PRESSURES ACROSS LINE 10 DOWNSTREAM OF JET SLOT

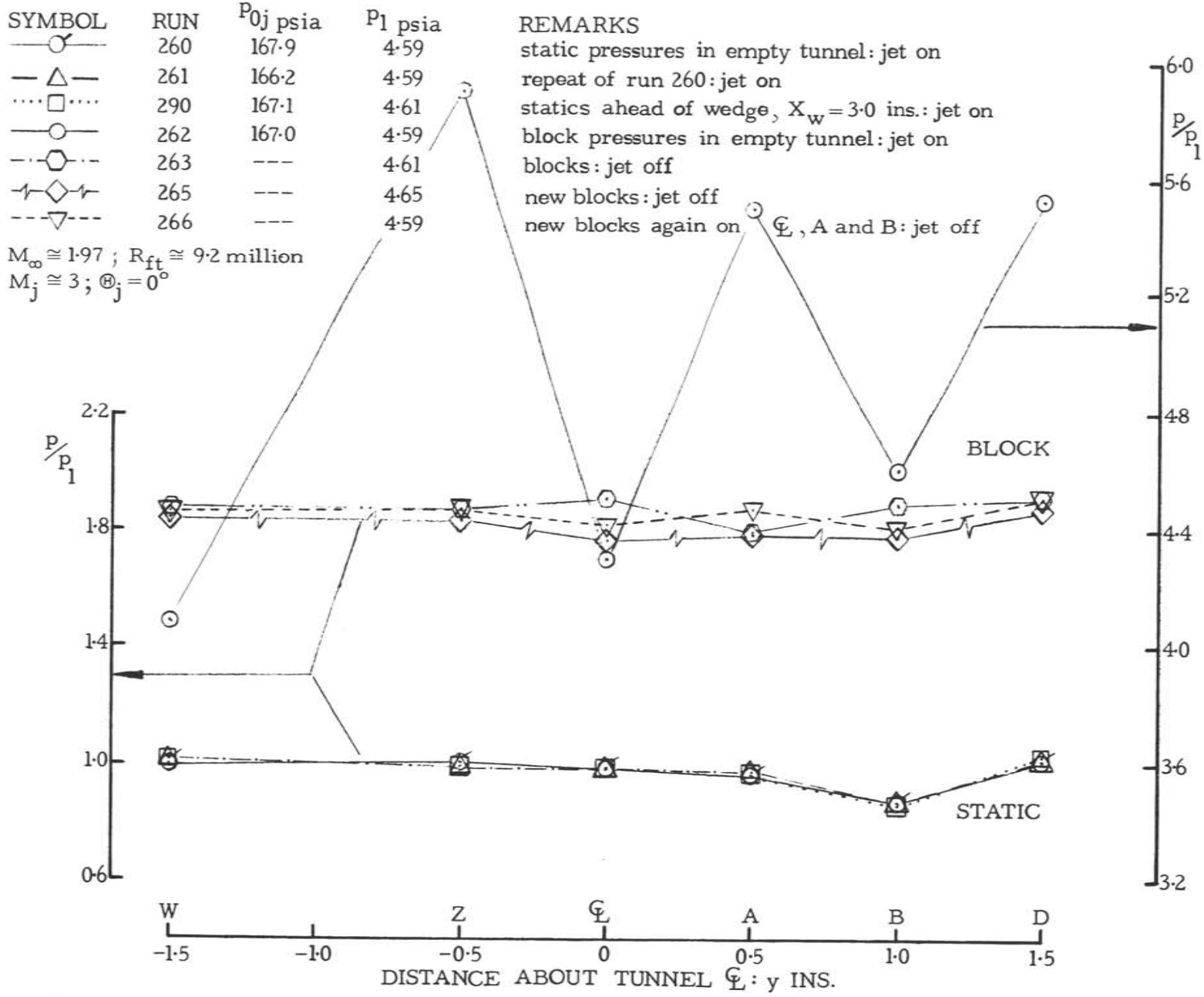

FIG. 92: STATIC AND OBSTACLE BLOCK PRESSURES ACROSS LINE 17 DOWNSTREAM OF JET SLOT

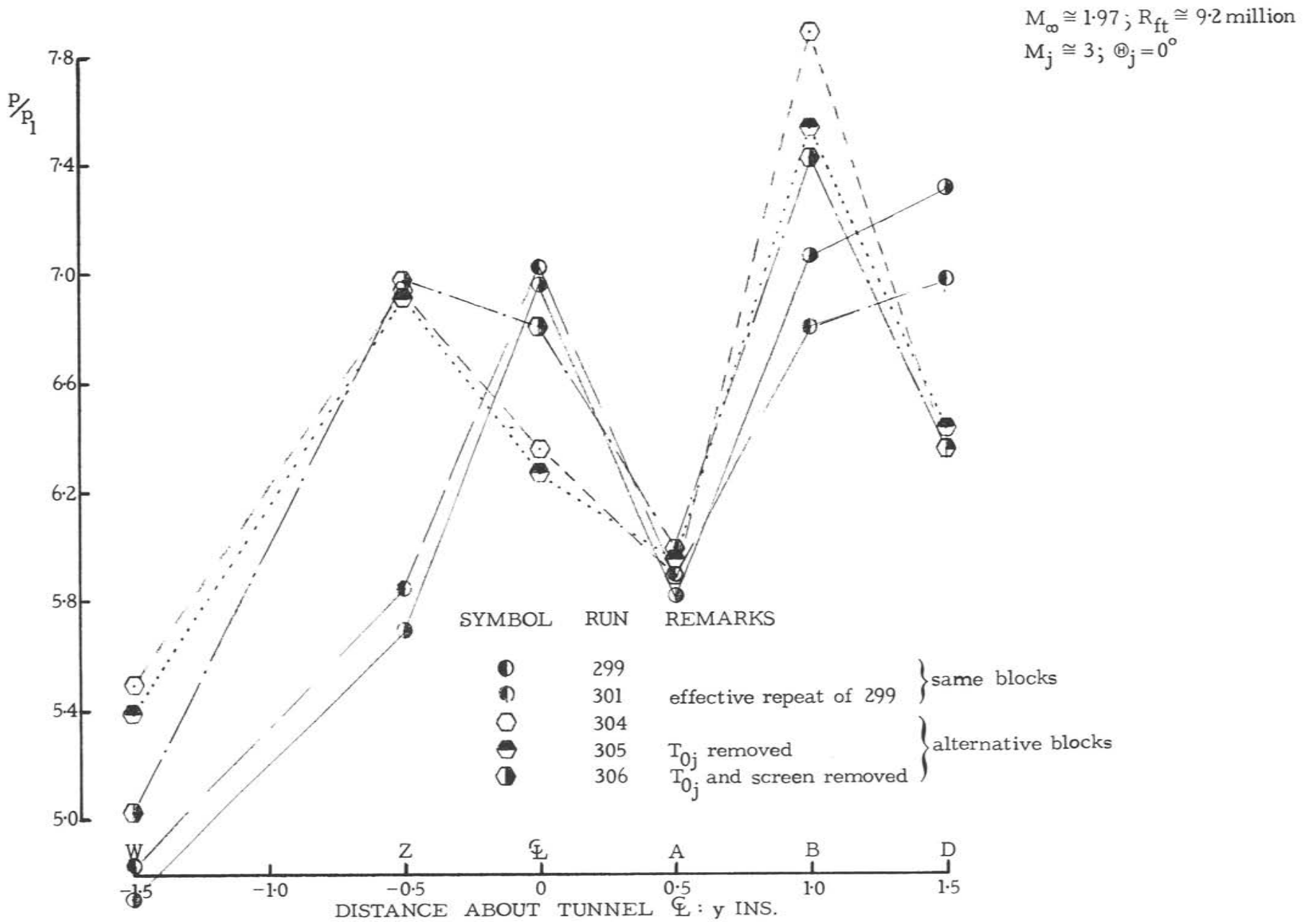

FIG. 93: OBSTACLE BLOCK PRESSURES ACROSS LINE 10 WITH SCREEN AND THERMOMETER REMOVED FROM JET NOZZLE

FLOOR

MAINSTREAM FLOW, $p_0 \cong 34$ psia

JET FLOW, $p_{0_j} \cong 167$ psia

UNDISTURBED BOUNDARY-LAYER THICKNESS
$\delta \cong 0.2$, $R_\delta = 1.5 \times 10^5$

$\theta_j = -20°$

FLOW VISUALIZATION

INTERSECTION OF WEDGE WITH FLOOR

RUN 295 $\theta_j = -12°$

PRESSURE DISTRIBUTIONS

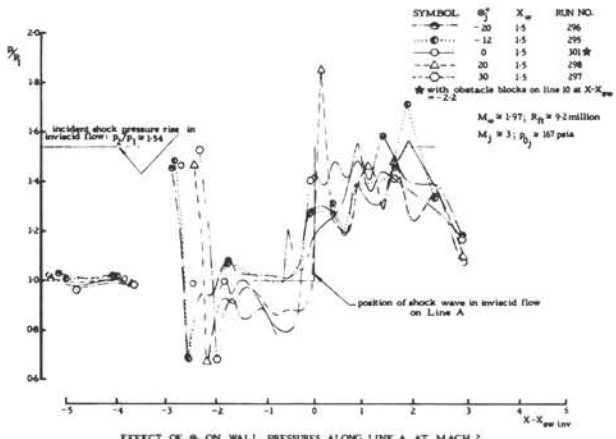

EFFECT OF θ_j ON WALL PRESSURES ALONG LINE A AT MACH 2
$\delta_w = 8°$; $X_w = 1.5$ IN.

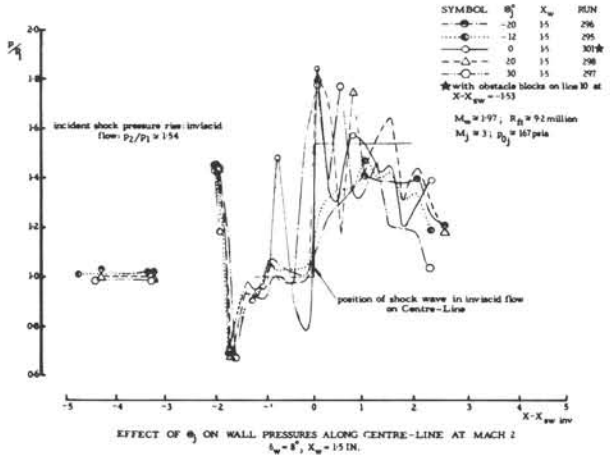

EFFECT OF θ_j ON WALL PRESSURES ALONG CENTRE-LINE AT MACH 2
$\delta_w = 8°$, $X_w = 1.5$ IN.

INTERSECTION OF WEDGE WITH FLOOR

RUN 301 $\theta_j = 0°$

STATION: JET EXIT X in. 0·625 WEDGE L.E. 2·625 18

RUN 298 $\theta_j = 20°$

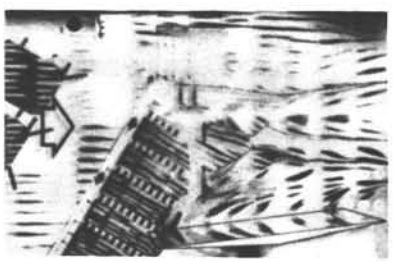

RUN 297 $\theta_j = 30°$

FIG. 94: AIR INJECTION: EFFECT OF θ_j AT $M_j \cong 3$ ON SURFACE PRESSURES AND FLOW VISUALIZATION FOR δ_w = 8-DEGREES AT MACH 2 WITH XWLE = 1.5-IN.

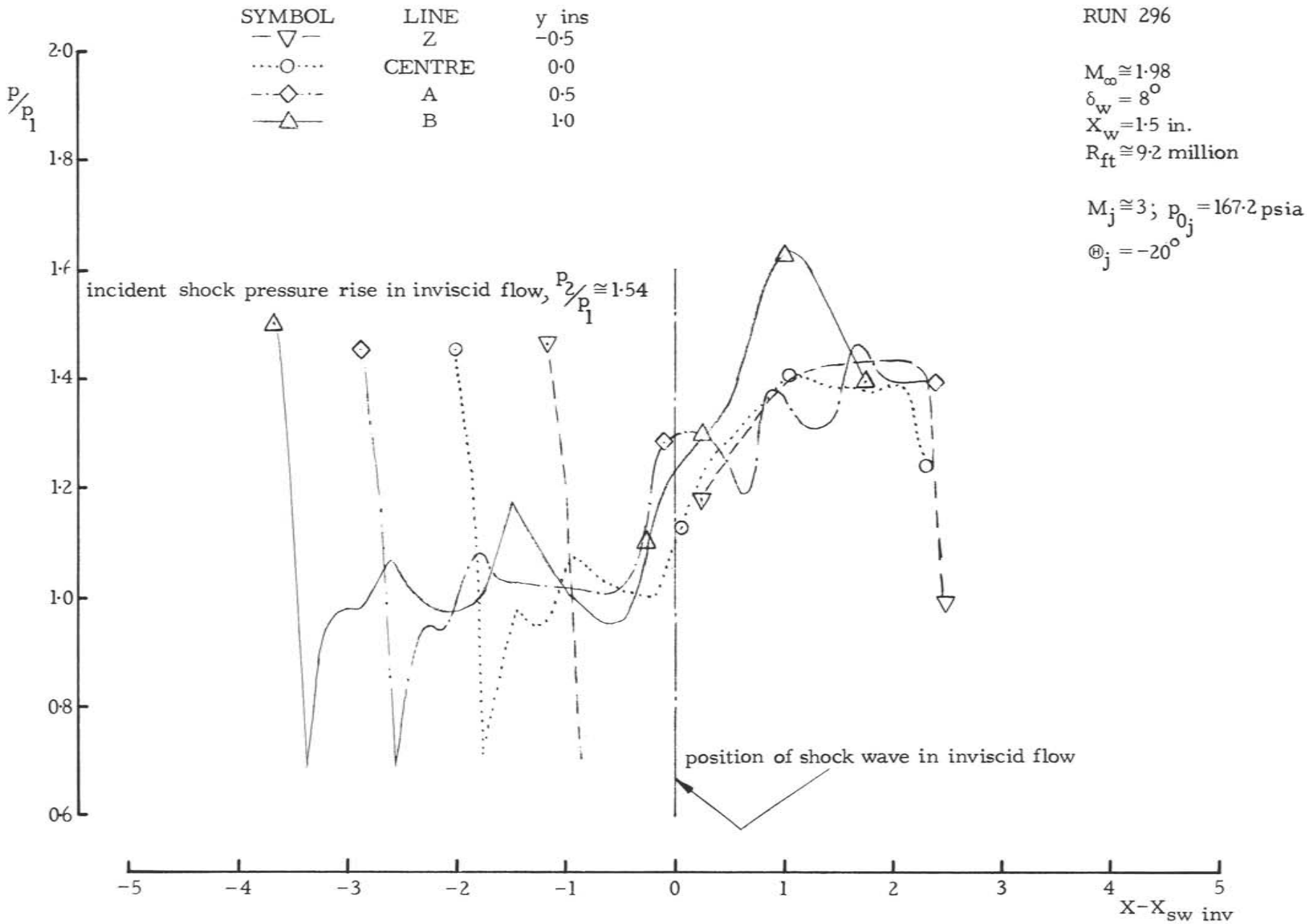

FIG. 95(a): PRESSURES ALONG TEST WALL AT MACH 2 AND WEDGE ANGLE OF 8-DEGREES AT A FIXED WEDGE POSITION, XWLE = 1.5-IN., WITH WALL JET ON: AT θ_j = -20-DEGREES

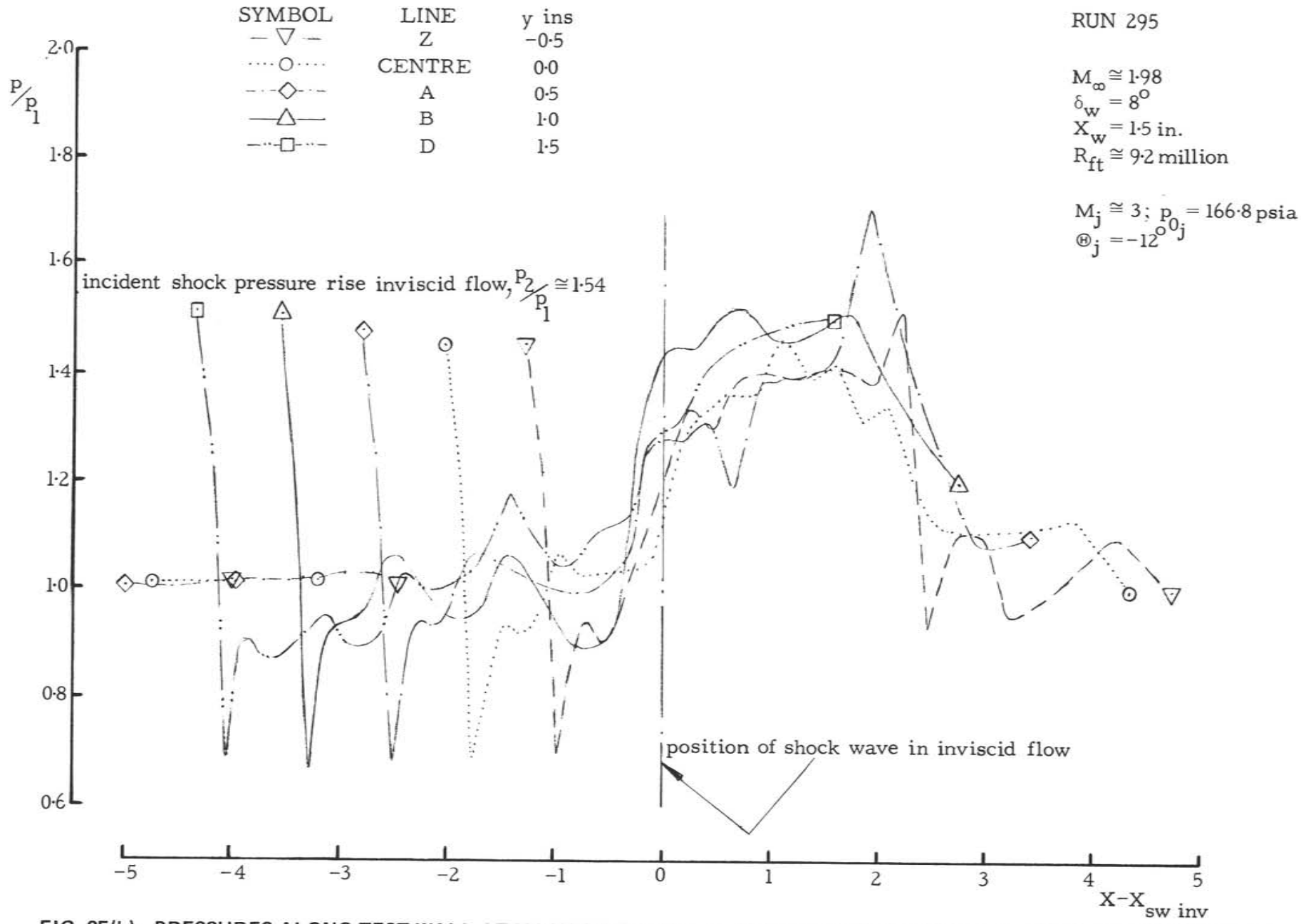

FIG. 95(b): PRESSURES ALONG TEST WALL AT MACH 2 AND WEDGE ANGLE OF 8-DEGREES AT A FIXED WEDGE POSITION, XWLE = 1.5-IN., WITH WALL JET ON: AT $\theta_j = -12$-DEGREES

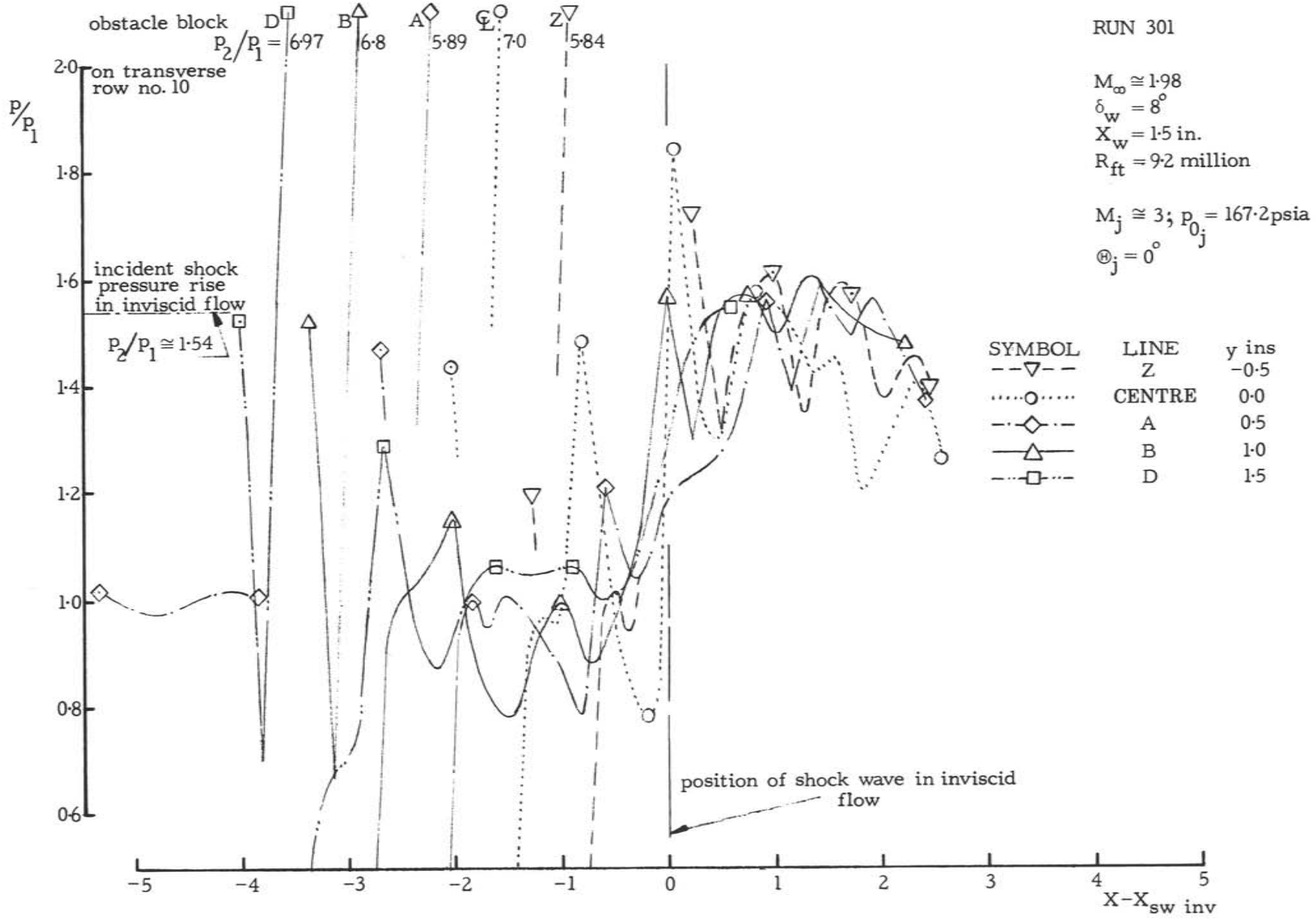

FIG. 95(c): PRESSURES ALONG TEST WALL AT MACH 2 AND WEDGE ANGLE OF 8-DEGREES AT A FIXED WEDGE POSITION, XWLE = 1.5-IN., WITH WALL JET ON: AT θ_j = 0-DEGREE (AND WITH OBSTACLE BLOCKS)

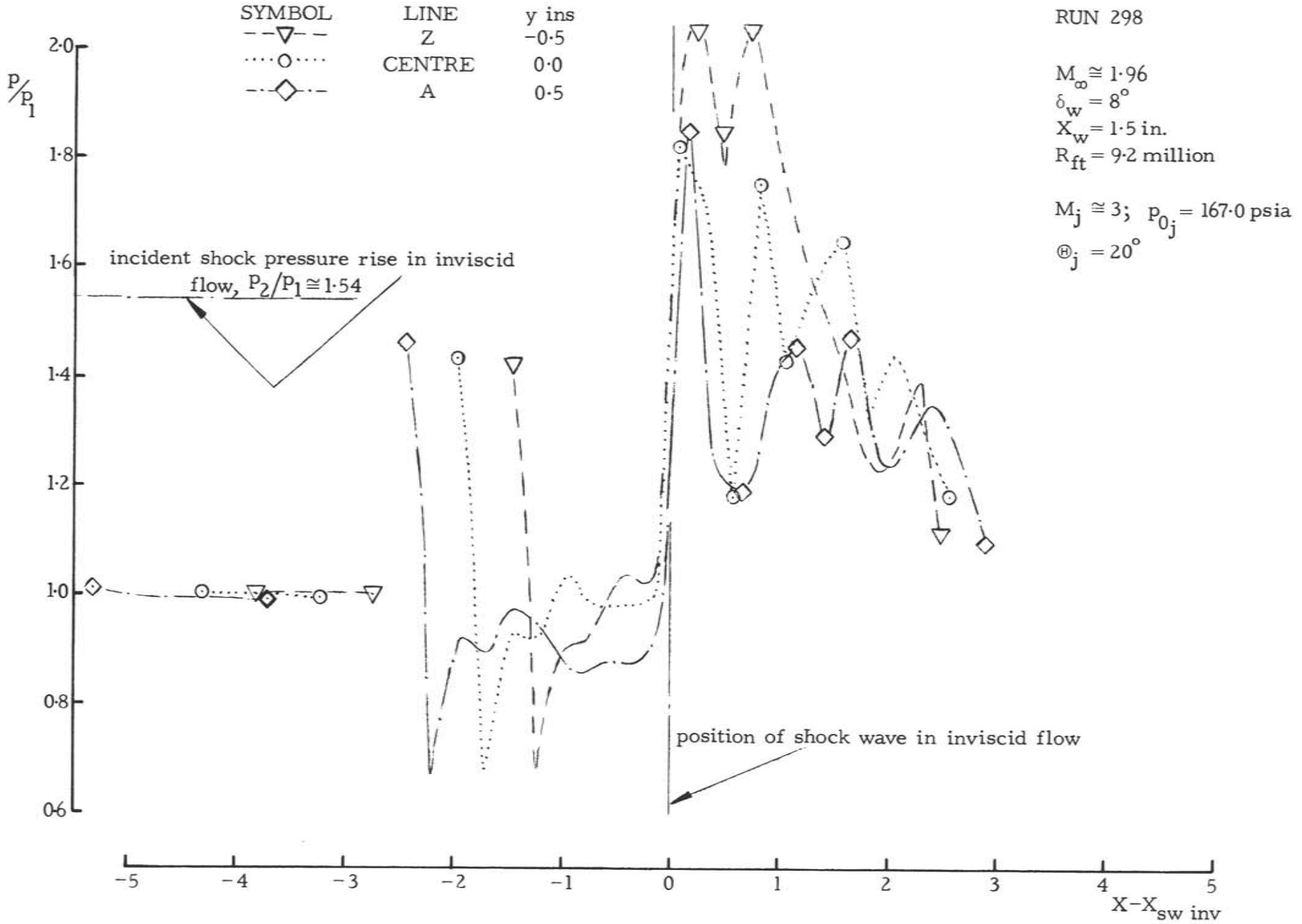

FIG. 95(d): PRESSURES ALONG TEST WALL AT MACH 2 AND WEDGE ANGLE OF 8-DEGREES AT A FIXED WEDGE POSITION, XWLE = 1.5-IN., WITH WALL JET ON: AT θ_j = 20-DEGREES

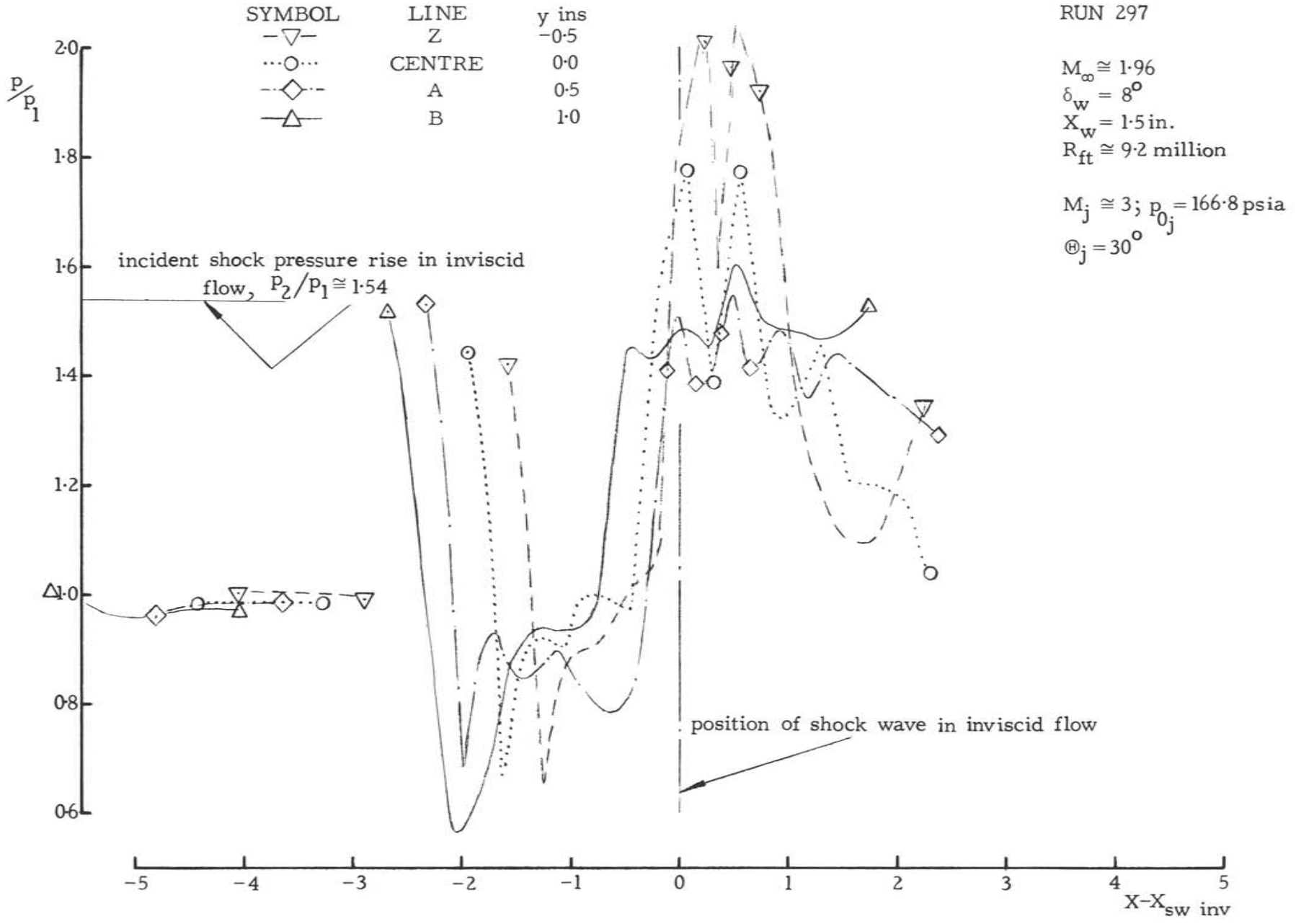

FIG. 95(e): PRESSURES ALONG TEST WALL AT MACH 2 AND WEDGE ANGLE OF 8-DEGREES AT A FIXED WEDGE POSITION, XWLE = 1.5-IN., WITH WALL JET ON: AT θ_j = 30-DEGREES

PRESSURE DISTRIBUTIONS

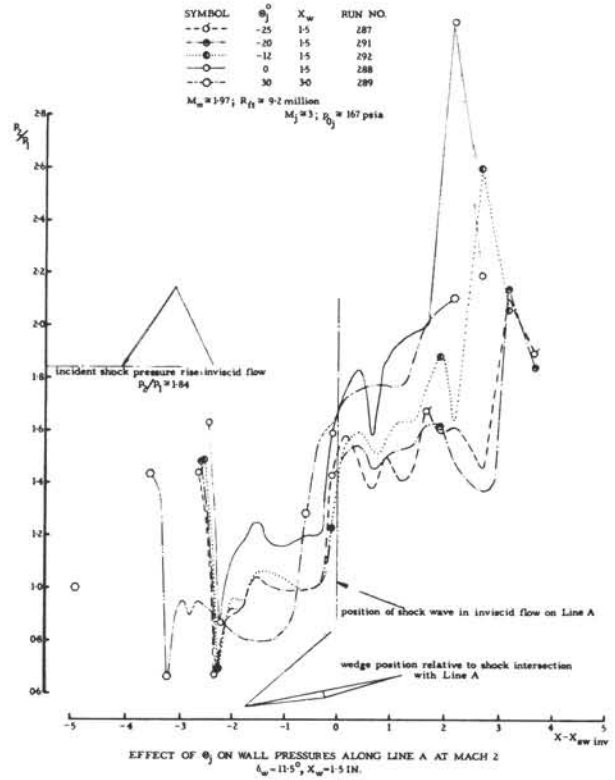

EFFECT OF θ_j ON WALL PRESSURES ALONG LINE A AT MACH 2
δ_w = 11·5°, X_{ew} = 1·5 IN.

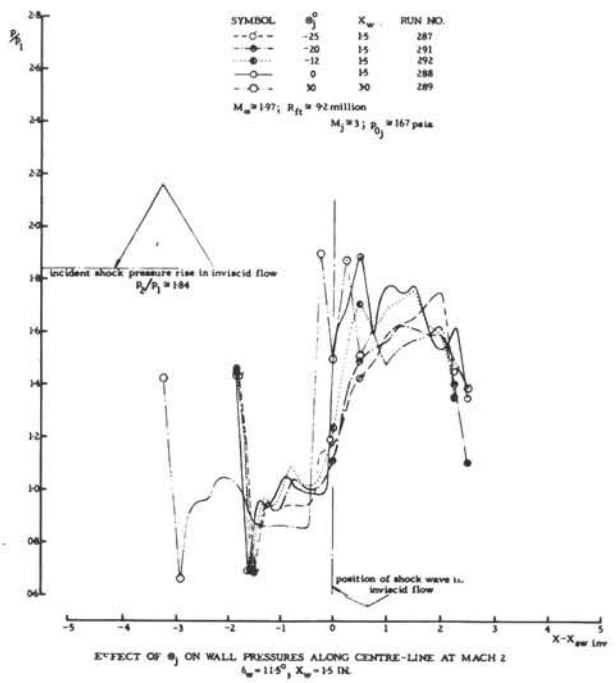

EFFECT OF θ_j ON WALL PRESSURES ALONG CENTRE-LINE AT MACH 2
δ_w = 11·5°, X_{ew} = 1·5 IN.

UNDISTURBED BOUNDARY-LAYER THICKNESS, $\delta \cong$ 0·2 in., $R_\delta \cong 1·5 \times 10^5$

FLOW VISUALIZATION

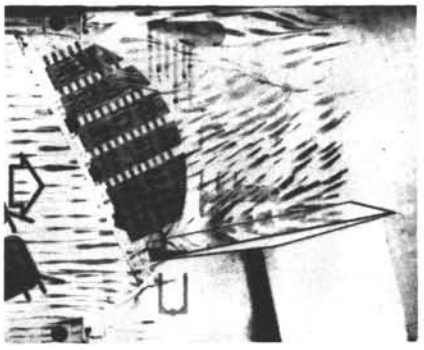

RUN 284 θ_j = -25°

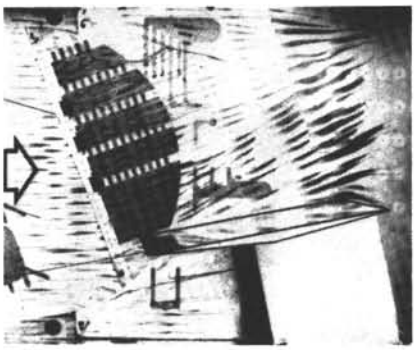

RUN 280 θ_j = -20°

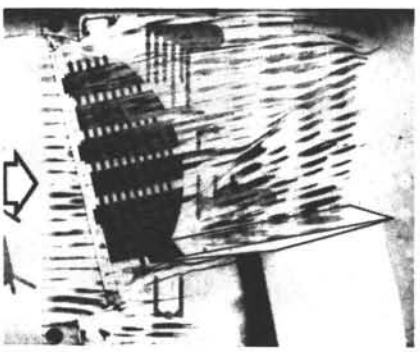

RUN 281 θ_j = -12°

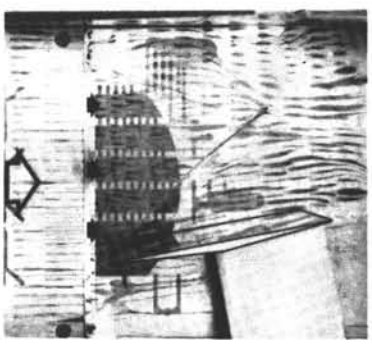

RUN 274 θ_j = 0°
STATION X in. JET EXIT 0·625 18 2·625
(XWLE = 1·0)

FIG. 96: AIR INJECTION: EFFECT OF θ_j AT $M_j \cong 3$ ON SURFACE PRESSURES AND FLOW VISUALIZATION FOR δ_w = 11.5-DEGREES AT MACH 2 WITH XWLE = 1.5-IN.

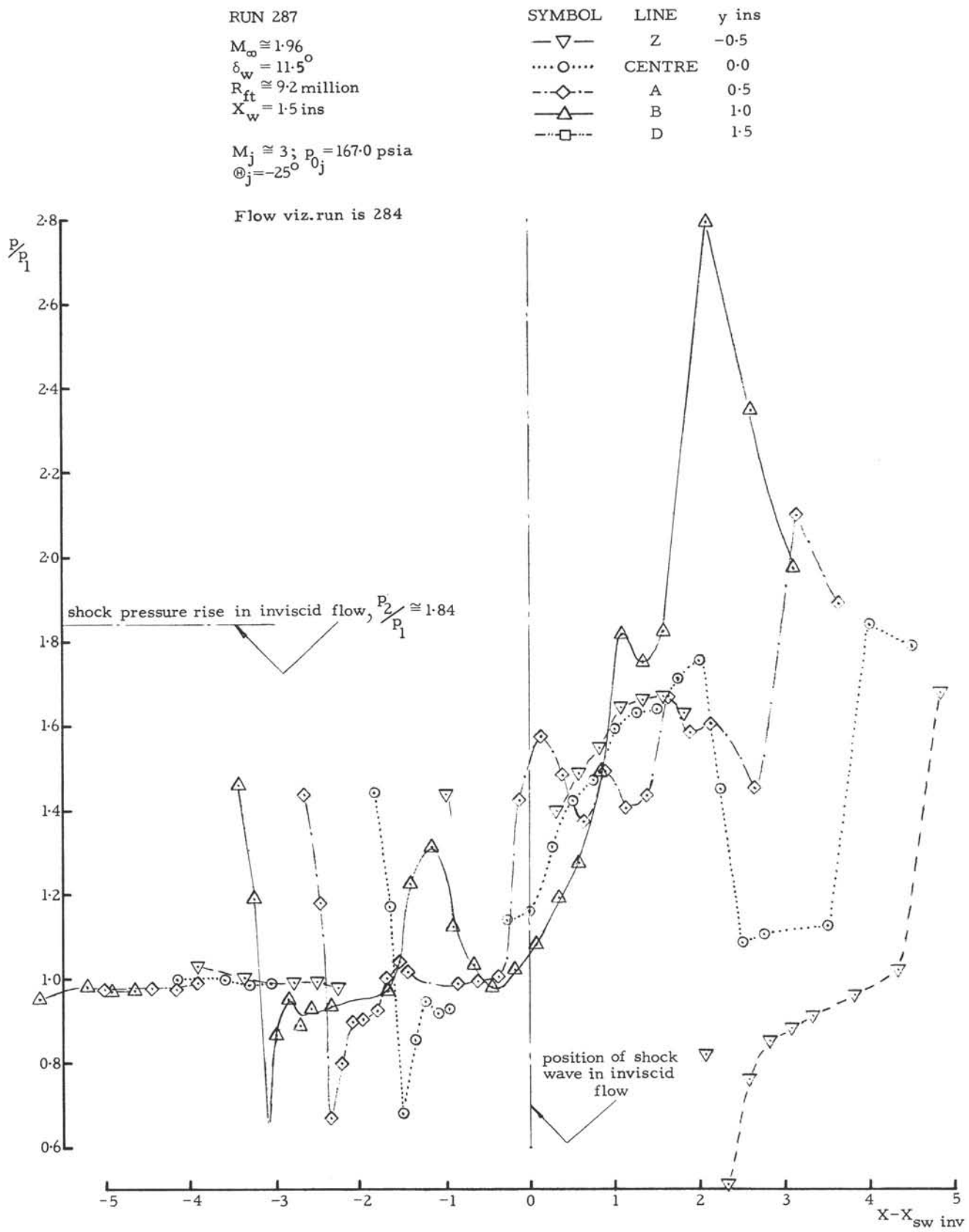

FIG. 97(a): PRESSURES ALONG TEST WALL AT MACH 2 AND WEDGE ANGLE OF 11.5-DEGREES AT A FIXED WEDGE POSITION, XWLE = 1.5-IN., WITH WALL JET ON: AT θ_j = −25-DEGREES

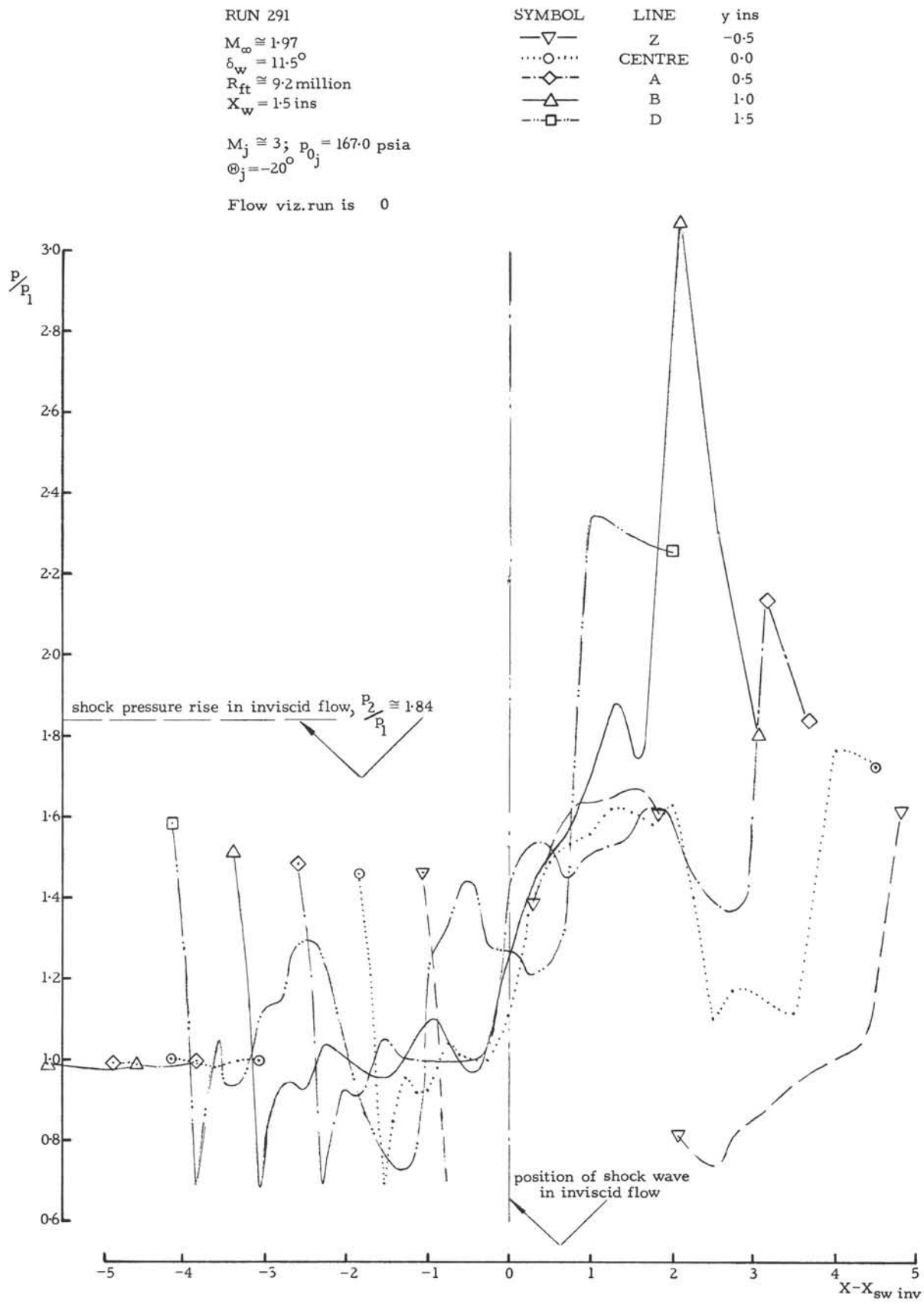

FIG. 97(b): PRESSURES ALONG TEST WALL AT MACH 2 AND WEDGE ANGLE OF 11.5-DEGREES AT A FIXED WEDGE POSITION, XWLE = 1.5-IN., WITH WALL JET ON: AT θ_j = -20-DEGREES

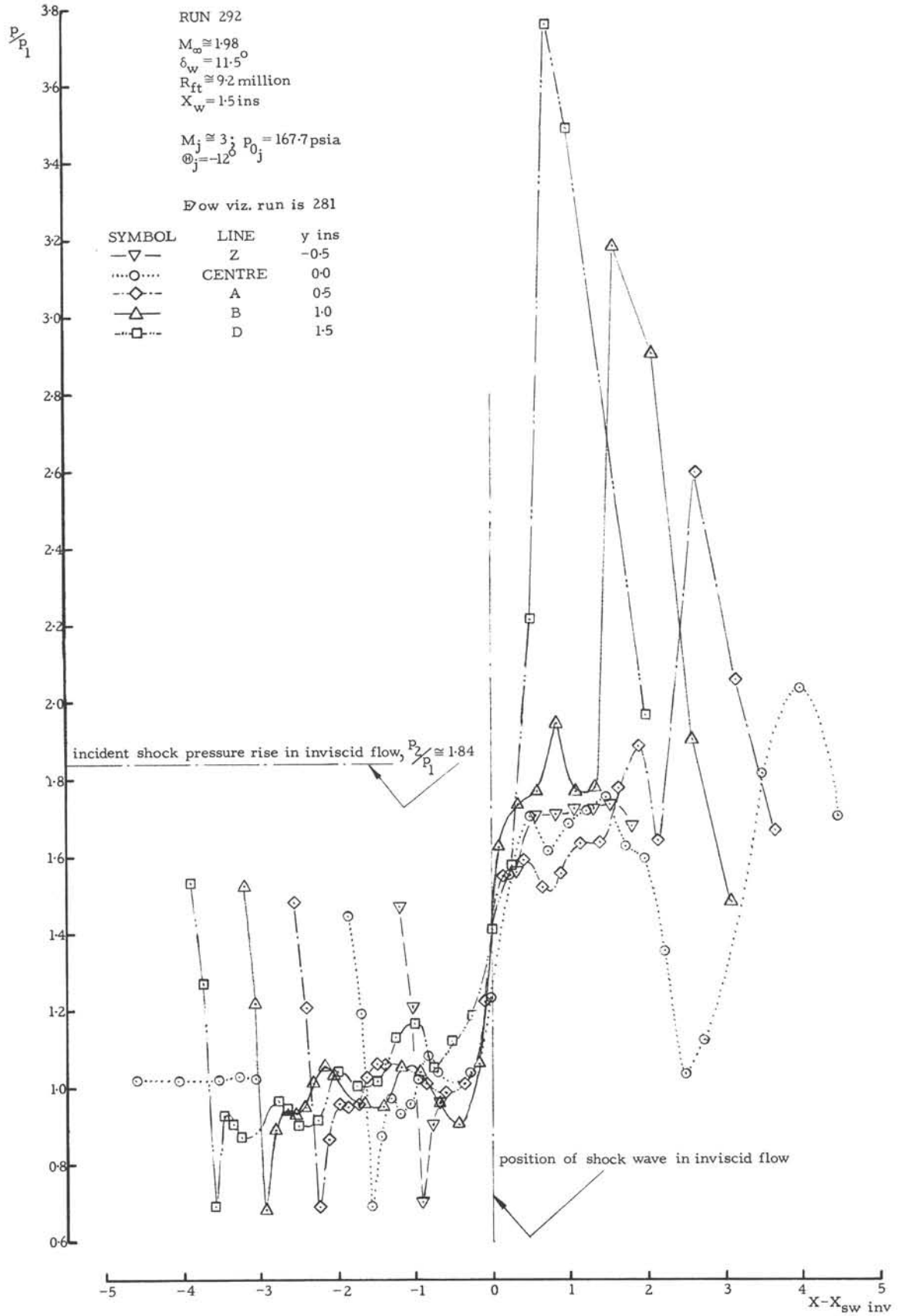

FIG. 97(c): PRESSURES ALONG TEST WALL AT MACH 2 AND WEDGE ANGLE OF 11.5-DEGREES AT A FIXED WEDGE POSITION, XWLE = 1.5-IN., WITH WALL JET ON: AT θ_j = -12-DEGREES

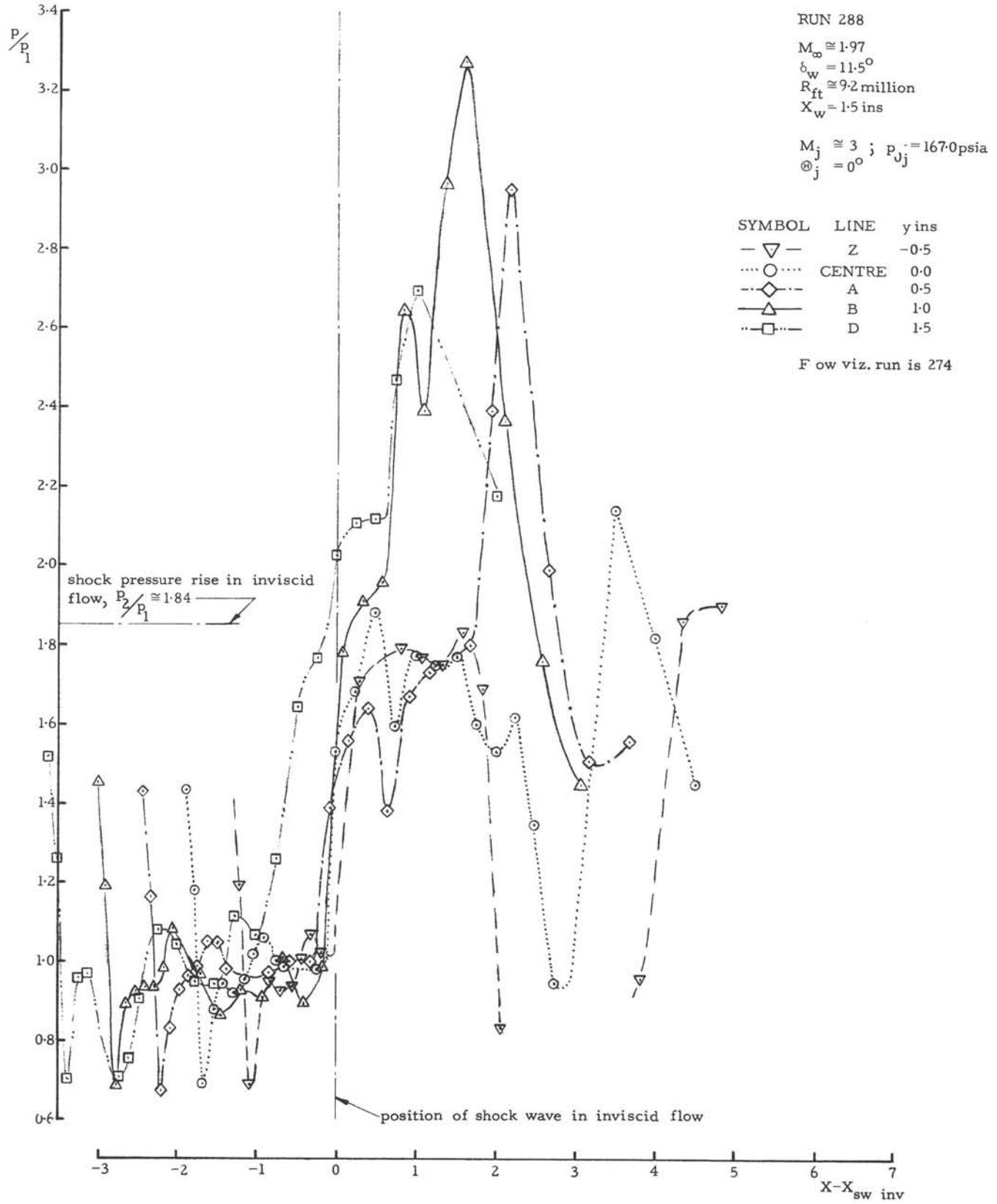

FIG. 97(d): PRESSURES ALONG TEST WALL AT MACH 2 AND WEDGE ANGLE OF 11.5-DEGREES AT A FIXED WEDGE POSITION, XWLE = 1.5-IN., WITH WALL JET ON: AT θ_j = 0-DEGREE

EMPTY TUNNEL

WITH WEDGE AT $\delta_w = 11.5°$

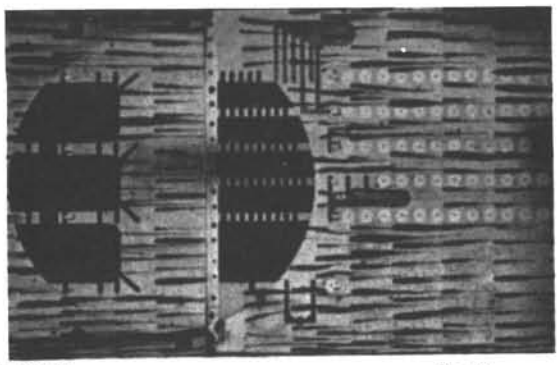

RUN 268 $P_{oj} = 0$

UNDISTURBED BOUNDARY-LAYER THICKNESS, $\delta \cong 0.2$ in., $R_\delta = 1.5 \times 10^5$

$P_0 \cong 34$ psia

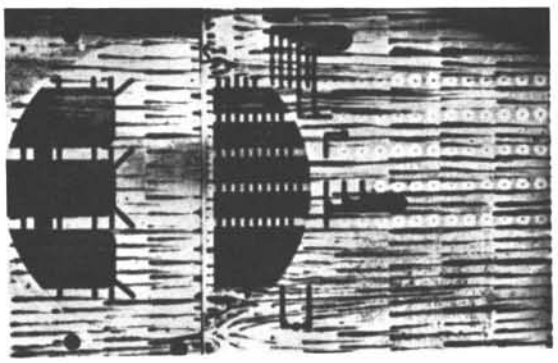

RUN 270 $P_{oj} = 114$ psia

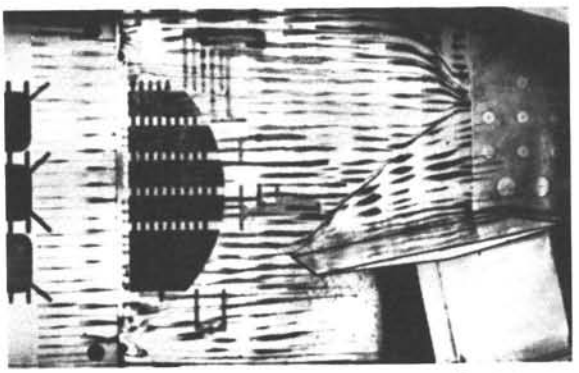

RUN 277 $P_{oj} = 114$ psia

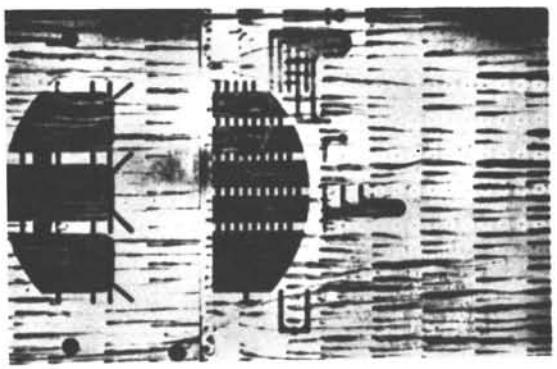

RUN 269 APPROX DESIGN CASE $P_{oj} = 171$ psia

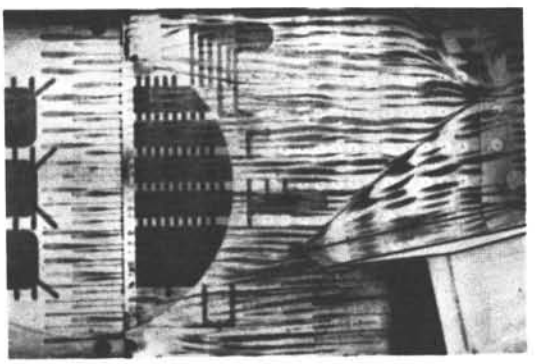

RUN 273 $P_{oj} = 171$ psia

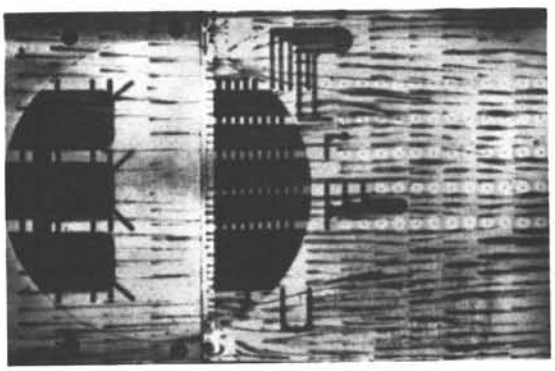

RUN 271 $P_{oj} = 214$ psia

STATION 1 X in -2.0 | JET EXIT 0.625 | 18 2.625

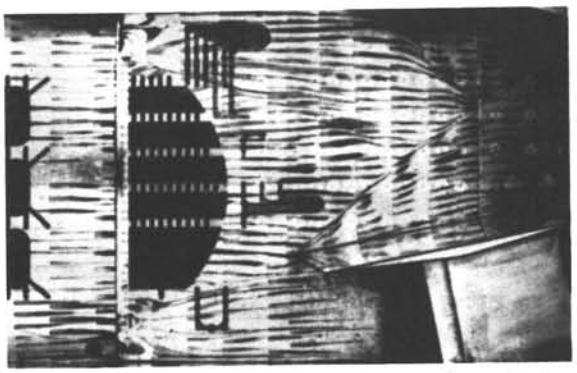

RUN 275 $P_{oj} = 214$ psia

FIG. 98: AIR INJECTION: SURFACE FLOW VISUALIZATION TO DEMONSTRATE INCREASING STAGNATION PRESSURE OF JET FLOW WITH θ_j = 0-DEGREE AND $M_j \cong 3$: IN EMPTY TUNNEL, AND AT δ_w = 11.5-DEGREES (XWLE = 3.0-IN.)

RUN 290

$M_\infty \cong 1{\cdot}97$
$\delta_w = 11{\cdot}5^\circ$
$R_{ft} \cong 9{\cdot}2$ million
$X_w = 3{\cdot}0$ ins

$M_j \cong 3$; $p_{0_j} = 167{\cdot}1$ psia
$\Theta_j = 0^\circ$

Flow viz. run is 273 (Fig. 98)

SYMBOL	LINE	y ins
—▽—	Z	−0·5
····○····	CENTRE	0·0
-·◇·-	A	0·5
—△—	B	1·0
-·□·-	D	1·5

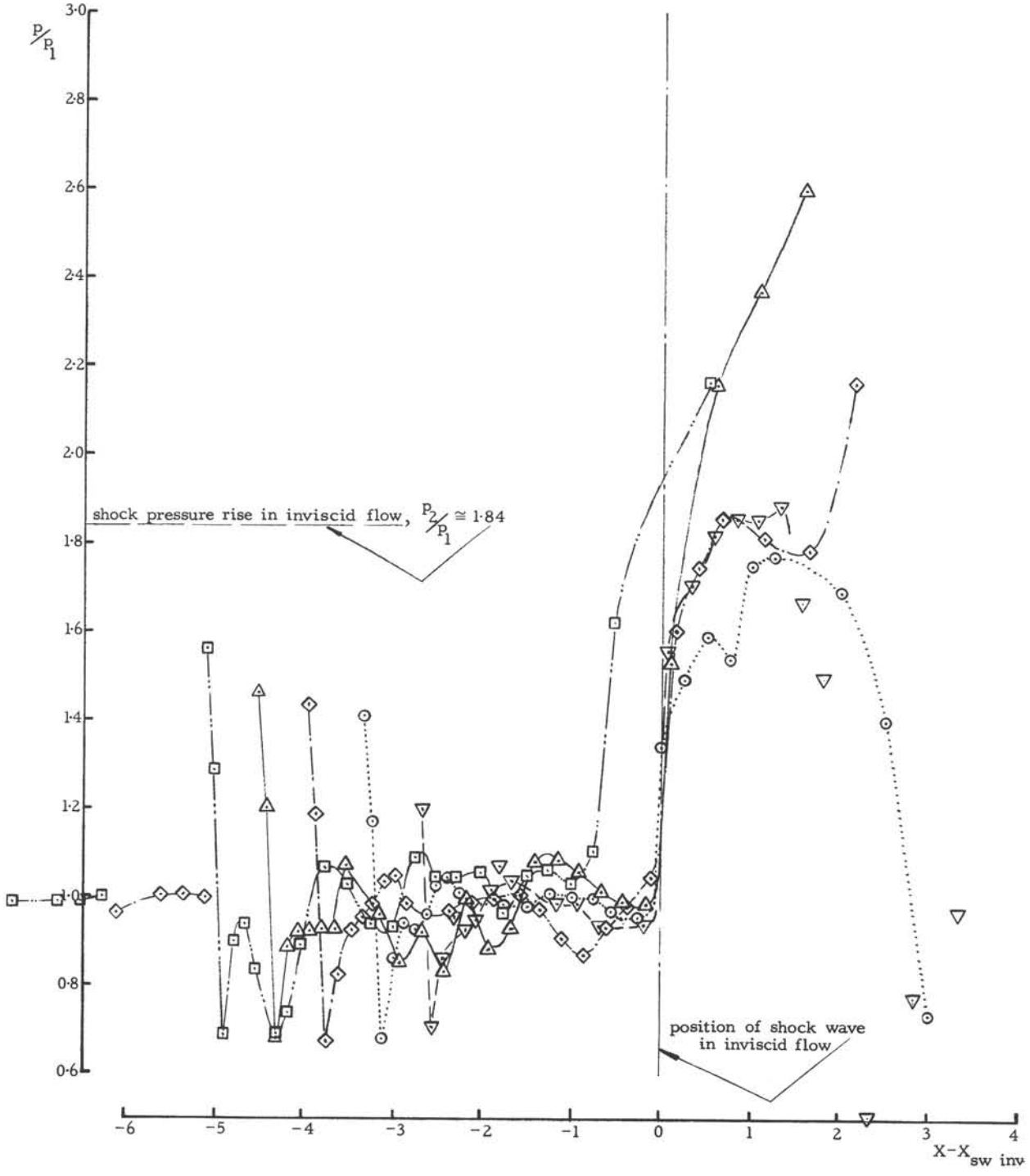

FIG. 99: PRESSURES ALONG TEST WALL AT MACH 2 AND WEDGE ANGLE OF 11.5-DEGREES AT A FIXED WEDGE POSITION, XWLE = 3.0-IN., WITH WALL JET ON: θ_j = 0-DEGREE

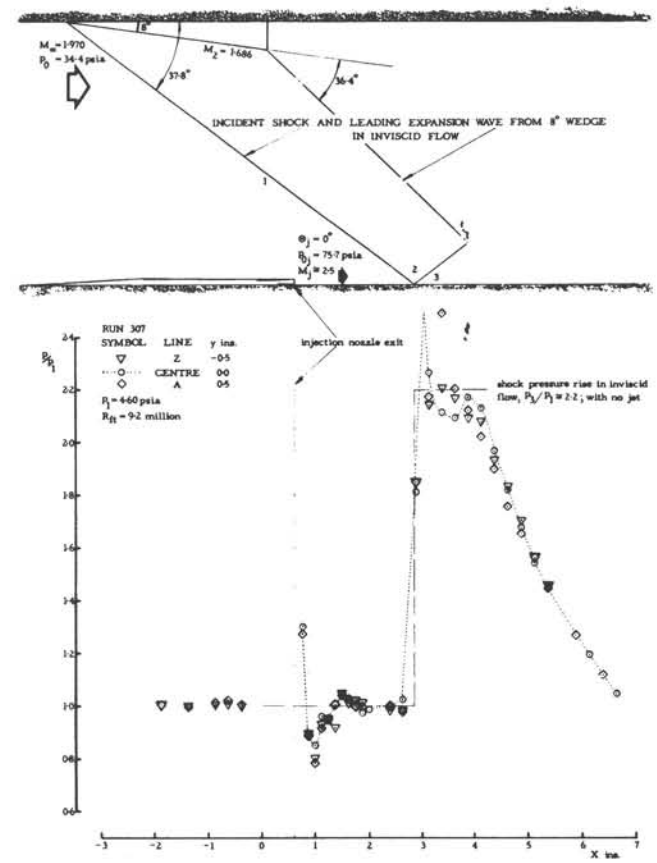

WALL PRESSURES THROUGH QUASI-2D SHOCK/BOUNDARY-LAYER INTERACTION AT MACH 2 AND WEDGE ANGLE OF 8°, WITH WALL JET ON, $M_j \cong 2{\cdot}5$

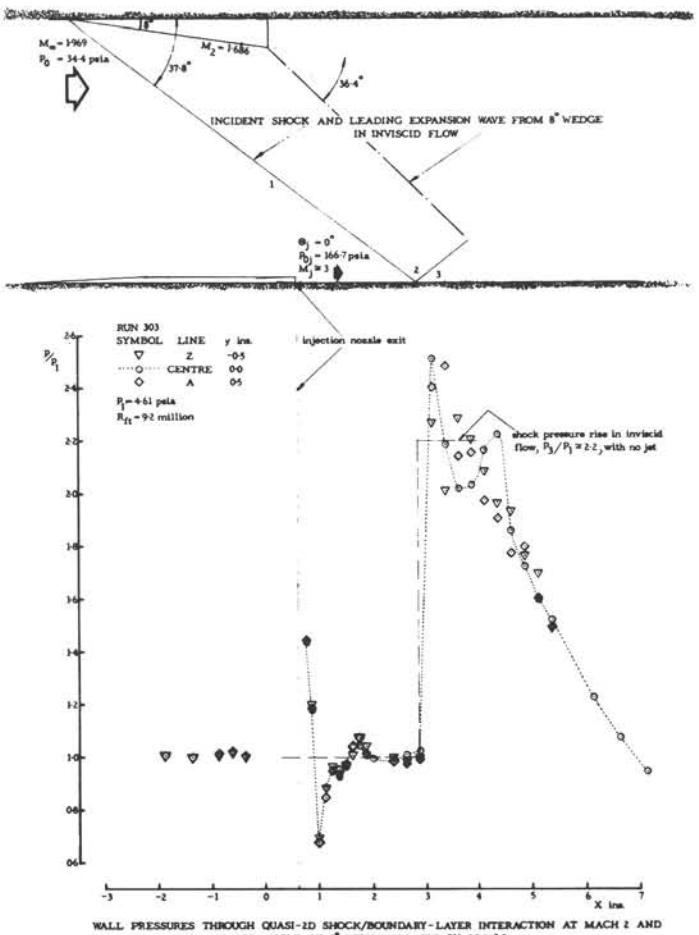

WALL PRESSURES THROUGH QUASI-2D SHOCK/BOUNDARY-LAYER INTERACTION AT MACH 2 AND WEDGE ANGLE OF 8°, WITH WALL JET ON, $M_j \cong 3{\cdot}0$

FLOW VISUALIZATION

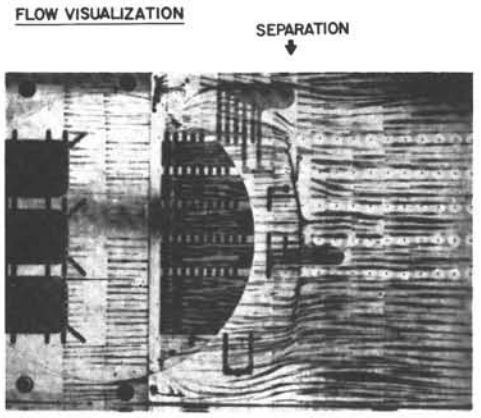

P_{oj} = 75·7 psia
$M_j \cong 2{\cdot}5$

UNDISTURBED BOUNDARY-LAYER THICKNESS, $\delta \cong 0{\cdot}2$ in., $R_\delta = 1{\cdot}5 \times 10^6$, P_o = 34 psia

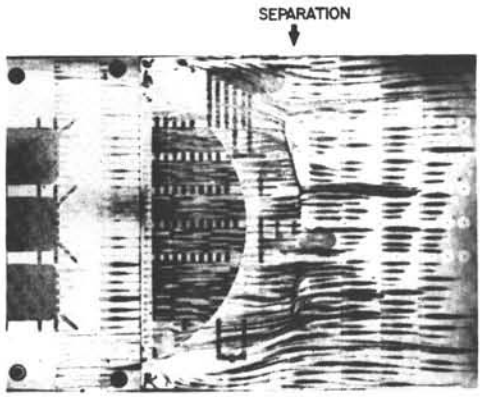

P_{oj} = 166·7 psia
$M_j \cong 3$

FIG. 100: AIR INJECTION: SURFACE PRESSURES AND FLOW VISUALIZATION THROUGH 2D SHOCK BOUNDARY-LAYER INTERACTION FOR δ_w = 8-DEGREES AT MACH 2, WITH $M_j \cong 2.5$ AND 3.0, AND θ_j = 0-DEGREE

PRESSURE DISTRIBUTIONS

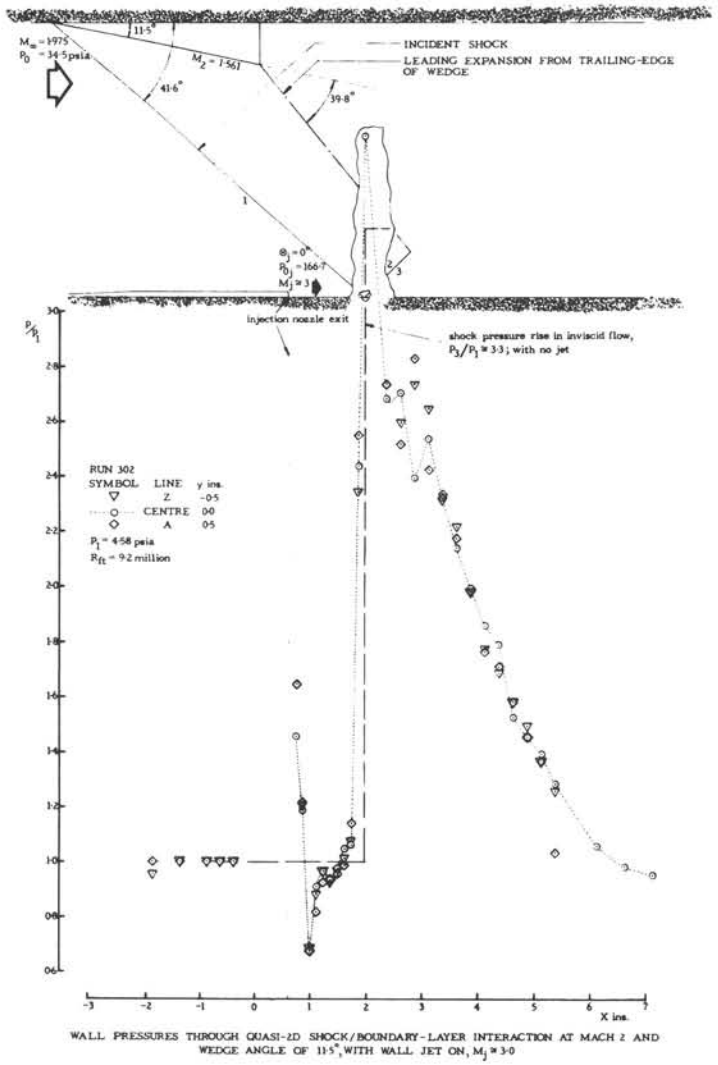

WALL PRESSURES THROUGH QUASI-2D SHOCK/BOUNDARY-LAYER INTERACTION AT MACH 2 AND WEDGE ANGLE OF 11·5°, WITH WALL JET ON, $M_j \cong 3{\cdot}0$

FLOW VISUALIZATION

UNDISTURBED BOUNDARY-LAYER THICKNESS, $\delta \cong 0{\cdot}2$ in., $R_\delta = 1{\cdot}5 \times 10^6$

$p_o = 34$ psia

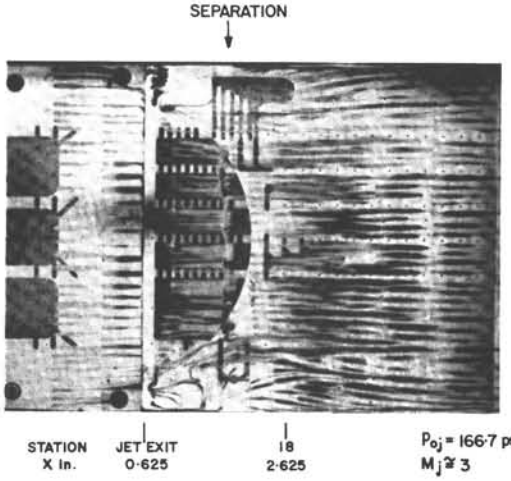

FIG. 101: AIR INJECTION: SURFACE PRESSURES AND FLOW VISUALIZATION THROUGH 2D SHOCK BOUNDARY-LAYER INTERACTION FOR δ_w = 11.5-DEGREES AT MACH 2, WITH $M_j \cong 3$, AND θ_j = 0-DEGREE

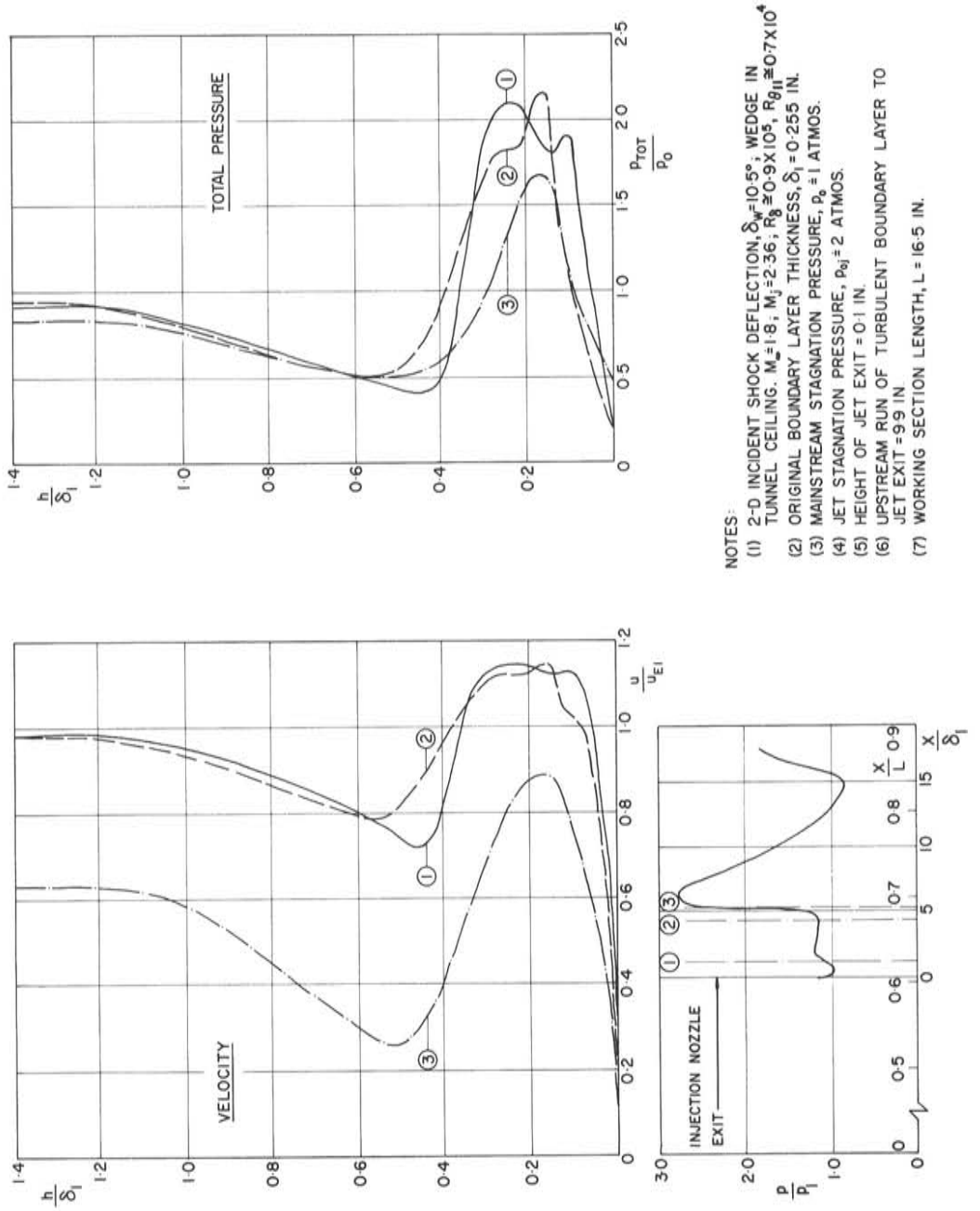

FIG. 102: TYPICAL PROFILES DOWNSTREAM OF JET EXIT IN 2D SHOCK BOUNDARY-LAYER INTERACTION, FROM REFERENCE 5

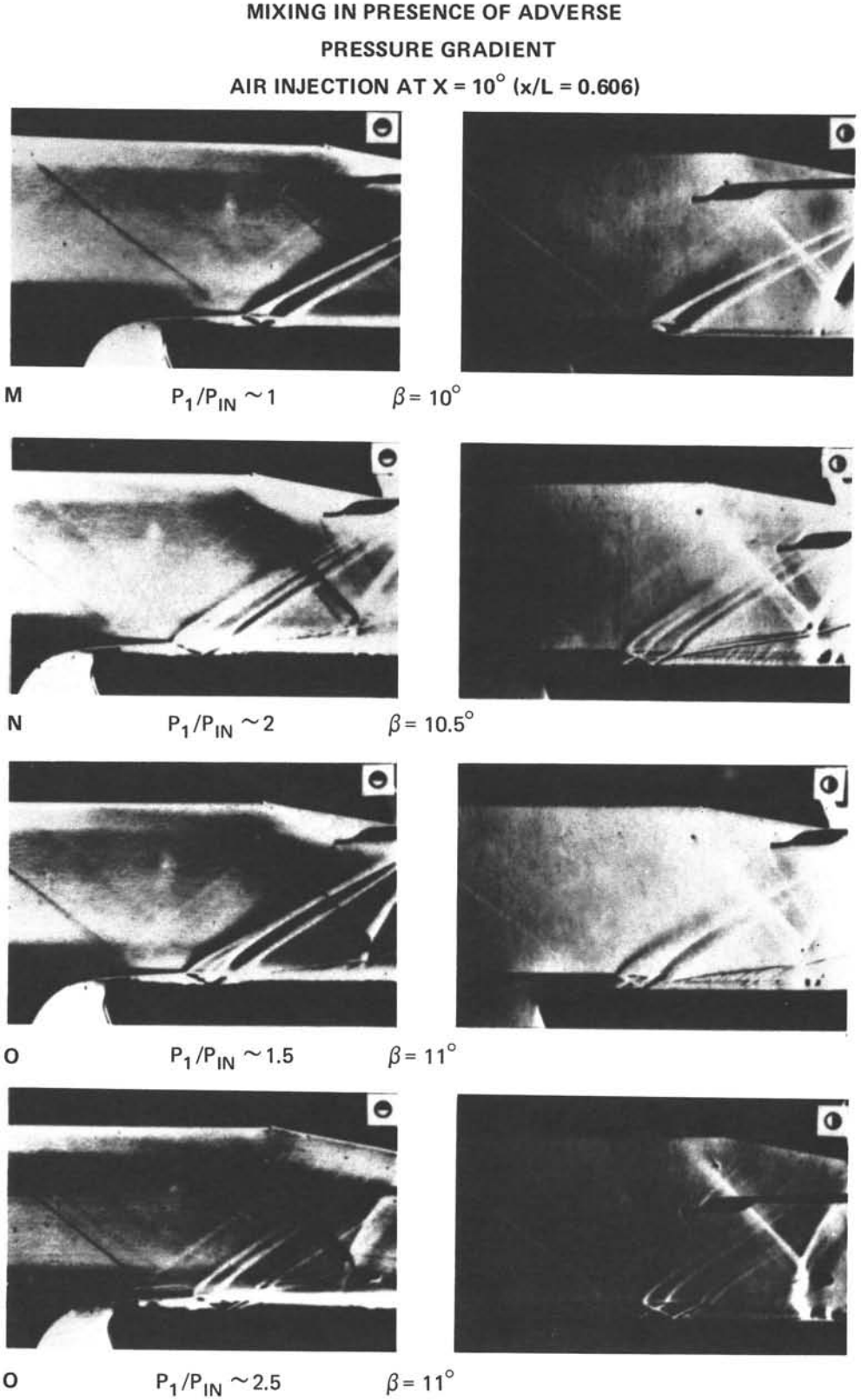

FIG. 103: TYPICAL SCHLIEREN FLOW VISUALIZATION ACCOMPANYING PROFILES OF FIGURE 102

APPENDIX 1

A RESUME OF THE THREE-DIMENSIONAL, COMPRESSIBLE TURBULENT BOUNDARY-LAYER CALCULATION METHOD OF NASH

As the 3D compressible turbulent boundary-layer calculation method of Nash has not been published in full, we have taken the liberty of excerpting the relevant equations, especially those treating the Reynolds stresses, from a NASA Contract Report[115] that has seen only limited distribution. We have followed the notation of Nash in this appendix to facilitate reference to his 3D turbulent boundary-layer calculation method in incompressible flow[121].

Briefly, Nash's method provides the capability of calculating profiles of mean velocity and turbulent shear stress in a fully three-dimensional flow field over a generally curved surface, in arbitrary pressure gradients and with no restrictions to small crossflows. The method involves the numerical integration of the equations of motion and the continuity equation, together with an empirical equation for the Reynolds stresses, that is based on the turbulent kinetic energy equation. The extension of the incompressible method to treat compressible flows is made with the assistance of the Crocco relation for temperature (rather than including the energy equation) which should be valid for Mach numbers at least up to two in the presence of an adiabatic wall.

In the formulation of the programme supplied to us by Nash, the general curvilinear co-ordinate system (x, y, z) is set up to calculate the flow over a flat plate swept wing with prescribed pressure distribution, where the wing root and tip are stream surfaces parallel to the undisturbed mainstream at infinity. The plane y = 0 represents the surface of the wing, the x- and z-axes are respectively parallel and perpendicular to the approaching mainstream flow, and the swept planform is situated in the positive x-z quadrant*. In view of the tunnel geometry in the swept interaction experiment, we adopted the present formulation and simply 'unswept' the wing. The plane x = 0 is far upstream in the nominal undisturbed boundary layer, while x = 1 is situated somewhere near the wedge trailing edge. The normalizing distance for x is that absolute length between the start and end points of the calculation, parallel to the tunnel centre-line (equivalent to the streamwise chord dimension of the swept wing flow). The test case chosen was with the deflected wedge angle, δ_W = 8-degrees at Mach 2, and we situated the deflected wedge leading-edge in the plane of the 'wing root'. However, since the boundary condition at the wing root prescribed a flow parallel to the oncoming mainstream, the deflected wedge surface was neglected, and the measured shock pressure rise plus the upstream undisturbed momentum deficit thicknesses were the essential inputs to the programme. The mean velocity and shear stress profiles at the commencement of the calculation were generated in the computer programme.

The symbols required to follow the general formulation are as follows: these are used only in this appendix, not in the main report.

a_1	empirical constant, identified with the ratio of the resultant shear stress to the resultant turbulent kinetic energy, see Equation (A-1.9)
a_2	empirical function of (y/δ), a diffusion parameter, see Equation (A-1.9)
h_1, h_3	metric coefficients
K_{13}, K_{31}	curvature parameters
L	dissipation length; function of (y/δ)

---

* Note that the co-ordinates (x, y, z) in the calculation correspond with (x, h, y) in the experiment, when the leading-edge is unswept.

M	Mach number
p	static pressure
Q	resultant mean velocity, $Q^2 = U^2 + W^2$, to the boundary-layer approximation
s	length of line in space
U, V, W	mean velocity components in the x, y, z directions
u, v, w	fluctuation velocity components, corresponding with U, V, W
x, y, z	orthogonal curvilinear co-ordinates, with y measured normal to wing surface. U, V, W are in the respective directions: x, y, z
Γ	constant in Equations (A-1.15)
δ	boundary-layer thickness
δ^*	displacement thickness, Equation (A-1.16)
ρ	air density
Φ_x, Φ_z	functions in Equations (A-1.9) and (A-1.10)
τ	magnitude of shear stress vector within boundary layer
τ_{Wx}, τ_{Wz}	skin friction components in the x, z directions

Subscripts

e	outer edge of boundary layer
∞	freestream at infinity

We choose an orthogonal curvilinear co-ordinate system (x, y, z) with the wing surface at y = 0. h_1 and h_3 are metric coefficients for distances measured in the x and z directions, such that the length of line element, ds, is

$$(ds)^2 = h_1^2(dx)^2 + (dy)^2 + h_3^2(dz)^2 \qquad \text{(A-1.1)}$$

The curvature parameter K_{13}, K_{31} are defined by

$$K_{13} = \frac{1}{h_1 h_3}\frac{\partial h_1}{\partial z}; K_{31} = \frac{1}{h_1 h_3}\frac{\partial h_3}{\partial x} \qquad \text{(A-1.2)}$$

and represent the geodesic curvatures of the lines x = constant, z = constant. The metric coefficient, h_2, associated with distances measured in the y direction is chosen to be unity, with the result that the curvature parameters K_{21}, K_{23} are identically zero[121].

The two momentum equations for the flow in a compressible turbulent boundary layer then are

$$\frac{U}{h_1}\frac{\partial U}{\partial x} + \frac{V\partial U}{\partial y} + \frac{W}{h_3}\frac{\partial U}{\partial z} + (K_{13}U - K_{31}W)W + \frac{1}{\rho h_1}\frac{\partial p}{\partial x} + \frac{1}{\rho}\frac{\partial}{\partial y}(\rho\overline{uv}) = 0 \qquad \text{(A-1.3)}$$

and

$$\frac{U}{h_1}\frac{\partial W}{\partial x} + \frac{V\partial W}{\partial y} + \frac{W}{h_3}\frac{\partial W}{\partial z} + (K_{31}W - K_{13}U)U + \frac{1}{\rho h_3}\frac{\partial p}{\partial z} + \frac{1}{\rho}\frac{\partial}{\partial y}(\rho\overline{vw}) = 0 \qquad \text{(A-1.4)}$$

where U, V, W are the mean velocity components in the x, y, z directions, u, v, w are the corresponding fluctuation components and the Reynolds direct stress gradient and laminar stress terms have been neglected. A bar over the products of fluctuating quantities denotes time average.

The continuity equation is

$$\frac{1}{h_1}\frac{\partial}{\partial x}(\rho U) + \frac{\partial}{\partial y}(\rho V) + \frac{1}{h_3}\frac{\partial}{\partial z}(\rho W) + \rho(K_{31}U + K_{31}W) = 0 \qquad \text{(A-1.5)}$$

In Equations (A-1.3) through (A-1.5), V is interpreted to mean

$$V + \frac{1}{\rho}\overline{(\rho' v)} \qquad \text{(A-1.6)}$$

where ρ' is the fluctuating component of density.

It is then assumed that the temperature at any point in the flow can be related to the magnitude of the local velocity vector, Q, via the Crocco relation. Accordingly, the density at a point within the boundary layer is related to the density and Mach number at the outer edge of the boundary layer by

$$\frac{\rho_E}{\rho} = 1 + \frac{\gamma - 1}{2} r M_e^2 \left(1 - \frac{Q^2}{Q_e^2}\right) \qquad \text{(A-1.7)}$$

where r = recovery factor (= 0.89) and Q is the resultant mean velocity

$$Q^2 = U^2 + W^2 \qquad \text{(A-1.8)}$$

to the thin boundary-layer approximation. The assumption implicit in Equation (A-1.7) is that the wall is adiabatic, and that the turbulent Prandtl number is unity.

The components $-\rho\overline{uv}$ and $\rho\overline{vw}$ of the Reynolds shear stress are determined from a pair of rate equations (see Ref. 121). For the case of the boundary layer developing on a non-developable surface of small but finite curvature, these rate equations can be written

$$\frac{U}{h_1}\frac{\partial}{\partial x}(\overline{uv}) + \frac{V}{h_2}\frac{\partial}{\partial y}(\overline{uv}) + \frac{W}{h_3}\frac{\partial}{\partial z}(\overline{uv}) + (K_{13}U - K_{31}W)\,\overline{vw} + 2a_1\left[(\overline{uv}^2 + \overline{vw}^2)^{1/2}\frac{\partial U}{\partial y}\right.$$

$$\left. + \Phi_x + \frac{\partial}{\partial y}(a_2\overline{uv}) + \frac{\overline{uv}}{L}(\overline{uv}^2 + \overline{vw}^2)^{1/4}\right] = 0 \qquad \text{(A-1.9)}$$

and

$$\frac{U}{h_1}\frac{\partial}{\partial x}(\overline{vw}) + \frac{V}{h_2}\frac{\partial}{\partial y}(\overline{vw}) + \frac{W}{h_3}\frac{\partial}{\partial z}(\overline{vw}) + (K_{31}W - K_{13}U)\,\overline{uv} + 2a_1\left[(\overline{uv}^2 + \overline{vw}^2)^{1/2}\frac{\partial W}{\partial y}\right.$$

$$\left. + \Phi_z + \frac{\partial}{\partial y}(a_2\overline{vw}) + \frac{\overline{vw}}{L}(\overline{uv}^2 + \overline{vw}^2)^{1/4}\right] = 0 \qquad \text{(A-1.10)}$$

where Φ_x, Φ_z have the property that

$$\overline{uv}\,\Phi_x + vw\,\Phi_z = 0 \qquad \text{(A-1.11)}$$

If Equations (A-1.9) and A-1.10) are combined into one for the magnitude of the turbulent shear stress vector,

$$(\overline{uv}^2 + \overline{vw}^2)^{1/2} = \tau/\rho \qquad \text{(A-1.12)}$$

the resulting equation is of the same form as the empirically modified turbulent kinetic-energy equation used by Bradshaw et al[122], which is

$$\frac{U}{h_1}\frac{\partial\tau}{\partial x} + \frac{V}{h_2}\frac{\partial\tau}{\partial y} + \frac{W}{h_3}\frac{\partial\tau}{\partial z} + 2a_1\left[\rho\overline{uv}\frac{\partial U}{\partial y} + \rho\overline{vw}\frac{\partial W}{\partial y} + \frac{\partial}{\partial y}(a_2\tau) + \frac{\tau^{3/2}}{\rho^{1/2}L}\right] = 0 \qquad \text{(A-1.13)}$$

On this basis, a_1 is taken to be the same constant, and a_2 and L the same functions of y/δ as in the 2D incompressible case; a_1 is identified with the ratio of the resultant shear stress to the intensity of the turbulence, $\overline{\rho q^2}$, L is identified with the dissipation length and a_2 is a diffusion parameter.

The terms

$$2a_1(\overline{uv}^2 + \overline{vw}^2)^{1/2}\frac{\partial U}{\partial y}\ ,\ 2a_1(\overline{uv}^2 + \overline{vw}^2)^{1/2}\frac{\partial W}{\partial y}$$

are assumed to represent the combined effect of production and the part of the pressure-strain correlation which opposes it, and the terms

$$\frac{2a_1}{L}\overline{uv}(\overline{uv}^2 + \overline{vw}^2)^{1/4}\ ,\ \frac{2a_1}{L}\overline{vw}(\overline{uv}^2 + \overline{vw}^2)^{1/4}$$

are identified with the remaining part.

By virtue of Equation (A-1.11), the functions Φ_x, Φ_z do not contribute to the magnitude of the shear stress vector but determine its directional response. The method of Nash can be regarded as corresponding with a particular choice of Φ_x, Φ_z, which leads to a rapid direction response of the shear stress vector to a rotation of the rate-of-strain vector, such that the two vectors are everywhere co-directional

$$\overline{uv} \Big/ \frac{\partial U}{\partial y} = \overline{vw} \Big/ \frac{\partial W}{\partial y} \tag{A-1.14}$$

The essential difference between the approaches of Bradshaw[123] and Nash is that Bradshaw makes $\Phi_x = \Phi_z = 0$, which yields a relatively slow direction response.

Φ_x, Φ_z are given by

$$\Phi_x = \Gamma \left[(\overline{uv}^2 + \overline{vw}^2)^{1/2} \frac{\partial U}{\partial y} + \overline{uv} \left\{ \left(\frac{\partial U}{\partial y} \right)^2 + \left(\frac{\partial W}{\partial y} \right)^2 \right\}^{1/2} \right]$$

$$\Phi_z = \Gamma \left[(\overline{uv}^2 + \overline{vw}^2)^{1/2} \frac{\partial W}{\partial y} + \overline{vw} \left\{ \left(\frac{\partial U}{\partial y} \right)^2 + \left(\frac{\partial W}{\partial y} \right)^2 \right\}^{1/2} \right] \tag{A-1.15}$$

in which Γ is some large number (from experience, any number greater than about four).

Equations (A-1.9), (A-1.10), and (A-1.15) are identical with their incompressible counterparts. It is assumed that they can be carried over to compressible flows without modification, and that the empirical constant a_1 (=0.15) and the empirical functions a_2 and L are the same as in incompressible flow (see Ref. 121). There is no direct experimental support for these assumptions in compressible 3D flow. However, Nash claims[115] that they are probably valid at least up to Mach 2. In 2D flow, they appear approximately valid up to higher Mach numbers, for comparisons between calculations performed by Nash using the Nash method with the experimental data of Peake et al[34] at Mach 4, showed reasonably good agreement.

The method of solution is relatively straightforward, if complex in programming detail. Equations (A-1.3), (A-1.4), (A-1.5), (A-1.9) and (A-1.10) form a hyperbolic set, and are integrated in a 3D domain (x, y, z) by an explicit finite difference method based on a one-step staggered mesh scheme (see Ref. 124). The calculation proceeds in the x-direction, and values of the five dependent variables: U, V, W, $\overline{uv}$, $\overline{vw}$ are computed on successive surfaces x = constant. Twenty collocation points are typically used in the y-direction (normal to the wing surface) and six or seven in the z (or spanwise) direction.

The numerical solution is matched at y = 0.05 δ (approximately) to a separate solution for the law of the wall region. In the inner layer, it is assumed that the resultant velocity Q, and the skin friction, τ_W, mutually satisfy the law of the wall. This assumption then provides an equation for τ_W in terms of Q at the matching station. The direction of the skin friction vector is determined from an extrapolation in the polar plane (U, W) making use of the correct limiting value of $\partial^2 W/\partial U^2$ as $U \to 0$ (or in other words, from the pressure gradient).

The boundary conditions at the wing surface (y = 0) and at the outer surface of the integration domain (at y = 1.25 δ approximately) are handled as in Reference 121. The boundary conditions on the sides of the integration domain call for special treatment. In the programme supplied by Nash, these were stream surfaces at z = constant, parallel to the undisturbed freestream velocity at infinity.

On Displacement Surface Thickness, δ^*

In a fully 3D boundary layer, δ^* cannot be related directly to an integral of the velocity profile at one position on the body surface[117,118]. Instead it can be determined from the normal component of velocity at the boundary-layer edge by means of the partial differential equation

$$\frac{U_e}{h_1}\frac{\partial \delta^*}{\partial x} + \frac{W_e}{h_3}\frac{\partial \delta^*}{\partial z} = \left\{ V - (y - \delta^*)\frac{\partial V}{\partial y} \right\}_{y > \delta} \qquad \text{(A-1.16)}$$

Once the velocity field is computed, this equation can be integrated to give δ^*. We see that Equation (A-1.16) is compatible with the 2D definition of δ^*

$$\delta^* = \int_0^\infty \left(1 - \frac{\rho Q}{\rho_e Q_e}\right) dy \qquad \text{(A-1.17)}$$

either where the velocity profiles are collateral (W proportional to U) or where deviations with respect to x or z vanish, as on an 'infinite' swept wing.

The appropriate boundary conditions required to integrate Equation (A-1.16) are provided by the conditions at the 'wing root' and 'wing tip' planes of symmetry, where $\partial \delta^*/\partial z = 0$, and by the initial velocity profiles.